Quelques études autour de la fission nucléaire

Stefano Matthias Panebianco

Habilitation à Diriger des Recherches

Stefano Matthias PANEBIANCO

Chercheur au CEA
IRFU

Université Paris Saclay
UFR de Physique

Quelques études autour de la fission nucléaire

Soutenue le 21 juin 2018 à Saclay

JURY

Président :	**M. Pierre DÉSESQUELLES**, Professeur, Université Paris Saclay and CSNSM, Orsay (France)
Rapporteurs :	**M^me^ Francesca GULMINELLI**, Professeur, Université de Caen and LPC, Caen (France) **M. Stephan OBERSTEDT**, Scientific Officer, Joint Research Center, Geel (Belgique) **M. Xavier LEDOUX**, Ingénieur chercheur CEA, GANIL, Caen (France)
Examinateurs :	**M^me^ Héloïse GOUTTE**, Ingénieur chercheur CEA, GANIL, Caen (France) **M. Jean-Luc SIDA**, Ingénieur chercheur CEA, Université Paris Saclay et CEA DRF, Saclay (France)

Irfu/DPhN
CEA - Saclay
Orme des Merisiers, Bât. 703
91191 Gif sur Yvette cedex

UFR Sciences
Université Paris Saclay
Bât. 301
91405 Orsay cedex

Table des matières

Avant propos

La rédaction de l'HDR (Habilitation à Diriger des Recherches) est devenue une étape obligée dans la carrière d'un chercheur, en France comme dans nombre d'autres pays. Pour certains, il s'agit de l'occasion, souvent inespérée, de pouvoir se poser, prendre le temps, mettre entre parenthèses la frénésie du travail quotidien et parcourir rétrospectivement ses activités de recherche, les analyser et les replacer dans un contexte plus général et étendu. Pour d'autres, l'HDR représente davantage une contrainte, soit parce qu'elle constitue le dernier obstacle avant un avancement de carrière, soit parce qu'elle officialise la capacité d'encadrement d'un chercheur alors que souvent elle est déjà bien établie. L'élément qui fait pencher la balance dans un sens ou dans l'autre est à mes yeux le manuscrit. En effet, c'est bien le travail rédactionnel qui, par son caractère chronophage, rentre en conflit avec les obligations professionnelles quotidiennes (qui ne sont pas toutes faciles à mettre en attente pendant des périodes significatives). D'autre part, c'est notamment le temps nécessaire à l'écriture qui rend possible et souvent alimente la réflexion, l'analyse profonde et fournit le recul nécessaire à la relecture d'une longue période d'activité scientifique.

Dans mon cas, le changement de domaine de recherche que j'ai effectué depuis plus de deux ans et qui m'a amené à m'impliquer au sein de l'expérience ALICE au LHC et à prendre en charge la coordination de l'un de ses détecteurs, constitue une difficulté supplémentaire. En effet, la distance temporelle qui me sépare de mes dernières activités de recherche en physique nucléaire de basse énergie est suffisamment importante pour que le travail d'analyse et de synthèse rétrospective, nécessaire à l'aboutissement d'un manuscrit lisible et intéressant, soit davantage complexe et périlleux que plaisant et linéaire. A cela s'ajoute l'impossibilité pour moi de fournir des perspectives articulées et crédibles aux différents sujets scientifiques qui m'ont intéressé par le passé et auxquels, par la force des choses, je n'ai plus rien de concret à apporter dans le court et moyen terme. En quelques mots, la tâche est rude et il serait hypocrite de le cacher, aussi bien à soi-même qu'aux éventuels lecteurs (certes peu nombreux) qui, comme les membres du jury qui m'ont fait l'honneur d'examiner mon travail, auraient, par choix ou par hasard, à se pencher sur ce texte.

Pour toutes ces raisons, mon choix rédactionnel pour ce manuscrit d'HDR a été de construire un court récit autour d'une compilation choisie d'articles publiés dans des journaux à comité de lecture. En effet, il me semble que le contenu de ces articles représente de manière suffisamment précise et honnête l'étendue et la diversité de mes activités scientifiques autour de la fission nucléaire. En outre, il me semble utile que ces articles ne fassent pas l'objet d'une réécriture ou d'un travail de paraphrase, ce qui serait à la fois stérile et plutôt inefficace, et qui nuiraient certainement à la compréhension. J'ai donc préféré inclure ces articles dans leur version publiée, sans modifications

ni ajouts. Cependant, le plaisir pour la parole écrite, qui m'habite depuis tout petit, et l'envie de replacer mes activités dans mon histoire de physicien, m'ont poussé à accompagner ces articles par des courts chapitres d'introduction. En effet, les années de travail qui ont amené à la production des résultats scientifiques publiés dans ces articles méritent, j'en suis convaincu, d'être racontées pour expliquer comment le travail de recherche s'est développé, de quelles considérations il est le fruit et pourquoi il a été mené dans une direction plutôt qu'une autre.

Cette approche a donc pour but d'établir un récit chronologique et logique de la démarche scientifique qui a été la mienne et celle des nombreux collègues avec qui j'ai eu le plaisir de collaborer pendant mes années de "*fissioniste*". Donner un aperçu de la méthode de travail, des hypothèses opérationnelles et du chemin souvent erratique de la recherche en physique me semble constituer une nécessité, surtout dans le cadre d'un manuscrit comme l'HDR, où les compétences purement scientifiques doivent s'accompagner, me semble-t-il, d'une certaine capacité de prise de hauteur, de recul et d'analyse. Enfin, je ne peux pas cacher au lecteur que ce choix rédactionnel est également le fruit de mes convictions philosophiques les plus profondes et qui reposent sur la nécessité d'intégrer expressément dans la pratique du métier de physicien une dimension plus méthodologique qui permette l'objectivation de la démarche, de son contexte sociologique, axiologique et opérationnel (je dirais même "artisanal"). D'une certaine manière, il s'agit d'un clin d'œil à mon collègue et ami Thomas Duguet et à nos interminables discussions sur la pratique du physicien qui ont abouti au constat partagé autour de la nécessité d'une production scientifique qui aurait comme devise "*How it really happened*".

Remerciements

Comme lors de la rédaction du manuscrit de thèse de doctorat, il est juste et plaisant pour moi de procéder au rituel des remerciements. C'est un exercice de style que j'approche avec le même soin, mais pas tout à fait avec la même naïveté, conscient que cette page risque d'être la plus lue de ce manuscrit.

Je tiens tout d'abord à remercier très chaleureusement les membres de mon jury pour leur disponibilité, les commentaires avisés sur le manuscrit et la discussion riche et passionnante que nous avons eue lors de la soutenance. Un grand merci donc à Francesca Gulminelli, Stephan Obersedt et Xavier Ledoux pour avoir également accepté d'être rapporteurs de ce travail et à Pierre Desesquelles d'avoir bien voulu présider mon jury. Un mot spécial va à Héloise Goutte que je tiens à remercier du fond du coeur pour son soutien continu et bienveillant pendant les années où elle a officié en tant que Chef du Service de Physique Nucléaire de l'Irfu. Enfin, il m'est difficile de trouver les mots pour exprimer l'honneur, le plaisir et la joie que j'ai eu à

Introduction

Les activités de recherche qui ont animé les quinze premières années de ma carrière de physicien s'inscrivent dans le programme scientifique mené au sein de l'équipe "*Mesures nucléaires et modélisation*" du Service (aujourd'hui Département) de Physique Nucléaire de l'Institut de recherche sur les lois fondamentales de l'univers (Irfu, anciennement Dapnia) au CEA Saclay. Ce programme a porté et porte encore aujourd'hui sur l'étude des mécanismes des réactions nucléaires de "basse" énergie (en réalité l'échelle en énergie s'étend, pour faire simple, du meV au GeV, c'est à dire de la fission thermique à la spallation). Dès mon recrutement au CEA au milieu des années 2000, la plupart des travaux effectués au sein l'équipe dans ce domaine visait à étudier les processus de transmutation des actinides mineurs. Il s'agissait d'utiliser des hauts flux de neutrons thermiques, typiquement ceux du réacteur à haut flux de l'Institut Laue-Langevin à Grenoble, pour explorer les longues chaines de transmutation et en extraire les sections efficaces de fission et capture radiative, ainsi que les rapports d'embranchement. C'était en particulier le but du projet Mini-Inca [1–3], fruit d'une collaboration entre l'ILL de Grenoble, le CEA Saclay et le CEA Cadarache, qui a permis de mesurer précisément les sections efficaces de fission et capture du Cm-243 et les sections efficaces de capture du Pu-238, Cm-248, Bk-249, Cf-249. Il faut noter que ces mesures présentaient un intérêt spécifique lié aux applications industrielles de la fission nucléaire. En effet, la transmutation des actinides mineurs fait partie d'une des stratégies actuellement envisagées pour la gestion à long terme des déchets le plus radiotoxiques issus des combustibles usés dans les centrales nucléaires. C'est la raison pour laquelle tous ces travaux étaient structurés, en France, autour d'un groupement de recherche appelé GEDEPEON qui associait CEA, CNRS, EDF et AREVA autour des systèmes du futur et de la transmutation des isotopes à vie longue. Au niveau international, l'élément structurant de la communauté scientifique travaillant sur les "données nucléaires" pour les applications était, et est encore aujourd'hui, le développement des bases de données, telles ENDF et JEFF, et plus généralement le travail que l'on appelle d'évaluation des données. C'est d'ailleurs dans ce même cadre que j'ai pu mener des travaux de recherche auprès de l'installation MEGAPIE, première cible de spallation en plomb-bismuth liquide développée pour supporter le dépôt de puissance d'un faisceau de protons de 1 MW, dans laquelle nous avions installé des chambres à fission micrométriques pour caractériser le spectre des neutrons et mesurer le taux de transmutation de l'Am-241 et du Np-237 [4].

C'est dans ce contexte que j'ai commencé à m'intéresser à l'étude de la fission via la caractérisation des ses fragments. Je pourrais lister ici une série extrêmement longue de références bibliographiques sur la fission, sa découverte, les principaux résultats théoriques et expérimentaux et, en particulier, sur les derniers 30 ans d'études systématiques sur les fragments de fission. Je préfère proposer au

lecteur deux seuls ouvrages de synthèse qui ont nourri mon apprentissage et ma réflexion et qui rendent hommage à deux collègues, fissionistes éminents, avec qui j'ai eu le plaisir et l'honneur d'échanger au cours de mes recherches : d'une part les notes, rédigées en français, du cours intitulé "*La fission : de la phénoménologie a la théorie*" tenu par Jean-François Berger du CEA Bruyères-le-Châtel dans le cadre de l'école Joliot Curie 2006 [5] et l'ouvrage de référence écrit par Cyriel Wagemans qui porte le simple titre "*The nuclear fission process*" [6]. Ces deux ouvrages et, comme le rappelle la formule consacrée, toutes les références qui s'y trouvent, fournissent un panorama vraiment complet des nombreuses observables associées à la fission et aux corrélations très riches qui existent entre ces quantités.

En effet, les observables liées à la fission nucléaire peuvent être schématiquement séparés en deux groupes, chacun correspondant à un ensemble spécifique de propriétés du processus. Dans une certaine mesure, la fission peut être simplement résumée à une réaction nucléaire impliquant un noyau composé excité et conduisant à sa division en deux ou plusieurs noyaux plus légers. Sous cette approximation on peut séparer ce mécanisme en deux phases : la formation du noyau composé et la production de fragments de fission, suivie de leur désexcitation.

En ce sens, le mécanisme de formation du noyau composé (capture de neutrons ou de particules chargées sur le noyau parent, excitation électromagnétique, réaction de transfert, etc.), son énergie d'excitation, son spin et donc sa structure nucléaire sont d'abord responsables de la probabilité pour ce noyau de fissionner (car la fission est un processus en compétition avec d'autres mécanismes de désexcitation) et fixent donc les conditions aux limites de son évolution jusqu'à la scission en fragments. Les principaux observables liés à cette phase «préparatoire» sont plutôt liées à la structure nucléaire du noyau composé et à l'énergie potentielle disponible pour le processus. Cette énergie est fonction de la déformation du noyau et est largement sensible à sa structure microscopique ; elle définit les barrières de fission et leurs caractéristiques, en particulier leur hauteur, transmission et pénétrabilité, qui ont un grand impact sur la section efficace de réaction et pilotent la dynamique du processus par les canaux dits de fission.

D'autre part, la compréhension de la dynamique du processus de fission, conduisant à la scission du noyau composé, est probablement l'un des problèmes les plus difficiles en physique nucléaire car seule une connaissance précise de l'état final peut conduire à une description fiable des principales caractéristiques du processus. C'est pour cette raison qu'un effort de recherche important, aussi bien du point de vue expérimental que théorique, a été consacré, depuis la découverte de la fission en 1939, à la mesure précise des rendements et des caractéristiques de production des fragments de fission : leur masse, leur charge nucléaire et leur énergie cinétique. De plus, la caractérisation de l'émission de neutrons et gamma issus de leur désexcitation a toujours été un outil fondamental pour décrire l'excitation et la déformation des fragments et donc pour comprendre le partage d'énergie entre les deux noyaux fils.

Un grand nombre de questions concernant les propriétés des fragments de fission étaient et, me semble-t-il, sont en grande partie encore ouvertes. Tout d'abord, il est très compliqué de décrire précisément et de manière prédictive comment l'énergie d'excitation du noyau parent est transférée aux fragments et comment ils la partagent. De plus, la force du couplage entre les excitations individuelles et collectives, l'impact des densités de niveaux et la disparition des effets de couche avec l'énergie d'excitation, la présence d'effets pair-impair sur les rendements en masse et en charge et la population en spin des fragments sont encore sujets à discussions sur leur interprétation et ne parviennent pas à être entièrement décrits par la théorie. Afin de répondre à ces questions, différentes observables sont nécessaires dans une large gamme de systèmes fissionnants et d'énergies d'excitation. Par exemple, la multiplicité des neutrons et l'énergie cinétique totale en fonction de l'énergie d'excitation du noyau composé sont nécessaires pour investiguer le partage d'énergie entre les fragments et, plus généralement, les propriétés des configurations de scission. L'évolution des effets de couche dans le système fissionnant et dans les fragments sont étudiés par l'analyse

des rendements en masse et isotopiques des fragments, ainsi que de la corrélation entre l'énergie du fragment et la multiplicité des neutrons. D'ailleurs, cette corrélation est souvent étudiée en fonction de l'énergie d'excitation du noyaux composé puisque les effets de couche sont supposés disparaître pour une énergie incidente élevée. La même chose peut être dite pour la compréhension des effets pair-impair où l'observable intéressante est l'évolution des rendements des fragments avec les propriétés du noyau composé (fissilité, asymétrie pair-impair, énergie d'excitation). Enfin, l'étude de la corrélation entre l'énergie cinétique totale et la masse du fragment renseigne sur l'énergie de déformation des fragments.

Au-delà de l'intérêt de recherche fondamentale, il est évident que l'application majeure pour laquelle une connaissance précise du processus de fission joue un rôle essentiel est le réacteur nucléaire. Ceci est déjà vrai pour le fonctionnement des centrales nucléaires actuelles, largement basées sur des réacteurs à eau légère utilisant la fission thermique des isotopes U-235 et Pu-239. D'autre part, le développement important de systèmes nucléaires innovants, dits de Génération IV, principalement basés sur des réacteurs à neutrons rapides et conçus, entre autres, pour transmuter des déchets nucléaires, nécessite de fournir de nouvelles données de haute qualité pour un grand nombre de noyaux (du Th au Cm) et dans la gamme d'énergie des neutrons allant de l'énergie thermique au domaine dit rapide ($\sim$ 2 MeV). En ce qui concerne ces développements, la communauté des évaluateurs et des utilisateurs de données nucléaires a initialement concentré ses efforts sur l'exploitation des sections efficaces, qui sont clairement le principal contributeur au calcul du réacteur à des fins de conception. Dans les années 2000, parallèlement à l'intérêt constant pour les sections efficaces, la communauté a commencé à s'intéresser de plus en plus aux rendements de fission et aux données de désintégration. Par exemple, les incertitudes sur les rendements en masse et isotopiques deviennent un facteur limitant pour les calculs de précision des assemblages caractérisés par un haut taux d'incinération qui sont directement liés au contrôle et à la sûreté du réacteur. Les rendements des fragments de fission ont une influence directe sur l'estimation de l'équilibre des neutrons dans les systèmes critiques puisqu'ils sont utilisés pour calculer la production des neutrons retardés, l'outil principal pour contrôler la réactivité. D'autre part, les rendements sont également utilisés pour calculer l'empoisonnement de l'élément combustible lié à certains produits de fission (Xe-135, Sm-149 et Gd-157 entre autres) ayant de grandes sections efficaces de capture de neutrons. Ceci est particulièrement important pour les études des combustibles innovants comme pour le cycle Th/U. En effet, les poisons neutroniques limitent le caractère surgénérateur du système en raison de la plus petite fraction de neutrons retardés émis dans le cycle du combustible Th/U par rapport au cycle U/Pu. Les rendements des fragments de fission sont également importants pour l'estimation de la radiotoxicité du combustible usé, ayant des conséquences non négligeables sur leur transport et sur les caractéristiques du dépôts à long terme des déchets nucléaires .

Cet ensemble vaste et hétérogène de motivations a animé mon activité de recherche autour de la fission nucléaire et a permis de bâtir un programme scientifique que je crois être pertinent et cohérent. Ce programme s'est articulé autour de deux grands axes qui constituent les deux sections de ce manuscrit. Tout d'abord, l'axe de recherche expérimentale : le programme de mesure auquel j'ai contribué visait à explorer les distributions des fragments de fission à partir de différents mécanismes d'excitation du noyau fissionnant (fission induite par neutrons, fission induite par réaction de transfert, fission électromagnétique) en utilisant et développant des techniques expérimentales très différentes. Dans la première section du manuscrit, je présente dans un premier temps les travaux effectués sur la fission induite par neutrons auprès du spectromètre de masse Lohengrin à l'ILL. Dans un deuxième chapitre, deux développements plutôt techniques sont illustrés : le premier concerne le spectromètre FALSTAFF qui est en cours de construction et qui utilisera, entre autres, l'installation NFS dans le cadre du projet SPIRAL2 au GANIL ; le deuxième est une étude visant à vérifier la faisabilité d'une chambre à projection temporelle (TPC) pour la détection d'ions lourds de basse énergie (projet FIDIAS). Ces projets étant ceux dans lequel mon implication a été

la plus importante, j'ai fait le choix de ne pas présenter dans ce manuscrit les mesures extrêmement intéressantes et riches concernant la production de neutrons retardés [7] et les résultats sur la fission obtenus en cinématique inverse par réaction de transfert auprès du spectromètre VAMOS au GANIL [8] et par excitation électromagnétique au GSI [9] auxquelles j'ai participé sans pour autant y contribuer de manière significative.

La deuxième section du manuscrit porte sur l'autre axe de recherche dans lequel je me suis impliqué et qui concerne la modélisation du processus de fission. En effet, parallèlement au programme expérimental, j'ai longuement travaillé au développement d'un modèle de point de scission appelé SPY (pour *Scission Point Yields*) et proposant une description statistique et microscopique des fragments de fission. Grâce à cette approche, il a été possible d'interpréter, entre autres, la présence d'une distribution asymétrique dans les rendements en masse des fragments issus de la fission du Hg-180 et de fournir pour la première fois une explication possible aux abondances de certains isotopes présents dans le système solaire.

Par souci de complétude et pour compenser la naturelle frustration que l'on prouve lorsqu'on doit choisir des sujets à traiter pour en laisser d'autres dans l'ombre, j'ai choisi d'inclure en annexe l'intégralité de mon dossier de candidature à l'HDR. Ce dossier contient, entre autres, un résumé de l'intégralité de mes activités de recherche depuis l'obtention de ma thèse de doctorat et peut donc fournir au lecteur une idée plus complète de mes contributions scientifiques et des compétences que j'ai pu développer.

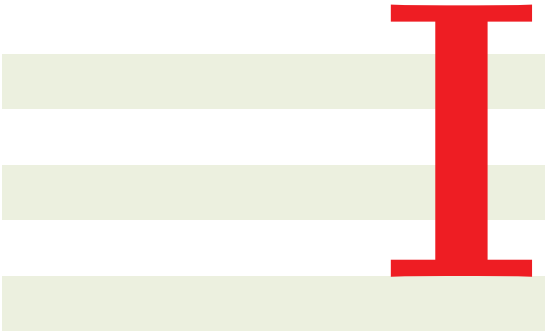

Etudes expérimentales sur la fission

1

Rendements de fission à l'ILL

Le spectromètre de masse Lohengrin auprès du réacteur de recherche à haut flux de l'Institut Laue-Langevin (ILL) à Grenoble est sans aucun doute une des installations qui a permis de produire le plus grand nombre de résultats autour des rendements en masse et isotopiques en fission induite par neutrons thermiques. Ce chapitre présente les mesures des rendements de fission de deux noyaux, le Pu-239 et Am-242, effectuées dans le cadre d'une collaboration entre le CEA Saclay, le CEA Cadarache, l'ILL et le LPSC Grenoble.

1.1 Pourquoi l'ILL ?

Dans l'histoire de la recherche sur la fission, de sa découverte à la description des principales caractéristiques du processus, la fission induite par neutrons a toujours joué le rôle le plus important. De plus, la majorité des applications sont basées sur cette réaction, ce qui fait de son étude la première étape dans la compréhension de l'ensemble du mécanisme. Enfin, comme les neutrons ne sentent pas la répulsion coulombienne des autres noyaux, les réactions nucléaires peuvent être induites par des neutrons d'énergie arbitrairement basse. A cet égard, le réacteur à haut flux HFR (*High Flux Reactor*) de l'ILL constitue un lieu de choix car c'est le réacteur de recherche qui produit le flux de neutrons thermiques le plus intense au monde (1.5×10^{15} n/cm^2/s) avec une puissance thermique de 58,3 MW.

D'autre part, mesurer des fragments de fission n'est pas une simple affaire. Tout d'abord il faut pouvoir extraire les fragments de l'échantillon où a lieu la fission pour pourvoir en mesurer les propriétés. Cela est possible par des méthodes radiochimiques mais les conditions pratiques pour effectuer cette séparation sont très contraignantes en termes de radioprotection et imposent des limites fortes sur l'activité des échantillons et, *in fine*, sur la précision des mesures. L'autre solution consiste à faire fissionner des échantillons extrêmement minces où l'énergie cinétique des fragments est suffisante pour qu'ils soient éjectés de l'échantillon. Cette solution présente l'avantage d'une séparation "spontanée" entre les fragments de fission et la matière fissile cible mais impose des contraintes sévères sur la masse de matière fissile qui peut constituer l'échantillon irradié (quelques microgrammes). Compte tenu des faibles masses en jeu, il est donc nécessaire de disposer d'un flux de neutrons très important pour assurer un taux de fission suffisant à une production statistiquement significative de fragments. Encore une fois, la pertinence du HFR de l'ILL est évidente.

Enfin, la caractérisation des propriétés (masse, charge nucléaire, énergie cinétique) des produits de fission requiert, une fois ces noyaux ayant été séparés de la matière fissile, l'utilisation de techniques spectrométriques de grande précision afin de pouvoir déterminer les rendements de production avec une résolution complète. C'est exactement dans ce but que le spectromètre Lohengrin, un des 40 instruments qui équipent l'ILL, a été conçu et développé dans les années '70.

Lohengrin [10] est un spectromètre de masse avec une vue directe sur une cible placée à environ 50 cm du cœur du réacteur, dans un tube à faisceau appelé H9, où le flux thermique est d'environ 5×10^{14} n/cm^2/s. La cible est constituée d'un isotope fissile (ou fertile) sous la forme d'un dépôt mince sur un support épais de Ti de 9×2 cm^2. En fonction de l'application, l'épaisseur du dépôt est comprise entre environ 100 et 400 μg/cm^2, résultant d'un compromis entre l'intensité souhaitée pour un fragment donné et l'élargissement de la distribution d'énergie cinétique (*straggling*) dû au passage du fragment dans la matière. Une feuille de Ni très fine (0,25 ou 0,5 μm d'épaisseur) recouvre le dépôt afin de réduire sa pulvérisation par les fragments de fission et évite ainsi une combustion trop rapide de la cible. Les fragments qui entrent dans le spectromètre sont déviés et séparés en fonction de leur masse A, de la charge ionique q et de l'énergie cinétique E_k par les actions combinées d'un champ magnétique suivi d'un champ électrique générés respectivement dans un aimant principal et entre les plaques d'un condensateur. Les fragments ayant les mêmes A/q et E_k/q sélectionnés sont ensuite détectés dans le plan focal du spectromètre par une chambre à ionisation à basse pression avec une résolution de masse d'environ 1/350 et une résolution en énergie de 1% pour une cible typique de 70×10 mm^2.

Le choix de l'ILL comme installation privilégiée où mener des études sur les fragments de fission a été aussi lié à la connaissance que l'équipe avait de cette installation. En effet, le guide faisceau utilisé par le spectromètre Lohengrin est le même que celui que nous utilisions dans le cadre du projet Mini-Inca pour la mesure des sections efficaces de capture et fission des actinides mineurs. C'est entre 2006 et 2007, en effectuant quelques shifts dans la casemate de Lohengrin en compagnie d'Herbert Faust (ILL) et Olivier Serot (CEA Cadarache), qu'Alain Letourneau et moi avons commencé à prospecter une implication de l'équipe dans les campagnes de mesure qui avaient lieu à ce moment-là pour améliorer la précision sur certains rendements en masse et isotopiques du Pu-239.

1.2 Les rendements du Pu-239

L'avantage frappant du spectromètre Lohengrin réside dans sa résolution en masse d'environ 1/350, à comparer à une incertitude plus typique de 3 amu sur d'autres expériences en cinématique directe. Cela en fait un instrument de référence pour la détermination des rendements de fission en spectre thermique. Cependant, la technique de détection associée à cet instrument présente deux limitations importantes.

Tout d'abord, un seul des deux fragments de fission est détecté dans le spectromètre, l'autre étant implanté dans le support de l'échantillon cible, et il n'y a évidemment aucun moyen de mesurer les neutrons évaporés ni d'en reconstruire la multiplicité. Par conséquent, cette méthode donne accès uniquement à des rendements de fragments secondaires, c'est-à-dire après évaporation des neutrons.

La deuxième limitation qui affectait Lohengrin à l'époque était liée à la combinaison du spectromètre de masse avec une chambre à ionisation de haute résolution et l'utilisation de la technique de séparation ΔE-E. En effet, cette technique assure une bonne discrimination de la charge nucléaire dans une ligne de masse, permettant une détermination précise du rendement isotopique mais ne peut être appliquée qu'aux produits de fission ayant une charge nucléaire inférieure à environ 40 (c'est-à-dire dans la région de masse légère). Bien qu'avec cette limitation, des nombreuses mesures

de rendements de fission dans la région de masse légère ont effectuées à Lohengrin jusqu'au milieu des années 2000 (^{229}Th, ^{233,235}U, ^{237,238}Np, ^{239,241}Pu, ^{242}Am, ^{245}Cm, ^{249}Cf).

C'est bien à ce moment de l'histoire glorieuse de cet instrument et dans le but de surmonter cette limitation qu'une collaboration est née entre le CEA Cadarache, l'ILL et le CEA Saclay pour développer une nouvelle méthode d'identification des fragments de fission basée sur la spectrométrie gamma. Le principe de la méthode consiste à refocaliser, à l'aide d'un deuxième aimant, les fragments séparés en masse pour les implanter sur une bande en face d'un système de détecteurs HPGe. En effet, les rayons γ émis après la désintégration bêta, caractéristiques de chaque noyau, sont utilisés pour identifier la charge nucléaire des fragments de fission dans la totalité de leur spectre de masse.

La mise en place de la méthode a présenté de nombreuses difficultés liées en grande partie au développement du système d'implantation des ions, basé sur une bande magnétique roulante, afin d'assurer l'évacuation des ions après la mesure, et au développement d'une technique d'analyse capable de prendre en compte les incertitudes associées aux données de décroissance des noyaux. En effet, une grande partie de l'incertitude sur les rendements isotopiques est liée à la connaissance et à la précision des rapports d'embranchement absolus. Après un long travail de développement instrumental et d'analyse, effectué sur un noyau fissile bien connu comme l'U-235, nous avons réussi à valider cette nouvelle méthode par la mesure des rendements isotopiques de Pu-239.

L'article qui suit [11] décrit en détail ces études et atteste d'une réduction globale de l'incertitude d'environ un facteur 2 sur les rendements les plus importants apportée par l'association de la spectrométrie de masse à l'identification des ions par spectroscopie gamma. Le développement de cette nouvelle technique et les mesures présentées dans cet article ont été effectués dans le cadre du travail de thèse d'Adeline Bail avec qui nous avons partagé joies et peines pendant les longues heures passées dans la casemate de Lohengrin ou en salle d'acquisition. Enfin, ces premières mesures des rendements lourds de l'U-235 et, surtout, du Pu-239, ont constitué le ciment d'une collaboration extrêmement fructueuse avec Olivier Serot et Olivier Litaize du CEA Cadarache, ainsi qu'avec Herbert Faust, père du spectromètre Lohengrin, Ulli Köster et Thomas Materna, à l'époque responsables de l'instrument.

1

PHYSICAL REVIEW C **84**, 034605 (2011)

Isotopic yield measurement in the heavy mass region for ^{239}Pu thermal neutron induced fission

A. Bail,* O. Serot, L. Mathieu,† and O. Litaize
CEA, DEN-Cadarache, F-13108 Saint-Paul-lez-Durance, France

T. Materna, U. Köster, and H. Faust
Institut Laue Langevin, 6 rue Jules Horowitz, B.P. 156, F-38042, Grenoble, France

A. Letourneau and S. Panebianco
CEA, DSM-Saclay, IRFU/SPhN, F-91191 Gif-sur-Yvette, France
(Received 14 June 2011; published 6 September 2011)

Despite the huge number of fission yield data available in the different evaluated nuclear data libraries, such as JEFF-3.1.1, ENDF/B-VII.0, and JENDL-4.0, more accurate data are still needed both for nuclear energy applications and for our understanding of the fission process itself. It is within the framework of this that measurements on the recoil mass spectrometer Lohengrin (at the Institut Laue-Langevin, Grenoble, France) was undertaken, to determine isotopic yields for the heavy fission products from the ^{239}Pu(n_{th},f) reaction. In order to do this, a new experimental method based on γ-ray spectrometry was developed and validated by comparing our results with those performed in the light mass region with completely different setups. Hence, about 65 fission product yields were measured with an uncertainty that has been reduced on average by a factor of 2 compared to that previously available in the nuclear data libraries. In addition, for some fission products, a strongly deformed ionic charge distribution compared to a normal Gaussian shape was found, which was interpreted as being caused by the presence of a nanosecond isomeric state. Finally, a nuclear charge polarization has been observed in agreement, with the one described on other close fissioning systems.

DOI: 10.1103/PhysRevC.84.034605 PACS number(s): 25.85.Ec, 29.30.Aj, 29.30.Kv

I. INTRODUCTION

Nuclear fission is a very complex phenomenon resulting from collective and intrinsic excitations within the nucleus in which fine structure effects and energy dissipation play a crucial role. Owing to this complexity and despite many theoretical works, this many-body problem is not yet well understood and the main fission observables are still extremely difficult to reproduce. In particular, various models were proposed to calculate the mass yield distributions (see Ref. [1] for a detailed review of these theoretical models): a statistical model [2], a microscopic-macroscopic model [3], or even a pure microscopic model including a dynamical treatment of the fissioning nucleus [4]. Unfortunately, mass yields obtained by these different calculations are still very far from providing the accuracy required by nuclear applications.

Because fission yield data are of importance in the various nuclear energy applications (reactivity or decay heat in nuclear power, postirradiation experiments, neutron flux determination, and so on), a large number of experiments have been carried out on this field during the last decades and were generally incorporated into the main evaluated nuclear data libraries such as JEFF-3.1.1 [5], ENDF/B-VII.0 [6], and JENDL-4.0 [7]. Nevertheless, strong efforts are needed to reduce fission yield uncertainties as well as to understand differences observed between these evaluated nuclear data libraries. This is caused by more stringent radiation protection security requirements and to intentions to extend reactor life times.

Measuring isotopic fission yields is not an easy task. Most common experiments use the radiochemical techniques. Coupled with γ-ray spectroscopy, this type of experiment provides a very accurate cumulative isotopic yield but is, unfortunately, limited to only few isotopes. Another very usual method is based on the specific fission product energy loss when crossing a given material, which allows good nuclear charge identification. However, the nuclear charge resolution is good enough only in the light mass region. A nice review of the experimental procedures used for mass and/or charge yield determination os goven in Ref. [8].

At the Lohengrin recoil mass spectrometer located at the Institut Laue-Langevin in Grenoble (France), various nuclei undergoing fission in a thermal neutron flux (^{229}Th [9], ^{233}U [10], ^{235}U [11–13], ^{237}Np [14], ^{238}Np [15], ^{239}Pu [16], ^{241}Pu [17], ^{242m,g}Am [18], ^{245}Cm [19], ^{249}Cf [20]) have been investigated up to now. Detailed results for kinetic energy, mass, and nuclear charge distributions were deduced with the best precision. However, only light fission products[1] were measured (except for ^{245}Cm [19,21], for which mass yields were determined in both light and heavy regions). Indeed, combining the Lohengrin mass spectrometer with a

*bailadeline@yahoo.fr; presently at CEA, DAM-Ile de France, F-91290 Arpajon, France.
†Presently at CENBG, Chemin du Solarium, le Haut Vigneau, BP 120, F-33175 Gradignan, France.

[1]In order to avoid any possible misunderstanding, the terminology "fission product," used in the present work, corresponds to nuclei before undergoing β decay but after prompt neutron emission.

high-resolution ionization chamber and using the $\Delta E - E$ separation technique allows good nuclear charge discrimination within a mass line, yielding an accurate isotopic yield determination. Unfortunately, this experimental procedure can only be applied for fission products with a nuclear charge Z less than ∼39 (Y) (i.e., in the light mass region). The use of a solid absorber located just in front of the ionization chamber increases the difference in energy loss for two successive Z values. Thus, with this technique isotopic yields have been measured up to $Z = 47$ (Ag) [19,22], but not heavier, because this energy discrimination increases with the kinetic energy of the fragment and decreases with its nuclear charge [10], making impossible the Z separation in the heavy mass region.

In order to benefit from the high performance of the Lohengrin spectrometer to study fission product characteristics also in the heavy mass region, a new experimental setup based on γ spectrometry for fission product identification has been installed at Lohengrin and is described in Sec. II. Results obtained from the ^{239}Pu(n$_{th}$,f) reaction are presented and discussed in Sec. III.

II. EXPERIMENTAL PROCEDURE

A. Sample and detection systems

The Lohengrin recoil-mass spectrometer [23] is a nuclear physics instrument that uses low-energy fission reactions for fission fragment production (Fig. 1). It allows studying fission product characteristics from thermal neutron induced fission with a very high resolution.

The target used for this experiment is a highly enriched ^{239}Pu target (99.5%) deposited on a titanium backing. Owing to the high enrichment and to the high ^{239}Pu thermal fission cross section, contributions from other fissioning nuclei are negligible. This sample (300 μg/cm^2) is placed close to the core of ILL's high-flux reactor in a thermal-neutron flux of 5.5×10^{14} n/(cm^2 s). Fission products emerging from the target are created with an ionic charge state q (ranging from about 15 to 30) and kinetic energy E_k from about 50 to 120 MeV (depending on their mass A). The selection of these fission products is performed by a combination of a magnetic (main magnet in Fig. 1) and an electric (condenser in Fig. 1) sector field, whose deflections are perpendicular to each other. At the exit slit of this parabola spectrometer, the combined action of the two fields separates ions according to their A/q and E_k/q ratios. The energy dispersion in the direction along each parabola amounts to 7.2 cm for 1% difference in kinetic energy, and the mass dispersion perpendicular to each parabola amounts to 3.24 cm for a 1% mass difference. Then a focusing magnet ("RED" magnet in Fig. 1) is installed at the exit slit of the spectrometer, which increases the particle density by a factor of 7 [24]. The flight path for the fission products is 23 m for an ∼2 μs time of flight, so that fission products reach the detector before undergoing β decay.

As already mentioned, the solid absorber and high-resolution ionization chamber associated with the Lohengrin spectrometer allowed determination of mass and isotopic yields only in the light mass region [19]. In order to investigate the heavy mass region by taking advantage of the very high

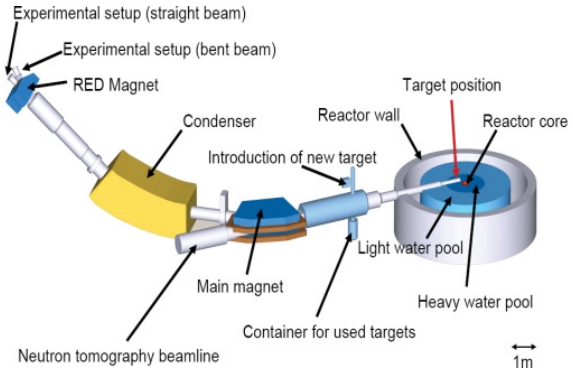

FIG. 1. (Color online) Schematic view of the Lohengrin mass spectrometer located at the Institut Laue Langevin in Grenoble, France.

thermal neutron flux as well as the very high mass and energy resolutions, a new experimental setup has been developed. It is based on γ spectrometry, which is, for the first time, coupled with the spectrometer. Indeed, because β decays of fission products are often followed by γ de-excitation, these γ rays can be used to identify the fission products and to determine their yields.

For this purpose, the measurement is performed in several steps.

(i) The electric and magnetic fields of the mass spectrometer are set to select fission products with a given mass (A), ionic charge (q), and kinetic energy (E_k).
(ii) These fission products are implanted during the measuring time (typically 1 h, depending on the fission product yield) in a tape located inside a vacuum chamber that is placed at the focal point of the spectrometer.
(iii) During this measuring time, γ rays are registered with two high-efficiency germanium clover detectors HPGe placed close to the vacuum chamber (see Fig. 2).

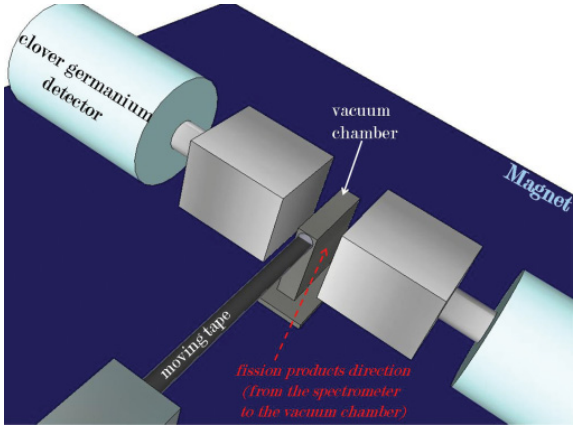

FIG. 2. (Color online) View of the experimental setup used in the present work and placed at the exit slit of the mass spectrometer.

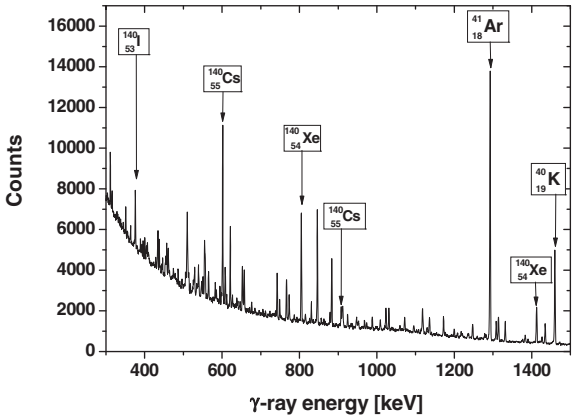

FIG. 3. Example of γ spectrum obtained after $T_{meas} = 1800$ s, for $A = 140$, $q = 22$, and $E_k = 62$ MeV. γ rays from ^{140}I, ^{140}Xe, and ^{140}Cs are clearly visible. ^{41}Ar and ^{40}K are contaminants.

(iv) Then the tape is moved to remove the residual activity, and a new measurement can start.

(v) Between two measurements, the fission product beam is blocked by an electrostatic deflector for a background determination.

In opposition to the usual experiments, which measure only a few isotopes for a given fissile nucleus, this procedure can be applied to all short-lived fission products with known γ-ray intensity ratios and decay constants. Still, certain fission products cannot be investigated because they either are stable or decay without γ-ray emission or with γ rays of an insufficiently well-known intensity. The analysis of the data is then based on the integration of Bateman equations [25] as explained in the following section.

B. Data reduction

For each measured γ spectrum, intensities of the γ rays are analyzed by using the fitting procedure TV code developed at Cologne (Germany) [26]. An example of such a γ spectrum is given in Fig. 3: it corresponds to the mass $A = 140$ (with $q = 22$ and $E_k = 22$ MeV) obtained in 0.5 h measuring time. γ rays from ^{140}I, ^{140}Xe, and ^{140}Cs can be clearly identified.

All γ rays used for the determination of the fission product yield are summarized in Table I with their branching ratios. As reported in this table, only a few γ rays (the most intense ones) were considered for a given fission product.

The analysis of a specific γ ray (after fitting the background) leads to the determination of the quantity $I_\gamma^{Exp}(A, Z, q, E_k)$, which corresponds to the measured number of γ rays emitted by a fission product with a mass number A and a nuclear charge Z, separated with an ionic charge q and a kinetic energy E_k. This quantity has to be corrected by the γ detector efficiency $\epsilon(E_\gamma)$, the γ-ray branching ratio BR(A, Z, E_γ), and the burn-up of the ^{239}Pu target BU(t) (where t corresponds to the

TABLE I. Decay γ-ray energies and their intensities used for fission product yield measurements (first isomeric states are followed by a superscript m). These nuclear data are taken from the mentioned international libraries JEFF-3.1.1 [5], NNDC [45], and LBNL [46]). An asterisk means that 10% arbitrary uncertainty was considered when nothing was mentioned in the library.

Mass	Nuclide	E_γ (keV)	BR (%)	Nuclear library
93	$_{36}$Kr	253.4	14.2 ± 2.6	JEFF-3.1.1
		323.9	24.1 ± 1.4	JEFF-3.1.1
	$_{37}$Rb	432.6	20.2 ± 2.0	JEFF-3.1.1
		986.1	7.9 ± 0.9	JEFF-3.1.1
	$_{38}$Sr	875.7	24.5 ± 1.7	JEFF-3.1.1
94	$_{37}$Rb	836.9	87 ± 3.0	NNDC
		1309.1	14.2 ± 8.0	NNDC
	$_{38}$Sr	1427.7	94 ± 0.7	JEFF-3.1.1
	$_{39}$Y	918.7	56 ± 3.0	JEFF-3.1.1
		1138.9	6 ± 0.5	JEFF-3.1.1
95	$_{37}$Rb	352	59 ± 2.0	JEFF-3.1.1
		204	18.2 ± 1.1	JEFF-3.1.1
	$_{38}$Sr	685.6	22.6 ± 1.2	JEFF-3.1.1
		2717.3	4.6 ± 0.6	JEFF-3.1.1
	$_{39}$Y	954	15.8 ± 0.7	JEFF-3.1.1
		2175.6	7 ± 0.4	JEFF-3.1.1
96	$_{38}$Sr	809.4	71.9 ± 2.6	JEFF-3.1.1
	$_{39}$Y^m	914.8	59.7 ± 2.7	JEFF-3.1.1
		617.2	57.9 ± 2.7	JEFF-3.1.1
98	$_{38}$Sr	119.4	72.9 ± 4.4	JEFF-3.1.1
	$_{39}$Y	1590.9	14.8 ± 1.4	JEFF-3.1.1
	$_{39}$Y^m	620.5	66.1 ± 3.8	JEFF-3.1.1
		647.6	52.2 ± 2.9	JEFF-3.1.1
99	$_{38}$Sr	125.1	16.1 ± 2.4	JEFF-3.1.1
	$_{39}$Y	121.8	44 ± 3.0	JEFF-3.1.1
	$_{40}$Zr	546.1	48.3 ± 2.1	JEFF-3.1.1
	$_{41}$Nb	137.7	$90.6 + 9.06^*$	JEFF-3.1.1
	$_{41}$Nb^m	97.8	6.7 ± 0.8	JEFF-3.1.1
133	$_{51}$Sb	1096.2	43 ± 2.4	JEFF-3.1.1
	$_{52}$Te	312.1	62.4 ± 0.5	JEFF-3.1.1
	$_{52}$Te^m	863.9	15.6 ± 0.8	JEFF-3.1.1
134	$_{51}$Sb^m	1279	100 ± 5.0	LBNL
	$_{52}$Te	767.2	29.6 ± 0.6	JEFF-3.1.1
		210.5	22.4 ± 0.8	JEFF-3.1.1
	$_{53}$I	847	95.4 ± 1.9	JEFF-3.1.1
		884.1	64.9 ± 1.9	JEFF-3.1.1
	$_{53}$I^m	272.1	79.1 ± 3.0	JEFF-3.1.1
136	$_{51}$Sb	2077.9	22.4 ± 2.5	JEFF-3.1.1
		333.9	18.8 ± 2.1	JEFF-3.1.1
	$_{53}$I	1321.1	24.8 ± 1.8	JEFF-3.1.1
	$_{53}$I^m	381.4	100 ± 6.0	LBNL
137	$_{53}$I	1218	13.1 ± 0.9	JEFF-3.1.1
	$_{54}$Xe	455.5	31.2 ± 0.5	JEFF-3.1.1
138	$_{53}$I	588.8	54 ± 6.3	JEFF-3.1.1
	$_{54}$Xe	258.4	31.5 ± 1.3	JEFF-3.1.1
		434.6	20.3 ± 0.8	JEFF-3.1.1
	$_{55}$Cs	1009.8	29.8 ± 0.6	JEFF-3.1.1
	$_{55}$Cs^m	191.9	15.4 ± 1.7	JEFF-3.1.1

TABLE I. *(Continued.)*

Mass	Nuclide	E_γ (keV)	BR (%)	Nuclear library
139	$_{53}$I	571.2	8.3 ± 0.7	ENDF/B-VI.8
	$_{54}$Xe	218.6	56 ± 6.0	ENDF/B-VI.8
		296.5	21.7 ± 2.4	ENDF/B-VI.8
	$_{55}$Cs	1283.2	7.1 ± 1.5	ENDF/B-VI.8
		627.2	1.5 ± 0.3	ENDF/B-VI.8
140	$_{53}$I	376.6	$90 + 9.0^*$	LBNL
	$_{54}$Xe	805.5	$20 + 2.0^*$	LBNL
		1413.6	12.2 ± 12.0	LBNL
	$_{55}$Cs	602.3	52.5 ± 16.0	LBNL
		908.3	8.56 ± 21.0	LBNL
141	$_{55}$Cs	1194	4 ± 0.3	JEFF-3.1.1
	$_{56}$Ba	190.3	46 ± 3.3	JEFF-3.1.1
		304.2	25.4 ± 1.8	JEFF-3.1.1
142	$_{55}$Cs	359.6	27.2 ± 2.7	JEFF-3.1.1
		1326.5	12.9 ± 1.3	JEFF-3.1.1
	$_{56}$Ba	255.3	20.5 ± 0.8	JEFF-3.1.1
		1204.3	14.2 ± 0.5	JEFF-3.1.1
	$_{57}$La	641.3	47.4 ± 0.5	JEFF-3.1.1
143	$_{56}$Ba	798.8	15.6 ± 3.0	LBNL
		643.8	1.55 ± 8.0	LBNL
144	$_{56}$Ba	103.9	23.3 ± 12.0	LBNL
	$_{57}$La	397.4	94.3 ± 16.0	LBNL
145	$_{56}$Ba	96.6	$17 + 1.7^*$	LBNL
		91.9	$7 + 0.7^*$	LBNL
	$_{57}$La	118.2	3.6 ± 0.6	JEFF-3.1.1
	$_{58}$Ce	724.3	44 ± 6.0	JEFF-3.1.1
		1148	9.6 ± 1.4	JEFF-3.1.1
146	$_{56}$Ba	251.2	19.6 ± 5.0	LBNL
	$_{57}$La	924.6	7.5 ± 0.4	JEFF-3.1.1
	$_{57}$La^m	514.6	23.8 ± 19.0	LBNL
		502.9	19.7 ± 15.0	LBNL
	$_{58}$Ce	316.7	56.2 ± 3.0	JEFF-3.1.1
147	$_{57}$La	117.7	12 ± 1.0	JEFF-3.1.1
		186.3	6.5 ± 0.6	JEFF-3.1.1
	$_{58}$Ce	268.8	6.3 ± 0.4	JEFF-3.1.1
		92.9	4 ± 0.4	JEFF-3.1.1
148	$_{57}$La	158.5	55.6 ± 1.4	JEFF-3.1.1
		989.9	9.3 ± 0.3	JEFF-3.1.1
	$_{58}$Ce	269.5	17 ± 9.0	JEFF-3.1.1
151	$_{59}$Pr	484.5	9.3 ± 5.0	LBNL
		495.3	8.5 ± 6.0	LBNL
	$_{60}$Nd	116.8	39 ± 5.0	LBNL
		255.7	14.8 ± 3.0	LBNL
152	$_{59}$Pr	226.7	7.8 ± 7.8	LBNL
	$_{60}$Nd	278.6	29 ± 17.0	LBNL

elapsed time from the beginning of the ^{239}Pu sample irradiation):

$$I_\gamma^{\mathrm{cor}} = \frac{I_\gamma^{\mathrm{Exp}}(A, Z, q, E_k)}{\epsilon(E_\gamma) \times \mathrm{BR}(A, Z, E_\gamma) \times \mathrm{BU}(t)}. \quad (1)$$

These three corrections (germanium efficiency, branching ratio, and burn-up) were determined as follows.

TABLE II. γ-ray energies (E_γ) and their branching ratio (BR) from ^{96m}Y decay (data taken from JEFF-3.1.1 [5]). These γ rays were used for determination of the detection efficiency.

E_γ (keV)	BR (%)
146.7	36.4 ± 2.6
173.7	2.4 ± 0.4
363.1	28.5 ± 5.1
475.6	3.1 ± 0.1
617.2	57.9 ± 2.6
631.5	10.5 ± 1.7
643.7	1.5 ± 0.1
690.0	1.6 ± 0.1
804.7	1.6 ± 0.1
906.2	27.6 ± 4.4
914.8	59.7 ± 2.6
960.2	3.5 ± 0.3
979.2	3.6 ± 0.3
1006.4	1.1 ± 0.1
1107.2	47.0 ± 1.0
1114.6	1.8 ± 0.1
1185.0	$3.4 \pm 0.$
1222.9	33.4 ± 3.5
1279.4	0.9 ± 0.1
1592.9	1.5 ± 0.2
1750.6	87.8 ± 0.8
1897.6	5.1 ± 0.1
2226.2	5.5 ± 0.3

1. Germanium efficiency

In order to determine the relative germanium detector efficiency, a fission product beam of mass 96 from the spectrometer was implanted on the tape, allowing the detection of a large number of γ rays stemming from the decay of ^{96}Sr and ^{96m}Y with energies ranging from 150 keV to 2.2 MeV (see Table II). The γ-ray energy area of this extended calibration source is rather identical to the one covered by the fission products that will be measured. Germanium detectors are placed far enough from the vacuum chamber, so that the sum peak effect can be neglected. In principle, the germanium efficiency curve can be well described by fitting experimental data with the following equation [27]:

$$\epsilon(E_\gamma) = \frac{\mathcal{K}[\tau + \sigma\,\mathcal{Q}\exp(-\mathcal{R}E_\gamma)]}{\tau + \sigma}[1 - \exp(-\mathcal{P}(\tau + \sigma)]. \quad (2)$$

In Eq. (2), τ and σ stand, respectively, for the photoelectric absorption coefficient and the Compton absorption coefficient at E_γ energy. $\mathcal{K}$, $\mathcal{Q}$, $\mathcal{R}$, and $\mathcal{P}$ are four free parameters. However, owing to the limited γ-energy range of the investigated fission products (from about 100 keV up to about 2.7 MeV), such a complete formula is not needed and experimental data (weighted by their error bars) were fitted using the following simplified equation:

$$\ln(\epsilon) = \sum_{i=1}^{N} a_i [\ln(E_\gamma)]^{i-1}, \quad (3)$$

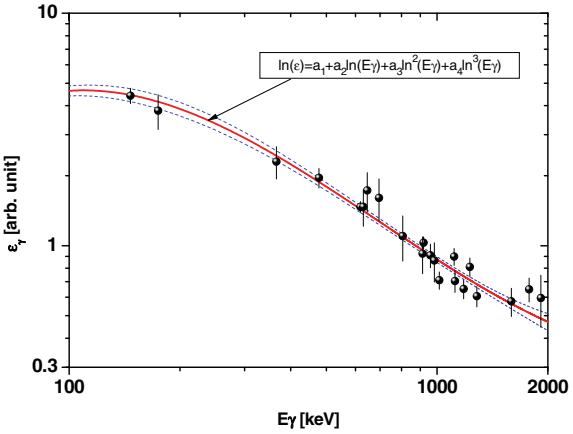

FIG. 4. (Color online) Germanium detector efficiency as a function of γ-ray energy. The measurement was carried out using a mass-96 beam. Experimental points were fitted using Eq. (3).

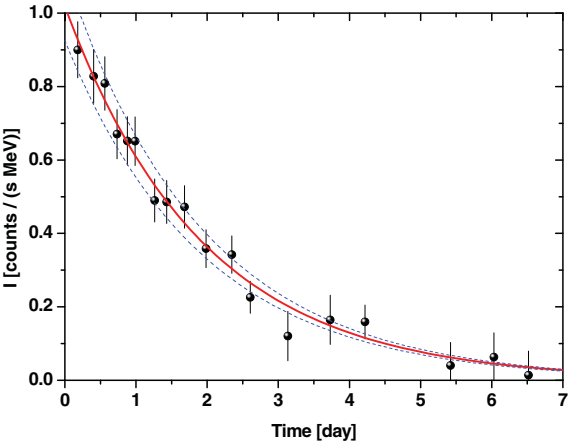

FIG. 5. (Color online) Example of burn-up measurement obtained for one ^{239}Pu target used during the experiment. I is the measured intensity of the 334-keV γ ray from the ^{136}Te decay. The fit on the experimental points [solid (red) curve)] was performed using Eq. (4).

where a_i are free parameters. As shown in Fig. 4, Eq. (3) with $N = 4$ was used to perform the fit.

2. *Nuclear decay data*

As shown in Eq. (1), each γ peak must be normalized to its branching ratio. The half-lives and branching ratio values used in the present work come from various nuclear data libraries (see Table I) and were chosen according to the consistency of the data and their associated uncertainties.

3. *^{239}Pu target burn-up*

Finally, the ^{239}Pu target burn-up has to be taken into account [28]. This burn-up was determined by measuring periodically (roughly every 12 h) the intensity of the 334-keV γ ray from the ^{136}Te decay. An example of the measured burn-up is given in Fig. 5. The experimental points are well described by using two decreasing exponential functions, one for describing the "slow" target burn-up owing to nuclear transmutation and self-sputtering and another, "fast" one for describing all phenomena that occur during the first hours of the target combustion (nuclear heating of the target to its equilibrium temperature):

$$\mathrm{BU}(t) = I_0 \exp(-\lambda_0 t) + I_1 \exp(-\lambda_1 t), \tag{4}$$

where I_0, I_1, λ_0, and λ_1 are four free parameters deduced from the fit.

The quantity defined in Eq. (1) is correlated with the number of fission products that are formed at time t (after the beginning of the implantation on the tape), by the following equation:

$$I_\gamma^{\mathrm{cor}}(A, Z, q, E_k) = k \int_0^{T\mathrm{meas}} \lambda(A, Z) \times N(A, Z, q, E_k, t)dt, \tag{5}$$

where T_{meas} is the measuring time and k a normalization constant that is discussed in Sec. II C2. The number of fission products arriving from the target to the tape is related to the partial independent yield through Bateman's equation:

$$\begin{aligned}\frac{dN(A, Z, q, E_k, t)}{dt} &= Y(A, Z, q, E_k)\mathcal{F} - \lambda(A, Z)N(A, Z, q, E_k, t) \\ &\quad + \sum_{j\geqslant 1} \lambda(A, Z-j)N(A, Z-j, q, E_k, t).\end{aligned} \tag{6}$$

The first term in Eq. (6) corresponds to the production of the $N(A, Z, q, E_k, t)$ nuclei by fission: $Y(A, Z, q, E_k)$ is the independent fission yield and $\mathcal{F}$ stands for the fission rate, which is included in the normalization constant k appearing in Eq. (5). The second term accounts for the disappearance of the (A, Z, q, E_k) nuclei by β^- decay. Finally, the third term corresponds to the creation of the (A, Z, q, E_k) nuclei by successive β^- decays of the $(A, Z-j, q, E_k)$ nuclei, which are also directly produced by fission. In the case of the isomeric state, all available decays are taken into account.

The differential equation from Eq. (6) was resolved by the fourth-order Runge-Kutta method, and in parallel, the partial independent fission product yields $Y(A, Z, q, E_k)$ have been determined from both Eq. (5) and Eq. (6) with a bisection method.

For fission products, where more than one γ ray can be determined quantitatively, the partial independent fission product yield is calculated from the weighted average of all considered γ rays.

C. Independant isotopic yield determination

1. *Integration over kinetic energies and ionic charges*

The procedure described in the previous section allows the determination of the partial independent yield $Y(A, Z, q, E_k)$. In principle, in order to calculate the independent yield

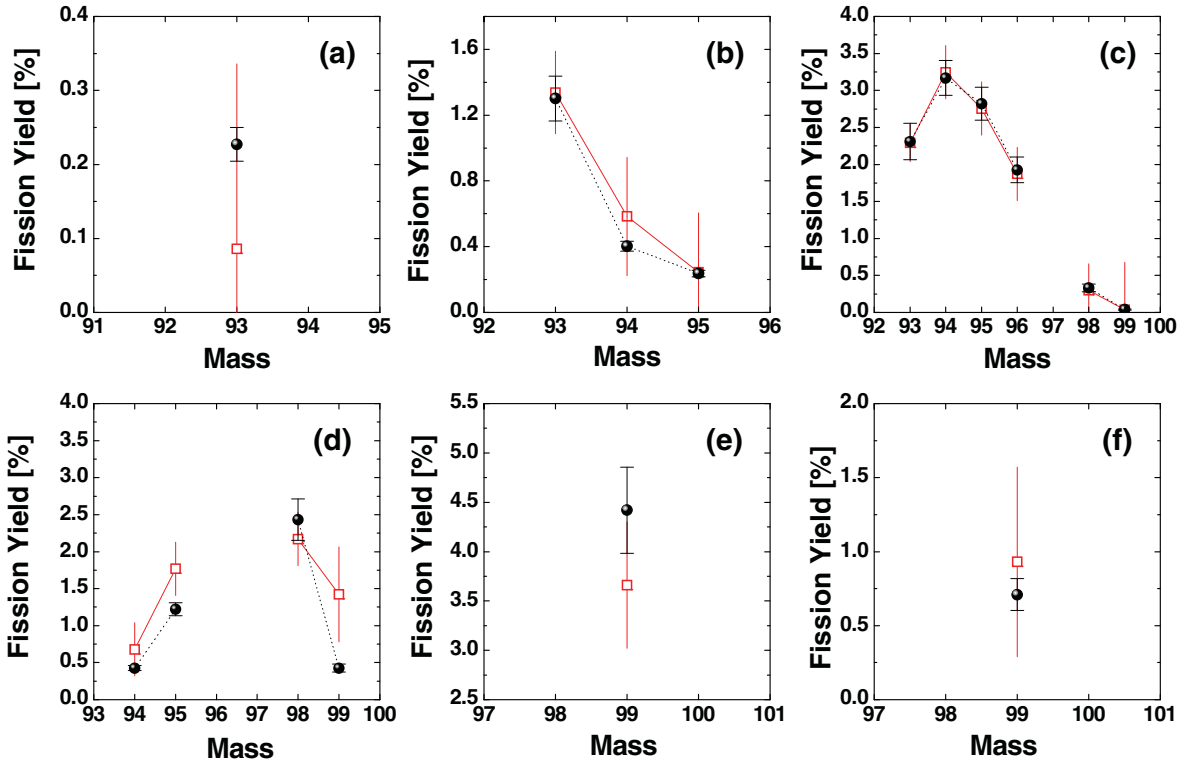

FIG. 6. (Color online) Isotopic yield measured in the light mass region by γ-ray spectroscopy [present work; filled (black) circles], compared with Schmitt's data [16] [open (red) squares], obtained with an ionization chamber: $_{36}$Kr (a), $_{37}$Rb (b), $_{38}$Sr (c), $_{39}$Y (d), $_{40}$Zr (e), and $_{41}$Nb (f).

$Y(A, Z)$, a complete scan over all kinetic energies and all ionic charge states is needed:

$$Y(A, Z) = \int \sum_q Y(A, Z, q, E_k) dE_k. \quad (7)$$

However, this method would be too time-consuming. Therefore, regardless of the fission region, each $Y(A, Z)$ can be determined by only measuring various kinetic energies at the average ionic charge $\overline{q}$ and by measuring various ionic charge states at the average kinetic energy $\overline{E_k}$:

$$Y(A, Z) = \frac{\int Y(A, Z, \overline{q}, E_k) dE_k \times \sum_q Y(A, Z, q, \overline{E_k})}{Y(A, Z, \overline{q}, \overline{E_k})}. \quad (8)$$

Measured ionic charge state and kinetic energy distributions are adjusted with Gaussian functions, and both $\int Y(A, Z, \overline{q}, E_k) dE_k$ and $\sum_q Y(A, Z, q, \overline{E_k})$ quantities are determined from the values of the Gaussian integrals. The shapes of these distributions are similar for all masses if one considers the isotopes without a nanosecond isomeric state (see Sec. III B4). If no correlation exists between the ionic charge state and the kinetic energy, the Eq. (8) is equivalent to the exact Eq. (7). Nevertheless, in the considered kinetic energy and ionic-charge-state ranges, a light correlation has been observed. It leads to an additional uncertainty, which is discussed in Sec. III.

2. *Normalization*

Because only the relative germanium detector efficiency is known, the absolute independent yield cannot be determined, and therefore, our data need to be normalized [parameter k in Eq. (5)]. To do this, the sum of the measured isotopic yields has been equalized to the sum of isotopic yields available in the JEFF-3.1.1 library for the same fission products. This sum (over the 65 measured fission products) represents 90.67% of the total fission yields (200%).

D. Validation of the experimental setup

In order to test the correct functioning of our new experimental setup, various fission product yields from ^{239}Pu(n$_{th}$,f) were measured in the light mass region and compared with the ones obtained previously by Schmitt *et al.* [16]. This measurement was performed in 1984 at the Lohengrin mass spectrometer, but with a completely different experimental setup (ionization chamber). Within the error bars, a good agreement can be achieved as shown in Fig. 6, except for the yttrium element, for which differences between both experiments are a bit larger.

TABLE III. ^{239}Pu(n_{th}, f) fission product yields measured in the light mass region by γ-ray spectroscopy (present work). Statistical (stat.) and systematic (syst.) uncertainties as well as uncertainties owing to nuclear data are listed (in %). The total uncertainty [Eq. (9)] is given in the last column. First isomeric states are indicated by a superscript m.

Mass	Nuclide	Yield (%)	Uncertainty					
			Stat. (%)	Syst. (%)	$\epsilon(E_\gamma)$	Nuclear data (%)	Decay (%)	Total (%)
93	$_{36}$Kr	0.227	1.17	3.40	3.78	5.54	0.00	10.01
	$_{37}$Rb	1.301	1.08	3.40	2.79	7.47	0.34	10.43
	$_{38}$Sr	2.31	1.08	3.40	3.64	6.94	0.05	10.68
94	$_{37}$Rb	0.402	1.08	3.40	2.34	3.44	0.00	7.64
	$_{38}$Sr	3.168	1.08	3.40	2.89	0.74	0.03	7.41
	$_{39}$Y	0.426	1.08	3.40	2.40	4.51	0.35	8.23
95	$_{37}$Rb	0.236	1.08	3.40	3.82	2.96	0.00	8.81
	$_{38}$Sr	2.82	1.08	3.40	1.70	4.92	0.01	7.90
	$_{39}$Y	1.221	1.08	3.40	1.88	3.50	0.28	7.27
96	$_{38}$Sr	1.927	1.08	3.40	3.76	3.62	0.00	9.00
	$_{39}$Y^m	1.678	1.08	3.40	2.72	3.25	0.50	7.91
	$_{39}$Y	1.956	1.08	3.40	2.72	9.46	2.89	12.23
	$_{39}$Y^m	0.477	1.08	3.40	2.93	3.99	1.77	8.60
98	$_{38}$Sr	0.331	4.04	3.40	6.67	6.04	0.00	15.35
	$_{39}$Y	1.956	1.08	3.40	2.72	9.46	2.89	12.23
	$_{39}$Y^m	0.477	1.08	3.40	2.93	3.99	1.77	8.60
99	$_{38}$Sr	0.04	1.08	3.40	6.60	14.91	0.00	18.57
	$_{39}$Y	0.426	1.08	3.40	6.64	6.82	0.35	13.05
	$_{40}$Zr	4.419	1.08	3.40	4.37	4.35	0.89	9.90
	$_{41}$Nb	0.568	1.08	3.40	6.45	10.00	0.58	14.83
	$_{41}$Nb^m	0.142	1.08	3.40	6.96	11.94	0.18	16.54

This agreement was very important to validate both the good functioning of our experimental setup and the procedure used for the data analysis. It gives confidence for extending this method to the heavy mass region.

III. RESULTS AND DISCUSSION

A. Accuracy of data

Potential sources of uncertainties induced by our experimental set-up as well as by the procedure used for the data analysis were identified and are discussed in this section. This discussion is very similar to the one presented by Laurec *et al*. [29].

1. Statistical uncertainties: Δ_{stat}

(i) The analysis of the measured γ spectra was performed using the TV code [26]. In particular, this code allows the performance of a fit of a selected γ peak and to deduce its area after fitting the background. The code deals by itself with statistical uncertainties as well as errors owing to the fit.

(ii) An additional statistical effect is caused by the thermal neutron flux stability. To take these fluctuations into account, we first consider the global reactor heat, which is recorded as a function of time. It is directly proportional to global neutron flux variations and gives a rough idea about neutron flux variations but does not reproduce local fluctuations exactly. This is why subsequently variations have been more accurately followed by measuring a given mass frequently during the experiment. Based on measurement reproducibility, variations have been estimated to be lower than 0.6%.

Both statistical uncertainties were combined quadratically to get the total statistical uncertainty (Δ_{stat}).

2. Systematic uncertainties: Δ_{syst}

(i) ^{239}*Pu target burn-up*. The uncertainty owing to the burn-up of the sample is deduced from the weighted fit performed on the burn-up measurement (see Fig. 5).

(ii) *Mass yield determination procedure*. As explained in Sec. II C1, the isotopic yield is determined by measuring the kinetic energy distribution associated with the mean ionic charge state $\bar{q}$ and the ionic-charge-state distribution associated with the mean kinetic energy $\bar{E}_k$ [Eq. (8)]. As already stated, this procedure is rigorous only when q and E_k are uncorrelated, which is not strictly the case [30,31]. In order to quantify properly the uncertainty owing to this correlation, one light mass ($A = 98$) and one heavy mass ($A = 136$) have been studied for all ionic-charge-state and kinetic energy combinations. Thus, yields have been determined directly by summing all these combinations without any approximation [Eq. (7)]. It has shown that the approximation owing to the use of Eq. (8) leads to an additional uncertainty of less than 1.3% [31].

TABLE IV. Same as Table III but for fission products belonging to the heavy mass region.

Mass	Nuclide	Yield (%)	Uncertainty					
			Stat. (%)	Syst. (%)	$\epsilon(E_\gamma)$	Nucl. data (%)	Decay (%)	Total (%)
133	$_{51}$Sb	1.231	1.62	3.40	3.30	5.53	0.00	9.99
	$_{52}$Te	1.881	1.08	3.40	5.22	0.80	1.04	9.79
	$_{52}$Te^m	2.898	1.25	3.40	3.66	5.13	0.32	9.78
134	$_{51}$Sb^m	0.571	1.25	3.40	3.06	5.00	0.00	9.19
	$_{52}$Te	3.581	1.71	3.40	3.21	1.76	0.01	8.50
	$_{53}$I	1.496	1.00	3.40	2.59	1.65	9.92	12.24
	$_{53}$I^m	1.116	1.80	3.40	5.43	3.79	36.90	38.59
136	$_{52}$Te	0.527	3.65	3.40	2.10	7.90	0.00	12.08
	$_{53}$I	0.807	1.08	3.40	3.01	7.26	1.13	10.49
	$_{53}$I^m	2.483	1.71	3.40	4.92	6.00	0.74	11.71
137	$_{53}$I	2.244	1.52	3.40	3.13	6.87	0.00	10.59
	$_{54}$Xe	3.653	1.90	3.40	4.65	1.60	0.48	10.08
138	$_{53}$I	0.475	1.80	3.40	4.25	11.65	0.00	15.00
	$_{54}$Xe	4.687	1.17	3.40	3.58	2.85	0.01	8.63
	$_{55}$Cs	0.564	2.67	3.40	3.42	2.01	6.03	11.42
	$_{55}$Cs^m	0.857	2.67	3.40	5.95	11.04	33.42	37.19
139	$_{53}$I	0.133	1.08	3.40	4.30	8.43	0.00	12.18
	$_{54}$Xe	3.115	2.18	3.40	3.90	7.70	0.03	12.21
	$_{55}$Cs	2.263	3.65	3.40	2.46	14.52	0.59	17.37
140	$_{53}$I	0.068	1.80	3.40	4.93	10.00	0.00	14.24
	$_{54}$Xe	1.512	1.52	3.40	2.30	7.07	0.05	10.11
	$_{55}$Cs	2.932	1.71	3.40	2.73	1.91	0.79	8.11
141	$_{55}$Cs	3.135	1.52	3.40	3.16	7.50	0.00	11.03
	$_{56}$Ba	1.583	1.43	3.40	3.95	5.04	0.27	10.13
142	$_{55}$Cs	0.953	1.00	3.40	2.57	7.07	0.00	9.93
	$_{56}$Ba	3.582	1.52	3.40	2.74	2.61	0.01	8.09
	$_{57}$La	0.406	1.43	3.40	4.12	1.05	4.88	10.25
143	$_{56}$Ba	2.851	1.52	3.40	3.78	1.92	0.00	8.92
	$_{57}$La	1.045	1.52	3.40	4.12	5.16	0.12	10.41
144	$_{56}$Ba	2.679	1.99	3.40	6.87	0.52	0.00	12.28
	$_{57}$La	1.228	1.99	3.40	4.85	1.70	1.81	10.54
145	$_{56}$Ba	0.824	1.99	3.40	4.96	7.07	0.00	12.54
	$_{57}$La	1.796	1.52	3.40	6.68	16.67	0.77	20.32
	$_{58}$Ce	0.430	1.80	3.40	2.49	9.96	2.76	12.89
146	$_{56}$Ba	0.511	1.90	3.40	5.55	2.55	0.00	11.14
	$_{57}$La	0.293	1.08	3.40	3.56	5.33	1.00	9.70
	$_{57}$La^m	0.742	1.34	3.40	3.17	5.51	1.71	9.79
	$_{58}$Ce	0.793	2.38	3.40	5.20	5.34	0.02	12.20
147	$_{57}$La	0.655	1.71	3.40	4.47	6.19	0.00	11.40
	$_{58}$Ce	1.619	1.90	3.40	4.31	5.36	0.25	11.00
148	$_{57}$La	0.191	1.80	3.40	3.02	1.98	0.00	8.46
	$_{58}$Ce	0.920	2.38	3.40	5.44	5.29	0.07	12.41
151	$_{59}$Pr	0.419	1.34	3.40	3.21	4.28	0.00	9.03
	$_{60}$Nd	0.289	1.90	3.40	4.26	1.25	0.14	9.64
152	$_{59}$Pr	0.028	2.28	3.40	5.70	5.13	0.00	12.49
	$_{60}$Nd	0.534	2.18	3.40	5.39	5.86	0.00	12.44

(iii) *Normalization factor*. Uncertainties owing to our normalization procedure. (see Sec. II C2) have been estimated at 1.5%.

The total systematic uncertainty (Δ_{syst}) is calculated by summing these three contributions.

TABLE V. Sum of the ground-state and the first isomeric-state yields ($S = Y^{GS} + Y^{m}$) and ratio between the isomeric yield and the sum [$R = Y^{m}/(Y^{GS} + Y^{m})$]. Results obtained in this work (Loh.) are compared with those from JEFF-3.1.1 [5].

Mass	Nuclide	$S_{\text{Loh.}}$ (%)	$S_{\text{JEFF-3.1.1}}$ (%)	$R_{\text{Loh.}}$ (%)	$R_{\text{JEFF-3.1.1}}$ (%)
98	$_{39}$Y	2.433 ± 0.280	2.310 ± 0.512	19.6 ± 3.3	80.8 ± 25.3
99	$_{41}$Nb	0.710 ± 0.108	0.850 ± 0.280	20.0 ± 4.2	18.8 ± 8.7
133	$_{52}$Te	4.779 ± 0.468	4.646 ± 0.534	60.6 ± 8.4	70.7 ± 11.5
134	$_{53}$I	2.612 ± 0.614	2.248 ± 0.545	42.7 ± 11.3	42.4 ± 14.6
136	$_{53}$I	3.290 ± 0.375	3.358 ± 0.591	75.5 ± 11.7	70.1 ± 17.4
138	$_{55}$Cs	1.420 ± 0.383	1.033 ± 0.348	60.3 ± 17.7	58.7 ± 28.0
146	$_{57}$La	1.035 ± 0.101	1.258 ± 0.213	71.7 ± 9.9	64.3 ± 15.4

3. *Uncertainties owing to the detection efficiency:* $\Delta_{\epsilon(E_\gamma)}$

As for the target burn-up uncertainty, the uncertainty owing to the detection efficiency is determined from the weighted fit performed on the experimental data (see Fig. 4).

4. *Uncertainties owing to the nuclear data:* Δ_{ND}

Uncertainties related to nuclear data (mainly γ-ray branching ratios) have an important impact on the final isotopic yield uncertainties. These uncertainties, denoted Δ_{ND}, were taken from nuclear data libraries mentioned in Table I.

5. *Uncertainties owing to the mother's data:* Δ_{Decay}

Owing to the β-decay constants that appear in the Bateman equation [Eq. (6)], the uncertainty of the mother nucleus yield has to be propagated to the uncertainty of the daughter nucleus yield. This uncertainty is evaluated by summing the Δ_{syst}, $\Delta_{\epsilon(E_\gamma)}$, and Δ_{ND} quantities of the mother nuclei, but weighted by the ratio between the detected mother nuclei and the detected daughter nuclei. Uncertainties are propagated from the first measured nuclei, unmeasured isotopes not being taken into account.

6. *Total uncertainties*

The total uncertainty is then calculated as follows:

$$\Delta_{\text{tot}} = \sqrt{(\Delta_{\text{stat}} + \Delta_{\text{syst}} + \Delta_{\epsilon(E_\gamma)})^2 + \Delta_{\text{ND}}^2 + \Delta_{\text{Decay}}^2}. \quad (9)$$

B. Isotopic yields

Isotopic yield values for the 65 measured fission products (19 in the light mass region and 46 in the heavy mass region)

TABLE VI. ^{239}Pu(n_{th}, f) fission product yields (in %) measured in the light mass region (present work) and compared with the three main libraries: JEFF-3.1.1 [5], ENDF/B-VII.0 [6] and JENDL-4.0 [7]. Relative differences (relat. diff.) are given for each library. Isomeric states are indicated by a superscript m.

Mass	Nuclide	Present work	JEFF-3.1.1	Relat. diff. (%)	ENDF/-B-VII.0	Relat. diff. (%)	JENDL-4.0	Relat. diff. (%)
93	$_{36}$Kr	0.227 ± 0.023	0.109 ± 0.037	-108.257	0.067 ± 0.005	-238.806	0.064 ± 0.005	-254.688
	$_{37}$Rb	1.301 ± 0.136	1.57 ± 0.313	17.134	1.355 ± 0.081	3.985	1.355 ± 0.081	3.985
	$_{38}$Sr	2.31 ± 0.247	1.988 ± 0.333	-16.197	2.144 ± 0.129	-7.743	2.144 ± 0.129	-7.743
94	$_{37}$Rb	0.402 ± 0.031	0.677 ± 0.202	40.620	0.704 ± 0.113	42.898	0.704 ± 0.113	42.898
	$_{38}$Sr	3.168 ± 0.235	3.061 ± 0.327	-3.496	2.925 ± 0.175	-8.308	2.925 ± 0.175	-8.308
	$_{39}$Y	0.426 ± 0.035	0.591 ± 0.205	27.919	0.675 ± 0.108	36.889	0.675 ± 0.108	36.889
95	$_{37}$Rb	0.236 ± 0.021	0.258 ± 0.087	8.527	0.432 ± 0.099	45.370	0.432 ± 0.099	45.370
	$_{38}$Sr	2.82 ± 0.223	2.987 ± 0.432	5.591	2.612 ± 1.175	-7.963	2.612 ± 1.175	-7.963
	$_{39}$Y	1.221 ± 0.089	1.586 ± 0.413	23.014	1.678 ± 0.755	27.235	1.678 ± 0.755	27.235
96	$_{38}$Sr	1.927 ± 0.174	2.011 ± 0.403	4.177	1.822 ± 0.82	-5.763	1.822 ± 0.82	-5.763
	$_{39}$Y^{m}	1.678 ± 0.133	1.473 ± 0.281	-13.917	2.238 ± 1.007	25.022	2.235 ± 1.006	24.922
98	$_{38}$Sr	0.331 ± 0.051	0.231 ± 0.081	-43.290	0.327 ± 0.209	-1.223	0.327 ± 0.209	-1.223
	$_{39}$Y	1.956 ± 0.239	0.444 ± 0.098	-340.541	1.187 ± 0.38	-64.785	0.361 ± 0.115	-441.828
	$_{39}$Y^{m}	0.477 ± 0.041	1.866 ± 0.413	74.437	1.187 ± 0.38	59.815	2.013 ± 0.644	76.304
99	$_{38}$Sr	0.04 ± 0.007	0.038 ± 0.013	-5.263	0.037 ± 0.024	-8.108	0.037 ± 0.024	-8.108
	$_{39}$Y	0.426 ± 0.056	1.294 ± 0.356	67.079	1.444 ± 0.159	70.499	1.444 ± 0.159	70.499
	$_{40}$Zr	4.419 ± 0.438	4.005 ± 0.488	-10.337	3.763 ± 1.204	-17.433	3.763 ± 1.204	-17.433
	$_{41}$Nb	0.568 ± 0.084	0.691 ± 0.227	17.800	0.075 ± 0.012	-657.333	0.776 ± 0.124	26.804
	$_{41}$Nb^{m}	0.142 ± 0.023	0.16 ± 0.053	11.250	0.881 ± 0.564	83.882	0.18 ± 0.115	21.111

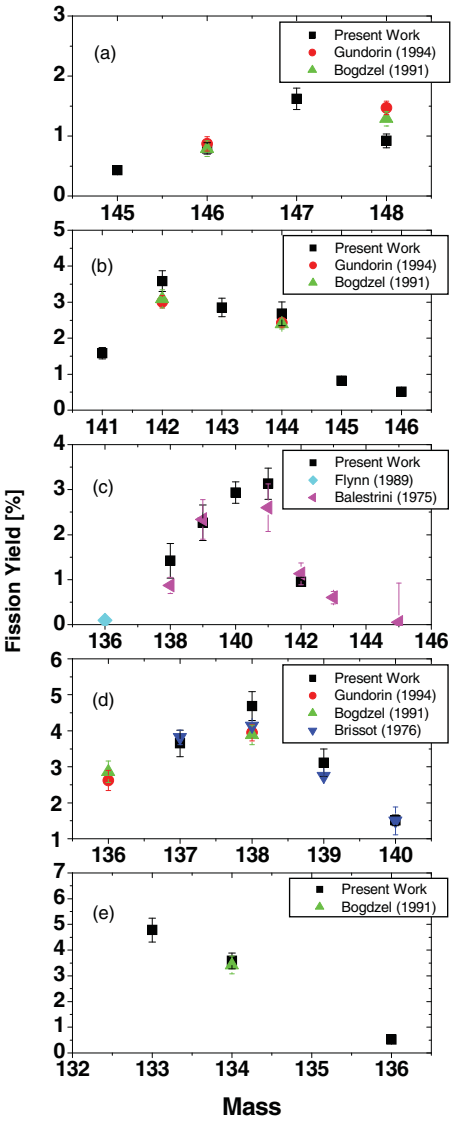

FIG. 7. (Color online) Isotopic yields obtained in this work in the heavy mass region and compared with data from the literature: $_{58}$Ce (a), $_{56}$Ba (b), $_{55}$Cs (c), $_{54}$Xe (d), and $_{52}$Te (e).

with their uncertainties are given in Table III (light fission products) and Table IV (heavy fission products).

1. Comparison with data from the literature

Our measurements performed in the heavy mass region were compared with the following data coming from the EXFOR database (see Fig. 7):

(i) Gundorin *et al.* [32]: $^{136}_{54}$Xe, $^{138}_{54}$Xe, $^{142}_{56}$Ba, $^{144}_{56}$Ba, $^{146}_{58}$Ce, $^{148}_{58}$Ce.

(ii) Bogdzel *et al.* [33]: $^{134}_{52}$Te, $^{136}_{54}$Xe, $^{138}_{54}$Xe, $^{142}_{56}$Ba, $^{144}_{56}$Ba, $^{146}_{58}$Ce, $^{148}_{58}$Ce.

(iii) Brissot *et al.* [34]: $^{137}_{54}$Xe, $^{138}_{54}$Xe, $^{139}_{54}$Xe, $^{140}_{54}$Xe.

(iv) Balestrini *et al.* [35]: $^{138}_{55}$Cs, $^{139}_{55}$Cs, $^{141}_{55}$Cs, $^{142}_{55}$Cs, $^{143}_{55}$Cs, $^{145}_{55}$Cs.

(v) Flynn *et al.* [36]: $^{136}_{55}$Cs.

As shown in Fig. 7, a general good agreement among all measured nuclear charges was found, except for $^{138}_{55}$Cs and $^{148}_{58}$Ce fission yields. Note that for both masses, 138 and 148, we have observed a strong deformed ionic-charge-state distribution, which corresponds to the presence of a nanosecond isomeric state (see Sec. III B4). However, it is probably not enough to explain the observed differences between the literature values and our data.

2. Comparison with evaluated nuclear data files

Our data are compared with the three main libraries (JEFF-3.1.1 [5], ENDB/B-VII.0 [6], and JENDL-4.0 [7]) in Table VI (light fission products) and Table VII (heavy fission products). The relative differences (derived as $1 - M/E$, where M corresponds to our measured data, and E to the evaluated yield) are also reported in these tables. In addition, the yields obtained in this work are plotted in Fig. 8 with the JEFF-3.1.1 yields.

One of the most important points that can be mentioned is the reduction of uncertainties for a large number of nuclei. This is illustrated in Fig. 9, where histograms of the 65 fission product yield uncertainties are given for both our data (top) and the JEFF-3.1.1 data (bottom). The average yield uncertainty reaches 11.9% (our measurements) and 23.3% (JEFF-3.1.1), respectively, which corresponds to a reduction of a factor of nearly 2. Nevertheless, some of them still show important uncertainties, which is partly caused by our poor knowledge of the decay data available in nuclear libraries and/or because of the difficulty of measuring low-intensity γ rays.

For the large majority of fission products, a very good agreement between the Lohengrin data and the JEFF-3.1.1 values is achieved. However, nine fission products (over the 65 measured nuclei) are not within the error bars (at 1σ): ^{98}Y, ^{99}Y, ^{133}Te, ^{134}Sb, ^{142}Ce, ^{146}Ba, ^{147}Ce, ^{152}Pr, and ^{152}Nd. In each case, our measurements are not in agreement with any of the three data libraries, except for the ^{133}Te yield, which is in accordance with ENDF/B-VII.0.

3. Isomeric-to-ground-state ratio

Yields of both ground state and isomeric state were measured for the following seven fission products: $^{98}_{39}$Y, $^{99}_{41}$Nb, $^{133}_{52}$Te, $^{134}_{53}$I, $^{136}_{53}$I, $^{138}_{55}$Cs, and $^{146}_{57}$La. For each fission product, the sum of the ground-state yield (Y^{GS}) and the isomeric-state yield (Y^m) is reported ($S = Y^{\rm GS} + Y^m$). The ratio of the isomeric-state yield to the sum ($R = Y^m/(Y^{\rm GS} + Y^m)$ is also listed in Table V.

The R and S quantities are compared with the JEFF-3.1.1 values. From Table V, various comments can be made.

TABLE VII. Same as Table VI but for fission products belonging to the heavy mass region.

Mass	Nuclide	Present work	JEFF−3.1.1	Relat. diff. (%)	ENDF B−VII.0	Relat. diff. (%)	JENDL−4.0	Relat. diff. (%)
133	$_{51}$Sb	1.231 ± 0.123	1.265 ± 0.368	2.688	1.174 ± 0.094	−4.855	1.173 ± 0.094	−4.945
	$_{52}$Te	1.881 ± 0.183	1.361 ± 0.156	−38.207	1.766 ± 0.194	−6.512	1.364 ± 0.150	−37.903
	$_{52}$Te^{m}	2.898 ± 0.284	3.285 ± 0.377	11.781	2.891 ± 0.173	−0.242	3.292 ± 0.198	11.968
134	$_{51}$Sb^{m}	0.571 ± 0.052	0.195 ± 0.068	−192.821	0.199 ± 0.128	−186.935	0.280 ± 0.179	−103.929
	$_{52}$Te	3.581 ± 0.304	4.110 ± 0.581	12.871	4.397 ± 0.264	18.558	4.397 ± 0.264	18.558
	$_{53}$I	1.496 ± 0.183e	1.294 ± 0.314	−15.611	1.436 ± 0.086	−4.178	1.509 ± 0.091	0.861
	$_{53}$I^{m}	1.116 ± 0.431	0.954 ± 0.231	−16.981	1.184 ± 0.379	5.743	1.111 ± 0.355	−0.450
136	$_{52}$Te	0.527 ± 0.064	0.68 ± 0.216	22.500	0.506 ± 0.324	−4.150	0.506 ± 0.324	−4.150
	$_{53}$I	0.807 ± 0.085	1.005 ± 0.177	19.701	1.250 ± 0.400	35.440	0.864 ± 0.277	6.597
	$_{53}$I^{m}	2.483 ± 0.291	2.353 ± 0.414	−5.525	1.642 ± 0.131	−51.218	2.027 ± 0.162	−22.496
137	$_{53}$I	2.244 ± 0.238	2.177 ± 0.519	−3.078	2.299 ± 0.138	2.392	2.299 ± 0.138	2.392
	$_{54}$Xe	3.653 ± 0.368	3.949 ± 0.564	7.496	3.684 ± 0.147	0.841	3.683 ± 0.147	0.815
138	$_{53}$I	0.475 ± 0.071	0.663 ± 0.223	28.356	1.272 ± 0.102	62.657	1.272 ± 0.102	62.657
	$_{54}$Xe	4.687 ± 0.405	4.364 ± 0.463	−7.401	3.926 ± 0.110	−19.384	3.925 ± 0.110	−19.414
	$_{55}$Cs	0.564 ± 0.064	0.427 ± 0.144	−32.084	0.308 ± 0.049	−83.117	0.372 ± 0.060	−51.613
	$_{55}$Cs^{m}	0.857 ± 0.319	0.606 ± 0.204	−41.419	0.593 ± 0.379	−44.519	0.529 ± 0.338	−62.004
139	$_{53}$I	0.133 ± 0.016	0.198 ± 0.069	32.828	0.319 ± 0.073	58.307	0.319 ± 0.073	58.307
	$_{54}$Xe	3.115 ± 0.380	3.231 ± 0.518	3.590	2.792 ± 0.112	−11.569	2.792 ± 0.112	−11.569
	$_{55}$Cs	2.263 ± 0.393	2.303 ± 0.512	1.737	2.324 ± 0.535	2.625	2.324 ± 0.534	2.625
140	$_{53}$I	0.068 ± 0.010	0.028 ± 0.010	−142.857	0.059 ± 0.038	−15.254	0.059 ± 0.038	−15.254
	$_{54}$Xe	1.512 ± 0.153	1.648 ± 0.387	8.252	1.540 ± 0.043	1.818	1.540 ± 0.043	1.818
	$_{55}$Cs	2.932 ± 0.238	2.772 ± 0.464	−5.772	2.277 ± 0.364	−28.766	2.276 ± 0.364	−28.822
141	$_{55}$Cs	3.135 ± 0.346	2.915 ± 0.450	−7.547	2.867 ± 0.459	−9.348	2.867 ± 0.459	−9.348
	$_{56}$Ba	1.583 ± 0.160	1.743 ± 0.428	9.180	1.828 ± 0.420	13.403	1.828 ± 0.420	13.403
142	$_{55}$Cs	0.953 ± 0.095	1.524 ± 0.367	37.467	1.397 ± 0.321	31.782	1.396 ± 0.321	31.734
	$_{56}$Ba	3.582 ± 0.290	3.040 ± 0.404	−17.829	3.077 ± 0.492	−16.412	3.076 ± 0.492	−16.450
	$_{57}$La	0.406 ± 0.042	0.296 ± 0.105	−37.162	0.299 ± 0.192	−35.786	0.299 ± 0.192	−35.786
143	$_{56}$Ba	2.851 ± 0.254	3.023 ± 0.349	5.690	2.886 ± 0.664	1.213	2.886 ± 0.664	1.213
	$_{57}$La	1.045 ± 0.109	0.822 ± 0.266	−27.129	0.815 ± 0.522	−28.221	0.815 ± 0.522	−28.221
144	$_{56}$Ba	2.679 ± 0.329	2.224 ± 0.321	−20.459	2.156 ± 0.690	−24.258	2.156 ± 0.690	−24.258
	$_{57}$La	1.228 ± 0.129	1.253 ± 0.311	1.995	1.309 ± 0.419	6.188	1.309 ± 0.419	6.188
145	$_{56}$Ba	0.824 ± 0.103	0.841 ± 0.212	2.021	0.803 ± 0.257	−2.615	0.803 ± 0.257	−2.615
	$_{57}$La	1.796 ± 0.365	1.722 ± 0.260	−4.297	1.697 ± 0.543	−5.834	1.697 ± 0.543	−5.834
	$_{58}$Ce	0.430 ± 0.055	0.451 ± 0.146	4.656	0.456 ± 0.292	5.702	0.456 ± 0.292	5.702
146	$_{56}$Ba	0.511 ± 0.057	0.248 ± 0.078	−106.048	0.238 ± 0.152	−114.706	0.238 ± 0.152	−114.706
	$_{57}$La	0.293 ± 0.028	0.449 ± 0.076	34.744	0.581 ± 0.372	49.570	0.415 ± 0.265	29.398
	$_{57}$La^{m}	0.742 ± 0.073	0.808 ± 0.137	8.168	0.581 ± 0.372	−27.711	0.747 ± 0.478	0.669
	$_{58}$Ce	0.793 ± 0.097	0.954 ± 0.206	16.876	1.038 ± 0.332	23.603	1.038 ± 0.332	23.603
147	$_{57}$La	0.655 ± 0.075	0.671 ± 0.161	2.385	0.611 ± 0.391	−7.201	0.610 ± 0.391	−7.377
	$_{58}$Ce	1.619 ± 0.178	1.190 ± 0.176	−36.050	1.216 ± 0.280	−33.141	1.216 ± 0.280	−33.141
148	$_{57}$La	0.191 ± 0.016	0.180 ± 0.060	−6.111	0.117 ± 0.075	−63.248	0.117 ± 0.075	−63.248
	$_{58}$Ce	0.920 ± 0.114	1.161 ± 0.123	20.758	0.890 ± 0.401	−3.371	0.890 ± 0.401	−3.371
151	$_{59}$Pr	0.419 ± 0.038	0.385 ± 0.068	−8.831	0.372 ± 0.238	−12.634	0.372 ± 0.238	−12.634
	$_{60}$Nd	0.289 ± 0.028	0.313 ± 0.065	7.668	0.292 ± 0.187	1.027	0.292 ± 0.187	1.027
152	$_{59}$Pr	0.028 ± 0.003	0.160 ± 0.045	82.500	0.160 ± 0.103	82.500	0.160 ± 0.103	82.500
	$_{60}$Nd	0.534 ± 0.066	0.393 ± 0.051	−35.878	0.370 ± 0.118	−44.324	0.370 ± 0.118	−44.324

(i) For the seven fission products, the sum of the isomeric- and ground-state yields obtained from our measurements is in good agreement with JEFF-3.1.1 within the error bars (at 1σ).

(ii) The ratio is also in good agreement with JEFF-3.1.1 for all fission products except for $^{98}_{39}$Y, where the R value is reversed between our data and JEFF-3.1.1, which is probably owing to a wrong assignment in the

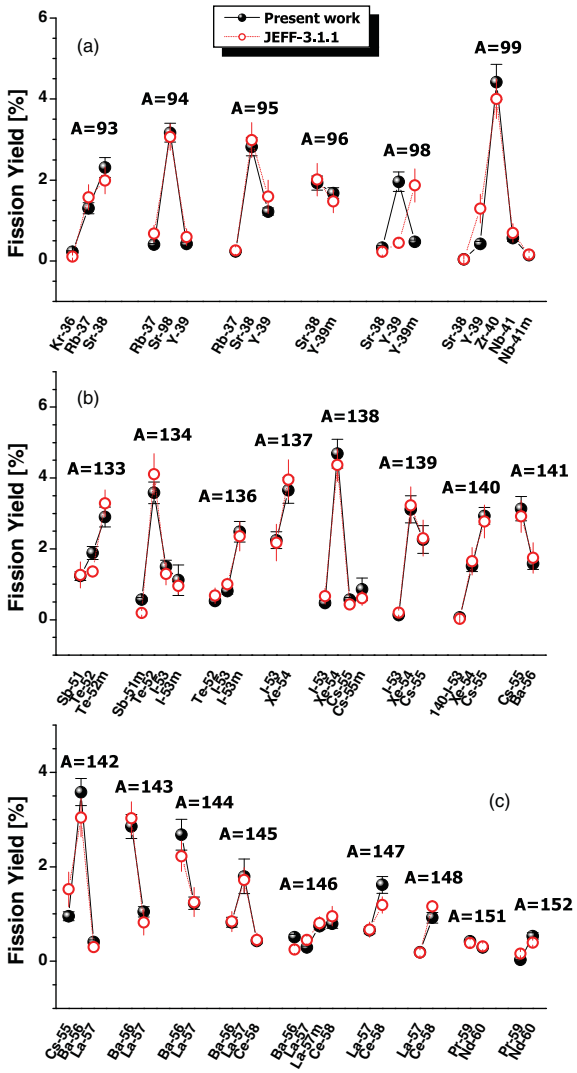

FIG. 8. (Color online) Isotopic yields measured in the present work and compared with JEFF-3.1.1 [5] in the light (a) and heavy (b, c) mass regions.

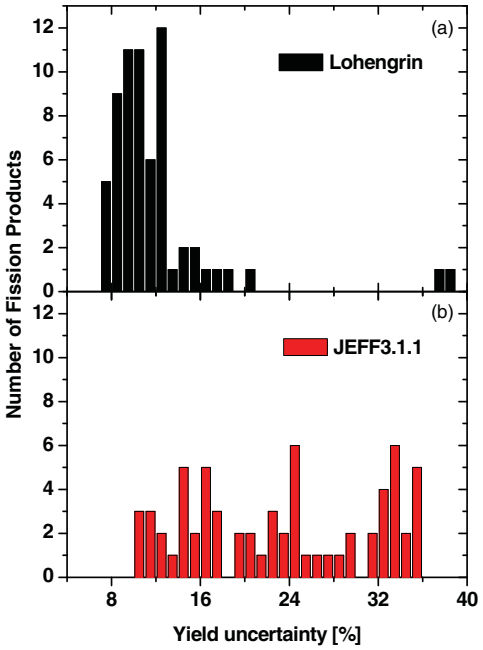

FIG. 9. (Color online) Histograms of the 65 fission product yield uncertainties for both our data (a) and JEFF-3.1.1 data (b).

European library between the isomeric and the ground state.

4. Nanosecond isomeric state

Some fission products show an asymmetric ionic charge distribution. In particular, an important tail for high ionic charge states can be observed. Such a distribution can not be explained by atomic considerations [37]. This effect, already observed in the past and explained by Wohlfarth [38], results from nanosecond isomers that decay by a highly converted internal transition. Owing to the short half-life of these isomeric states (of the order of some nanoseconds), conversion electrons, which are emitted between the target and the first dipole of the spectrometer, increase the ionic charge of the fission product. This new ionic charge state is maintained during the flight through Lohengrin and can therefore be detected. Unfortunately, because the isomeric decay has happened before the fission product arrives at the detection position, it is not possible to provide any spectroscopic information on the isomeric state, except a rough estimate of its half-life.

An example of such an isomeric state is given in Fig. 10. In this figure, the ionic charge distributions were measured by γ spectrometry for both $^{140}_{54}$Xe and $^{140}_{55}$Cs. A "normal" Gaussian shape was found for $^{140}_{54}$Xe (no nanosecond isomer), while for the $^{140}_{55}$Cs nucleus, a strong deformed distribution was observed, showing the presence of a nanosecond isomer. By this method, new nanosecond isomers for masses 137, 138, 140, 142, and 144 were identified and reported in detail by Materna *et al.* in Ref. [39].

5. Nuclear charge polarization

Isobaric charge distributions were investigated for all masses where at least three fission product yields were measured: $A = 94$, 95, 99 (light fission products) and $A = 134$, 138, 139, 142, 145, 146 (heavy fission products). Assuming a Gaussian shape distribution, the first moment [most probable charge: $Z_P(A)$] and the second moment [variance: $\sigma_Z(A)$] were determined (see Table VIII).

In low-energy fission, fission products present an average charge density different from the fissioning nucleus charge

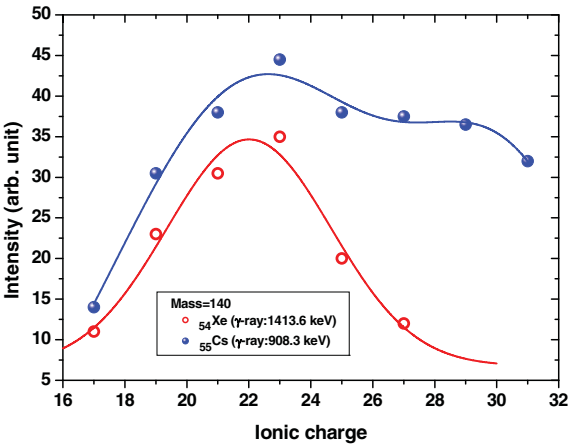

FIG. 10. (Color online) γ-ray intensity of $_{54}$Xe (1413.6 keV) and $_{55}$Cs (908.3 keV) for the mass 140 as a function of the ionic charge state. The Cs distribution clearly highlights a nanosecond isomeric state because of its asymmetric shape peaked on the high ionic charge states.

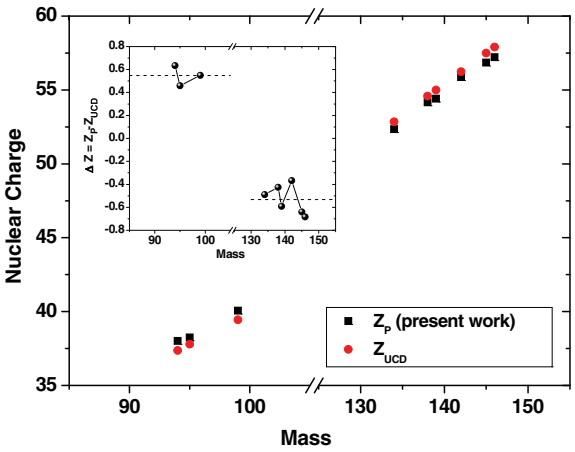

FIG. 11. (Color online) Most probable nuclear charge, Z_P, deduced from the present work and compared with $Z_{\rm UCD}$ calculated from Eq. (10). Inset: The difference $\Delta Z = Z_P - Z_{\rm UCD}$ as a function of mass. A clear nuclear charge polarization of about 0.5 unit can be observed.

density. This observation has been measured in a great number of experiments (see Refs. [40–42] and references therein). Compared to the unchanged charge density nuclear charge $Z_{\rm UCD}$, which is defined by Eq. (10), light fragments are found to have a smaller nuclear charge while heavy fragments show the opposite tendency:

$$Z_{\rm UCD}(A') = \frac{Z_F}{A_F}[A + \overline{\nu}(A')]. \qquad (10)$$

A represents the mass after prompt neutron emissions, while A' is the mass before prompt neutron emissions.

The difference ($\Delta Z = Z_P - Z_{\rm UCD}$) implies the existence of a charge polarization of nuclear matter. It is clearly apparent in Fig. 11 for the present ^{239}Pu($n_{\rm th}$, f) data, where $\overline{\nu}(A)$ values used in Eq. (10) come from evaluated data of Wahl [43]. The inset in Fig. 11 shows a consistent behavior of the average difference ($\langle\Delta Z\rangle$) between light and heavy mass regions. Indeed, we found 0.55 ± 0.05 and -0.53 ± 0.05, respectively, for light and heavy fission products. These values are in very good agreement with data from the literature (see, e.g., Ref. [42]). Besides, similar results were observed for close fissioning systems [40,41]. In addition to these remarks, results from K.-H. Schmidt [44] have revealed that the mean nuclear charge in the heavy mass region is centered around 54. The few ^{239}Pu($n_{\rm th}$, f) average nuclear charges reported in Table VIII seem to be in accordance with this observation.

TABLE VIII. Most probable (Z_P) and width (σ_Z) of nuclear charge distributions determined from the present measurements for various masses.

A	Z_P	σ_Z
94	38.0	0.5
95	38.2	0.5
99	40.1	0.5
134	52.4	0.7
138	54.2	0.5
139	54.4	0.5
142	55.9	0.5
145	56.9	0.7
146	57.2	1.0

C. Limitation of the method

As for all experiments based on γ spectrometry, the first main limitation is caused by the knowledge of decay data. Until now, despite many efforts made in γ-ray spectroscopy, a large number of nuclei (in particular, exotic nuclei) have not yet been measured with sufficient accuracy.

Another limitation for measuring isotopic yields by γ spectrometry is caused by the isotope lifetimes. Indeed, the isotopic yield determination of a long-living nucleus is experimentally too time-consuming. Thus, in general, yields can be measured only for isotopes with half-lives of less than a few hours, and of course, the γ spectrometry method completely rules out the investigation of stable nuclei.

Table IX summarizes the reasons why some isotopic yields could not be measured.

TABLE IX. Survey of the main reasons why some masses were not measured during our experimental campaign.

Mass	$T_{1/2}$ too long for at least one isotope	Nuclear decay data not well enough known	Yield too low
$\leqslant$132		X	
135	X		
149	X	X	
150	X	X	
$\geqslant$153			X

IV. CONCLUSION

Despite the insufficient knowledge of decay data, isotopic yield determination by γ-ray spectrometry has greatly improved yield measurements with the Lohengrin mass-spectrometer. Indeed, Lohengrin is today still the most accurate instrument for measuring thermal neutron fission yields, and with the present work, its range of application is practically doubled, now allowing also the study of isotopic yields of heavy fragments.

The experimental setup developed in the present work was shown to be a powerful tool for investigation of isotopic yields in all fission regions. Results presented in this work are very encouraging considering how uncertainties have been decreased compared to some other experiments and/or evaluated data.

Experimental campaigns are now starting to measure accurately the fission yields of various fissioning systems important for practical applications and for our knowledge of the fission process.

[1] J. Moreau and K. Heyde, in *The Nuclear Fission Process*, edited by C. Wagemans (CRC Press, Boca Raton, FL, 1991), p. 227.
[2] B. D. Wilkins *et al.*, Phys. Rev. C **14**, 1832 (1976).
[3] P. Möller *et al.*, Nature **409**, 785 (2001).
[4] H. Goutte, J. F. Berger, P. Casoli, and D. Gogny, Phys. Rev. C **71**, 024316 (2005).
[5] M. Kellett *et al.*, JEFF Report 20, NEA NØ6287 (OECD, 2009).
[6] M. B. Chadwick *et al.*, Nucl. Data Sheets **107**, 2931 (2006).
[7] K. Shibata *et al.*, J. Nucl. Sci. Technol. **48**, 1 (2011).
[8] H. O. Denschlag in *Experimental Techniques in Nuclear Physics*, edited by D.-N. Poenaru and W. Greiner (Berlin, 1997), p. 535.
[9] J. P. Bocquet *et al.*, Z. Phys. A **335**, 41 (1990).
[10] U. Quade *et al.*, Nucl. Phys. A **487**, 1 (1988).
[11] H. G. Clerc *et al.*, Nucl. Phys. A **247**, 74 (1975).
[12] G. Sieger *et al.*, Phys. Lett. B **53**, 45 (1974).
[13] J. L. Sida *et al.*, Nucl. Phys. A **502**, 233 (1989).
[14] G. Martinez *et al.*, Nucl. Phys. A **515**, 433 (1990).
[15] I. Tsekhanovich *et al.*, Nucl. Phys. A **688**, 633 (2001).
[16] C. Schmitt *et al.*, Nucl. Phys. A **430**, 21 (1984).
[17] T. Friedrichs, Ph.D. thesis, University of Brunswick, 1998.
[18] I. Tsekhanovich *et al.*, Nucl. Phys. A **658**, 217 (1999).
[19] D. Rochman *et al.*, Nucl. Phys. A **710**, 3 (2002).
[20] M. Djebara *et al.*, Nucl. Phys. A **496**, 346 (1989).
[21] D. Rochman, Ph.D. thesis, Strasbourg University, 2001.
[22] J. P. Bocquet *et al.*, Nucl. Instrum. Methods Phys. Res. A **267**, 466 (1988).
[23] E. Moll *et al.*, Nucl. Instrum. Methods **139**, 213 (1976).
[24] G. Fioni *et al.*, Nucl. Instrum. Methods A **332**, 175 (1993).
[25] H. Bateman, Proc. Cambridge Philos. Soc. **15**, 423–427 (1910).
[26] J. Theuerkauf *et al.*, *Program Tv*, unpublished (University of Cologne, Cologne, Germany).
[27] G. F. Knoll, in *Radiation Detection and Measurement*, 3rd ed. (John Wiley and Sons, New York, 1999), p. 448.
[28] U. Köster *et al.*, Nucl. Instrum. Methods A **613**, 363 (2010).
[29] J. Laurec *et al.*, Nucl. Data Sheets **111**, 2965 (2010).
[30] A. D. Belyaev *et al.*, Nucl. Instrum. Methods Phys. Res. Sec. B **43**, 5 (1989).
[31] A. Bail, Ph.D. thesis, University of Bordeaux, 2009.
[32] N. A. Gundorin *et al.*, in *Proceedings of the International Conference on Nuclear Data for Science and Technology, ND1994, Gatlinburg, Tennessee, May 9–13, 1994*, edited by J. K. Dickens (ANS, La Grange Park, IL, 1994), p. 139.
[33] A. A. Bogdzel *et al.*, in *Proceedings of the International Conference on Nuclear Data for Science and Technology, ND1991, Juelich (Germany), May 13–17, 1991*, edited by S. M. Qaim (Springer-Verlag, Berlin, 1991), p. 150.
[34] R. Brissot *et al.*, J. Phys. **37**, 241 (1976).
[35] S. J. Balestrini *et al.*, Phys. Rev. C **12**, 413 (1975).
[36] K. F. Flynn *et al.*, J. Inorg. Nucl. Chem. **37**, 869 (1975).
[37] Y. Baudinet-Robinet, Phys. Rev. A **26**, 62 (1982).
[38] H. Wohlfarth *et al.*, Z. Phys. A **287**, 153 (1978).
[39] T. Materna *et al.*, in *Proceedings of the International Workshop on Nuclear Fission and Fission Product Spectroscopy, Cadarache (France), May 13–16, 2009*, edited by A. Chatillon *et al.* (AIP Conference Proceedings, 2009), p. 367.
[40] H. Naik *et al.*, J. Phys. G **30**, 107 (2004).
[41] H. Naik *et al.*, Nucl. Phys. A **781**, 1 (2007).
[42] V. A. Roshchenko, V. M. Piksaikin, S. G. Isaev, and A. A. Goverdovski, Phys. Rev. C **74**, 014607 (2006).
[43] A. C. Wahl, At. Data Nucl. Data Tables **39**, 1 (1988).
[44] K. H. Schmidt *et al.*, Nucl. Phys. A **665**, 221 (2000).
[45] [http://www.nndc.bnl.gov].
[46] [http://ie.lbl.gov/toi.html].

1.3 Les rendements de l'Am-242

Grâce à la validation de la nouvelle méthode d'identification isotopique par spectroscopie gamma, nous avons développé un programme scientifique afin de mesurer précisément les rendements en masse et isotopiques dans la région des fragments lourds. Au-delà des motivations déjà présentées, il faut noter que les données évaluées et intégrées aux bases de données dans cette région de masse étaient (et sont encore aujourd'hui) basées largement sur des calculs et modèles qui utilisent comme données d'entrée des rendements mesurés avec une assez faible résolution en masse ($\Delta A \geqslant 3$) et en charge. Du fait de ce mode d'évaluation des données, des structures assez fines apparaissaient dans les rendements en masse évalués (par exemple autour de la masse 136 dans la librairie JEFF-3.1.1), ce qui rendait essentielle une confirmation que seule une mesure précise comme celle accessible à Lohengrin ($\Delta A \ll 1$) pouvait fournir. Dans ce cadre, la collaboration déjà active depuis 2006 a pu s'étendre au laboratoire LPSC de Grenoble, en particulier grâce à l'impulsion de Grégoire Kessedjian.

Une nouvelle campagne expérimentale a donc débuté en 2010 avec la mesure des rendements en masse et isotopiques des fragments issus de la fission thermique de l'U-233 et du Pu-241 [12,13]. Ces mesures se sont concentrées de manière essentielle sur l'amélioration de la précision dans la région des fragments lourds, inaccessible sans l'identification par spectroscopie gamma, et la région de la fission symétrique, où une grande statistique est nécessaire compte tenu des faibles rendements de fission. La plus grande difficulté à surmonter dans ces travaux a été la prise en compte précise de l'évolution des distributions en charge et en énergie avec le taux d'incinération de la cible fissile, cet élément étant le contributeur principal à l'incertitude systématique sur la mesure.

Dans le cadre de cette collaboration élargie, nous avons pu mener un programme expérimental pour étudier de manière détaillée les rendements en masse et isotopiques issus de la réaction ^{242}Am (n_{th}, f). La fission de ce noyau, ainsi que celle d'autres actinides de courte durée de vie (Pa-232, Np-238, ...) ne peut être mesurée qu'à Lohengrin car, étant donné l'impossibilité de fabriquer des cibles fissiles, on peut profiter du flux neutronique de l'ILL et induire la fission par double capture de neutrons sur une cible fertile, c'est à dire par la réaction ^{241}Am ($2n_{th}$, f). L'Am-242 est un noyau impair-pair pour lequel les effets d'appariement des protons sont à priori moins prononcés mais toutefois existants, ce qui nécessite des mesures précises. De plus, il présente un état isomère d'énergie très proche du fondamental (48.6 keV de différence d'énergie), de très longue durée de vie (141 ans), et dont le moment angulaire (5^-) est différent de celui de l'état fondamental (1^-). Les sections efficaces de capture et de fission de ce noyau avaient déjà été mesurées à l'ILL dans le cadre du projet Mini-Inca [2]. En particulier, les sections efficaces de fission au point thermique des deux états de l'Am-242 sont très différentes l'une de l'autre (plus de 6000 b pour la section efficace de fission de l'état isomère à comparer à moins de 3000 b pour l'état fondamental), ce qui a été attribué à la différence de moment cinétique. Il a donc semblé intéressant d'explorer plus en détail l'impact du moment angulaire sur la distribution en masse et isotopique des fragments, ainsi que leur énergie cinétique. Jusqu'à alors, les rendements de fission du système composé ^{243}Am* n'étaient connus qu'avec une précision médiocre et seuls les rendements en masse de la réaction ^{242m}Am (n_{th}, f) avaient été mesurés à Lohengrin dans la région des fragments légers avec des résultats plutôt contradictoires.

Les différentes campagnes de mesure des rendements de fission de l'Am-242 ont eu lieu entre 2011 et 2014 et ont fait l'objet de la thèse de doctorat de Charlotte Amouroux [14]. Bien que la précision obtenue n'ait pas permis de différentier de manière statistiquement significative les rendements issus de la fission de l'état isomère de ceux issus de la fission du fondamental, le travail contenu dans cette thèse propose un effort d'interprétation et de modélisation de grande qualité. En effet, les données mesurées avec Lohengrin ont nourri une grande quantité d'améliorations et progrès dans le

développement du modèle semi-empirique GEF, travaux effectués en collaboration avec Karl-Heinz Schmidt [15]. L'article qui suit présente les résultats des mesures sur les rendements de fission de l'Am-242 effectuées à Lohengrin et qui sont aujourd'hui intégrées à la base de données évaluées européenne JEFF-3.3 [16].

EPJ Web of Conferences **62**, 06002 (2013)
DOI: 10.1051/epjconf/20136206002

1

Measurement of fission yields from the ^{241}Am($2n_{th}$,f) reaction at the Lohengrin Spectrometer

Ch. Amouroux[1], A. Blanc[3], A. Bidaud[2], N. Capellan[2], S. Chabod[2], A. Chebboubi[2], H. Faust[3], G. Kessedjian[2], U. Köster[3], J.-F. Lemaitre[1,5], A. Letourneau[1], F. Martin[2], T. Materna[1], S. Panebianco[1], Ch. Sage[2], and O. Serot[4]

[1] CEA, Centre de Saclay, IRFU/SPhN, 91191 Gif-sur-Yvette, France
[2] LPSC Grenoble, CNRS/IN2P3, 53 rue des Martyrs, 38026 Grenoble Cedex, France
[3] Institut Laue Langevin, 6 rue Jules Horowitz, BP. 156, 38042, Grenoble, France
[4] CEA, DEN-Cadarache, 13108 Saint-Paul-lez-Durance, France
[5] CEA, DAM-DIF, Arpajon, France

Résumé. The study of fission yields has a major impact on the characterization and understanding of the fission process and is mandatory for reactor applications. While the yields are known for the major actinides (^{235}U, ^{239}Pu) in the thermal neutron-induced fission, only few measurements have been performed on ^{242}Am. This paper presents the results of a measurement at the Lohengrin mass spectrometer (ILL, France) on the reaction ^{241}Am($2n_{th}$,f): a total of 41 mass yields in the light and the heavy peaks have been measured and compared with the fission process simulation code GEF. Modus operandi and first results of a second experiment performed in May 2013 on the same reaction but with the goal of extracting the isotopic yields are presented as well: 8 mass yields were re-measured and 18 isotopic yields have been investigated and are being analyzed. Results concerning the kinetic energy and its comparison with the GEF Code are also presented in this paper.

1. Motivations

Among the actinides presenting an interest for fundamental research and applications, ^{242}Am is a very good example of an high radiotoxicity odd-odd short-lived nucleus. ^{242}Am possesses also two long-lived states: a high-spin isomer (5^-) with a half-life of 141 years and the ground state (1^-) with a half-life of 16 hours. The measured fission cross sections are (5972 ± 173) barn for the isomer and (1751 ± 55) barn for the ground state [1]. This reveals that the entrance channel of the fission reaction is affected by the spin. One of the remaining questions is consequently the influence of the spin on the final state (i.e. fission yields, kinetic energy of the fission products, ...). No data are nowadays available for the comparison of the final state issued from the fission of a nucleus in its (spin) isomeric state and in fundamental state. In a phenomenon where odd-even effects are present it is also interesting to notice that the most studied nuclei are nuclei with an even nuclear charge (^{235}U, ^{239}Pu, ^{233}U, ^{252}Cf) whereas

$Z_{Am} = 95$, the only other odd charge nucleus where thermal neutron induced fission had been studied in detail before was ^{237}Np.

Nuclear waste management is another motivation for the studies on the fission of ^{242}Am. ^{242}Am is produced by radiative capture on ^{241}Am, which is the main responsible of the radiotoxicity of Plutonium-separated nuclear waste from PWR reactors between 200 and 1000 years after irradiation. The best way to reduce its radiotoxicity is to transmute it, which consequently leads to the fission of ^{242}Am. Fission of ^{242}Am, like of any other actinide, produces fragments with large neutron cross-sections that are considered as neutron poisons for reactor operation as well as delayed neutrons, which play a role in a reactor control. A precise estimation of their quantity is important to design dedicated transmutation facilities where the fraction of minor actinides is not negligible any more.

2. Experiment

The double capture reaction was used to overcome the impossibility of using a ^{242}Am target and to produce ^{242}Am in both its isomeric ($T_{1/2} = 141$ y) and ground state ($T_{1/2} = 16.02$ h). Because of the rather low reaction rate in the double capture process, a high neutron flux is required. The experiment was performed at the High Flux Reactor (RHF) of the Institut Laue-Langevin (ILL) in Grenoble (France) which provides the highest thermal neutron flux in the world for on-line fission studies ($5 \cdot 10^{14}$ n $\cdot$ cm$^{-2} \cdot$ s^{-1}) combined with a mass and energy separation of fission products thanks to the mass spectrometer Lohengrin.

The target is placed 50 cm away from the core of the reactor. It consists in a 300 μg/cm^2 thick deposit of ^{241}Am (purity $> 99\%$) on a Ti backing and is covered by a 0.25 μm thick nickel foil that prevents a too large loss of fissile material by fission fragment sputtering. The fission products fly through a beam pipe under vacuum to reach the mass spectrometer called Lohengrin [2], composed of a dipole magnet followed by an electrostatic deflector. The magnet deflects the nuclei according to their momentum over ionic charge ratio (Av/q) while the electrostatic deflector allows their selection according to the kinetic energy over ionic charge ratio (E/q). The kinetic energy considered in this selection process is the energy of the fission product, after prompt neutron emission and minus the energy lost in the target and the cover foil. Fission products are produced stripped in the fission process ($q = Z$) and capture electrons as they go through matter. At the exit of the cover foil, they generally present an ionic charge close to $q = 20$-22.

A second magnet called RED Magnet (Reverse Energy Dispersion) allows to switch between an ionization chamber in straight direction (mass measurements) or refocus into a vacuum chamber with a tape where fragments are implanted (isotopic measurements). The ionization chamber [2] measures the energy of the fission product so, thanks to the E/q and A/q selection done by the spectrometer, we know q and deduce the mass of the fission product (A). When the fragments are deflected and implanted on a tape, γ rays produced after beta decay are registered with two high-efficiency HPGe clover detectors placed around the implantation position. Knowing the γ intensity, isotopic yields can be deduced. The same set up was previously used to measure the isotopic yields of ^{239}Pu(n_{th},f) and ^{233}U(n_{th},f) [3–5].

3. Data analysis and uncertainties

As Lohengrin selects nuclei according to their given ionic charge q and energy E, to obtain the yield of a fission product with a given mass A (Y(A)) one needs to integrate the measured fragments differential yields Y(A,q,E) over charge and energy:

$$Y(A) = \int \sum_{q} Y(A,q,E)dE.$$

Table. 1. Sources of relative uncertainties and their respective contributions.

Source	Contribution
Statistical	∼1%
Extrapolation of the low part of the energy distribution	1.5%
Extrapolation of the high part of the energy distribution	1%
Reproducibility	3%
Correlation between E and q	3%
Relative Normalisation (Burn-up)	∼3%
Total of the systematic error	5.5%

Assuming that there is no correlation between q and E, this integral can be rewritten as the product of the energy distribution (E-Scan) measured at a fixed ionic charge $Y(A,q_0,E)$ and the ionic charge distribution (q-scan) at a fixed energy $Y(A,q,E_0)$, divided by the differential yield at the common point $Y(A,q_0,E_0)$. The number of measurements can thus be drastically reduced to an E-scan and a q-scan. The influence of the correlation between energy and ionic charge distribution on the yield values was studied in reference [3] and estimated to add less than 3% on the relative uncertainty. Table 1 resumes the different sources of uncertainties and their contribution. As no analytical function was found to describe precisely the energy distributions with a reasonable number of parameters, a quadratic interpolation between the data points and a linear extrapolation on the edges were used. These extrapolations lead to systematic uncertainties that have been estimated from the maximum fluctuation of the extrapolated part contribution to the total distribution area observed in the set of E-scans (around 30) available for $A = 105$.

The reproducibility uncertainty was evaluated from the dispersion of the values measured for the same $Y(A,q_0,E_0)$ during the q-scan and E-scan. This point has the lowest statistical error (<1%). Such a comparison was performed systematically as a function of time for three masses ($A = 105$, $A = 98$, $A = 136$) and measured once for all the measured masses. Even if no common bias in the mean value is observed, a standard deviation of 3% cannot be explained only by statistics and is consequently considered as systematic uncertainty.

In order to obtain the fission yields, the number of fission products measured at a given mass should also be normalized to the number of fissions that occur in the target during the measurement. As this number cannot be directly measured at Lohengrin, the chosen procedure is to normalize all the measurements to the fission yield of a given mass (here $A = 105$), typically the most produced one, which is measured every 8 or 12h. As a consequence, relative fission yields are obtained. The mass used for the relative normalization is affected like all the other masses by the same uncertainties as mentioned before.

Another possible source of uncertainty is a change in the neutron flux that can occur between two normalization measurements. This possibility was evaluated by monitoring the neutron flux with ^{3}He detectors. No variation above the statistical ones was observed over a mass measurement cycle.

4. Physics results

4.1 Kinetic energy distributions

Due to a rather large variation of the kinetic energy during the experiment (a shift of up to 7 MeV was observed on the energy distribution made at $A = 105$) which we believe is a consequence of a

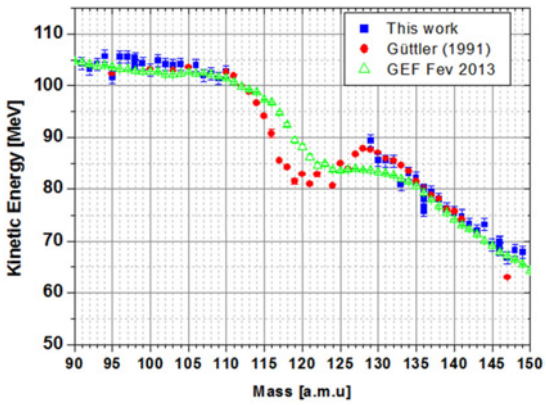

Figure 1. Kinetic energy of the fission products as a function of their mass. The energies obtained in this work are normalized to the kinetic energy of the mass 105 measured by Güttler and compared to the GEF predictions.

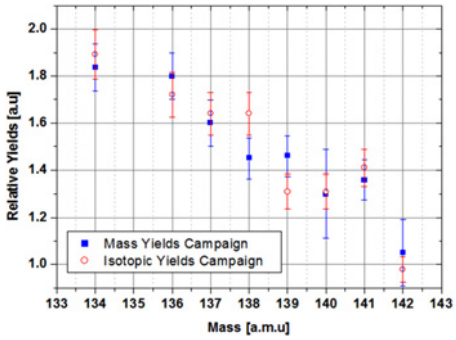

Figure 2. Fission Mass Yields obtained in the two measurement campaigns. The normalization of each set was performed on the sum from A = 136 to A = 142.

degradation of the target and its cover foil, only relative kinetic energies could be obtained. Since this distribution is not Gaussian, the most probable value is taken as kinetic energy. The associated uncertainty originates from the following two different effects. A first uncertainty of 0.6 MeV is due to the determination method of the most probable value from the measured energy distribution. Secondly, an error of 0.6 MeV is due to the correlation between the energy and the ionic charge. This error has been estimated from the data obtained in references [3, 6].

We used the kinetic energy mean value of the mass 105 measured by U. Güttler at the Lohengrin spectrometer in 1991 [6] to shift our data. The results are plotted on Figure 1 showing a very good agreement with the past measurement.

The two measurements are also compared with the GEF Code prediction [7]. While the GEF predictions agree with the experiments on the asymmetric mass region it presents a shift in the symmetric region. The same behaviour was observed for ^{235}U but not on ^{239}Pu neither on ^{233}U.

4.2 Mass fission yields

During the isotopic yield measurement campaign, eight mass yields were re-measured on the heavy peak. The comparison with the values obtained in the mass yield campaign (Fig. 2) shows that the new measurements agree with the previous ones, proving the reproducibility of the measurement.

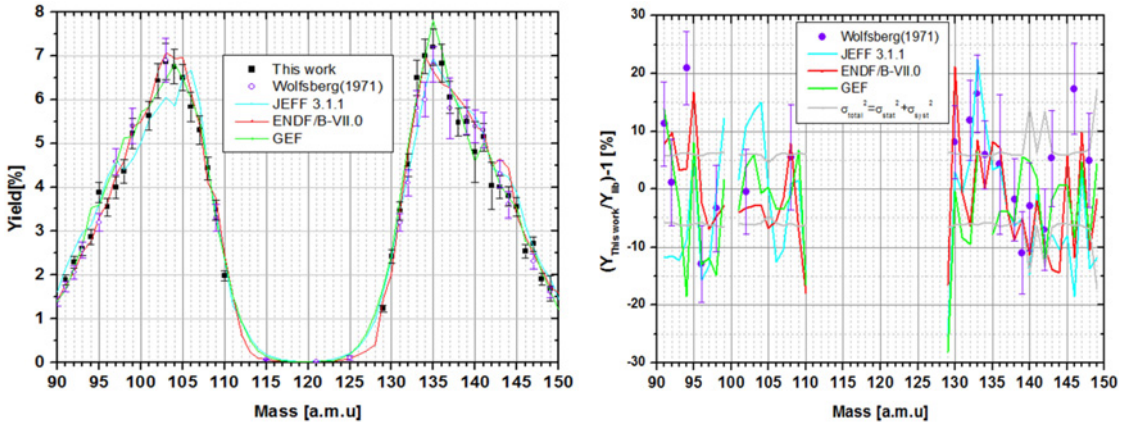

Figure 3. (Left) fission mass yields of ^{242}Am compared with JEFF-3.1.1 and ENDF/B-VII.0 libraries as well as the experimental data from Wolfsberg [7] and the GEF model. (Right) relative difference between the measured yields and the ones given by JEFF-3.1.1, ENDF/B-VII.0 and Wolfsberg.

Table. 2. List of mass chain nuclei measured. The green symbols indicate the nuclei from which we can obtain an independent isotopic yield and the red crosses the ones we cannot. (Preliminary results).

A\Z	Sb	Te	I	Xe	Cs	Ba	La
134	✓(m) X (gs)	✓	✓	X	X	X	X
136	X	✓	✓	X	X	X	X
137	X	X	✓	✓	X	X	X
138	X	X	✓	✓	✓	X	X
139	X	X	X	✓	✓	X	X
140	X	X	X	✓	✓	X	X
141	X	X	X	X	✓	✓	X
142	X	X	X	X	✓	✓	~

The preliminary results of our measured mass yields are shown on Figure 3. Each mass yield is normalized to the yield of the mass 105 ($Y_{105} = 6.5\%$, according to JEFF-3.1.1). The experimental results have been compared with the most commonly used nuclear data libraries, JEFF-3.1.1 and ENDF/B-VII.0, as well as with the experimental data obtained by Wofsberg in 1971 [8] on which the evaluations are mainly based. As shown on Figure 3, the largest discrepancies occur in the heavy mass region. Concerning the light peak, our measurement is closer to the ENDF/B-VII.0 library. It has to be noticed the good agreement within the quoted uncertainties with the GEF code. Finally, our results agree with the yields measured by Wolfsberg et al. for the fission of ^{242m}Am. It should be noted that the mass 95 seems to present a large yield which is not compatible with the evaluated data.

4.3 Isotopic fission yields

The isotopic yields were measured for 8 masses: 134, 136, 137, 138, 139, 140, 141 and 142. According to a preliminary analysis, we will be able to extract yields for the nuclei listed in Table 2. The fission yields of the very light tail were measured in [9] and show evidence of an odd-even effect. However according to previous measurement on ^{241}Am(n,f) and ^{243}Am(n,f) this effect is not expected for the mass peak regions [10]. A previous experiment using the Lohengrin spectrometer with an absorber [11] studied the odd-even effect for proton and neutron on the light peak. An odd-even effect was observed on neutron but not on proton. The study of the heavy mass region was performed in this experiment.

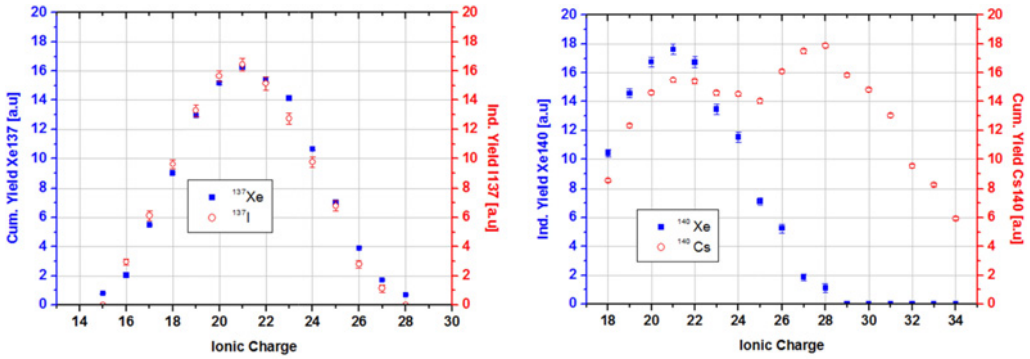

Figure 4. Ionic charge distribution for different isotopes. ^{137}Xe and ^{137}I (left part) and ^{140}Xe and ^{140}Cs (right part).

In contrast to the procedure followed in most of the past experiments at Lohengrin (including the one described in [11]), during the present measurement campaign, the whole ionic charge distribution was measured. It is indeed known that the presence of nanosecond isomers disturbs the ionic charge distribution [12] and that it can affect strongly the estimation of the fission yields if this effect is not taken into account. For example, it was clearly the case for the Güttler experiment [6]. Since isomeric states are more found in odd-odd nuclei, it has an impact on the so-called odd-even effect observed in the fission yield. The impact (up to 80%) of the presence of nanosecond isomers is shown for A = 140 in Figure 4 (right); as a comparison a "normal" distribution for A = 137 is given in Figure 4 (left). We can see that, in the case of mass 137, the Xe and I present a Gaussian distribution while, for mass 140, Xe shows a Gaussian distribution but Cs is affected by a nanosecond isomers, characterized by a second Gaussian distribution with a mean charge of 28.

5. Conclusion & perspectives

The presented measurement of the ^{241}Am($2n_{th}$,f) fission yields shows that our results largely improve the experimental data on the mass yields by enlarging the range of measured mass and by reducing the experimental uncertainties. These results are in better agreement with the ENDF/B-VII.0 library in the light mass region and are consistent with JEFF-3.1.1 and ENDF/B-VII.0 in the heavy one. A good agreement was also found with the results of the GEF model. Even if the mass fission yields are of great interest on themselves, they are also a step towards the measurement of isotopic yields. These are needed for application purposes as well as for the improvement and validation of fission models. A first campaign of measurement of the isotopic yields was performed at Lohengrin. According to the preliminary analysis, 18 isotopic yields are expected. Such a method has already been applied successfully to measure isotopic yields of heavy fission products in ^{239}Pu(n_{th}, f) [3, 4].

Références

[1] A. Letourneau et al, *in preparation*
[2] E. Moll et al., Nucl. Instrum. And Methods **139**, 213 (1976)
[3] A. Bail, Ph.D. Thesis, Bordeaux, 2009 (in French) and references therein
[4] A. Bail, Phys. Rev. C **84**, 034605 (2011)
[5] F. Martin, Proc. of the International Conf. on Nuclear Data for Science and Technology (ND-2013) March 4-8, 2013, New York
[6] U. Güttler, Ph.D. Thesis, Johannes Gutenberg-Universität Mainz, 1991 (in German)
[7] K.-H. Schmidt, B. Jurado JEF/DOC 1423

[8] K.Wolfsberg et al., Phys. Rev., C **3**: 1333-7 (March 1971)
[9] P. Stumpf et al, S.M. Quim (Ed.), Nuclear Data for Science and Technology, Springer, Berlin, 1992, p. 145
[10] H. Naik, S. P. Dange, A. V. R. Reddy, Nucl. Phys. A **781** (2007)
[11] P. Siegler et al, S.M. Quim (Ed.), Nuclear Data for Science and Technology, Springer, Berlin, 1992, p. 128
[12] T. Materna et al AIP Conf. Proc. **1175**, 367–370 (2009)

1.4 Préparer le futur de Lohengrin

Le développement de la technique d'identification des fragments de fission par spectroscopie gamma que nous avons développée s'est revelé de grand intérêt pour l'exploration de la structure des noyaux riches en neutrons produits lors de la fission. En effet, l'étude de ces noyaux permet à la fois de contraindre les paramètres du potentiel nucléaire et leur évolution loin de la vallée de stabilité, mais aide également à la compréhension de la création d'éléments lourds dans les processus astrophysiques. La fission induite par neutrons thermiques est donc un outil important pour produire une grande variété d'isotopes riches en neutrons loin de la stabilité et la spectroscopie est le moyen le plus précis pour étudier leur structure.

Dans ce cadre, une campagne de mesure appelée EXILL (*EXogam at ILL*) a eu lieu en 2012 et 2013 grâce à l'installation du détecteur de haute efficacité EXOGAM sur la ligne intense de faisceau de neutrons froids PF1B à l'ILL. Ces expériences ont permis d'effectuer la spectroscopie d'isotopes très riches en neutrons provenant de la fission de l'U-235 et du Pu-241 par des techniques de coïncidence γ-γ ou γ-γ-γ. Dans cette campagne, la masse et la charge nucléaire ont été identifiées par des coïncidences avec des rayons γ connus du noyau d'intérêt ou de son fragment complémentaire [17].

Cependant, la contrainte due à la nécessité de détecter au moins trois rayons γ en coïncidence implique que seuls les noyaux produits avec un rendement relativement important peuvent être mesurés (typiquement de l'ordre de 10^{-4} par fission ou plus). Il nous a donc paru clair qu'une meilleure option serait l'identification non ambiguë d'un fragment associé à la détection d'un ou de plusieurs rayons γ dans le fragment complémentaire. En effet, cela permettrait l'attribution précise des rayons γ encore inconnus à un produit de fission identifié de manière unique et permettrait l'étude de noyaux produits à un taux beaucoup plus faible.

Dans ce contexte, nous avons commencé à travailler au développement d'un nouvel instrument, appelé FIPPS (*FIssion Product Prompt γ-ray Spectrometer*), et ayant la propriété de combiner la spectroscopie γ de haute résolution à un grand spectromètre de recul suivant le même principe que Lohengrin [18, 19]. Aujourd'hui, le projet FIPPS est l'un des 7 nouveaux instruments à construire dans le cadre du programme de modernisation de l'ILL baptisé "*ENDURANCE*" et sera déployé en deux phases. Dans une première phase, actuellement en cours, seul un ensemble de 8 clovers HPGe, très similaire au setup réalisé pendant la campagne EXILL, est installé dans le but d'identifier, toujours avec la technique de triple coïncidence, les fragments de fission issus de cibles d'U-235 et d'U-233. Dans la seconde phase, un spectromètre de recul sera ajouté au setup pour remplacer les coïncidence γ-γ-γ avec des coïncidences γ-γ-ion. Or, il faut noter que les spectromètres de recul tel Lohengrin, malgré leur excellente résolution en masse et en énergie, souffrent d'une très faible acceptance (<0,01%). Pour surmonter cette limitation, le spectromètre FIPPS utilisera le principe du GFM (*Gaz Filled Magnet*), méthode développée dans les années '60 à Oak Ridge, où la séparation des ions est obtenue dans un aimant dipolaire rempli d'un gaz opportunément choisi.

FIPPS est un instrument de grande complexité et qui nécessite d'investissements importants, notamment pour le développement d'un GFM de grande acceptance et d'un système de détection utilisant une TPC (*Time Projection Chamber*). L'intérêt suscité au sein de la communauté des physiciens travaillant sur la structure des noyaux exotiques, bien plus nombreuse (en France comme ailleurs) que celle des fissionistes, a donné une impulsion importante au projet et à son programme scientifique. L'espoir est que l'ILL reste dans les années à venir une installation de choix pour la production et l'étude des fragments de fission. Cela est de bon augure pour que Lohengrin puisse enfin envisager sereinement de prendre une retraite bien méritée.

2

Quelques développements expérimentaux

Caractériser les propriétés des noyaux issus de la fission en cinématique directe, c'est à dire avec le noyaux fissionnant au repos, est un défis depuis les premières mesures qui ont suivi la découverte de la fission. En effet, lorsque les fragments de fission ne possèdent que l'énergie cinétique venant de la répulsion colombienne entre eux (de l'ordre du MeV par nucléon, au mieux !), ces ions de basse énergie sont très rapidement arrêtés par la matière qu'ils traversent et laissent des signaux faibles et peu discriminants dans les détecteurs (qu'ils soient gazeux ou semi-conducteurs). De plus, l'émission de neutrons change le nombre de masse et la cinématique de ces fragments et complique davantage la détermination précise de l'état finale de la réaction. Formé à l'utilisation des détecteurs gazeux depuis ma thèse de diplôme, c'est naturellement vers cette technique que je me suis orienté dans le développement de techniques de détection innovantes pour la fission. Je présente ici deux développements instrumentaux, l'un autour du spectromètre FALSTAFF et l'autre sur la TPC FIDIAS, deux projets dans lesquels je me suis beaucoup impliqué et qui me semblent constituer un bon exemple des enjeux et des difficultés à surmonter dans la détection d'ions lourds de basse énergie.

2.1 Le spectromètre FALSTAFF

Comme déjà évoqué dans le chapitre 1.1, une des limitations de Lohengrin est que, compte tenu du type de cible qu'il est possible d'insérer dans le cœur du réacteur de l'ILL, seul un des deux fragments de fission est éjecté de la cible et peut être détecté dans le spectromètre. Cette limitation empêche de reconstruire l'état final de la réaction de fission, en particulier car toute information relative à la masse des fragments avant émission des neutrons est totalement inaccessible. De manière générale, toutes les corrélations entre fragments, aussi bien en termes d'énergie cinétique que d'énergie d'excitation, ne sont pas mesurables alors que leur étude constitue une étape indispensable pour arriver à une compréhension détaillée de la dynamique du processus.

C'est à partir de l'année 2010 qu'une collaboration entre le CEA/Irfu, le GANIL, le LPC de Caen et le CEA/DAM s'est structurée autour d'un projet visant à développer un instrument capable de mesurer les distributions des fragments de fission avant et après évaporation des neutrons,

fournissant ainsi la multiplicité des neutrons associée à chaque fragment. Ce spectromètre, appelé FALSTAFF (*Four Arm Clover for the Study of Actinide Fission Fragments*) par Diane Doré qui en est vite devenue la responsable scientifique, vise à détecter en coïncidence les deux fragments de fission éjectés d'une cible très mince irradiée par un faisceau de neutrons. La mesure combinée de la vitesse et de l'énergie cinétique des deux noyaux permet de déterminer la masse des fragments avant et après émission des neutrons. L'article qui suit [20], décrit de manière synthétique le spectromètre FALSTAFF, les détecteurs qui le composent, et présente l'état d'avancement de la R&D en 2014. Il est évident que les développements ont procédé de manière significative depuis cette époque relativement lointaine, en particulier dans le cadre de la thèse de Loïc Thulliez [21]. Néanmoins, il me semble intéressant de commenter les difficultés que ce projet a connu et qui sont dues à la complexité de la mesure.

La première difficulté que le développement d'un tel dispositif a posé à l'équipe a été la détermination des détecteurs à utiliser pour mesurer la vitesse et l'énergie des fragments de fission. Pour la mesure de vitesse, nécessaire pour déterminer la masse des fragments avant évaporation par ce que l'on appelle la "méthode 2V", il est apparu rapidement qu'un système de temps de vol était le seul à permettre d'atteindre une résolution en masse unitaire (ou proche de l'unité). Profitant de l'expérience accumulée et des développements menés en particulier par Julien Pancin entre l'Irfu et le GANIL, nous nous sommes concentrés sur un système de temps de vol basé sur des feuilles émissives couplées à des détecteurs d'électrons secondaires (SED, *Secondary Electron Detectors*). Des nombreuses années de R&D ont été nécessaires pour que la technique arrive à maturité et permette d'atteindre une résolution en temps meilleure que à 200 ps (FWHM) et une résolution en position d'environ 1 mm (FWHM), performances nécessaires compte tenu de la base de vol de 50 cm disponible pour FALSTAFF. En particulier, le choix du matériau constituant les feuilles émissives (le Mylar aluminisé), son épaisseur et sa technique de fabrication, ont fait l'objet de nombreuses études. La dernière en date à laquelle j'ai participé et qui fait l'objet du deuxième article [22] présenté dans ce chapitre, porte sur les mesures d'homogénéité des feuilles émissives, paramètre dont la connaissance précise est fondamentale pour limiter les effets systématiques dus aux pertes d'énergie des fragments dans les feuilles.

Également les SED, détecteurs gazeux à basse pression (quelques dizaines de mbar) utilisés depuis les années '80 pour la trajectographie d'ions de basse énergie, ont fait l'objet de nombreuses étapes d'optimisation. En particulier, plusieurs prototypes ont été fabriqués pour déterminer le meilleur compromis entre les propriétés de multiplication du gaz à basse pression, le profil longitudinal et transverse du champ électrique d'amplification, la segmentation de l'anode de collection des charges et la minimisation du budget matière de la feuille d'entrée du détecteur. Du fait du champ électrique intense nécessaire à assurer le gain suffisant pour amplifier le petit nombre d'électrons secondaires produits dans la feuille émissive, le SED est un détecteur dans lequel le taux de claquages peut se révéler rédhibitoire et cela demande un soin tout particulier dans la technique d'assemblage de la chambre proportionnelle multifils qui le constitue.

En ce qui concerne la mesure de l'énergie cinétique, le choix de la technique de détection s'est également porté très rapidement sur un détecteur gazeux de type chambre à ionisation. Le mode chambre à ionisation assure l'excellente résolution en énergie (de l'ordre de 1 %) qui est nécessaire pour déterminer avec bonne précision la masse des fragments après émission des neutrons (par la méthode dite "E-V" qui combine la mesure de l'énergie et de la vitesse des fragments complémentaires). En plus, une chambre à ionisation segmentée permet de mesurer la perte d'énergie des ions dans le gaz et d'identifier, un peu comme c'est le cas au plan focal de Lohengrin, leur charge nucléaire par la technique ΔE-E. Bien qu'une chambre à ionisation soit un type de détecteur plus conventionnel que le SED, la résolution en énergie à atteindre, accompagnée à la nécessité de réduire, encore une fois, au minimum le budget matière des fenêtres d'entrée, ont rendu nécessaires

plusieurs années de développement, en particulier au LPC de Caen, qui ont amené à la fabrication du détecteur CALIBER. L'enjeu ici a été de développer une chambre à ionisation axiale pour mesurer le profil de perte d'énergie des fragments de fission et ainsi déterminer leur charge.

Les enjeux et les difficultés liées à au développement expérimental de FALSTAFF ne sont pas uniques ni surprenants, bien au contraire. Un des premiers dispositifs 2V-EV qui a été conçu, fabriqué et installé à l'ILL dans les années '80, "COSI FAN TUTTE" [23], a nécessité des années de développement et d'améliorations, en particulier en ce qui concerne la chambre à ionisation axiale permettant la mesure de la charge [24, 25], avant de produire ses premiers résultats. Il en est de même pour les spectromètres 2V-EV qui sont également en développement dans le monde depuis le début des années 2010, c'est à dire VERDI [26] au JRC-IRMM (Belgique), SPIDER [27] au Los Alamos National Laboratory aux USA, STEFF [28] à l'Université de Manchester en Grande Bretagne. Ces instruments, bien que similaires dans le principe, utilisent chacun des détecteurs différents : par exemple, le TOF dans VERDI est assuré par des détecteurs au diamant alors que dans SPIDER et STEFF le choix s'est porté sur des Micro-Channel Plates (MCP). Il est évident que, mis à part la passion effrénée pour l'opéra et ses protagonistes, les équipes qui développent des spectromètres pour la mesure en coïncidence des fragments de fission en cinématique directe partagent la même difficulté à trouver le bon compromis entre les différentes contraintes et atteindre les performances nécessaires pour être compétitifs avec le bon vieux Lohengrin.

Pour autant, la difficulté des mesures en cinématique directe est compensée par la diversité des installations dans lesquelles des spectromètres 2V-EV peuvent être installés, ce qui au demeurant explique la diversité des développements ayant lieu en parallèle dans différents pays. En Europe, des faisceaux de neutrons dans la gamme d'énergie d'intérêt pour la fission des actinides sont disponibles sur les installations n-TOF au CERN [29] et à GELINA [30], nELBE à Dresden [31] ou, seulement en France, LICORNE à Orsay [32] et NFS au GANIL [33, 34]. A l'origine, le spectromètre FALSTAFF a été conçu et développé ayant comme cible l'installation NFS (*Neutron For Science*) qui vient d'être construite au GANIL dans le cadre du projet SPIRAL2. L'installation NFS sera bientôt en mesure de délivrer des faisceaux de neutrons quasi-monoénergétiques allant jusqu'à 31 MeV et des spectres blancs jusqu'à 40 MeV dont l'énergie pourra être mesurée avec grande précision grâce à une base de vol de 30 m. Il est donc évident que FALSTAFF, à l'instar d'autres instruments "mobiles", pourra être utilement employé à NFS mais également dans d'autres installations pour produire un ensemble cohérent de mesures des distributions des fragments issus de la fission de différents actinides en fonction de l'énergie du neutron incident.

EPJ Web of Conferences **69**, 00021 (2014)
DOI: 10.1051/epjconf/20146900021

2

FALSTAFF: a novel apparatus for fission fragment characterization

Stefano Panebianco[1], Diane Doré[1], Fanny Farget[2], François-René Lecolley[3], Grégory Lehaut[3], Thomas Materna[1], Julien Pancin[2] and Thomas Papaevangelou[1]

[1]CEA Centre de Saclay, Irfu, 91191 Gif-sur-Yvette, France
[2]GANIL, CEA/DSM-CNRS/IN2P3, Bd H. Becquerel, 14076 Caen, France
[3]LPC Caen, ENSICAEN, Université de Caen, CNRS-IN2P3, 14050 Caen, France

Abstract. The study of nuclear fission and in particular the correlation between the produced fragments and the associated neutrons is encountering renewed interest since new models are available on the market and a large set of applications show a rather stringent demand on high quality nuclear data. The future Neutrons For Science installation, being presently built at GANIL (Caen, France) in the framework of the SPIRAL2 project, will produce high intensity neutron beams from hundreds of keV up to 40 MeV. In view of this opportunity, the development of an experimental setup called FALSTAFF (Four Arm cLover for the Study of Actinide Fission Fragments) has been undertaken since 2011. This novel apparatus is meant to provide a full characterization of fission fragments in terms of mass, nuclear charge and kinetic energy. Moreover, it will provide a measurement of the mass before and after neutron evaporation, leading to the determination of the neutron multiplicity as a function of the fragmentation. The FALSTAFF setup is presently in its R&D phase in order to achieve the required specifications, especially in terms of time, space and energy resolution of the different detectors.

1 Introduction

A regained interest in studying nuclear fission has been recently triggered by both the need to answer fundamental physics questions related to the fine structure of the process and the necessity of providing more accurate data for applications. A large number of open questions are still on the table concerning fission fragments properties. First of all, it is not fully clear how the excitation energy of the parent nucleus is transferred to the fragments and how they share this energy. In addition, the strength of the coupling between individual and collective excitations, the impact of level densities and the disappearance of shell effects with the excitation energy, the presence of even-odd effects on mass and charge yields and the spin population of the fragments are still subjects open to discussions on their interpretation and failing to be fully described by theory. In order to answer these questions, different observables are needed in a large range of fissioning systems and excitation energies. For instance, neutron multiplicity and total kinetic energy as a function of the excitation energy of the compound nucleus are needed to address the energy sharing between fragments and, more generally the properties of the scission configurations. The evolution of shell effects in the fissioning system and in the fragments could be enlighten by the study of fragment mass and isotopic yields, together with

Article available at http://www.epj-conferences.org or http://dx.doi.org/10.1051/epjconf/20136900021

the correlations between the fragment energy and neutron multiplicity and the fragment mass and nuclear charge. These correlations need to be studied as a function of the excitation energy of the compound nucleus, since shell effects are supposed to disappear for high incident energy. The same can be said for the understanding of even-odd effects where the interesting observable is the evolution of the fragment yields with the compound nucleus properties (fissility, even-odd asymmetry, excitation energy). The most effective insight on the deformation energy of the fragments comes from the correlation between the total kinetic energy and the fragment mass. Finally, the study of intrinsic excitation at scission requires the measurement of scission neutrons and/or light charged particle emission. On the other hand, there is no doubt that the major application for which a precise knowledge of the fission process plays an essential role is a nuclear reactor. This is already true for the operation of the present nuclear plants, largely based on Light Water Reactors using the thermal fission of ^{235}U and ^{239}Pu isotopes. On the other hand, the large development of innovative nuclear systems, the so-called Generation IV, mostly based on fast neutrons reactors and designed to transmute nuclear wastes, requires a large effort to provide new high quality data for a large set of fissioning nuclei (from Th to Cm) and in the neutron energy range going from thermal to fast (~2 MeV).

Based on these motivations, an exceptional opportunity is opened by the Neutrons For Science (NFS) facility being built at GANIL (Caen) in the framework of the SPIRAL 2 project [1]. Thanks to its competitive neutron flux, together with the possibility to perform experiments with radioactive targets, this neutron Time of Flight installation will allow exploration of the underexploited fast energy domain in order to provide data for fundamental physics and nuclear technology. These arguments have motivated the development of a new detection system called FALSTAFF (Four Arm cLover for the STudy of Actinide Fission Fragments) [2]. This novel apparatus is meant to provide a full characterization of fission fragments in terms of mass, nuclear charge and kinetic energy. Moreover, it will provide a measurement of the mass before and after neutron evaporation, leading to the determination of the neutron multiplicity as a function of the fragmentation. The experimental technique giving access to these observables is based on the coincidence measurement of the velocity and energy of the two fragments. The velocity is provided by a time-of-flight system while the residual energy is measured by ionization chambers. The simultaneous measurement of the energy loss within the chamber gas will also provide the nuclear charge of the light fragment. Finally, the apparatus is being designed to be eventually installed in other installations and to be possibly coupled to neutron or gamma detection systems. The FALSTAFF setup is presently in its R&D phase in order to achieve the required specifications, especially in terms of time and space resolution of the TOF detectors. Time of flight of the fission fragments is measured in transmission mode by emissive foils coupled to secondary electron detectors (SED). A fully equipped arm, composed of two TOF detectors and an ionization chamber, is presently being tested at CEA Saclay with a spontaneous fission source. These tests are an essential step to assess and qualify our technical choices and compare the experimental results with simulations.

2 The FALSTAFF setup

The aim of the FALSTAFF setup is to perform a combined time of flight and residual energy measurement of complementary fission fragments in coincidence to determine their mass, nuclear charge and kinetic energy. The *2v* technique [3], based on the simultaneous measurement of the two fragment velocities, gives access to their masses before neutron evaporation (initial masses) under the assumption that the average fragment velocity is not modified by the evaporation process. The mass after neutron evaporation (final mass) is determined by the *Ev* technique [3] from a coincidence measurement of the fragment energy and velocity. Therefore, the mean neutron multiplicity as a function of the fragment mass may be deduced directly from the difference between initial and final mass. The velocity is provided by a time-of-flight system (TOF) while the residual energy is measured by ionization chambers (IC). The simultaneous measurement of the energy loss within the chamber gas will also provide the nuclear charge of the light fragment.

CNR*13

The major challenge of the FALSTAFF setup is to provide an efficient and precise detection of low energy heavy ions in direct kinematics. These experimental conditions are clearly the most difficult since, given the low energy of ions, their energy loss through all the crossed materials is important and constitutes the main limitation to the detector resolution. These losses have to be taken into account to correctly reconstruct the velocity and energy. This implies that the thickness of material layers has to be reduced as much as possible and that the ion positions on the different layers have to be precisely measured to calculate the crossed thickness and then apply energy loss corrections. In order to achieve the desired mass resolution, the TOF and IC required performances are rather constrained. The TOF system should provide a time resolution better than 150 ps, together with a position resolution of 1.5 mm. The energy resolution required of the IC is 1%. Moreover, given the neutron flux at a 5 m distance from the NFS converter (1.8 10^6 n/cm^2/s for an incident deuteron intensity of 50 µA), an actinide target of 150 µg/cm^2, a required statistics of 1000 events for the mass yields of 1% and, assuming a 1 MeV bin size for the neutron energy, a geometrical acceptance of about 2% of 4π is needed to allow for a beam time shorter than two weeks.

As a consequence, the use of large detectors providing low budget materials and high resolution performance is mandatory. For the TOF measurement, the necessary timing resolution will be obtained by a combination of an emissive foil and a MWPC (Multi Wire Proportional Counter) as secondary electrons detector (SED) [4]. A large area can be covered with this type of detector without degrading the time and spatial resolution. The most recent results on the R&D on two prototype SEDs are presented in the next section. The fragment energy will be measured with ionization chambers, this type of detector being able to reach the desired 1% energy resolution [5]. The fragment nuclear charge identification will be provided by ΔE-E correlation up to Z=40. Among the different types of existing ionization chamber setups, segmented or axial chambers are foreseen. In addition, a more advanced detector, providing the collection of the scintillation photons generated by ions crossing the gas, is under study [6]. This latter solution could provide a fast time signal in addition to the energy measurement. This could allow elimination of the time-stop detector. Since this innovative R&D is still in progress, an axial chamber, not presented here, will be constructed for the first version of the setup.

Figure 1. Schematic view of the two-arm FALSTAFF setup.

The first version of the setup will be composed of one arm consisting of two SED detectors together with an existing ionization chamber (called MiniHarpee). This setup will be tested with a ^{252}Cf

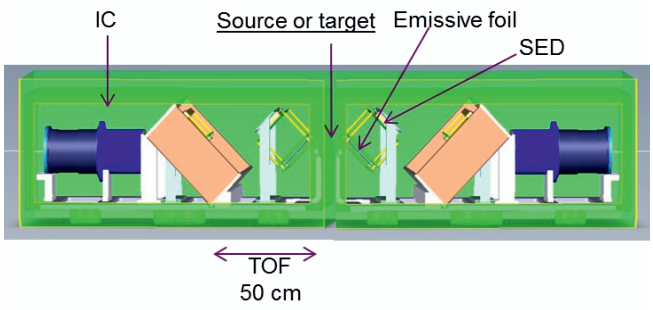

spontaneous fission source in order to measure the final mass of light fragments (the heavy ones cannot be reconstructed with this setup because of their large nuclear charge). In a second step, a second arm will be added in order to realize the coincidence 2v and Ev techniques (Figure 1). For this setup, two axial ionization chambers will replace the MiniHarpee. A spectroscopic ^{252}Cf source, providing the two fission fragments, is presently under development specifically for this setup. It will first allow verification of the resolutions obtained for the determination of the initial and final mass of light and heavy fragments. Then the setup will be moved to NFS for a day-one experiment using a ^{238}U target. In a last step, the solid angle of the FALSTAFF setup will be increased by adding two other arms thus allowing the collection of better statistics or the use of thinner targets.

2.1 The R&D on SED

The TOF measurement is provided by a system of two SEDs, one to measure the time of start and the other for the stop. A SED system is made of an emissive foil and a MWPC detector (Figure 2) [4]. A aluminized Mylar (0.9 µm thickness), inclined at 45° with respect to the horizontal direction and polarized at -10 kV, is placed along the path of the fission fragments. A grounded grid placed at 1 cm from this emissive foil provides a high electric field close to the foil. The secondary electrons extracted by the crossing ion from the Mylar foil are then accelerated to 10 keV and fly towards the MWPC detector. The accelerated electrons pass through the MWPC entrance foil (0.9 µm aluminized Mylar) with 70% efficiency. They produce ionization electrons inside the gas which are then amplified while drifting towards the cathode. The amplification takes place over the whole drift path thanks to the low pressure of the gas (4-6 torr). The time signal is then read from the wire plane by a fast amplifier. The spatial information is extracted from the charge induced on a 2D pixelized cathode read by a high frequency sampling Front End Electronics card based on the AFTER chip [7].

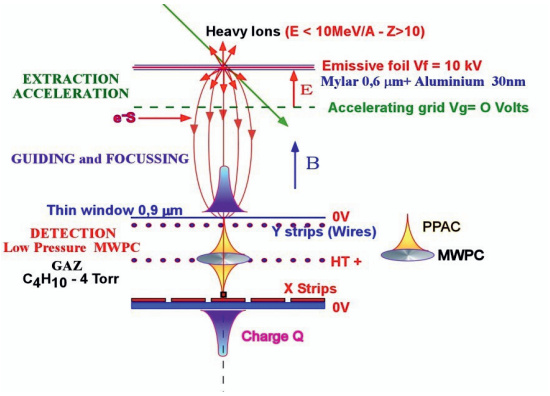

Figure 2. Working principle of a SED detector.

A MWPC-SED prototype of 15 cm x 20 cm active area with a pixelized cathode (68x48 pads) and a gap of 1.6 mm between the entrance window and the anode has been built and tested in laboratory with fission fragments from a 252Cf source. Both time and position resolutions have been measured [2]. The time resolution as a function of the voltage applied between the entrance window and the anode is shown for different pressures in the left panel of Figure 3. The best obtained resolution is 120 ps but further improvements are expected from noise reduction, possibly improving the resolution down to 100 ps. The position resolution of the SED depends on the focalization of the secondary electrons reaching the MWPC entrance window. Therefore, the SED has been placed inside a dipole providing a magnetic field up to 150 gauss. The right panel of Figure 3 shows the position resolution in the X and Y directions as a function of the magnetic field. A resolution of 1.5 mm is reached for a field of 90 gauss. The achieved time and position resolutions are already satisfactory since they correspond rather well to the needed specifications. Moreover, the position resolution requirements on the start SED being less demanding, this detector does not need to be placed inside a magnetic field (Figure 1). The actual experimental values of time and position resolutions are used in the simulation of the full setup.

CNR*13

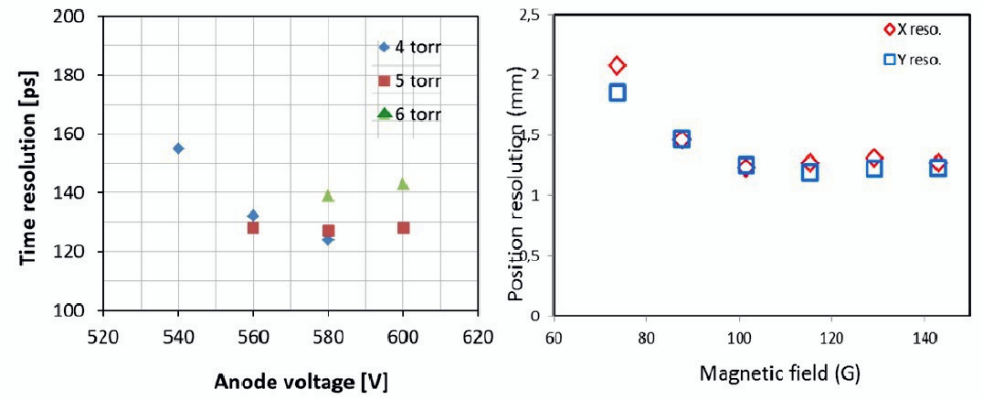

Figure 3. Time resolution as a function of the anode voltage for different gas pressures (left). Position resolution in the X and Y directions as a function of the magnetic field (right).

2.2 The R&D on IC

The design of an axial ionization chamber, providing a high ΔE and E resolution measurement and covering a large solid angle, is presently ongoing. Two major constraints limit the needed energy resolution of 1%. First of all, the entrance window of the IC should be large enough to cover the needed acceptance, keeping a thin and uniform thickness. Moreover, given the differential pressure the window has to stand (around 20 mbar inside the IC and secondary vacuum outside), its bending has to be reduced to avoid a ballistic deficit. For the moment, the foreseen solution is a polypropylene window of 0.9 μm thickness. For the FALSTAFF preliminary test, the existing MiniHarpee IC from GANIL is being used.

A more fancy possibility is under R&D with the aim of providing an IC capable of performing a combined measurement of energy and time. This IC is based on the scintillation properties of the IC gas and is meant to collect by a PMT the photons generated by ions crossing the gas [6]. This solution would provide a fast time signal in addition to the energy measurement, which will allow elimination of the time-stop detector. Preliminary tests have been performed on an IC prototype coupled to 2 PMT and using CF_4 and N_2 gas at different pressures. An energy resolution of 1.2% has been obtained with CF_4 at 250 mbar, together with a time resolution of 200 ps. Although these values do not fulfill FALSTAFF specifications, they are very encouraging since the identified margin of improvement is rather high.

3 Simulation of the setup

In order to assess precisely the feasibility of the measurement a full and detailed simulation of the FALSTAFF two-arm setup (Figure 1) has been performed using the GEANT4 Monte-Carlo code [8]. The simulation activity also allows developing the analysis method and optimizing the achievable mass and charge resolutions taking into account the different layers of material and the position, time and energy resolutions of the different detectors. To reconstruct initial and final mass of both fission fragments from their velocity and energy, the analysis is based on an event-by-event iteration procedure. This procedure was first developed for events simulated without any energy straggling or experimental resolution. Indeed, assuming that the nuclear charge of the light ion is known (which implies the knowledge of the heavy one from charge conservation), the energy loss corrections are applied to each ion from the crossed material thickness. Then, the initial and final masses of the two fragments are reconstructed from the simulated velocities and energies. As an example, the initial and final masses of two typical fission fragments in coincidence (^{140}Cs and ^{98}Rb) are correctly reconstructed with a mass resolution better than 0.01 amu, coming only from the energy loss correction uncertainty in the simulation. With the addition of the energy straggling and the experimental resolutions, we ob-

tain a resolution better than 1 amu for the initial mass and 1.9 amu (1.6 amu) for the heavy (light) fragment final mass.

For the simulation of the whole fission fragments mass distribution, the ^{252}Cf(sf) initial mass yields, together with the mean neutron multiplicities, have been generated using the GEF code [9]. Then, the reconstructed initial and final mass distributions are obtained with and without including in the simulation the energy straggling and the experimental resolutions. The two results are shown in Figure 4 (without and with energy straggling and experimental resolutions in the left and right panels respectively). As expected, the energy straggling and the experimental resolutions have the effect of smearing out the reconstructed mass distributions. Nevertheless, when the evaporation process is included, the feasibility of extracting the neutron mean multiplicity as a function of the initial mass could be demonstrated. In the analysis of the simulated data, the neutron multiplicity is determined on an event-by-event basis. Then, for a given initial mass, the average neutron multiplicity ($<A_i\text{-}A_f>$) and its uncertainty ($<A_i\text{-}A_f> /\sqrt{N}$) are calculated over N events. The reconstructed neutron multiplicity, together with the simulated neutron multiplicity, is shown in Figure 5. One can clearly see that the extracted correlation is very satisfactory. The lack of statistics in the wings and the symmetric valley of the mass distribution lead to larger uncertainties and some discrepancies between simulated and reconstructed values. We observe also a steeper slope for reconstructed light fragments that has to be investigated further.

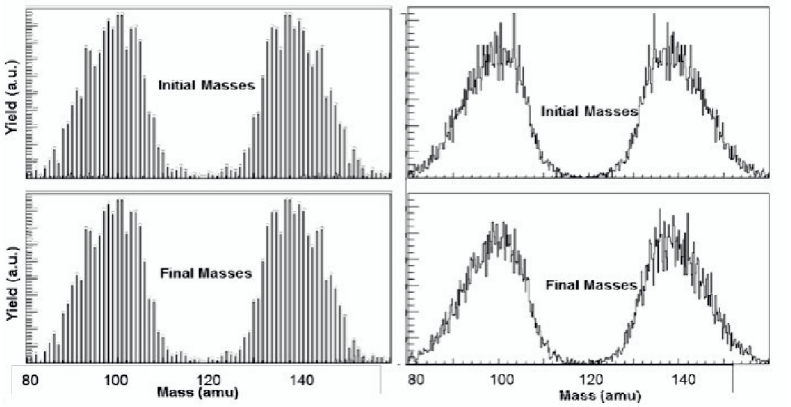

Figure 4. Initial (top range) and final (bottom range) fragment mass distributions from ^{252}Cf(sf) without (left column) and with (right column) energy straggling and detection resolutions.

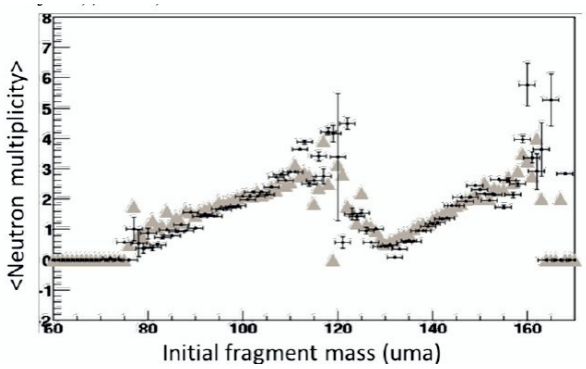

Figure 5. Mean neutron multiplicity as a function of the initial fragment mass. The grey triangles represent the simulated multiplicity while the cross represents the reconstructed one.

CNR*13

4 Conclusion and perspectives

A new experimental apparatus, called FALSTAFF and devoted to the full characterization of fission fragments is being developed. In addition to measuring the masses before and after neutron evaporation, the nuclear charge and the kinetic energy of both fragments in coincidence, it will give access to the mean neutron multiplicity associated with each fragment. The detailed simulation of the setup has proven the feasibility of the measurement with the already achieved detector resolution. The R&D activity on both the SED detectors and IC shows that the time, position and energy resolution requirements are fulfilled. The first tests on a one-arm setup (Figure 6) are in progress with a ^{252}Cf(sf) source. The mid-term plans foresee the installation of a two-arm setup, eventually equipped with scintillation-based IC, to be fully tested by 2015 with a spectroscopic Cf source. Then, once the commissioning of the NFS installation is completed, the FALSTAFF setup will be moved to GANIL for a Day-One experiment with a ^{238}U target. Finally, a full experimental program at NFS is foreseen, eventually with a 2 x two-arm setup, to explore fission fragment characteristics of major and minor actinides as a function of the neutron energy in the range 0.5-5 MeV.

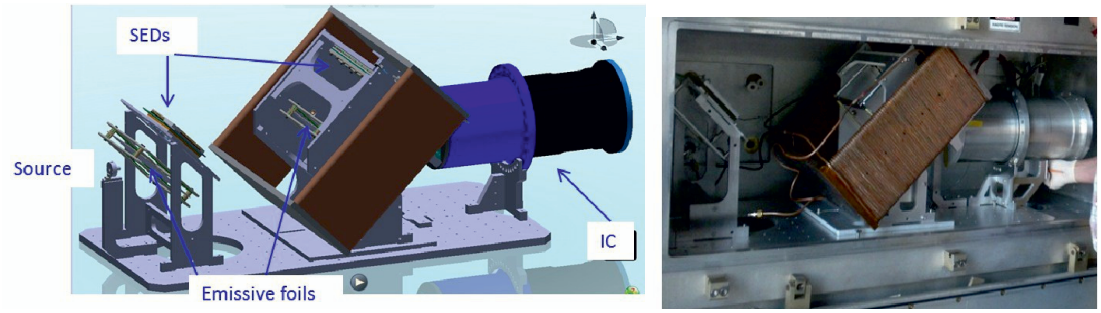

Figure 6. Design of the FALSTAFF one-arm setup (left) and picture of the present installation (right).

References

1. X. Ledoux et al., Proc. *« Nuclear Data for Science and Technology 2013»,* New York (USA), 4-8/03/2013
2. D. Doré et al., Proc. *«Fission 2013»,* Caen (France), 28-31/05/2013
3. H. C. Britt et al., Instr. Meth. 24, 13 (1963)
3. J. Pancin et al., Journ. Instr. Sc. Tech. 4, 120012 (2009)
4. J.P. Bocquet et al., Nucl. Instr. Methods A 267, 466 (1988)
5. F. R. Lecolley et al., Proc. « XVIIIth Colloque Ganil », Port-en-Bessin (France), 23-27/09/2013
6. P. Baron et al., IEEE TNS 55-3, 1744 (2008)
7. R. Brun et al., Computer Physics Communications, 180-12, 2499 (2009)
9. K.-H. Schmidt, B. Jurado, JEF/DOC 1423, OECD Nuclear-Energy Agency, Paris (2012)

EPJ Web of Conferences **146**, 04028 (2017) DOI: 10.1051/epjconf/201714604028
ND2016

2

Impact of material thicknesses on fission observables obtained with the FALSTAFF experimental setup

L. Thulliez[1,a], D. Doré[1], E. Berthoumieux[1], S. Panebianco[1], P. Legou[1], M. Kebbiri[1], Y. Piret[1], J.P. Mols[1], M. Combet[1], M. Riallot[1], A. Marcel[1], F. Farget[2], J. Pancin[2], M.O. Frégeau[2], X. Ledoux[2], F.-R. Lecolley[3], J. Perronnel[3], D. Goupillère[3], and S. Oberstedt[4]

[1] Irfu, CEA, Université Paris-Saclay, 91191 Gif-sur-Yvette, France
[2] GANIL, 14050 Caen, France
[3] LPC, 14076 Caen, France
[4] European Commision, DG Joint Research Center, Directorate G – Nuclear Safety and Security, Unit G.2 Standards for Safety, Security and Safeguards, 2440 Geel, Belgium

Abstract. In the past years, the fission studies have been mainly focused on thermal fission because most of the current nuclear reactors work in this energy domain. With the development of GEN-IV reactor concepts, mainly working in the fast energy domain, new nuclear data are needed.

The FALSTAFF spectrometer under development at CEA-Saclay, France, is a two-arm spectrometer which will provide mass yields before (2V method) and after (EV method) neutron evaporation and consequently will have access to the neutron multiplicity as a function of mass. The axial ionization chamber, in addition to the kinetic energy value, will measure the energy loss profile of the fragment along its track. This energy loss profile will give information about the fragment nuclear charge. This paper will focus on recent developments on the FALSTAFF design. A special attention will be paid to the impact of the detector material thickness on the uncertainty of different observables.

1. Introduction

Most of the innovative nuclear reactors under development are based on fast reactor technologies. In this fast energy domain, from hundreds keV to several MeV, new accurate fission fragment mass yields are needed in order to predict the residual decay heat and the poisoning of the nuclear fuel which are important parameters for nuclear reactor management. Experiments are also needed to answer some theoretical questions on the fission process such as how the energy is shared between the two fission fragments. Actually it has been unexpectedly observed that the heavy fragments take the additionnal energy brought by the fast neutron, leading to an enhancement of prompt neutron emission from the heavy fragment while the neutron emission from the light fragments remains the same [1,2].

To answer these questions, a spectrometer named FALSTAFF is under development at CEA-Saclay (France) [3]. The aim of the FALSTAFF spectrometer is to study neutron-induced fission in a neutron energy range from hundreds keV to several MeV. This energy range will be accessible in installing the spectrometer at the Neutrons For Science (NFS) facility [4]. The advantage of the direct kinematic technique is an accurate definition of the the initial state of the compound nucleus which undergoes fission. However, fission fragments have a low kinetic energy. As a consequence they loose a non-negligible amount of energy when they interact with materials making their identification difficult. To correctly identify the fission fragments, the energy losses suffered by the fragments have to be taken into account. This requires the knowledge of the fragment nuclear charge and the material thicknesses crossed by the fragment.

The first part of this paper will describe the setup and the observables accessible with the FALSTAFF spectrometer. The second part will focus on the impact of the detector material thickness uncertainties on the observables. The third part will deal with the impact on the observables, of using thinner materials.

2. Description of the FALSTAFF spectrometer

The FALSTAFF spectrometer will provide the full characterization of the fission fragments, i.e. their masses before and after neutron evaporation process, their kinetic energies and their nuclear charges. The deduced neutron multiplicity as a function of mass will provide information on the energy sharing between the two fragments at the scission point.

The mass before neutron evaporation is obtained *via* the 2V (Double Velocity) method. To apply this method the assumption is made that the neutron emission, in average, does not change the velocity of the fragments in the center of mass frame. It requires the measurement of both fragment velocities in coincidence. The velocity is determined with two time-of-flight (ToF) Secondary

[a] e-mail: loic.thulliez@cea.fr

EPJ Web of Conferences **146**, 04028 (2017) DOI: 10.1051/epjconf/201714604028
ND2016

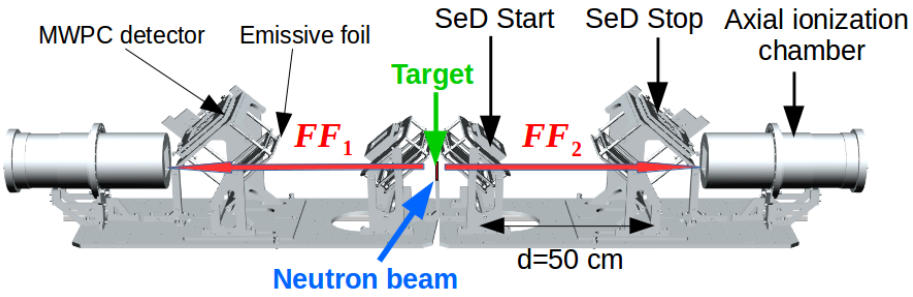

Figure 1. Drawing of the two-arm FALSTAFF spectrometer. Each arm is made of two ToF Secondary Electron Detectors (SeD) and one axial ionization chamber.

Electron Detectors (SeD) [5], represented in Fig. 1. Each detector gives the arrival time and position of a particle on the detector. Those detectors have a timing resolution of $\sigma_t \sim 120$ ps and a spatial resolution of $\sigma_X \sim 1$ mm [6]. The distance between the two SeDs is 50 cm. A SeD is made of an emissive foil and a Multi-Wire Proportional Chamber (MWPC) detector. When a fragment crosses an emissive foil, it looses kinetic energy leading to electron production on the foil surface. The electrons, thanks to an electric field, are then accelerated and detected by the MWPC detector.

The mass after neutron evaporation is obtained with the EV (Energy-Velocity) method. In addition to the velocity information, the kinetic energy value of the fragment is then required. This information is obtained with an axial ionization chamber, CALIBER, placed after the Stop detector. The kinetic energy value measured in the chamber has to be corrected for energy losses suffered by the fragment in the target, in the emissive foils and in the chamber entrance window. Those corrections require the knowledge of the fragment nuclear charge and the thicknesses of the materials the fragments have passed through. The crossed thickness is deduced from the thickness given by the manufacturer and the angle between the detector and the particle trajectory. The nuclear charge information is provided by the energy loss of the fragment along its track.

3. Impact of the material thickness uncertainty on fission observables

This section investigates whether or not the average mylar thickness given by the manufacturer can be taken for granted in order to correctly determine the observables and looks at the impact of the thickness uncertainty given by the manufacturer on the observables. The impact of the thickness inhomogeneities on the observable determination is also investigated.

3.1. Impact of the thickness uncertainty given by the manufacturer

The emissive foils of the ToF detectors are made of mylar foil having a thickness, given by the manufacturer, of 0.5 μm $\pm$20% and a thin evaporated Aluminium layer of around 30 nm $\pm$4 nm. The following is dedicated to the investigation of the impact of the thickness uncertainty of the mylar foil on the observables. It is performed in three steps:

a) A Geant-4 [7] geometry of the FALSTAFF spectrometer is implemented in setting the SeD foil thicknesses to dx $= 0.5\mu$m. The simulation is performed with the software version Geant4.10.02.p01 and with the Physics-List "QGSP_ BERT_ EMV", from which the fragment energy losses depend.
b) Fission events, from the spontaneous fission of ^{252}Cf, from GEF code [8] are then generated. The software version 2015/2.2 (01/2016) is used. The number of neutron emitted by each fragment is provided by this software, leading to the neutron multiplicity as a function of mass represented by the red curve in Fig. 2. It shows a plateau around masses 140–155, perhaps due to too high shell corrections.
c) The simulated data collected in the detectors are analysed under different assumptions on the foil thicknesses.

In the following, the impact of the hypothesis is investigated by looking at their effects on the neutron multiplicity as a function of mass.

For this study the analysis is performed with different assumptions: emissive foils have a thickness of **1)** dx $= 0.5\,\mu$m (red curve), **2)** dx $= 0.4\,\mu$m (green curve) and **3)** dx $= 0.6\,\mu$m (blue curve) representing respectively the lower limit -20% and the upper limit of $+20\%$. The results are shown in Fig. 2. The hypothesis **1)** corresponds to the case where the material thickness is fully known and thus can be considered as the reference. The difference between green and blue curves represents the neutron multiplicity uncertainty due to the thickness uncertainty. This amplitude range goes from 1 to 4 neutrons for the light fragments and from 4 to 6 neutrons for the heavy ones. The neutron uncertainty is bigger for heavy fragments than for light ones because they suffer more energy losses, so more energy loss corrections have to be applied. The blue result in Fig. 2 presents a negative neutron multiplicity associated to the heavy fragments. This is due to an overestimation of the foil thickness compared to the real one. In fact, this overestimation leads to too large energy loss corrections, leading to too large final masses. It does not affect initial masses which are obtained *via* the 2V method for which less energy loss corrections are needed.

The results show that the average thickness value given by the manufacturer can not be taken for granted because

EPJ Web of Conferences **146**, 04028 (2017) DOI: 10.1051/epjconf/201714604028
ND2016

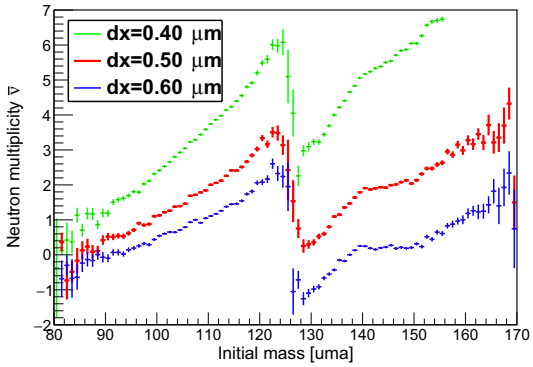

Figure 2. Impact of the thickness uncertainty given by the manufacturer on the neutron multiplicity as a function of mass from the reaction ^{252}Cf(sf).

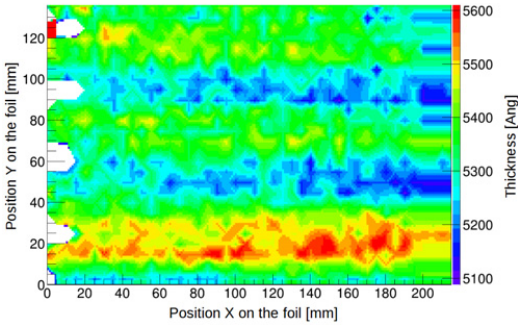

Figure 3. A typical foil thickness profile obtained after thickness measurements based on the energy loss of alpha-particles from ^{241}Am.

of the high impact of the thickness uncertainty given by the manufacturer on the observables.

3.2. Thickness measurement setup and thickness profile reconstruction method

To reduce the thickness uncertainty given by the manufacturer, a thickness measurement setup has been developed based on the α-transmission technique. The detection setup is made of an ^{241}Am source and a PIPS Silicon detector which has an energy resolution of 12 keV [9], leading to a measurement thickness precison of $\pm$10 nm. The energy loss of alpha particles through a foil is measured and then converted in mylar thickness with the help of energy loss/thickness table, built with the SRIM software [10]. A scan of the $14 \times 22\,\mathrm{cm}^2$ foil is performed and then the entire foil profile is reconstructed with a Delaunay triangulation interpolation [11]. A typical thickness profile is presented in Fig. 3. The visible structures depend on the way the mylar foil is stretched and sticked to its frame.

3.3. Impact of the thickness inhomogeneity

Once the foil profile is obtained, the impact of the thickness inhomogeneity of the foil on the observable is studied. The spatial resolution of the thickness measurement setup is equal to 5 mm. This determines the minimum size of the measurement step. The foil profile

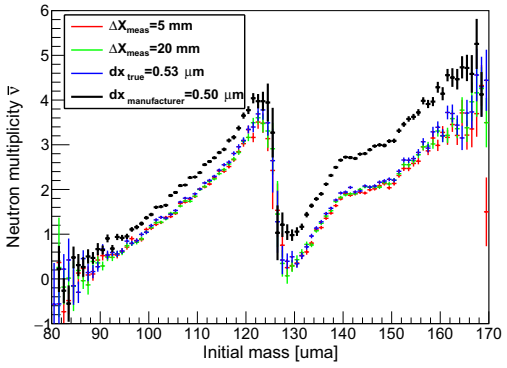

Figure 4. Impact of the measurement step on the neutron multiplicity as a function of mass.

reconstructed from measurements performed every 5 mm, represented in Fig. 3, is implemented in Geant-4. Fission events are then generated.

The analysis of the simulated data collected by the detectors are then performed with different assumptions. The neutron multiplicity as a function of initial mass, represented in Fig. 4, are obtained according to the following hypothesis:

1) a complete knowledge of the profile, red results.
2) a partial knowledge of the profile (basically one point out of four is kept from measurements performed every 5 mm), green results.
3) an average thickness of 0.53 μm, blue results.
4) an average thickness of 0.5 μm, black results.

The similarities of those results, depicted in Fig. 4 by red ($\Delta X = 5$ mm) and green ($\Delta X = 20$ mm) symbols, show that the determination of the fission observables does not depend on the measurement step. Moreover only the knowledge of the true average thickness is necessary (blue line). This true average thickness is defined as the mean of the measured thicknesses from the profil in Fig. 3. Thus measurements have to be performed to find the true average thickness. In this case, the measured average thickness is 0.53 μm, which is different from the one given by the manufacturer (0.5 μm). So far the measured average thickness does not depend on the measurement step (5 mm or 20 mm). Special attention is needed in the accuracy of this statement since only few foils have been characterized.

4. Impact of the foil thickness on velocity observable

The main difficulty of studying fission in direct kinematic is the particle identification due to energy losses in the different detectors. Previously the study of inhomogeneity impact was also performed for a 0.9 μm thick emissive foil. The conclusions are the same as those drawn for the 0.5 μm thick foil. As a consequence, to minimize the impact of the energy loss correction and its uncertainty, the thinner foil is used.

As shown in Fig. 5, the measured velocity, determined by fitting each peak by a gaussian, is then shifted up by $\sim$0.04 cm/ns for the light and heavy fragments when a foil of 0.5 μm is used instead of 0.9 μm one. This corresponds approximately to an energy loss reduction

EPJ Web of Conferences **146**, 04028 (2017) DOI: 10.1051/epjconf/201714604028
ND2016

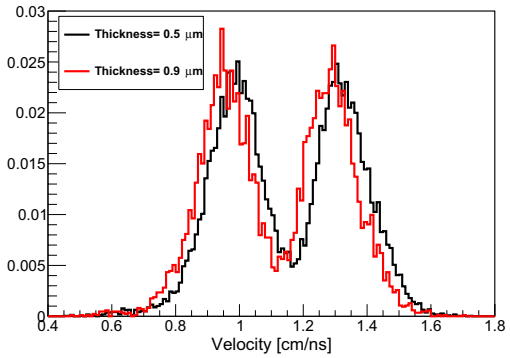

Figure 5. Comparison of velocity measurements performed with emissive foils made from mylar of thickness 0.5 μm (black line) and 0.9 μm (red line).

of around $\sim$10 MeV (Geant-4 results). As a consequence the kinetic energy measured value in the axial ionization chamber with a foil of 0.5 μm is higher than with the one of 0.9 μm. This also leads to a longer energy loss profile measurement, which consequently brings more information for the fragment nuclear charge determination.

5. Conclusion

One key point in the studies of neutron-induced fission is to take correctly into account the energy losses suffered by the fission fragments in the detector materials in order to correctly identify the fragments. The present study has shown the non-negligible impact of the thickness uncertainty given by the manufacturer on the observables. As a consequence a thickness measurement setup has been built to determine the thickness profile of the SeD emissive foils and of the ionization chamber entrance window. This measured average thickness might be different from the average thickness given by the manufacturer and has to be known. It has been pointed out that taking into account the thickness inhomogeneities is not necessary, and that only the measured average foil thickness is needed. It was also shown that using a foil of 0.5 μm instead of the original 0.9 μm one, has been successfully conducted leading to smaller energy loss corrections. Usage of foil thinner than 0.9 μm was a technical challenge in itself.

The next step for the development of the FALSTAFF spectrometer is to characterize the new axial ionization chamber, CALIBER. Its characterization will be made with a ^{252}Cf source and its energy calibration will be made with ion beams. A method for the fragment nuclear charge determination from the fragment energy loss profile in CALIBER will be investigated. The full characterization of the first arm of the spectrometer will be done in 2017 and the two-arm FALSTAFF spectrometer will be ready for data taking in 2018.

This work was supported by EURATOM 7 Framework Programme CHANDA and the French programme NEEDS.

References

[1] A.A. Naqvi et al., Phys. Rev. C **34**, 218 (1986)
[2] R. Müller et al., Phys. Rev. C **29**, 885 (1984)
[3] D. Doré et al., Nuclear Data Sheets **119**, 346 (2014)
[4] X. Ledoux et al., Nuclear Data Sheets **119**, 353 (2014)
[5] A. Drouart et al., Nucl. Instr. Meth. Phys. Res. A **477**, 401 (2002)
[6] M. Vostinar et al., JINST **119** (2013)
[7] S. Agostinelli et al., Nucl. Instr. Meth. Phys. Res. A **506**, 250 (2003)
[8] K.H. Schmidt et al., Tech. rep., JEFF Report 24 (2014)
[9] `http://www.canberra.com/products/detectors/pips-detectors-standard.asp`, accessed: 01/04/2014
[10] J. Ziegler, `http://www.srim.org`, accessed: 05/2014
[11] P. Lancaster and K. Salkauskas, *Curve and Surface Fitting, an introduction*, 3rd edn. (Academic Press, 1990)

2.2 La TPC FIDIAS

Parallèlement aux activités instrumentales autour du spectromètre FALSTAFF présentées dans la section 2.1, j'ai mené à partir de 2010 un programme de R&D dans le but de développer une TPC (*Time Projection Chamber*) pour la détection d'ions lourds de basse énergie. En effet, la problématique d'associer une mesure précise de l'énergie (et du profil de perte d'énergie dans un gaz) des fragments de fission à la trajectographie de ces ions permettant de corriger des effets d'angle était un véritable challenge, aussi bien pour des petites chambres à ionisation comme dans FALSTAFF, que dans des systèmes de grande acceptance tel le GFM de FIPPS évoqué dans le chapitre 1.4. De manière générale pour un détecteur gazeux, le compromis entre la linéarité d'amplification nécessaire à l'obtention d'une très bonne résolution en énergie et le haut gain typique pour atteindre des mesures de position précises est extrêmement difficile à trouver.

C'est dans ce cadre que, fort de l'expérience présente dans mon Institut sur les techniques de TPC et grâce à l'enthousiasme contagieux de Yannis Giomataris et Sotirios Harrisopoulos, nous avons constitué une collaboration avec une équipe de l'Institut de Physique Nucléaire et des Particules "Demokritos" du NCSR à Athènes (Grèce) pour évaluer la faisabilité d'une TPC multi-usage basé sur le détecteur Micromegas [35] pour la reconstruction complète et l'identification d'ions lourds des basse énergie.

En vertu de l'échantillonnage aussi bien spatial que temporel qui les caractérisent, les TPC offrent de très bonnes performances de trajectographie permettant la reconstruction en 3D d'événements à forte multiplicité. Lorsqu'elles sont couplées à un champ magnétique externe, les TPC sont très appropriées pour la mesure d'impulsion, ce qui conduit à l'identification des particules. Grâce à leur bonne résolution en énergie, elles permettent l'identification isotopique des particules légères à partir de la perte d'énergie ou de la mesure du pouvoir d'arrêt dans le gaz. Enfin, une TPC peut être facilement construite pour couvrir de grandes surfaces en gardant un faible budget matière et un coût modéré. D'autre part, les détecteurs gazeux montrent leurs meilleures performances de trajectographes en mode transmission avec des particules au minimum d'ionisation, c'est-à-dire en physique des hautes énergies, et ont rarement été utilisés pour effectuer la trajectographie et l'identification des ions lourds à basse énergie. En physique nucléaire de basse énergie, les TPC ont commencé à être développées à partir des années 2010 plutôt comme cibles actives, où le gaz de la chambre agit à la fois comme détecteur et comme cible, principalement pour étudier des réactions nucléaires en cinématique inverse. Dans ce cas, l'intérêt d'une TPC est principalement dû à la possibilité de disposer de cibles épaisses sans perte de résolution, conduisant à la mesure et à l'identification de particules de recul à faible énergie. Plus généralement, les réactions nucléaires à basse énergie étant souvent caractérisées par des sections efficaces de réaction très faibles, l'intérêt principal d'une TPC, en mode cible active ou en mode cible fixe, provient de son efficacité de détection élevée et de sa couverture angulaire. Enfin, une TPC est un détecteur très compact, permettant un couplage facile avec d'autres dispositifs (par exemple des détecteurs de neutrons ou de gamma) et améliorant sa polyvalence.

Le projet a pris le joli nom de FIDIAS (*FIssion Detector In AStrophysics*) car, à côté du programme scientifique autour de la fission sur lequel je travaillais, l'équipe de Demokritos était intéressée à l'utilisation d'une TPC pour l'étude des réactions de capture alpha pertinentes pour la nucléosynthèse stellaire, en particulier celles qui interviennent dans le processus p, c'est-à-dire la nucléosynthèse d'isotopes stables déficitaires en neutrons. Ce détecteur multi-usage a donc été développé dans le but de d'effectuer une reconstruction complète des ions lourds de basse énergie en utilisant un TPC Micromegas dans un champ magnétique.

Le gaz choisi pour cette TPC est l'He car il est le seul à remplir les principales exigences liées aux deux applications envisagées. En effet, l'He à pression atmosphérique fournit le plus long parcours pour les fragments de fission et il permet également l'étude des réactions induites par

alpha en cinématique inverse, en utilisant le volume de gaz TPC comme cible active. Les produits d'ionisation générés dans le volume de la TPC sont détectés par un plancher Micromegas [35], détecteur gazeux de type *micro-pattern*, choisi pour sa résolution spatiale très élevée qui résulte d'un fort champ d'amplification très localisé obtenu grâce à une microgrille et qui permet de garder une bonne proportionnalité de réponse dans l'espace de dérive.

Un prototype de cette TPC a été conçu, fabriqué et caractérisé en détail en utilisant les fragments issus de la fission spontanée du Cf-252. Les résultats de ces études, qui doivent beaucoup à l'engagement de Paco Iguaz, sont présentés dans l'article qui suit [36] et qui, à l'instar de celui sur le spectromètre FALSTAFF, constitue un exemple très typique des développements instrumentaux en physique nucléaire de basse énergie. Grâce aux résultats encourageant obtenus avec de l'He à pression atmosphérique, nous avons pu tester la TPC FIDIAS à basse pression et dans le plan focal du spectromètre Lohengrin à l'ILL. Cette dernière étude, réalisée avec l'aide d'Aurélien Blanc dans le cadre de la R&D du projet FIPPS a permis de mettre en évidence une dégradation sensible des performances du détecteur Micromegas à basse pression due à la difficulté de maintenir un mélange gazeux uniforme et à l'équilibre avec l'air résiduelle à l'intérieur de la TPC.

Nuclear Instruments and Methods in Physics Research A 735 (2014) 399–407

Contents lists available at ScienceDirect

Nuclear Instruments and Methods in Physics Research A

journal homepage: www.elsevier.com/locate/nima

2

The FIDIAS project: Development of a Micromegas TPC for the detection of low-energy heavy ions

Francisco José Iguaz [a,b], Stefano Panebianco [a,*], Michael Axiotis [c], Frédéric Druillole [a], George Fanourakis [c], Theodoros Geralis [c], Ioannis Giomataris [a], Sotirios Harissopulos [c], Anastasios Lagoyannis [c], Thomas Papaevangelou [a]

[a] CEA, Centre de Saclay, Institut de Recherche sur les lois Fondamentales de l'Univers, 91191 Gif-sur-Yvette, France
[b] Laboratorio de Fisica Nuclear y Astroparticulas, Universidad de Zaragoza, 50009 Zaragoza, Spain
[c] Institute of Nuclear Physics, NCRS Demokritos, 15310 Aghia Paraskevi, Athens, Greece

ARTICLE INFO

Article history:
Received 4 June 2013
Received in revised form
19 September 2013
Accepted 26 September 2013
Available online 10 October 2013

Keywords:
Micromegas
TPC
Fission
Heavy ions
Low energy

ABSTRACT

Time Projection Chambers are widely used since many years for tracking and identification of charged particles in high energy physics. We present here a new R&D project, called FIDIAS, meant to investigate the feasibility of a Micromegas TPC for low energy heavy ions detection. In this framework, a TPC prototype based on Micromegas bulk technique has been extensively tested with spontaneous fission source. A deep analysis of the experimental results has been realized leading to a full characterization of the prototype in terms of gain, energy resolution and track reconstruction as a function of three working gas: helium, neon and argon. The encouraging results have also been compared to simulations, showing the Micromegas TPC is a very well suited detector for the detection of heavy ions in nuclear reactions at low energy.

1. Introduction

Gaseous detectors and in particular Time Projection Chambers (TPCs), firstly introduced by Nygren [1], are widely used since many years in nuclear and particle physics. Thanks to the multiple-time sampling of pads, they provide very good tracking performances allowing 3D reconstruction of high multiplicity events. When coupled to an external magnetic field, TPCs are very suitable for momentum measurement, leading to particle identification. Thanks to their good energy resolution, they provide isotopic identification of light particles by energy loss or range measurements. Finally, TPCs can cover large surfaces keeping a low material budget and moderate cost. On the other hand, gaseous detectors show their best tracking performances in transmission mode on the detection of minimum ionizing particles, i.e. in high energy physics. However, they have been rarely used to perform tracking and identification of heavy ions at low energy. In nuclear physics, TPCs are starting to be developed as active targets, where the chamber gas acts as both detector and target, mostly to study nuclear reactions in inverse kinematics [2–4]. In this context, the use of a TPC is an attractive option for disposing thick targets without significant loss of energy resolution, leading to the measurement and identification of low energy recoil particles. More generally, since low energy nuclear reactions are often characterized by very low reaction cross-sections, the main interest of a TPC, both in active target mode or in fixed target mode, comes from its high detection efficiency and its 4π angular coverage. Moreover, a TPC is a very compact detector, allowing an easy coupling to other devices (for example neutron or gamma detectors) and enhancing its versatility.

Among the different detection techniques, micropattern gaseous detectors are particularly suited thanks to their very good granularity as well as good spatial and energy resolution. In particular, Micromegas detectors [5] have already proven their performances both in astrophysics [6–8] and nuclear physics applications [9]. Moreover, new manufacturing techniques, namely bulk [10] and microbulk [11], where the amplification region is produced as a single entity, have been developed. These techniques can be transferred to industry allowing the production of large, robust and cheap detector modules.

This paper describes the developments realized in the framework of a R&D project called FIDIAS [12] which started at the beginning of 2010 as a collaboration between CEA-Irfu (France) and NCRS-Demokritos (Greece). The project aims at evaluating the feasibility of a multi-purpose TPC based on bulk Micromegas

* Corresponding author. Tel.: +33 169087357.
E-mail address: stefano.panebianco@cea.fr (S. Panebianco).

0168-9002/$ - see front matter © 2013 Elsevier B.V. All rights reserved.
http://dx.doi.org/10.1016/j.nima.2013.09.061

detectors for the full reconstruction and identification of low energy heavy ions. In this context, a set of physics cases has been identified, showing the expected versatility of this detector and will be shortly presented in Section 2. Section 3 describes the strategy of the FIDIAS project and the different phases of the R&D. In Section 3.1 we discuss in detail the design of the two first prototypes, the experimental set-up and the gas mixtures used for their characterization. Section 4 is devoted to the results obtained in the reconstruction of alpha particles and fission fragments. Finally, some conclusions and perspectives are discussed in Section 5.

2. The physics cases

In the framework of the project, three physics cases have been identified to assess the possible versatility of this detector.

The first one is the study of the nuclear fission reaction through the characterization of fission fragments. Indeed, the TPC, coupled with an external magnetic field, is a suitable device for systematic measurements of the mass, nuclear charge and kinetic energy of fragments produced by neutron or photon induced fission of actinides in a large range of excitation energies and for a large number of fissioning nuclei. This systematic approach is important both for fundamental physics and applications. The development of fission models [13–16], based on phenomenology or on more microscopic physics ingredients, needs a large set of experimental data to improve their predictive power and reliability. For example, the correlation of the total kinetic energy release with the fragment mass gives information concerning the properties of the fissioning nucleus at the scission point. Although a lot of data are available at thermal energies, there is a lack of knowledge on the evolution of the fission properties with the incident neutron energy (from thermal to MeV range) and only few fissioning actinides have been studied in the keV–MeV range. The latter are very important for the design of future fast reactors (Generation IV) and for the optimization of Radioactive Ion Beam facilities [17]. A space resolution better than 100 μm has already been achieved with a TPC based on Micromegas detector, together with high momentum resolution. These performances make the FIDIAS TPC an excellent setup for the detection of high ionizing particles as fission fragments, where the mass determination relies on a very precise determination of the ion trajectory bent by the magnetic field. Moreover, the advantage of using a compact and versatile setup as FIDIAS is its full efficiency detection and the possible study of thin and low mass radioactive samples. Finally, it can easily fit to different neutron facilities, thus providing coherent data at different energy ranges. For these reasons, together with measurements in the thermal energy range (for example at ILL-Grenoble [18] or Orphée-Saclay [19] research reactors), the FIDIAS TPC can be used to perform measurements in the epithermal and fast region, for example at nTOF-CERN [20], GELINA-Geel [21] or at the NFS ToF facility that is being built in the framework of SPIRAL2 in GANIL [22].

The second physics case is the study of alpha capture reaction cross-sections which are relevant for the stellar nucleosynthesis. In particular, the study of the p-process, i.e. the nucleosynthesis of proton rich stable isotopes referred as to p-nuclei, is actually a key field in the understanding the isotopic solar-system abundances [23]. Such nuclei cannot be synthesized in neutron-capture processes, followed by beta decays, which are responsible for synthesis of the majority of the stable nuclei. In particular, it is well known from observations that the abundance of p-isotopes is on average two or three orders of magnitude smaller than the neighboring stable s- or r-nuclei. Despite the fact that p nuclei are a bunch of only 35 stable nuclei, the modeling of their production mechanism is based on a reaction network involving hundreds of nuclei and reactions (mostly γ-n, γ-p, γ-α and their inverse). These reaction cross-sections are very difficult to measure and the corresponding statistical model predictions can often be very uncertain as they depend strongly on accurate knowledge of optical models, gamma strength functions and level densities. A well-established program has been already set up for the study of alpha-induced reactions in inverse kinematics at LISEIII in GANIL [24]. The TPC detector would be a very suitable solution to continue this program by enlarging the systematics of measured reactions using stable and radioactive beams available at ISOLDE [25] and in the future at SPIRAL2 [26] in the mass region 80–140 and 170–200 and in the energy range between 1 and 3.5 MeV/A, which are typical for the explosion of a massive type II supernova. The main advantage of the FIDIAS setup is that the 3D tracking in a TPC allows determining with good precision the incoming beam together with the scattered ion. Thanks to the fast response of the Micromegas detector, the FIDIAS TPC is particularly well suited in high rate experiments like the measurement of low reaction cross-sections.

A third example of application is related to the measurement of stopping force of heavy and super-heavy elements in gas. The experimental determination of physical and chemical properties of the heaviest known elements represents an interesting and challenging topic in the current nuclear chemistry and nuclear physics research. Chemistry experiments with super-heavy elements formed in complete fusion reactions are usually performed with the gas-jet technique where all reaction products are collected in a gas-filled thermalization chamber adjacent to the target and transported as gaseous species or attached to aerosols. Thanks to the development of a physical pre-separation between target and collection chamber [27], a TPC detector is suitable for stopping force (STF) measurements and therefore to crosscheck and improve the commonly used codes to calculate STF, like SRIM [28]. This scientific program is led by the Laboratory of Radiochemistry and Environmental Chemistry at the Paul Scherrer Institute (Villigen, Switzerland). In this case, the main interest of the FIDIAS setup relies on the precise measure of the deposed energy of the ion all along its path on the gas, thanks to the high frequency sampling electronics that is used in the FIDIAS TPC.

3. The FIDIAS project

The scope of FIDIAS (FIssion Detector at the Interface with AStrophysics) [12] is to explore the possibility to perform a full reconstruction of low energy heavy ions using a Micromegas TPC in a magnetic field. The ionizing gas foreseen for the TPC is He, which is the only one fulfilling the main requirements of the two first physics cases, fission and astrophysics studies. Indeed, the He gas at atmospheric pressure gives the longest path for fission fragments and it will allow studying alpha-induced reactions in inverse kinematics, using the TPC gas volume as an active target. For the study of fission fragments, the detector will be arranged as a double-sided TPC, with the actinide target placed in the middle, in order to detect both fragments in coincidence. We recall that the main advantage of this setup is its full angular coverage, leading to high detection efficiency. This fact must be compared with a “standard” two-arm setup [29] which has an efficiency rarely higher than 10%. The TPC ionization products are detected by a Micromegas detector. This micro-pattern gaseous detector has been chosen because of its very good spatial resolution, even at high rate. Their performances at high rate are due to its localized electron cloud and its fast ion evacuation (more than two orders of magnitude compared to standard gaseous detectors) provided by the presence of a micromesh. Moreover, the Micromegas is quite

insensitive to gammas and its material budget is very low, further improving its generic radiation hardness.

In the case of fission measurement, two fission fragments (each one characterized by its mass, ionic charge and velocity) are detected in coincidence in a double-sided TPC. Given collinear electric and magnetic fields, the trajectories of two ions will be two helicoids described by six equations of motion (three for each fragment) that can be completed by three momentum conservation equations (one for each coordinate). This implies that a total of nine equations are available to extract the needed unknown (two masses, two ionic charges and 2×3 velocity components). Provided that the TPC active volume is large enough to stop the ions, the total deposited energy will give a measurement of the fragment kinetic energy. Moreover, the nuclear charge Z of the fragment can be extracted by the ion range measurement or from its $\Delta E-E$ correlation. The energy measurement can add two more equations to the system, i.e. making use of the kinetic energy definition. However, it should be noted that the extraction of the ion mass from the energy measurement only gives access to the so-called final mass, i.e. the fragment mass after prompt neutron emission. On the other hand, one can use the nuclear charge Z and the velocity v measurements to express the ionic charge q as $q=Z^{1/3}v/v_0$, where v_0 is the Bohr velocity. This approximation can give a reasonable q value that can be used as a first step in the fit of the fragment trajectory. This first step is also necessary since heavy ions at low energy show an evolving ionic charge along their path within the gas. This means that the fragment trajectory can be described by the above equations only locally, i.e. for a thickness of gas that does not modify too much the ionic charge. Therefore, the extraction of the needed observables (mass and velocity) from the trajectories of the fragments needs the development of an iterative procedure, i.e. Kalman filter technique [30], where the whole helicoid is reconstructed by a constraint fit taking into account the mean charge evolution. This procedure is one of the major challenges of this type of measurements.

In the FIDIAS project, a large effort has been devoted both on prototyping and simulation to optimize the TPC geometry and developing the track reconstruction algorithm. Prior to these developments, the choice and the validation of the simulation code has been assessed by a benchmark study of the GEANT4 code [31], developed originally for high energy physics and only recently used to simulate the interaction of low energy heavy ions with matter. This code has been benchmarked against other two simulation codes, SRIM [28] and Lise++ [32], which have been developed specifically to calculate the transport of heavy ions at low energy and have proven their reliability. The energy loss, lateral straggling and range of fission fragments in different gases (helium, neon, argon) have been calculated with the three codes. As an example, the calculated range of four fragments (two light and two heavy) in helium and argon is showed in Fig. 1. The main result of this comparison is that the disagreement between GEANT4 and the other codes depends quite much on the gas type and on the ion mass but never exceeds 15% [12]. Similar results are obtained looking at the energy loss and the lateral straggling, even for mixed gas like Ar-isobutane. Another observable which has been benchmarked is the evolution of the ionic charge of the fission fragments in the gas. The codes comparison showed that GEANT4 calculation using the standard electromagnetic physics description is incompatible with the Lise default model. On the other hand, in the Lise code one can choose between several models depending on the ion energy and on the target type. In particular, the Shima model [33] shows the best agreement with experimental data on fission fragment ionic charge evolution in noble gases. This model has been integrated in GEANT4 and is now used as default for the simulation of the FIDIAS TPC. Finally, a simplified model for the production, drift and diffusion of ionization electrons has been also integrated within GEANT4. This fact allowed performing a fair comparison with the data taken during the first test campaign. The details of the simulation activities will not be discussed here and can be found in Ref. [34].

From the very beginning of the FIDIAS project, a test campaign on prototypes has been realized to characterize the response of a Micromegas TPC detector with heavy ions at low energy and therefore provide data to be compared with simulations.

3.1. Description of the prototypes

The first TPC prototype has been developed at Demokritos and consists in a $10\times10\times10$ cm^3 gaseous vessel equipped a field shaper cage and a Micromegas bulk detector. A scheme of the setup is shown in Fig. 2. The field cage is made by a 10 cm high bus flat cable, surrounding the gas volume. The cables of the flat bus are connected in pairs by resistors of 1 MΩ and the first and last one are respectively connected to a copper plate and to ground. The copper plate works as drift cathode. In the middle of the plate, a 3 cm-diameter hole allows the detector irradiation by a ^{252}Cf

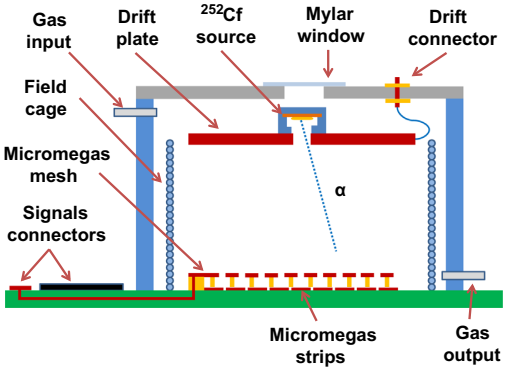

Fig. 2. Schema of the FIDIAS TPC prototype. The dimensions of the Micromegas detectors are over-scaled in comparison to other parts, in order to distinguish the mesh from the strips.

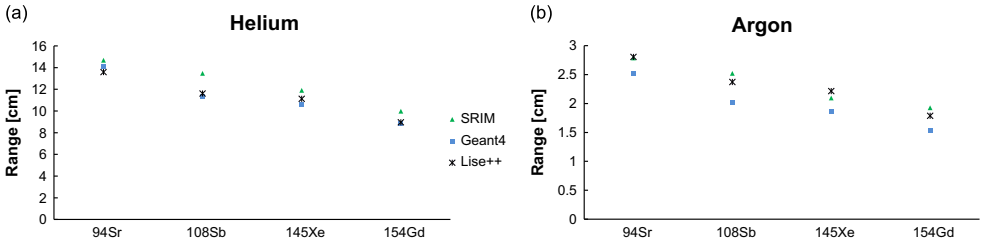

Fig. 1. Simulated range of four fission fragments (^{94}Sr, ^{108}Sb, ^{145}Xe, ^{154}Gd) in Helium and Argon, calculated with GEANT4, SRIM and Lise++.

source placed on the drift plate, or by a ^{55}Fe source, situated outside on a 10 μm Mylar window.

The drift cage, providing an effective drift gap of 8 cm, is coupled with a Micromegas bulk detector built from a Printed Circuit Board using the bulk technique [10]. In bulk Micromegas a woven mesh is laminated on the printed circuit board, covered by a photoimageable film, and the pillars sustaining the grid are made by a photochemical technique. The first Micromegas detector (called FIDIAS-1D) realized for the FIDIAS project was based on the design of a Micromegas detector for MAMMA and RD51 tests at CERN [35]. This detector is equipped with 96 strips in one direction with a pitch of 250 μm, allowing an active area of only 2.4×10 cm^2 and an amplification gap of 128 μm. Although the design of FIDIAS-1D prototype was made to be read out by the GASSIPLEX electronics [36], a different readout electronics has been chosen, based on the AFTER chip [37], originally developed for the TPC used in the T2K neutrino experiment. The main advantage of this electronics, compared to GASSIPLEX, is that it provides a sampling of the signal, while the GASSIPLEX chip provides only its maximum amplitude. The AFTER chip, fabricated in 0.35 μm CMOS technology, is a 72-channel front-end Application Specific Integrated Circuit (ASIC) which includes, for each channel, a low noise charge preamplifier, a pole zero compensation stage, a second order Sallen-Key low pass filter and a 511-cell Switched Capacitor Array. This electronics offers a large flexibility in sampling frequency (up to 50 MHz), shaping time (16 values from 100 ns to 2 μs) and gain (120, 240, 360 and 600 fC). The ADC coupled to each channel has a dynamical range of 2 V coded on 12 bits. Despite the fact that the AFTER electronics has been developed for very low rate MIP detection, its sampling capabilities make it very suitable for tracking purposes. On the other hand, this electronics was not proven to be adapted to the detection of highly ionizing particles because of its dynamical range and protection circuit. For the FIDIAS-1D prototype, the connection between the GASSIPLEX connector on the Micromegas cathode and the AFTER Front-End Card (FEC) is ensured by a mezzanine-adaptor and Kapton cables which give the possibility to set up the FEE far from the TPC. The AFTER FEC is then connected to a Front-End Mezzanine (FEM) which is a pure digital electronics card that gathers the events digitized by the FEC, performs optionally pedestal subtraction and zero suppression, and sends data to the DAQ system through a full-duplex gigabit optical link or, as in our first tests, through a USB link. The avalanche signal induced on the mesh has been used as an external trigger for the electronics.

Although the FIDIAS-1D prototype had a small active area, it could provide a first characterization of the general behavior of the detector and its coupling to the AFTER electronics. With the aim of providing a full characterization of the tracking capabilities of the system, a second bulk Micromegas, called FIDIAS-2D, was produced following a modified design of MIMAC detector [7] (shown in Fig. 3, left). The active surface of 10×10 cm^2 is composed of 288×288 pads, which are electrically connected to 144 strips (700 μm pitch) in each diagonal direction through metallized holes of 100 μm diameter. This x–y structure reduces the number of channels with a fine granularity covering a larger anode surface. The amplification gap of the detector is again 128 μm. The FIDIAS-2D detector was connected to the AFTER electronics by four flat cables as shown in Fig. 3 (right).

The two TPC prototypes have been tested in Saclay without magnetic field using a ^{55}Fe and a ^{252}Cf source. The ^{55}Fe source was used to assess the general performances of the detector in terms of gain and energy resolution. The ^{252}Cf source was used to study the TPC response to alphas, fission fragments and neutrons. This is possible since the Cf deposit of the source is unsealed, making the alphas and the fission fragments escape the deposit. Note that in our setup, only one fragment can be observed.

Although the gas foreseen for the final FIDIAS TPC is Helium, the FIDIAS-1D prototype was only tested with the standard gas mixture Ar(95%)–Isobutene(5%) at atmospheric pressure. In the first tests, the drift field has been set to 425 V/cm so as to the electron drift velocity is around 4 cm/s. The amplification field has been set to 52 kV/cm, corresponding to a low gain (around 90) which is justified by the high ionization generated by heavy ions.

For more extended tests, the response of the FIDIAS-2D prototype has been tested with three different base gases: Argon, neon and Helium, all mixed with 5% Isobutene. During all the tests, a continuous flow of 6 l/h of the desired gas was ensured. The FIDIAS-2D prototype response was characterized as a function of the drift and amplification field.

For all the tests, strips pulses have been sampled by AFTER electronics every 20 ns and the shaping time has been fixed to 100 ns. The dynamic range is set to 120 fC, which makes 4096 ADC units be equivalent to 7.5×10^4 electrons.

An offline analysis program has been developed to extract the strips pulses from the raw files generated by the DAQ and to record them into a ROOT-like file [38]. The same program reconstructs the projection of each event from the strips pulses, using the pulse amplitudes and the readout decoding (shown in Fig. 3, left). An example of the strips pulses of the 2D prototype and the XZ reconstruction of one event is shown in Fig. 4.

4. Experimental results

The general behavior of the TPC detector under fission fragments has been deduced from the test campaign on FIDIAS-1D prototype. The tests showed a very large signal over noise ratio, in average larger than 100. This comes from the fact that fission fragments deposit their whole energy in the TPC gas, giving a very

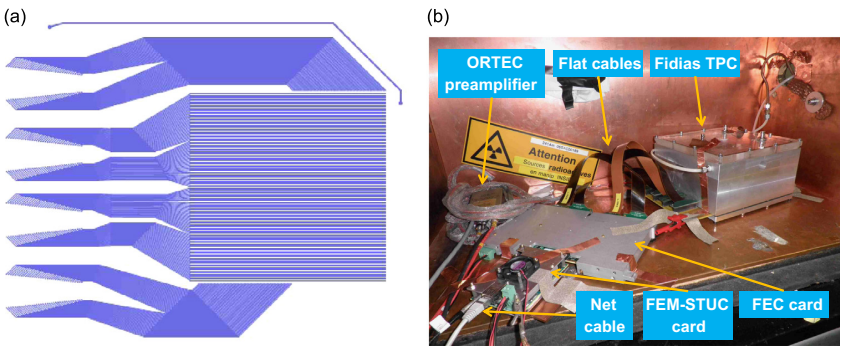

Fig. 3. Left: Design of the Fidias-2D Micromegas cathode. Right: Picture of the setup described in the text.

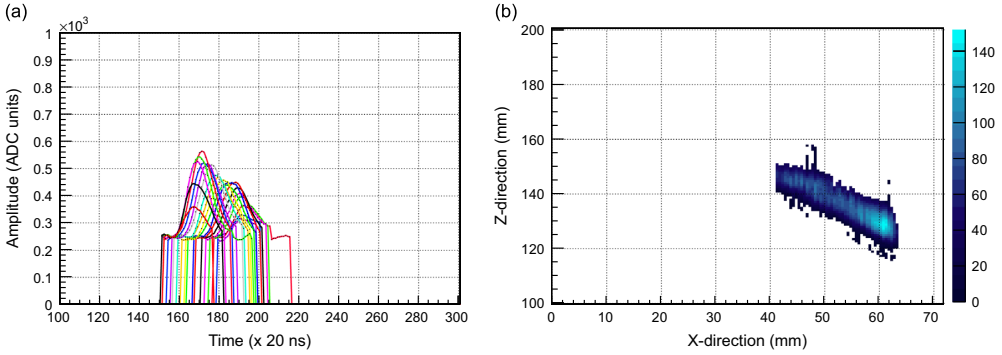

Fig. 4. Left: Example of pulses induced on the strips and recorded by the AFTER electronics. Right: Reconstruction of the XZ projection of a 6.1 MeV alpha in Ar+5%iC$_4$H$_{10}$.

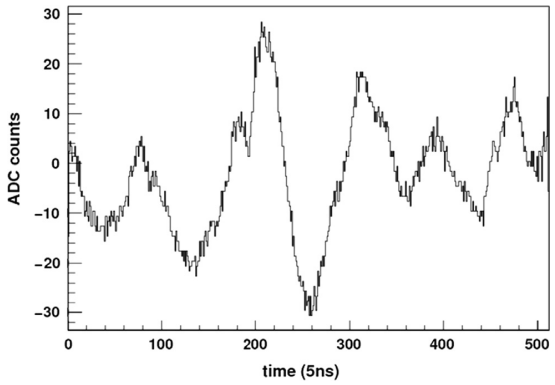

Fig. 5. Common mode noise from a random channel in a high ionization event.

large ionization signal. On the other hand, the presence of high amplitude signals was observed in around 10% of the fission events. Although these events do not saturate the ADC, they induce a large time-structured noise in some of the readout channels (Fig. 5). This noise is not related to cross-talk between strips since it affects randomly around 5% of all the channels of the FEC and not necessarily the channels which are close to the fired ones. The origin of the problem seems to be correlated with the AFTER FEC design and has been cured by simply removing those noisy channels from the event reconstruction. Apart from this effect, the common mode noise of the detector and the FEC+FEM readout is very low, around eight ADC channels (corresponding roughly to 150 e^-_{RMS}) and quite stable over time.

A basic track reconstruction in the FIDIAS-1D was performed from the linear correlation between the signal time at 10% of its maximum amplitude and the channel number, corresponding to the strip position in the anode plane. Therefore, the charge distribution of the fission events could be obtained showing the expected double-hump structure of fission fragments. On the other hand, given the strip design and the small active area of the FIDIAS-1D prototype, only part of the fragment track could be detected and it was not possible to identify the alpha tracks and to measure the track length. Although the general behavior of the detector was found encouraging on the 1D prototype, only the test campaign on the FIDIAS-2D prototype led to a rather complete characterization of the detector characteristics.

4.1. Gain and energy resolution

For these tests, the FIDIAS-2D detector was then irradiated with a ^{55}Fe source located outside the drift cage, on the Mylar TPC window. The source mainly emits X-rays of 5.9 and 6.4 keV which are converted in the detector window. The mesh negative signal induced by electron avalanche is amplified and read by a multi-channel analyzer (MCA) for spectra building. The experimental spectrum is fitted by two Gaussian functions, corresponding to the K_α (5.9 keV) and K_β (6.4 keV) lines of the ^{55}Fe source, to get the peak position and the energy resolution. One example is shown in Fig. 6 (left) for the Argon–Isobutene gas mixture.

Varying the drift voltage for a fixed mesh field, the electron transmission curve was measured to study the mesh transparency to primary electrons generated in the conversion volume. As shown in Fig. 6 (right), in Ar+5%iC$_4$H$_{10}$ there is a small plateau where the electron transmission is maximum for a ratio of drift-to-amplification fields lower between 0.005 and 0.01. For ratios over this value, the mesh stops being transparent because of the too high secondary ionization in the drift gap and, as we will see both the gain and the energy resolution degrades for high drift fields. This part of the curve matches with a previous measurement obtained with a similar bulk detector [7]. As expected, we also see that the maximum transparency is reached at higher ratios in neon- and helium-isobutene mixtures because of their ionization potential. Moreover, in all mixtures we observe that in the case of FIDIAS prototype the maximum transparency degrades at low drift fields. This is due to attachment effects since noble gases are known to be very sensitive to the presence of water and oxygen impurities [39]. It must be stressed that during the tests of FIDIAS prototypes the level of impurities was not controlled and the plastic gas tubes and the vessel were not pumped to reduce the outgassing effects.

After this first test, the ratio of drift-to-amplification fields was chosen so as the mesh showed the maximum electron transmission. The mesh voltage was then varied to measure the gain curve from the peak position variation as a function of the mesh voltage. The results are shown in Fig. 7 (left). The detector reaches a gain higher than 2×10^5 in helium- and neon-isobutene mixtures, and higher than 7×10^4 in Ar+5%iC$_4$H$_{10}$ before reaching the spark limit. In Argon mixture, the gain curve obtained with FIDIAS agree rather well with the one measured with a similar bulk detector [7]. We also observe that the required voltage to reach the same gain is lower for neon than for helium or argon. For instance, an amplification field of 28 kV/cm must be applied to reach a gain of 10^4 in Ne+5%iC$_4$H$_{10}$. This field increases up to 30 kV/cm in the case of helium and 32 kV/cm for argon. This difference comes from the different ionization potential and is therefore correlated with the amplification gap. In particular, as an amplification gap of 128 μm is best suited for neon-based mixtures [40].

As shown in Fig. 7 (right), the energy resolution at 5.9 keV stays rather constant for a wide range of amplification fields. At low fields, the resolution degrades because the signal is comparable to

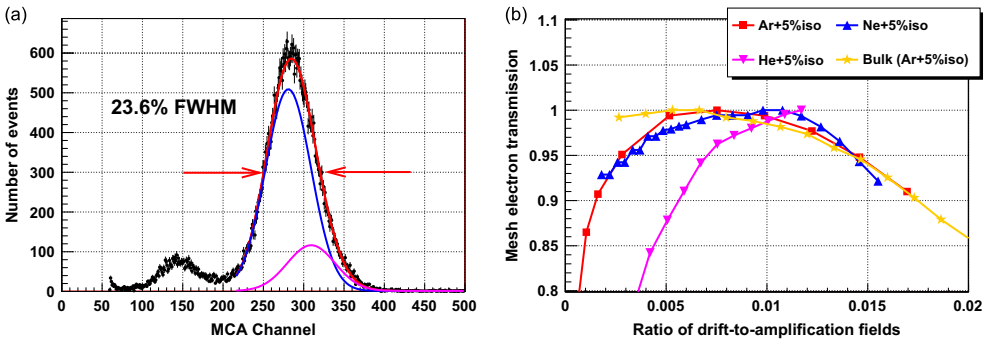

Fig. 6. Left: Example of ^{55}Fe energy spectrum obtained with the FIDIAS-2D detector in Ar+5%iC$_4$H$_{10}$. The main peak has been fitted by two Gaussian functions (blue and magenta lines), corresponding to the K_α and K_β lines. The escape peak, generated by X-ray conversion in argon, is situated at around 3 keV. Right: Mesh electron transmission as a function of the drift-to-amplification fields ratio in Ar+5%iC$_4$H$_{10}$ (red squares), Ne+5%iC$_4$H$_{10}$ (blue triangles) and He+5%iC$_4$H$_{10}$ (inverted magenta triangles). As a comparison, the curve by a pixelized bulk detector in Ar+5%iC$_4$H$_{10}$ [7] (orange stars) has been included. (For interpretation of the references to color in this figure caption, the reader is referred to the web version of this article.)

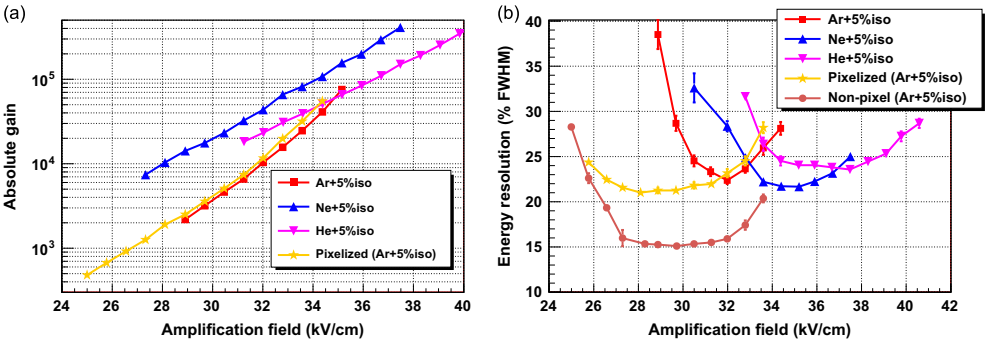

Fig. 7. Absolute gain (left) and energy resolution at 5.9 keV (right) as a function of the amplification field for the FIDIAS-2D prototype in Ar+5%iC$_4$H$_{10}$ (red squares), Ne+5% iC$_4$H$_{10}$ (blue triangles) and He+5%iC$_4$H$_{10}$ (inverted magenta triangles). As a comparison, the measurements obtained with a similar pixelized (orange stars) and non-pixelized (brown points) bulk detectors in Ar+5%iC$_4$H$_{10}$ have been included. (For interpretation of the references to color in this figure caption, the reader is referred to the web version of this article.)

Table 1
Energy resolution measured using 5.9 keV X-rays and 6.1 MeV alphas with the FIDIAS-2D prototype for three gas mixtures.

Gas mixture	Energy resolution (% FWHM)	
	5.9 keV	6.1 MeV
Ar+5%iso	23.6 ± 0.4	9.9 ± 0.1
Ne+5%iso	21.7 ± 0.3	12.4 ± 0.2
He+5%iso	23.6 ± 0.4	–

the noise level. At high fields, it worsens due to the proximity to the spark limit. As shown in Table 1, the best values measured at 5.9 keV are respectively 21.7% FWHM in neon- and 23.6% FWHM in helium- and argon-isobutene mixtures. This last value is compatible with the measurement obtained with a similar bulk pixelized detectors [7] and is limited by uniformities of the mesh and the PCB. Indeed, a detector with a continuous anode shows a better resolution of 16% FWHM at 5.9 keV. It should be noted that the energy resolution in Helium is degraded by the fact that X-ray conversion can occur anywhere within the drift volume, leading to a partial collection of the electrons and a degraded signal over noise ratio. Finally, we expect getting a better resolution in future prototypes since the gap distance will be increased to 256 μm. This will reduce the influence of local non-uniformities at the avalanche since the quality of both the mesh and the PCB will be improved.

4.2. Detection of low energy heavy ions

The study of the FIDIAS-2D response with low energy heavy ions (alphas and fission fragments) has been performed using an unsealed ^{252}Cf source. The ^{252}Cf decays by alpha emission (BR=96.9%) and spontaneous fission. The emitted alphas have an energy of 6118 keV (I=85.2%) and 6076 keV (I=15.7%) and fission fragments have a mass around 90 and 140 amu with a mean energy around 1 MeV/A. Since the Cf deposit of the source is unsealed, the ions can escape the source (it should be noted that, in case of fission, only one fragment is able to leave the source). This is the reason why the ^{252}Cf source had to be placed inside the TPC gas volume. For this purpose, a copper drift electrode, provided with a hole in the middle, was set below the original aluminum anode and the source was put on its top in order to let the ions cross only the TPC gas. The presence of this target holder reduces the drift gap to 8 cm.

Given the high energy deposited by ions, the amplification voltage was adjusted to get an absolute gain around 10. For this purpose, the gain curves obtained with the Iron source were fitted using the Rose–Korff model [41] which describes the gain dependence on the amplification field as:

$$\ln(G) = \frac{d}{\lambda} \exp\left(\frac{-I_e}{\lambda\, E_{amp}}\right) \quad (1)$$

where G is the gain, E_{amp} is the amplification field, d is the gap distance (here 128 μm), λ is the electron mean free path and I_e is

the threshold energy for ionization (these letters depend on the gas mixture and are kept as free parameter in the fit). The resulting curves (Fig. 8) were then used to determine the amplification voltage for each desired gain. For each gas mixture, the drift field was adjusted according to Fig. 6(right) to get the maximum mesh electron transmission. The energy threshold, imposed by the logic signal used as a trigger for the electronics, was also adjusted to get the largest dynamics range and detect both alphas and fission fragments.

As shown in Fig. 9, fission fragments can be easily distinguished from alphas from their topology in the XZ or YZ projections. The first two examples are obtained with Argon mixture. The first event shows a rather long track while in the second example all the energy is deposited within a very short distance. Because of the energy loss in Argon, the long tracks are created by alpha particles which deposit most of their energy at the end of their path (creating a Bragg peak). Fission fragments have a very short range in Argon and induce big signals in just few strips that may even saturate the electronics. Moreover, some cross-talk signals are induced on the neighboring channels by the flat cables connecting the detector to the electronics. To get rid of these effects a software threshold higher than the one set by the electronics was used in the analysis (350 instead of 250 ADC units). Cross-talk induced by fission fragments also appear in neon-Isobutene mixtures while it is negligible for Helium. In this latter case (Fig. 9, right), fission fragments have a longer range (while alphas are not fully stopped) and deposit most of their energy at the beginning of their path.

To extract the deposited energy spectrum, the event energy is calculated by summing the pulse integrals of all fired strips and applying the equation:

$$E_{event} = Q_{strips} \times F_{T2K} \times W_{gas}/G \quad (2)$$

where Q_{strips} is the strips integrated charge (in ADC units), F_{T2K} is the calibration factor of T2K electronics (18.3 e^-/ADC), W_{gas} is the gas electron–ion pair energy (respectively 26.1, 35.7 and 41.3 eV for argon, neon and helium-isobutene mixtures [43]) and G is the detector gain, calculated with Eq. (1).

The reconstructed energy spectra are shown in Fig. 10 for the three gas mixtures. In argon and neon, the peak, produced by the fully absorbed 6.1 MeV alphas (which are fully stopped in the gas volume), is clearly visible. Then, a second peak coming from pile-up effects is visible: this is due to two-alpha events which are rather probable given the high activity of the Cf source (around 300 kBq). Finally, a characteristic double humped distribution is created by fission fragments. In the case of Helium, the alpha peak is absent since alphas are not fully stopped within the 8 cm conversion gap due to their low energy loss. For comparison, the energy distributions obtained with FIDIAS have been compared to the spectrum obtained with a Silicon detector. We can see that in Argon and neon the energy deposited by alphas corresponds to their initial energy, in agreement with measurements made in Ref. [44]. Indeed, a reconstructed energy extracted from the total strips charge is in agreement with expectation when using the gain calculated with the Rose–Korff fit.

The energy resolution of alphas is rather modest (around 10% FWHM), as shown in Table 1, and it does not scale with the energy from the one obtained at 5.9 keV. This fact can be explained by

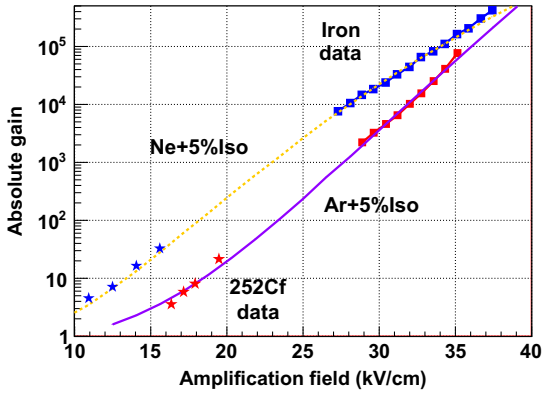

Fig. 8. Absolute gain as a function of the amplification field for the 2D prototype in Ar+5%iC_4H_{10} and Ne+5%iC_4H_{10} measured with the iron source (squares) and with 6.1 MeV alphas from Californium (stars). The fitted Rose–Korff model (lines) is also included.

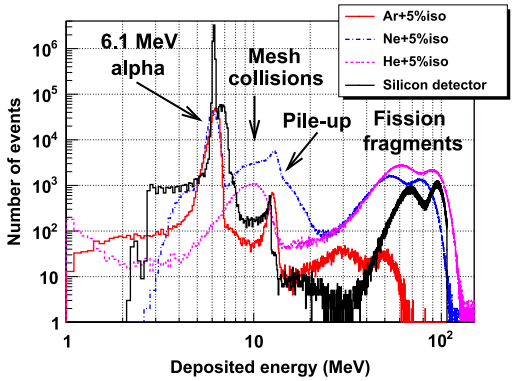

Fig. 10. Reconstructed energy spectrum measured with the FIDIAS-2D prototype irradiated with the ^{252}Cf source in Argon (red line), neon (blue line) and Helium +5% Isobutene (magenta line). For comparison, the energy spectrum measured with a silicon detector is included (black line) [42]. (For interpretation of the references to color in this figure caption, the reader is referred to the web version of this article.)

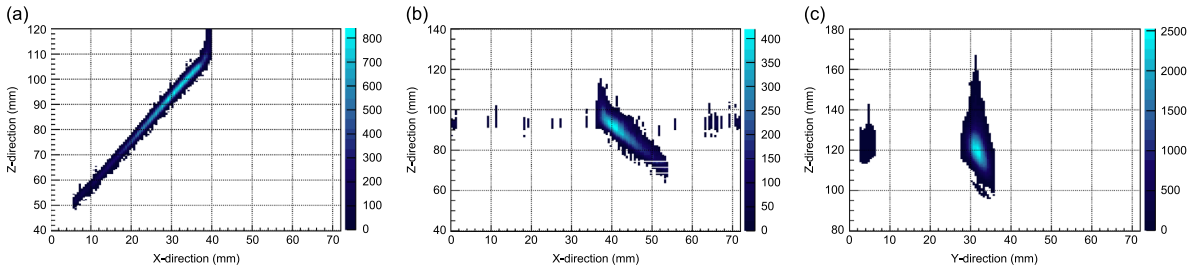

Fig. 9. Examples of events observed by the 2D prototype: a fission fragment in He+5%iC_4H_{10} (left), Ne+5%iC_4H_{10} (center) and Ar+5%iC_4H_{10} (right). The cross-talk effects of fission fragments present in argon are absent in helium.

two combined effects. First, the Cf deposit in the source is protected by two thin layers, one of gold (25.9 nm) and one of Mylar (0.9 μm), in order to prevent from sputtering. Although the energy loss in these layers is small (around 1%), the induced energy straggling, which degrades the energy resolution, is more than 20%. Moreover, given the present setup, there is dead gap of around 5 mm between the active volume and the deposit (corresponding to the combined thickness of the copper holder and the source box) where the converted electrons cannot be collected. Since the fission fragments deposit most of their energy at the beginning of their path, this loss shifts the energy spectrum to lower energy. This effect, which depends on the gas, is very visible in argon, as shown in Fig. 10, since the ion path is very short, around 2 cm. The maximum deposited energy is respectively 60 and 100 MeV, far from the expected 120 MeV [45]. This agreement improves for lighter gases as the energy left in the first millimeters is little in comparison to the total value. This collection defect has also an impact on the detection efficiency since, in argon-isobutene, only a fraction of 2.76% of the events was identified as fission fragments, instead of the expected 3.09%.

To assess this specific point, the track length of ion events has been calculated from the experimental data thanks to the 3D capabilities of the TPC. The event is first divided into slices along the time axis (Z). For each slice and 2D view (XZ and YZ), the mean position is extracted and the total length of the track is calculated by summing the partial distances between the mean positions of time-consecutive slices. The reconstructed range and its correlation with the deposited energy are shown for the three mixtures in Fig. 11. In addition, the range distribution of fission fragments has been compared to GEANT4 simulations (Fig. 11, bottom right). In argon, alpha tracks show a length around 6 cm, rather compatible with GEANT4 simulations (in average 6.7 cm). For fission fragments in argon, the experimental range distribution is fairly compatible with simulations. As expected, the largest discrepancy is visible helium where fission fragments show a shorter range due to the energy losses in the source holder dead zone. The energy-range correlation has been also used to estimate the capability of the detector to discriminate alphas from fission fragments. In particular, the number of fission fragments which may be misidentified as alphas has been calculated by selecting the fission fragments by two straight lines on the energy-range correlation plot. The number of selected events is then compared to the number of events in the 5–7 MeV range. We found that the alpha contamination in the fission fragment sample is around 10–5. This value is only an upper limit since rather naif cuts are applied to make the selection. Nevertheless, this limit is already fully satisfactory since in typical mass yield experiments the best achievable precision on the less produced fragments is on the order of one per cent.

In neon and helium, an unexpected population of events with total energy around 10 MeV appears. They present a range of 5 and 2 cm respectively (Fig. 11) and a sharp energy deposition at the end of their path (Fig. 12) and only central strips are fired. We have attributed them to fission fragments emitted perpendicular to the cathode, which lose their energy in the collision against the mesh. In light gases, the tracks of these events are longer than the drift distance, which is not the case of argon, and the apparent shorter range in helium can be explained by the fact that the mean energy loss is lower in helium than in neon.

5. Conclusions and perspectives

A new and original project called FIDIAS and aiming at the development of a Micromegas-based TPC for the detection of low energy heavy ions, is presently in its R&D phase. A rich set of

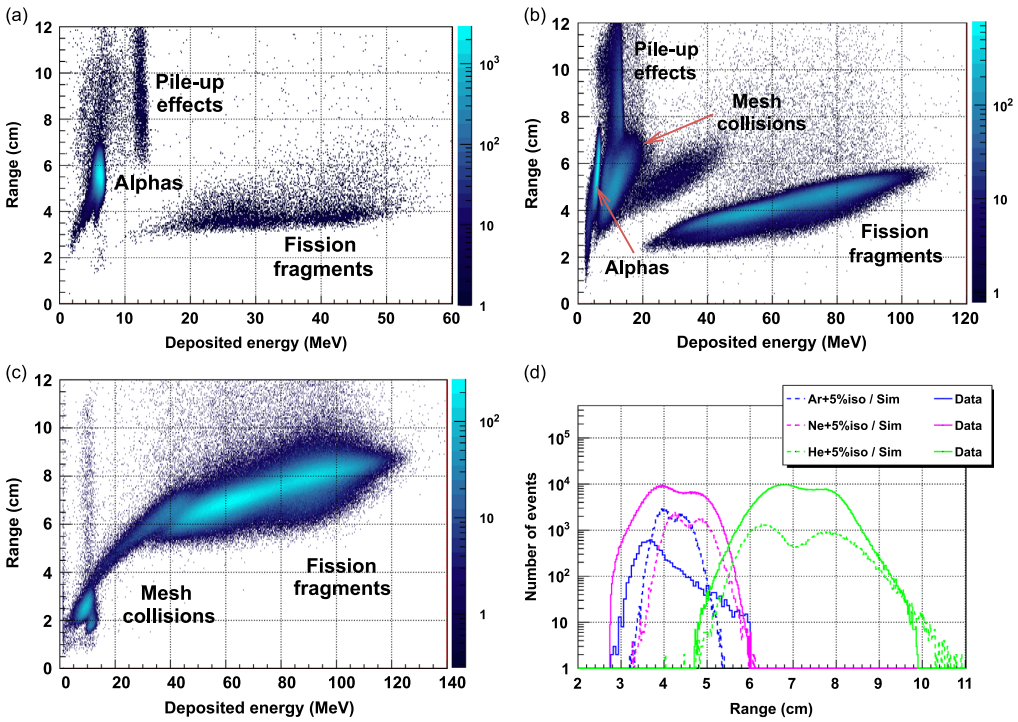

Fig. 11. Reconstructed ion range as a function of its deposited energy in Ar+5%iC_4H_{10} (top left), Ne+5%iC_4H_{10} (top right) and He+5%iC_4H_{10} (bottom left). Bottom right: Reconstructed range of fission fragments in argon- (blue line), neon- (magenta line) and helium-5% isobutene (green line). As a comparison, the expected range simulated with Geant4 is also plotted (dashed lines). (For interpretation of the references to color in this figure caption, the reader is referred to the web version of this article.)

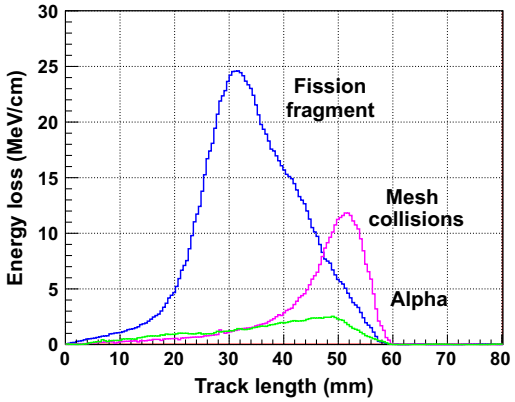

Fig. 12. Reconstructed energy loss along the track in Ne+5%iC_4H_{10} for a fission fragment (blue line), a light ion (magenta line) and an alpha (green line). (For interpretation of the references to color in this figure caption, the reader is referred to the web version of this article.)

physics cases has been identified and the technological challenges of the R&D program make it interesting for a rather large community.

In parallel to a large simulation effort, a test campaign with a Micromegas-2D TPC prototype has been realized and the results are considered as rather encouraging. Despite the limitations imposed by the setup, the FIDIAS-2D prototype has been proven to be able to correctly detect low energy heavy ions in a very large dynamic range, from alphas to fission fragments. The tracking capabilities of the TPC make this detector very well suited for range measurements and energy-range studies. The energy resolution of the FIDIAS detector will be improved by increasing the amplification gap and ensuring a better purity of the gas. These two points are fundamental to enlarge the working point plateau and decrease the gain of the detector around unity, thus reaching a better resolution. Moreover, the coupling of the TPC with the AFTER electronics was shown to be well adapted to the detection of high ionizing particles. This prototyping phase is continuing by testing the present FIDIAS-2D detector coupled with a new front-end electronics called GET [46]. This electronics is presently under development to fit a large number of applications (active targets and TPC) and provide self-triggering capabilities and overcome the AFTER trigger rate limitations. This latter point is very important, mainly for astrophysics applications, since the FIDIAS TPC should be able to withstand high intensity ion beams. Finally, the test of an improved 2D prototype with a fission source is presently foreseen inside a vertical solenoid at CEA-Irfu laboratory to acquire important data on the behavior of the TPC with fission fragments in a magnetic field up to 3.5 T.

Acknowledgments

This work is supported in part by the FP7/REGPOT/LIBRA project (Grant No. 230123). F.I. acknowledges the support from the Eurotalents program.

References

[1] D.R. Nygren, The time projection chamber: a new 4π detector for charged particles, in: Proceedings of the PEP Summer Study, Berkeley, CA (1975) 58, PEP-0144.
[2] C.E. Demonchy, et al., Nuclear Instruments and Methods in Physics Research Section A 583 (2007) 341.
[3] R. Raabe, et al., ACTAR: an active target detector for the study of extreme exotic nuclei, available at ⟨https://perswww.kuleuven.be/u0004046/actar.pdf⟩.
[4] M. Heffner, et al., A Time Projection Chamber for precision ^{239}Pu(n,f) cross section measurement, in: Proceedings of the Compound Nuclear Reactions and Related Topics Workshop, Fish Camp, USA, 2007.
[5] Y. Giomataris, et al., Nuclear Instruments and Methods in Physics Research Section A 376 (1996) 29.
[6] S. Aune, et al., Journal of Physics: Conference Series 179 (2009) 012015.
[7] F.J. Iguaz, et al., Journal of Instrumentation 6 (2011) 07002.
[8] S. Cebrian, et al., Journal of Cosmology and Astroparticle Physics 10 (2010) 1010.
[9] N. Colonna, et al., Nuclear Instruments and Methods in Physics Research Section B 269 (2011) 3251.
[10] Y. Giomataris, et al., Nuclear Instruments and Methods in Physics Research Section A 560 (2006) 405.
[11] S. Adriamonje, et al., Journal of Instrumentation 5 (2010) 02001.
[12] S. Panebianco, et al., AIP Conference Proceedings FINUSTAR3 1377 (2010) 200.
[13] C. Wagemans, The Nuclear Fission Process, CRC Press, 1991.
[14] U. Brosa, Physical Review C 38 (1988) 1944.
[15] S. Panebianco, et al., Physical Review C 86 (2012) 064601.
[16] H. Goutte, et al., Physical Review C 71 (2005) 024316.
[17] M. Salvatores, NEA/WPEC-26, OECD (2008).
[18] W.J. Drexel, IEEE Transactions on Nuclear Science NS-29 (1982) 123.
[19] P. Monceau, M. Alba, Neutron News 14 (3) (2003) 10.
[20] U. Abbondanno, et al., Report CERN-SL-2002-053 ECT (2002).
[21] A. Bensussan, et al., Nuclear Instruments and Methods in Physics Research Section A 155 (1978) 11.
[22] X. Ledoux, et al., Neutron For Science, LoI of SPIRAL2 (2006).
[23] M. Arnould, S. Goriely, Physics Reports 384 (2003) 1.
[24] S. Harissopulos, et al., Alpha-capture reactions and the alpha-nucleus optical potential for p-process nucleosynthesis, in: Proceedings of the International Symposium on Nuclear Astrophysics IX, CERN, 2006.
[25] E. Kugler, et al., ISOLDE Collaboration, Nuclear Instruments and Methods in Physics Research Section B 70 (1992) 41.
[26] ⟨http://pro.ganil-spiral2.eu/spiral2⟩.
[27] D. Wittwer, et al., Nuclear Instruments and Methods in Physics Research Section B 268 (2010) 28.
[28] J.F. Ziegler, J.P. Biersack, M.D. Ziegler, SRIM: The Stopping and Range of Ions in Matter, ⟨http://www.srim.org⟩.
[29] P. Koczon, et al., Physics Letters B 191 (1987) 249.
[30] D.M. Walker, International Journal of Bifurcation and Chaos 16-4 (2006) 1067.
[31] S. Agostinelli, et al., Nuclear Instruments and Methods in Physics Research Section A 506 (2003) 250.
[32] O.B. Tarasov, D. Bazin, Nuclear Physics B 746 (2004) 411.
[33] K. Shima, et al., Nuclear Instruments and Methods 200 (1982) 605.
[34] L. Vernoud, Développement d'une chambre à projection temporelle pour la détection des fragments de fission, Internship Report ENSICAEN (2010), available at ⟨http://irfu.cea.fr/Documentation/Publications/⟩ as report Irfu-10-148.
[35] V. Polychronakos, et al., Development of muon chambers based on Micromegas technology (MAMMA), ATL-M-MN-0001 (2007). RD51 collaboration for the development of Micro-Pattern Gas Detector Technologies ⟨http://rd51-public.web.cern.ch⟩.
[36] J.-C. Santiard, et al., Nuclear Instruments and Methods in Physics Research Section A 360 (1995) 8, CERN-ECP/95-17.
[37] P. Baron, et al., IEEE Nuclear Science Symposium Conference Record NS-57 (2010).
[38] Rene Brun, Fons Rademakers, Nuclear Instruments and Methods in Physics Research Section A 389 (1997) 81.
[39] H. Shimamori, H. Hotta, Journal of Chemical Physics 81 (1984) 1271.
[40] Y. Giomataris, Nuclear Instruments and Methods in Physics Research Section A 419 (1998) 239.
[41] M.E. Rose, S.A. Korff, Physical Review 59 (1941) 850.
[42] M. Kebbiri, reproduced with permission.
[43] L.G. Christophorou, Atomic and Molecular Radiation Physics, Wiley, 1971.
[44] Th. Dafni, et al., Nuclear Instruments and Methods in Physics Research Section A 608 (2009) 259.
[45] M. Forte, et al., Physical Review B 14 (1976) 956.
[46] E. Pollacco, et al., Physics Procedia 37 (2012) 1799.

Modélisation de la fission

3

SPY : un modèle de point de scission

Interpréter les nombreux résultats expérimentaux sur les distributions des fragments de fission n'est pas toujours simple, ni direct. D'un côté on pourrait se contenter de la description phénoménologique, souvent de bonne qualité, fournie par exemple dans le cadre de l'évaluation pour les bases de données utilisées pour les applications de la fission. D'autre part, lorsqu'on souhaite disposer d'un minimum de pouvoir prédictif dans des régions quelque peu éloignées des actinides pertinents en physique des réacteurs, on est obligé de se tourner vers des modèles théoriques plus détaillés, tels les approches de champs moyen de type Hartree-Fock (HF) et Hartree-Fock-Bogoliubov (HFB) décrivant la nature microscopique et quantique des noyaux et de leurs interactions, et donc souvent relativement limités car bien plus gourmands en ressources computationnelles. Pris dans l'impossibilité pour moi de trouver le juste milieu entre ces deux approches interprétatives, c'est la rencontre scientifique avec Jean-Luc Sida et Stéphane Hilaire qui a permis de dégager une troisième voie, celle qui consiste à utiliser les résultats issus de calculs théoriques extrêmement poussés et prédictifs dans le cadre d'un modèle simplifié mais très bien délimité dans ses hypothèses et son champ d'application. Cette approche a donné lieu au développement d'un modèle, appelé SPY, qui a permis de produire des résultats très intéressants concernant le rôle de la structure microscopique des fragments dans le partage d'énergie d'excitation qui a lieu à une phase cruciale du processus de fission, la scission.

3.1 Le modèle de Wilkins revisité

Il est bien connu par les calculs microscopiques adiabatiques que l'asymétrie de masse dans la fission thermique des actinides apparaît au second point selle et est favorisée par les effets de structure nucléaire des fragments naissants, ce qui explique la stabilisation du pic de masse lourde dans les distributions des fragments. Ceci étant dit, la détermination précise du moment où l'asymétrie de masse est déterminée tout au long du processus de fission n'a pas de réponse définitive. D'autre part, même dans un traitement théorique totalement microscopique, un grand nombre de grandeurs sont extraites directement d'une configuration particulière où les énergies de déformation, cinétique et d'excitation des fragments sont déjà fixées : c'est le point de scission. Bien que la définition exacte de ce point présente des ambiguïtés, on peut dire sans trop se tromper que la scission est l'instant où la densité nucléaire dans la region du col entre les deux fragments naissants est négligeable, ce qui implique que les fonctions d'onde des deux fragments sont localisées

et ne se recouvrent pas. C'est donc à la scission (ou bien à proximité de ce point) que les propriétés des fragments (masse, charge, énergie d'excitation) sont fixées.

A la fin des années '70, B. D. Wilkins a développé un modèle statistique de point de scission [37] basé sur l'hypothèse que les distributions de fragments de fission peuvent être déterminées à partir de l'énergie libre absolue des différentes configurations au point de scission. Ces travaux ont eu un grand impact dans la communauté car ce modèle arrivait à reproduire, entre autres, la fission asymétrique des actinides et le comportement en dents de scie du nombre de neutrons évaporés en fonction de la masse des fragments. Son modèle présente cependant des limites importantes car il comporte plusieurs paramètres libres dont la définition physique n'est pas bien établie. D'autre part, la description statistique utilisée n'exploitait pas l'ensemble des informations disponibles sur la structure nucléaire des fragments.

Trente ans plus tard, une première version améliorée du modèle de Wilkins, développée dans le cadre de la thèse de doctorat de Sophie Heinrich [38], montrait qu'il est possible de corriger les défauts conceptuels du modèle de Wilkins en utilisant les potentiels microscopiques de chaque noyau et leur densité de niveaux. C'est à partir de cette étude exploratoire qu'un tout nouveau modèle de point de scission, appelé SPY (*Scission Point Yields*), a été développé dans le but de proposer une description statistique et microscopique des fragments de fission sans aucun paramètre libre.

Dans le modèle SPY, une fois le point de scission défini, la première étape consiste à réaliser un bilan en énergie précis pour tous les couples possibles de fragments de fission, en fonction de leurs déformations. Puisque la compétition entre la fission symétrique et asymétrique est liée aux effets de couches dans les fragments, il est essentiel de disposer de la description la plus précise et fiable de ces potentiels jusqu'à des états très déformés. Pour ce faire, nous avons choisi de décrire le potentiel individuel de chaque fragment dans le cadre de calculs microscopiques avec la force effective nucléon-nucléon de Gogny [39,40]. La probabilité d'une fragmentation particulière est alors liée à l'énergie absolue disponible au point de scission et peut être calculée dans un ensemble micro-canonique en utilisant les densités des niveaux des fragments. Par ailleurs dans cette approche, le traitement statistique via les densités des niveaux constitue un contrepoids naturel à la stabilisation plus forte des noyaux sphériques ou pairs-pairs, qui conduisent à des distorsions non physiques des rendements.

En extrême synthèse, le but de cette approche a été d'inclure la description la plus détaillée et microscopique de la structure nucléaire des fragments de fission pour obtenir des informations pertinentes à la scission. Cependant, aucune information sur le noyau composé ne rentre dans le modèle, à l'exception de sa masse, de sa charge et de son énergie d'excitation, et la dynamique du processus n'est pas explicitement traitée. Par conséquent, les hypothèses sous-jacentes le modèle ne permettent pas de décrire exactement toutes les propriétés expérimentales des fragments de fission mais fournit plutôt des tendances générales, comme la compétition entre la fission symétrique et asymétrique, et ouvre à l'exploration des régions exotiques qui n'ont jamais été calculées ou mesurées. C'est le cas du premier succès du modèle SPY qui est lié à l'interprétation des résultats surprenants de la fission du Mercure.

3.2 Le cas particulier de la fission du Hg-180

Il est relativement bien connu que la fission des actinides donne lieu à des distributions de masse asymétriques alors que les noyaux plus légers, comme le Plomb, le Bismuth et certains isotopes du Mercure, fissionnent de manière symétrique en deux fragments de masses à peu près égales. Ce comportement a été traditionnellement attribué à la structure en couches des fragments qui favorise la formation de noyaux magiques ou proches de la magicité. Or, une mesure effectuée

en 2010 au CERN auprès de l'installation ISOLDE [41] avait mis en évidence que, contre toute attente, la distribution en masse des fragments issus de la fission β-retardée du Hg-180 est fortement asymétrique. Nous avions accueilli ce résultat étonnant avec surprise car on s'attendait à ce que la fission la plus probable du Hg-180 soit symétrique car elle donnerait lieu à deux noyaux de Zr-90, qui est magique en neutrons et semi-magique en protons. Puisque ce comportement nous paraissait donc inexplicable à partir de la seule structure en couches des fragments, nous en avons fait le premier banc d'essai du modèle SPY.

Par ailleurs, des nombreux théoriciens invoquaient, avec des arguments tout à fait pertinents que nous partagions, la nécessité de prendre en compte toute la dynamique complexe du noyau lorsqu'il fissionne et de ne pas considérer que la structure en couches des fragments de fission puisse être suffisante pour expliquer le caractère asymétrique ou symétrique de leur distribution en masse. Pour essayer de trancher ce débat au sein de la communauté scientifique, nous avons utilisé le modèle SPY pour calculer, dans une vision totalement statique de la configuration de scission, dans quelle mesure la structure microscopique des fragments influence le caractère asymétrique du partage de masse dans la fission du Hg-180. Pour cette étude nous nous sommes contentés d'une première version du modèle permettant de déterminer l'énergie disponible pour les différentes partitions possibles au point de scission en utilisant le potentiel microscopique de chaque noyau. Ces potentiels, calculés par une approche de type HFB avec la force de Gogny, constituent une systématique de plus de 7000 noyaux qui a été obtenue grâce aux outils du CEA DAM en calcul intensif haute performance. L'emploi de ces potentiels microscopiques, effectué dans le cadre d'une collaboration en physique nucléaire, appelée *Cophynu*, entre le CEA-DAM et le CEA-DSM, a permis de montrer que la seule structure microscopique des fragments, en particulier en présence d'états isomériques, est suffisante pour expliquer la fission asymétrique du Hg-180. Plus en général cette approche théorique est capable de rendre compte du caractère symétrique ou asymétrique du partage de masse entre les deux fragments aussi bien pour les actinides que pour les noyaux légers de la région du Pb et du Hg. Ces premiers résultats font l'objet de l'article qui suit [42] et qui a constitué le premier véritable succès du modèle SPY.

PHYSICAL REVIEW C **86**, 064601 (2012)

Role of deformed shell effects on the mass asymmetry in nuclear fission of mercury isotopes

Stefano Panebianco, Jean-Luc Sida, Héloise Goutte, and Jean-François Lemaître
IRFU/Service de Physique Nucĺeaire, CEA Centre de Saclay, F-91191 Gif-sur-Yvette, France

Noël Dubray and Stéphane Hilaire
CEA, DAM, DIF, F-91297, Arpajon, France
(Received 9 October 2012; published 3 December 2012)

3

Until now, the mass asymmetry in the nuclear fission process has been understood in terms of the strong influence of the nuclear structure of the nascent fragments. Recently, a surprising asymmetric fission has been discovered in the light mercury region and has been interpreted as the result of the influence of the nuclear structure of the parent nucleus, totally discarding the influence of the fragments' structure. To assess the role of the fragment shell effects in the mass asymmetry in this particular region, a scission-point model, based on a full energy balance between the two nascent fragments, has been developed using one of the best theoretical descriptions of microscopic nuclear structure. As for actinides, this approach shows that the asymmetric splitting of the ^{180}Hg nucleus and the symmetric one of ^{198}Hg can be understood on the basis of only the microscopic nuclear structure of the fragments at scission.

DOI: 10.1103/PhysRevC.86.064601 PACS number(s): 24.75.+i, 25.85.−w, 27.80.+w

I. INTRODUCTION

Fission is one of the most complex processes in nuclear physics, involving a strong interplay between nuclear structure and dynamics. Despite the huge theoretical effort pursued by several generations of physicists, there is no theory able to correctly describe and, more importantly, to reliably predict the whole set of observables. Soon after the discovery of the neutron-induced fission of uranium in 1939 [1], a characteristic asymmetric mass splitting was observed. The system evolution favors the production of a light fragment of mass around 100 and a heavy one of mass around 140, leading to a double-humped fragment mass distribution [2]. This experimental evidence was particularly surprising since a hydrodynamic description of the nucleus, suitable to describing the evolution of the nuclear matter binding energy, would lead to the formation of two fragments of nearly the same mass. The microscopic quantum effects are then found to be responsible for the asymmetric mass split. The question of where the most important quantum effects act on the mass asymmetry of the system during its evolution has been debated for a long time.

On the one hand, the position of the heavy mass peak in the thermal neutron-induced fission of actinides is found to be independent of the parent nucleus. This indicates a strong influence of the structure of the nascent fragments, for instance the heavy one for these systems. On the other hand, the fragment mass yields in the spontaneous fission of heavier actinides, like for certain fermium isotopes [3], or in the fission induced by light charged particles in the lead region [4] are found to be symmetrical. More recently, in the electromagnetic-induced fission of nuclei lighter than thorium [5], a symmetric splitting has been observed. This evolution from an asymmetric to a symmetric mass splitting was interpreted in the framework of a scission-point model [6,7] where only the nuclear structure of the fragments is considered. This statistical model is based on an energy calculation of all possible configurations at scission. The Wilkins model [6] involves the macroscopic nuclear properties of the two nascent nuclei, described by the liquid-drop model, together with phenomenological shell corrections. This rather simple approach showed that the double spherical shell closure around ^{132}Sn, associated with a deformed neutron shell closure around $N = 90$, is responsible for the stability of the heavy mass peak in the fission of actinides. For the fermium region, the proton shell closure $Z = 50$ is not sufficient to drive the system to a symmetric splitting, except when approaching the neutron shell closure $N = 82$. Finally, the absence of strong shell structures of the fragments for fission nuclei in the lead region leads to a natural symmetric splitting. However, more advanced models [8–10], involving the potential energy surface of the parent nucleus and accounting for the system evolution to the final state, are also able to describe rather correctly the experimental mass splitting.

Recently, a surprising result appeared in the fission of ^{180}Hg where the fragment mass yields were found to be asymmetric [11]. Recent models involving the evolution of the potential energy between the parent nucleus ground state to the final state of separated nuclei [12,13] were able to describe the asymmetric fission of ^{180}Hg without considering explicitly the nascent fragment structure. In a crude approximation of the Wilkins model, the symmetric fragmentation was expected to be favored since it would lead to the formation of two nuclei stabilized by a semimagic ($Z = 40$) and a magic shell closure ($N = 50$). Does it mean that the mass split is not driven by the structure of the fragments at scission for this particular system?

In this work we show that, as for the fission of actinides, the asymmetric split favored in the ^{180}Hg fission can be interpreted in the framework of an improved scission-point model on the sole basis of the nuclear structure of the daughter nuclei. Our approach, inspired by the first scission-point model [6], presents two major improvements, for instance in the absolute character and in the physical content of our energy balance calculation. As it will be explained in the next section, a detailed calculation of the energy balance between the two

fragments at scission will be derived using one of the best theoretical descriptions of their microscopic nuclear structure, going far beyond the liquid-drop description used by Wilkins *et al.* [6]. Thanks to this approach, the absolute available energy at scission can be calculated for all possible fragmentations and in a large range of nuclear deformation.

II. MICROSCOPIC SCISSION-POINT MODEL

To study precisely the impact of the nascent fragment nuclear structure on the mass distribution, a renewed statistical scission-point model based on microscopic ingredients has been developed. The scission-point description is the unique way to assess theoretically the energy distributions including kinetic, excitation, and available energy for each couple of primary fission fragments since their properties (mass, nuclear charge, etc.) are fully defined at this point and do not evolve anymore. Based on the assumption of a statistical equilibrium, the probability of a given fragmentation is related to its available energy. The symmetric-asymmetric mass splitting could then be discussed on the basis of only a careful calculation of the available energy at scission. Different prescriptions have been proposed to identify the scission configurations from microscopic potential energy surfaces [14–16]. We assume in our study the one used by Wilkins *et al.* [6]: scission is fully described by two ellipsoidal nuclei aligned along the same axis and with their surfaces separated by a fixed distance d, kept fixed for all fissioning nuclei. In particular, a distance of $d = 5$ fm, larger than the prescription of Wilkins *et al.* ($d = 1.4$ fm), has been chosen because of recent results from systematic studies in the framework of Hartree-Fock-Bogoliubov (HFB) calculations with the Gogny force [7,14]. This choice of the scission distance and its sensitivity will be discussed later for the mercury case.

A. Energy balance

To span the whole phase space of the scission configuration, the available energy at scission ($E_{\rm av}$) is calculated for all possible pairs of fragments, where the two nascent nuclei are characterized by their number of neutrons and protons (Z_1, N_1, Z_2, N_2) and, for each pair, for all possible deformations of the two fragments (β_1, β_2). The available energy is calculated as the difference between the total energy of the compound nucleus, defined by the entrance channel of the reaction, and the potential energy of the two-fragment system. This potential energy is expressed as the sum of the individual energies of the two nuclei and their interaction energy, composed by a nuclear and a Coulomb term:

$$\begin{aligned} E_{\rm av}(Z_{1,2}, N_{1,2}, \beta_{1,2}, d) &= E_{\rm tot} - E_{\rm HFB}(Z_1, N_1, \beta_1) - E_{\rm HFB}(Z_2, N_2, \beta_2) \\ &\quad - E_{\rm nucl}(Z_{1,2}, N_{1,2}, \beta_{1,2}, d) - E_{\rm Coul}(Z_{1,2}, N_{1,2}, \beta_{1,2}, d). \end{aligned} \quad (1)$$

The total energy $E_{\rm tot}$ is the binding energy of the compound nucleus (for spontaneous fission), eventually increased by its excitation energy in the case of induced fission.

The individual potential energy of each daughter nucleus $E_{\rm HFB}$ is calculated as a function of the deformation β (β is linked to the ratio between the ellipsoid axis and ranges from -0.6 to 1.5 in steps of 0.05, i.e., covering both prolate and oblate deformations) within the Hartree-Fock-Bogoliubov framework based on the Gogny D1S nucleon-nucleon interaction [17]. These HFB potentials have been calculated and compiled in the Amedee database [18,19], which contains more than 7000 nuclei and represents one the most up-to-date microscopic descriptions of the nuclear chart. Moreover, to ensure the best estimation of the absolute available energy in the balance, the HFB ground state energy of even-even nuclei has been renormalized to the measured mass (or to an evaluated mass [20] in case of unmeasured values). For odd nuclei, the mass normalization is interpolated between the even-even neighboring nuclei in order to wash-out even-odd effects. In the future, the more recent Gogny D1M interaction, developed mainly to ensure a better agreement with measured masses, will be tested in this model. However, its impact is expected to be rather small since each HFB potential is already renormalized to the measured mass.

For the nuclear interaction term $E_{\rm nucl}$, the Blocki proximity potential [21] is used. This interaction energy varies very rapidly for short scission distances (smaller than 2 fm) while it is found to nearly vanish for a distance of the order of 5 fm, having no effect on the interaction potential. Nevertheless, this nuclear term has been kept in the model to ensure an overall coherence and, more practically, to test the model's sensitivity to the scission distance and compare it with the Wilkins prescription. The Coulomb interaction energy between the two nuclei ($E_{\rm Coul}$) is calculated on the basis of the Cohen-Swiatecki prescription [22] which represents a very good approximation of the Coulomb repulsion of an axially symmetric system composed of two ellipsoidal charged nuclei.

The microscopic calculation of the individual potential energy $E_{\rm HFB}$ and the absolute character of the available energy are the most important improvements of this model. This has to be compared with the Wilkins approach which only gives access to the available energy relative to its highest value and was based on the macroscopic liquid-drop formalism with phenomenological shell effects and pairing corrections.

To interpret the surprising experimental result presented in Ref. [11], the available energy at scission has been calculated for all possible fragmentations of the compound nucleus ^{180}Hg at 10 MeV excitation energy. The available energy as a function of the two fragment deformations is presented in Fig. 1 for the fragmentation leading to the highest available energy and for the symmetric one.

From an energetic point of view, the asymmetric splitting [Fig. 1(a)] leading to ^{104}Pd and ^{76}Se fragments is favored in the fission of ^{180}Hg. In the symmetric case [Fig. 1(b)], the two ^{90}Zr fragments tend to be almost spherical (the minimum energy is found around $\beta = 0$), thus leading to a high Coulomb repulsion which, using the Cohen-Swiatecki formula, leads to a kinetic energy of 145 MeV. In the most probable fragmentation, which is found to be asymmetric, the ^{76}Se is rather deformed ($\beta \simeq 0.8$) while the ^{104}Pd has a relatively soft shape around sphericity. The total kinetic energy

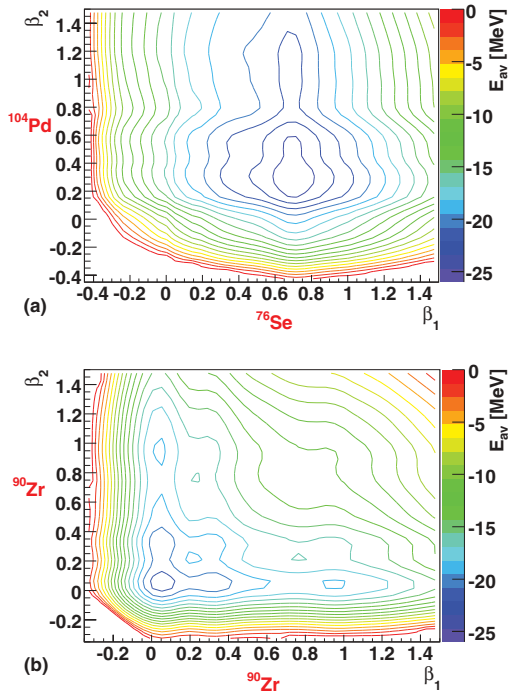

FIG. 1. (Color online) Available energy at scission as a function of the two fragment deformations calculated for the fission of the compound nucleus ^{180}Hg at 10 MeV excitation energy. (a) The asymmetric fragmentation (^{180}Hg $\rightarrow$ ^{104}Pd + ^{76}Se) leads to the highest available energy, around 25 MeV. (b) The symmetric splitting (^{180}Hg $\rightarrow$ ^{90}Zr + ^{90}Zr) leads to a 5 MeV lower available energy.

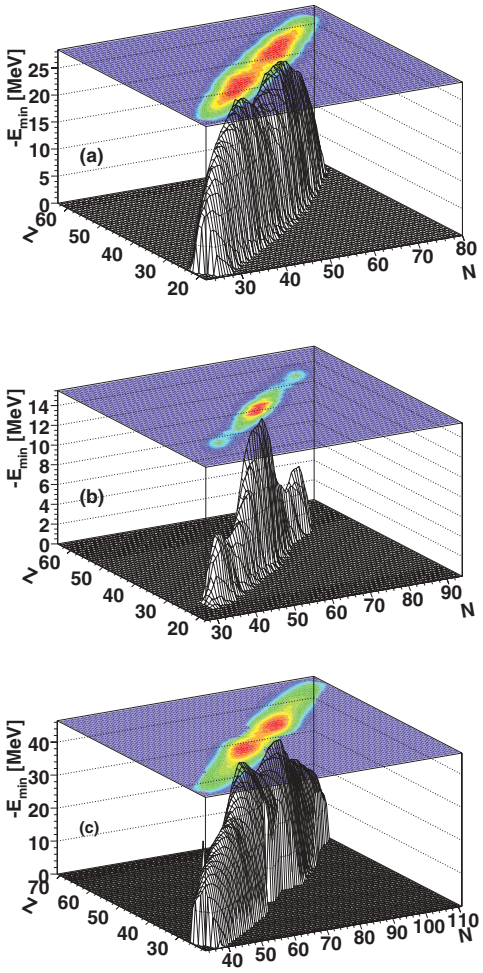

FIG. 2. (Color online) Minimum absolute available energy at scission calculated for all possible fragmentations in (a) ^{180}Hg and (b) ^{198}Hg fission at 10 MeV and in (c) the thermal n-induced fission of ^{235}U.

associated with this configuration will then be lower than the symmetric case, around 125 MeV, in good agreement with the experimental values from Ref. [11]. The light fragment will carry the largest part of the excitation energy because of its higher deformation. This recalls the fact that fission leads naturally to the splitting into nuclei with large deformations and that the relevant shell effects driving the fragmentation are the deformed ones. This conclusion had been already drawn by Wilkins *et al.* for the thermal neutron-induced fission of ^{235}U. More generally, one should note that although it is often said that the spherical ^{132}Sn is responsible for the stabilization of the heavy peak in the fragment distribution for the thermal fission of actinides, this heavy peak is always centered around the mass 140 [2]. This fact can only be explained by considering the deformed shell effects, leading to an enhancement of the asymmetric splitting.

To go further, we can now calculate the minimum available energy for each possible fragmentation [Fig. 2(a)]. It gives a more complete indication that, on the basis of only the scission-point study, the fission of ^{180}Hg leads preferentially to an asymmetric fragmentation. Although this result cannot be directly compared with the experimental fragment yields, we have checked that using a microcanonical statistical description of the system involving a simple Fermi gas level density, the calculated fragmentation probabilities still present a marked double-humped structure. This is explained by the Fermi gas level density which is an exponential function of the available energy and thus leads, to the first order, to an enhancement of the peak over valley ratio. In the future, a statistical treatment based on the microscopic state density of the fragments will be integrated in our model, providing an overall coherent approach and giving access to the main fragment observables that can be directly compared with experimental data.

For comparison, the same calculation has also been performed for the fission of ^{198}Hg at 10 MeV excitation energy [Fig. 2(b)], which presents a strong symmetric component [4], and for the thermal fission of ^{235}U [Fig. 2(c)] which, as already said, is known to be asymmetric. These two additional cases reinforce our conclusion.

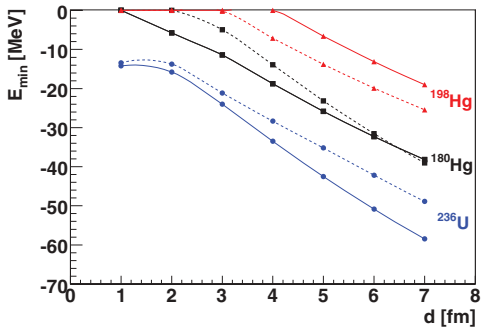

FIG. 3. (Color online) Minimum available energy as a function of the scission distance d for the asymmetric (solid line) and the symmetric (dashed line) fragmentations in ^{180}Hg (squares), ^{236}U (dots), and ^{198}Hg (triangles) fission.

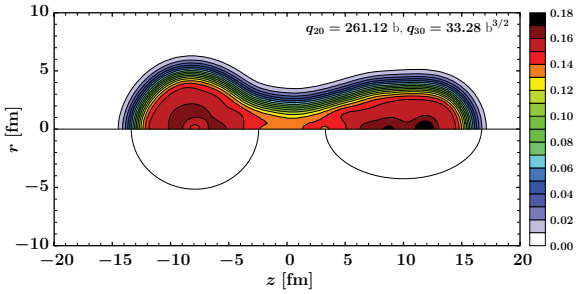

FIG. 4. (Color online) Total nuclear density for the most energetically favorable scission configuration in ^{180}Hg fission, extracted from a self-consistent HFB calculation. In the lower part of the figure, two coaxial ellipsoids are fitted to the density profile in order to have the same center of mass of the lowest localized individual states and the lowest order deformation and the mass of the nascent fragments.

B. Scission distance

Compared to the three parameters used by Wilkins *et al.*, the only parameter of our model is the distance associated with the scission definition. For the moment, this distance is kept fixed ($d = 5$ fm) in the calculation of all fissioning systems presented above. It is therefore crucial to study the stability of our results as a function of d. Figure 3 shows the variation of the minimum available energy with d for the asymmetric and symmetric splitting in the case of the three already mentioned fissioning systems. The increase of the scission distance has two expected effects. First, the rapid decrease of the Coulomb repulsion between the two ellipsoids induces a general increase of the absolute value of the available energy. Second, the increase of the distance makes the available energy more sensitive to structure effects at lower deformations. For instance, if one performs an energy balance between two fragments at infinite distance, the ground state structure will be dominant.

A domain of validity emerges between 3 and 6 fm, coherently with the microscopic studies we performed on the scission point. For very short distances ($d < 2$ fm), like for the prescription of Wilkins *et al.* ($d = 1.4$ fm), the description of the system via two uniformly charged ellipsoids does not lead to physical configurations since they are energetically unreachable, like for ^{198}Hg. On the other side, in the well-known case of the thermal neutron-induced fission of ^{235}U, the total excitation energy, given by the mean number of evaporated neutrons, is of the order of 30 MeV, leading in our model to a scission distance of 4–5 fm. Large distances ($d > 7$ fm) lead to unphysical configurations because of the too high excitation energies, incompatible with the observed number of evaporated neutrons.

From Fig. 3, it can be seen that, as expected, the absolute value of the available energy depends rather strongly on d. Moreover, while for ^{236}U (^{198}Hg) the absolute value of available energy for asymmetric (symmetric) fragmentation stays larger than for the symmetric (asymmetric) one, the case of ^{180}Hg presents an intermediate behavior. For instance, when $d > 6.5$ fm the absolute energy available in the symmetric fragmentation becomes larger than in the asymmetric case, showing that ^{180}Hg is a very rich case. This effect is due to the Coulomb interaction between the two nuclei, which decreases more rapidly with distance in the case of symmetric fragmentation (where the two nuclei are almost spherical) than in the asymmetric case (where the Coulomb interaction acts between two nuclei with slightly different deformations).

Some exploratory microscopic calculations have been carried out to examine the relevance of the range in distance that was extracted from purely energetic considerations. These calculations have been performed in the framework of the self-consistent HFB formalism with the Gogny D1S nucleon-nucleon effective interaction with constraints on collective variables (nucleus elongation and mass asymmetry) where the scission configurations have been defined using a criterion on mass density in the neck [10,14]. The microscopic scission distances are extracted from such calculations by fitting the total nuclear density with two coaxial ellipsoids. An example is given in Fig. 4. Although this approach is based on very different physics than for the scission model, they both aim at extracting the total kinetic energy of the fragments using similar quantities, i.e., their nuclear charges and the distance between them. It is therefore reasonable to assume that the scission distances calculated from the two approaches can be compared one to the other.

In this configuration, corresponding to the most energetically favorable fragmentation obtained with such a HFB calculation, a distance of 5.7 fm is found between the surfaces of the ellipsoids. More generally, the scission distance is predicted to range between 4 and 6.5 fm. These results indicate a reasonable agreement with the scission distance range deduced in our model from energetic considerations. However, the distances extracted from such HFB calculations do not enable us to draw any conclusion regarding the relevance of the use of a constant scission distance in our model. In the future, we will pursue the study on the microscopic description of fragment formation in order to improve our definition of the scission distance, in particular its possible dependence on fragment mass and charge.

III. CONCLUSIONS

In the framework of a fully renewed scission-point model, we have shown that a detailed energy balance at scission, involving a complete microscopic description of the nuclear structure of the two fragments, is able to explain qualitatively the evolution from asymmetric to symmetric fragmentation for intermediate mass nuclei as well as heavy actinides. Although these results depend on the choice of the scission distance, the study of the particular case of ^{180}Hg shows that the general statement claiming that the microscopic effects in fragments are not relevant to the description of mass splitting is clearly an argument that should be used with great care. On the one hand, it is known that the yields are governed by the combined influence of both the system dynamics and fragment nuclear structure at scission. On the other hand, as already noticed by Wilkins *et al.*, our model confirms that mass asymmetry in fission can be qualitatively understood from the fragment's microscopic structure and that the relevant shell effects driving fragmentation are the deformed ones.

ACKNOWLEDGMENT

The authors are grateful to Dr. Navin Alahari for valuable discussions and comments.

[1] L. Meitner and O. R. Frisch, Nature **143**, 239 (1939).
[2] C. Wagemans, *The Nuclear Fission Process* (CRC, Boca Raton, FL, 1991).
[3] D. C. Hoffman, Nucl. Phys. A **502**, 21 (1989).
[4] M. Itkis *et al.*, Yad. Fiz. **53**, 1225 (1991), and references therein.
[5] K.-H. Schmidt, S. Steinhuser, C. Bckstiegel, A. Grewe, A. Heinz, A. Junghans, J. Benlliure, H.-G. Clerc, M. de Jong, J. Mller, M. Pftzner, and B. Voss, Nucl. Phys. A **665**, 221 (2000).
[6] B. D. Wilkins, E. P. Steinberg, and R. R. Chasman, Phys. Rev. C **14**, 1832 (1976).
[7] S. Heinrich, Ph.D. thesis, Université Paris XI, 2006.
[8] P. Möller *et al.*, Nature **409**, 785 (2001).
[9] J. Randrup and P. Möller, Phys. Rev. Lett. **106**, 132503 (2011).
[10] H. Goutte, J. F. Berger, P. Casoli, and D. Gogny, Phys. Rev. C **71**, 024316 (2005).
[11] A. N. Andreyev *et al.*, Phys. Rev. Lett. **105**, 252502 (2010).
[12] P. Möller, J. Randrup, and A. J. Sierk, Phys. Rev. C **85**, 024306 (2012).
[13] M. Warda, A. Staszczak, and W. Nazarewicz, Phys. Rev. C **86**, 024601 (2012).
[14] N. Dubray, H. Goutte, and J.-P. Delaroche, Phys. Rev. C **77**, 014310 (2008).
[15] W. Younes and D. Gogny, Phys. Rev. Lett. **107**, 132501 (2011).
[16] L. Bonneau, P. Quentin, and I. N. Mikhailov, Phys. Rev. C **75**, 064313 (2007).
[17] J. Dechargé and D. Gogny, Phys. Rev. C **21**, 1568 (1980).
[18] S. Hilaire and M. Girod, Eur. Phys. J. A **33**, 237 (2007).
[19] http://www-phynu.cea.fr/HFB-Gogny.htm.
[20] P. Möller, J. Nix, and K.-L. Kratz, Tech. Rep. LA-UR-94-3898, 1994.
[21] J. Błocki, J. Randrup, W. J. Światecki, and C. F. Tsang, Ann. Phys. (NY) **105**, 427 (1977).
[22] S. Cohen and W. Swiatecki, Ann. Phys. (NY) **19**, 67 (1962).

3.3 Le modèle SPY en détail

L'interêt suscité per les premiers résultats obtenus dans le cas particulier du Hg-180 présenté dans la section 3.2 a motivé la poursuite des développements du modèle SPY dans la cadre de la thèse de doctorat de Jean-François Lemaître [43]. L'article qui suit [44] présente cette approche théorique dans le détail, du calcul de l'énergie disponible à la scission à partir des énergies microscopiques des fragments au traitement statistique du système, supposé en équilibre thermodynamique, où la probabilité d'une configuration est obtenue par un dénombrement des états énergiquement accessibles associés à cette configuration. Ce traitement statistique permet de calculer un grand nombre d'observables associées aux fragments de fission telles que les rendements en masse et isotopiques, la distribution en énergie cinétique ou le nombre de neutrons évaporés. D'une certaine manière, ce modèle constitue un cadre interprétatif permettant de faire le lien entre les observables physiques mesurables et des grandeurs internes au système comme l'énergie de déformation des fragments ou leur énergie d'excitation totale.

Les résultats présentés dans cette publication montrent que les rendements de fission des actinides prédits par le modèle SPY sont dominés par le Sn-132 à cause de sa double fermeture de couche sphérique. Clairement, l'importance de la structure en couches est surestimée dans une approche statique comme celle d'un modèle de point de scission. Cependant, malgré des écarts entre les rendements prédits et les données expérimentales, la transition entre la fission symétrique et la fission asymétrique est assez bien reproduite dans la région des actinides. C'est également le cas de la transition entre fission symétrique et fission asymétrique observée expérimentalement en fission coulombienne dans la région des actinides légers. On note également que la largeur des distributions calculées est environ un facteur 2 plus petite que celle mesurée. Ceci est dû encore une fois à l'absence de dynamique dans le modèle et, comme il a pu être montré plus tard, est également sensible aux densités des niveaux qui sont utilisées dans le traitement statistique.

Cette approche nous a également permis de montrer que l'évaporation de neutrons par les fragments n'est pas directement liée à la valeur du paramètre de déformation, ce malgré le fait qu'il existe une apparente corrélation entre la déformation moyenne d'un fragment et son nombre de neutrons évaporés. Cette évaporation n'est due qu'à l'énergie d'excitation totale des fragments, c'est à dire à la somme de leur énergie de déformation et de leur énergie d'excitation intrinsèque. Par conséquent, le caractère symétrique ou asymétrique de la fission semble essentiellement déterminé par le nombre de neutrons du système fissionnant. Il faut reconnaitre que Wilkins était arrivé à la même conclusion sans pour autant en apporter une preuve quantitative. Enfin, nous avons pu étudier la correlation entre l'évolution de l'énergie cinétique totale et la déformation moyenne en fonction du système fissionnant. En effet, le modèle SPY est capable de reproduire plus que raisonnablement la systématique de l'énergie cinétique totale en fonction de la fissilité du noyau fissionnant.

Après la publication de cet article, des nombreux aspects du modèles ont été précisés et détaillés, à commencer par une étude très étendue des énergies individuelles obtenues par les calculs HFB et disponibles dans la base de données AMEDEE [45]. Toujours en lien avec ces travaux, une étude de sensibilité vis-à-vis de la distance inter-surfaces entre les deux fragments (considérée constante et égale à 5 fm dans la version de référence de SPY) a pu montrer que cette quantité, seul véritable paramètre du modèle (encore que défini une fois pour toutes), n'a qu'un faible impact sur les rendements de fission et qu'une description en formes quadripolaires constitue la meilleure approximation des distributions de charge microscopiques. Enfin, une avancée tout à fait considérable, toujours dans le calcul d'énergie disponible à la scission, a consisté à inclure dans le modèle les distributions de protons issues des calculs HFB, s'affranchissant ainsi de l'hypothèse restrictive d'une répartition uniforme et d'améliorer les distributions en énergie cinétique des fragments. Enfin, la description

statistique de la configuration de scission a pu être enrichie en utilisant des densités d'états microscopiques issues, comme les énergies individuelles, des calculs HFB. Grâce à ces densités d'états, l'impact du Sn-132 sur les rendements de fission est sensiblement réduit, ce qui permet d'améliorer la prédiction de certains rendements de fission mais déplace la zone de transition entre la fission symétrique et la fission asymétrique.

Les développements sur le modèle SPY ont été poursuivi jusqu'en 2015 lorsqu'ils ont atteint leur fin. En effet, un cadre simplifié comme celui d'un modèle de point de scission ne tire sa richesse que des ingrédients qui l'alimentent. En ce sens, nous avons pu inclure dans SPY la description des noyaux la plus avancée et précise que l'on soit capable de produire actuellement et ceci a permis de fournir un cadre interprétatif de grande richesse. Il est intéressant de noter que les résultats obtenus avec SPY peuvent être analysés comparativement à d'autres approches faisant appel à l'utilisation de données expérimentales ou à des considérations phénoménologiques. A ce propos il est indispensable de citer deux exemples marquants : tout d'abord le code FIFRELIN [46], qui permet de calculer avec une précision tout à fait satisfaisante l'émission de neutrons et gamma par les fragments en combinant des rendements expérimentaux à un traitement statistique très avancé, similaire à celui utilisé dans SPY, et qui fait appel aux densités de niveaux microscopiques. L'autre exemple est le code GEF [15], utilisé massivement dans l'évaluation des données nucléaires pour les applications, qui arrive à décrire de manière extrêmement précise les rendements de fission dans une plage très étendue de noyaux fissionnants grâce à une description paramétrique très optimisée des modes de fission.

PHYSICAL REVIEW C **92**, 034617 (2015)

New statistical scission-point model to predict fission fragment observables

Jean-François Lemaître
CEA Centre de Saclay, Irfu/Service de Physique Nucléaire, F-91191, Gif-sur-Yvette, France and CEA, DAM, DIF, F-91297, Arpajon, France

Stefano Panebianco and Jean-Luc Sida
CEA Centre de Saclay, Irfu/Service de Physique Nucléaire, F-91191, Gif-sur-Yvette, France

Stéphane Hilaire and Sophie Heinrich*
CEA, DAM, DIF, F-91297, Arpajon, France

(Received 26 January 2015; revised manuscript received 23 May 2015; published 28 September 2015)

The development of high performance computing facilities makes possible a massive production of nuclear data in a full microscopic framework. Taking advantage of the individual potential calculations of more than 7000 nuclei, a new statistical scission-point model, called SPY, has been developed. It gives access to the absolute available energy at the scission point, which allows the use of a parameter-free microcanonical statistical description to calculate the distributions and the mean values of all fission observables. SPY uses the richness of microscopy in a rather simple theoretical framework, without any parameter except the scission-point definition, to draw clear answers based on perfect knowledge of the ingredients involved in the model, with very limited computing cost.

DOI: 10.1103/PhysRevC.92.034617 PACS number(s): 24.75.+i, 25.85.−w, 27.80.+w

I. INTRODUCTION

"A satisfactory theoretical interpretation of the asymmetric mass distribution observed in nuclear fission at low excitation energies has been sought since the discovery of this complex nuclear reaction." With this affirmation begins one of the major reference papers on the interpretation of the fission process, published in 1976 by Wilkins, Steinberg, and Chasman [1], and it is still relevant forty years later despite a huge theoretical and experimental effort. So what makes this physics process so difficult to describe?

A proper fission reaction description faces all the difficulties associated with theories describing the atomic nucleus. This phenomenon only occurs for rather heavy nuclei for which an exact quantum description of the many-body problem is out of reach. However, several recent models seek to provide a detailed description based on mean-field [2] and macro-microscopic approaches [3–5]. It is not yet possible to provide an exact description of the system by quantum thermodynamics given the lack of knowledge on the partition of numerous degrees of freedom involved during the system evolution. In addition, they all require significant computing time.

Together with theoretical developments, many experiments have been performed since the 1980s to explore new fissioning systems, from exotic light nuclei within the lead region [6], up to new superheavy nuclei [7,8]. In addition, a very rich set of data on the charge yields has been measured from lead to uranium in inverse kinematics [9]. Taken together, these data highlight a transition from symmetric fission for proton-rich nuclei to asymmetric fission for neutron-rich nuclei. Understanding the origin of this transition requires a fission model based on a coherent theoretical framework applicable to the entire nuclei chart.

A new theoretical approach, based on a statistical modeling of the scission point, has been developed using a microscopic description of the fragment nuclear structure. These microscopic ingredients [10] are calculated with the Gogny interaction [11]. Therefore, this approach is complementary with the historical mean-fields theories based on the same interaction [2].

This new model, called SPY (scission-point yield), is largely inspired by the scission-point model originally developed by Wilkins *et al.* However, there are reasons pointing to a need for a renewal of historical formalism. First, major theoretical advances in nuclear structure description have been made since the late 1970s and they have never been included in an updated version of the Wilkins model. Second, a predictive and fast model is useful to generate nuclear data to study the fission process over a large range of nuclei, from light nuclei such as mercury to heavy ones like fermium. This is why the SPY model has been developed: it is capable of making reasonable predictions for every fissionable nucleus, while achieving very moderate computation cost. This makes it very appealing for several applications, in particular astrophysics calculations [12]. Finally, a statistical description of the scission point that is as complete as possible allows for the estimation of effects which are not included in the model, especially coming from the system dynamics, and for an assessment of the sensitivity to the reaction entrance channel. This model will favor discussions on experimental results interpretation.

As mentioned by Wilkins, "the principal aim is to investigate the general validity and applicability of our model and not to attempt to achieve the optimum fit to the experimental data for each fissioning system." The SPY model has been

*Former member of the laboratory.

developed keeping the same spirit and no adjustments to any data have been done.

II. THE SPY MODEL

SPY is a renewed version of the well-known scission-point model developed by Wilkins *et al.* [1] in the late 1970s. It is based on the basic assumption that the gross properties of the fission fragment distributions can be determined from the available energy of the different configurations at the scission point. Assuming a thermodynamic equilibrium at scission, a statistical treatment can be used to calculate the fission fragments' distributions. The model is based on two pillars: the definition of the scission point (Sec. II A), on the one hand, and the calculation of the absolute available energy for each configuration (Sec. II B) allowing the statistical description (Sec. II C), on the other.

A. The scission-point definition

During the fission process, the system evolves from a quasispherical or slightly deformed compound nucleus to two fragments flying away from one another due to their Coulomb repulsion. The dynamical evolution of the system presents two characteristic points: the outer saddle point and the scission point. The first is defined as the configuration where the fission of the system is inevitable and it is clearly defined by a topological criterion on the potential energy surface of the fissioning system. After the saddle point the system continues to deform; a neck appears and becomes more and more thin until breaking, giving rise to two fragments. The scission point, somewhere between the saddle point and the two separated fragments far apart, is difficult to define unambiguously. At scission, the nuclear density in the neck region between the nascent fragments may be considered as vanishing, and the wave function of any nucleon spreads over each of the fragments. In this configuration, all fragments properties (mass, charge, and deformation) can therefore be considered as fixed. Nevertheless, the scission configuration presents an ambiguous topological definition, and different criteria have been used for its identification. In particular, in several microscopic approaches (see for example [2,13]) the scission configuration is identified by energy criteria, i.e., the sudden drop of the total binding energy, or according to the ratio between the nuclear interaction and the Coulomb repulsion between fragments [14]. In all cases, the scission configuration topology depends on the chosen criteria, and, contrary to what Wilkins et al. stated, scission can hardly be defined by the sole distance between the two fragments. Nevertheless, the potential energy surface (PES) of the system, calculated through a self-consistent Hartree-Fock-Bogoliubov (HFB) formalism, is rather smooth between the saddle point and the scission point, at least for major actinides, and the nuclear matter density extracted near the scission line gives a scission distance ranging from 3 to 7 fm [2,15].

Therefore, as in Wilkins's work, the system at scission is modeled by two coaxial nuclei separated by a fixed distance, and the fragment shape is described by quadrupole deformations. This simple but realistic first-order description of the nuclear deformation of the fragments allows for reliable calculations of the energy of the system, and more importantly can be unambiguously connected to the HFB potential energies of the nuclei. Given this definition of the scission configuration, each nucleus is characterized by its neutron and proton numbers (N,Z) and its deformation parameter $(\tilde{q})$.

A fixed scission distance of 5 fm is used in all calculations presented in this work. It ensures that the quadrupole shape family used for the scission description is relevant and somehow corresponds to a first-order optimum as discussed in [16]. The chosen value is different from the initial choice of Wilkins who considered a distance of 1.4 fm, based on the range of the strong interaction. The influence of this choice on the energy balance at scission has already been discussed in [16] and will be further discussed in this work.

B. The energy balance at scission

Once a system configuration at scission is defined, the first stage of the SPY model consists of achieving detailed energy balance for all possible fragmentations (around 1000 for actinide fission) as a function of the deformation parameter of the two fragments. The available energy (E_A) is calculated as the difference between the scission potential energy of the system composed by the two nascent fragments in interaction and the excited compound nucleus energy (E_{CN}):

$$\begin{aligned} E_A = {} & E_{\rm ind}(Z_1,N_1,\tilde{q}_1) + E_{\rm ind}(Z_2,N_2,\tilde{q}_2) \\ & + E_{\rm coul}(Z_1,N_1,\tilde{q}_1,Z_2,N_2,\tilde{q}_2,d) \\ & + E_{\rm nucl}(Z_1,N_1,\tilde{q}_1,Z_2,N_2,\tilde{q}_2) \\ & - E_{CN}. \end{aligned} \tag{1}$$

The scission potential energy is obtained as the sum of

(i) The individual energy for each of the two fragments $(E_{\rm ind})$, which is a function of their deformation.

(ii) The interaction energy between the fragments, described as the sum of a Coulomb repulsion term $(E_{\rm coul})$ and a nuclear interaction term $(E_{\rm nucl})$. The interaction energy depends on the deformation parameters of the fission fragments and on their distance.

As a consequence, a given configuration is energetically reachable only if the available energy of the system at scission is lower than the total energy of the compound nucleus. In other words, a scission configuration is possible only if $E_A < 0$. By convenience, the absolute value of the available energy will be used thereafter and only energetically reachable scission configurations will be taken into account.

A prescission kinetic energy could be taken into account and would modify this equation. Since there is no proper well-defined formalism to introduce it and it depends on the scission point definition, this energy is not taken into account.

The axial symmetry of the compound nucleus is supposed to be conserved in the system formed by the two fragments. Moreover, the scission potential energy depends rather weakly on high-order deformations, typically higher than the quadrupole momentum. Therefore, the deformation parameter used in the SPY model only accounts for quadrupole deformation, i.e., elongation. The compound nucleus energy

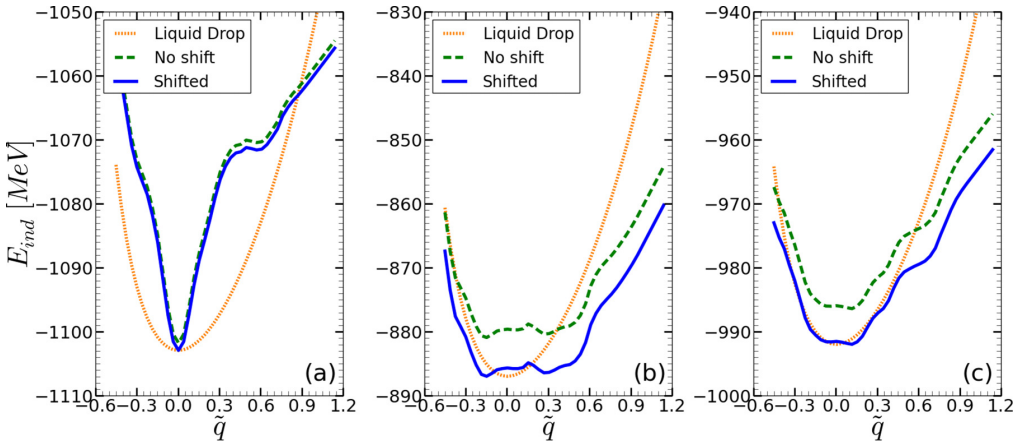

FIG. 1. (Color online) Liquid drop (orange dotted line), HFB (green dashed line), and shifted HFB (blue solid line) potential energy as a function of deformation for ^{132}Sn (a), ^{104}Mo (b), and ^{118}Pd (c). Liquid drop ground state energy is shifted to HFB ground state energy.

E_{CN} is defined as the sum of the ground state energy of the fissioning nucleus and its excitation energy. The excitation energy depends on the involved reaction (neutron-, proton-, photo-induced or spontaneous fission) and is distributed among all degrees of freedom. The ground state energy of the compound nucleus is taken as its experimental mass (when available) or as a theoretical prediction calculated on the basis of mass systematic [17]. The mass, charge, and excitation energy of the compound nucleus are the only inputs of the model since they totally define the initial condition of the fission reaction. At this stage, SPY does not include any deformation-dependent nuclear structure property or angular momentum of the compound nucleus nor its possible deexcitation prior to fission. This latter constraint restricts the possible comparison with data only to low-energy induced fission.

1. The individual energy

The individual energy ($E_{\rm ind}$) of each nucleus is derived from an up-to-date microscopic description of its nuclear structure. This potential energy is calculated within the framework of a self-consistent HFB formalism using the Gogny D1S nucleon-nucleon interaction [11]. The HFB equations are solved iteratively by expanding the quasiparticle wave functions in a truncated harmonic oscillator basis under the axial hypothesis where the quadrupole momentum operator is projected into a fixed value (and triaxiality is neglected). The so-called reduced quadrupole momentum ($\tilde{q}$) is linked to the quadrupole momentum (q_{20}) by the relation

$$\tilde{q} = \frac{q_{20}}{A R_0^2} \qquad (2)$$

where A is the nuclear mass and R_0 its radius ($R_0 = r_0 A^{1/3}$). The individual energies used in SPY are compiled within the AMEDEE database [10,18] which contains the nucleus' potential energy as a function of its deformation parameter over a large range of deformations, from very oblate ($\tilde{q} = -0.45$) to very prolate shapes ($\tilde{q} = 1.14$), and for all the nuclei of the whole nuclear chart (see for example Fig. 1).

The ground state energy calculated within the HFB formalism is known to differ from the experimental mass. This is mainly due to the mean field approximation and the use of a finite basis in the HFB states expansion [10,19,20]. The difference between the measured mass and the HFB ground state energy can be several MeV, especially in the case of "soft" nuclei where shape coexistence is involved or neutron-rich nuclei. Nevertheless, the predictive power of the microscopic calculations mostly concerns the description of the nuclear structure as a function of the deformation, instead of the absolute value of the potential energy. Therefore, to achieve precise energy balance, the whole HFB potential energy surface (E_{HFB}) is globally shifted so that the ground state energy fits the experimental masses or a theoretical value calculated on the basis of mass systematics (for instance [17]).

The shifted energy, which keeps all relevant microscopic information on the structure evolution with the deformation, is used to perform the energy balance defined in (1). The three examples presented in Fig. 1 show the typical shape of the HFB energy of a nucleus as a function of its deformation. The shift to the actual mass varies from a few keV for magic nuclei up to 10 MeV for midshell nuclei.

The importance of a microscopic description is visible when comparing the HFB energy with a liquid drop potential energy [21,22]. The richness brought by microscopy lies in the natural appearance of shell effects, which will finally influence the available energy for the different fragmentations at scission.

During the descent from saddle to scission, the system could dynamically increase in temperature. At scission, a potential energy calculated in a finite-temperature HFB framework would thus be better adapted. The main impact of the temperature on the potential energy would be a decrease in the nuclear shell and pairing effects. This effect, taken into account by Wilkins *et al.* by an intrinsic temperature-dependent shell correction term, is not taken into account due to the lack of a proper modeling of dissipation from saddle to scission and to to

the absence of temperature-dependant microscopic individual energy. Moreover, the statistical description of a system with a potential energy calculated in a finite-temperature framework must be properly handled in order to avoid double counting of temperature-dependent effects (shell and pairing effects).

The influence of pairing energy on the available energy at scission can be rather large since it is around 2 MeV between an even-even and an odd-odd fission fragment in the case of actinides. This difference is generally quite significant with respect to the energy variation between two successive even nuclei due to shell effects. Therefore, the impact of pairing on fission observables is too strong and, as a first step, it is suppressed by washing the pairing effect on the nuclear masses. In the case of an odd-odd nucleus, its mass is interpolated between the four neighboring even nuclei (the two adjacent proton-even and the two adjacent neutron-even).

2. The interaction energy

The fission fragments at scission are separated by a few fm and are submitted to the nuclear interaction and to the Coulomb repulsion.

The nuclear interaction is determined from the Blocki prescription [23], which mainly depends on the distance between fragment surfaces, the isospin asymmetry of the fissioning nucleus and the fragments curvature along the scission axis. However, since the scission distance of 5 fm is greater than the mean range of nuclear interaction, this term is always below 1 MeV and can be neglected compared to the Coulomb energy that is of the order of 200 MeV. Nevertheless, the nuclear interaction is always included in the calculation for completeness.

The fission fragments are rather close at scission and induce a high Coulomb interaction. Therefore, a proper calculation requires a detailed description of their charge distributions since they cannot be considered as point-like. The charge distribution of a given fragment depends on its proton and mass numbers and on its deformation. In the present version of the SPY model, the fragments are considered as uniformly charged without diffusivity. The nuclear shape is fully described by the quadrupole deformation of an axially symmetric nucleus to ensure the best coherence with respect to the individual HFB energy, which is calculated imposing a constraint (via a Lagrange parameter) on a quadrupolar momentum operator. The nuclear shape is described by a parametrization defined as $R(\theta,\varphi,\alpha_{20})$, where α_{20} is the quadrupole component of the nuclear shape, expanded over a Legendre polynomial basis:

$$R(\theta,\varphi,\alpha_{20}) = R_0\lambda(\alpha_{20})^{-1}\left(1+\alpha_{20}\sqrt{\frac{5}{4\pi}}\frac{3\cos(\theta)^2-1}{2}\right). \tag{3}$$

The coefficient $\lambda(\alpha_{20})$ ensures volume conservation according to the deformation

$$\lambda(\alpha_{20}) = \left(1+\frac{3}{4\pi}{\alpha_{20}}^2+\frac{2}{35}\left(\frac{5}{4\pi}\right)^{3/2}{\alpha_{20}}^3\right)^{1/3}. \tag{4}$$

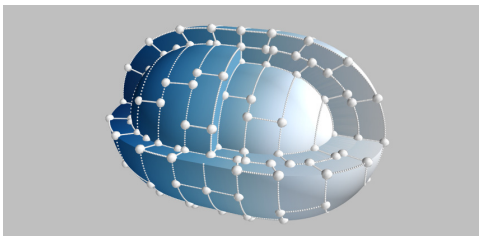

FIG. 2. (Color online) Integration mesh for ^{132}Sn with quadrupole deformation $\tilde{q} = 0.4$. The points and the dotted lines represent vertices and edges of the elementary volumes.

The dimensionless reduced quadrupole momentum, used throughout this work, is defined as

$$\begin{aligned}\tilde{q} &= \frac{2}{A{R_0}^2}\int r^2\rho(\vec{r})\frac{3\cos(\theta)^2-1}{2}d\vec{r}\\ &= \sqrt{\frac{9}{5\pi}}\lambda(\alpha_{20})^{-5}\left(\alpha_{20}+\frac{4}{7}{\alpha_{20}}^2\left(\frac{5}{4\pi}\right)^{1/2}+\frac{6}{7}{\alpha_{20}}^3\frac{5}{4\pi}\right.\\ &\quad\left.+\frac{20}{77}{\alpha_{20}}^4\left(\frac{5}{4\pi}\right)^{3/2}+\frac{53}{1001}{\alpha_{20}}^5\left(\frac{5}{4\pi}\right)^2\right).\end{aligned} \tag{5}$$

At the first order in α_{20}, $\tilde{q} = \sqrt{\frac{9}{5\pi}}\alpha_{20} + o(\alpha_{20})$. The Coulomb interaction energy is then calculated explicitly through numeric integration over the two fragment volume with uniform charge densities $\rho_1 = \frac{Z_1}{V_1}$ and $\rho_2 = \frac{Z_2}{V_2}$:

$$E_{\text{coul}} = \int_{V_1}\int_{V_2}\frac{\rho_1\rho_2}{\|\vec{r}_1-\vec{r}_2\|}d\vec{r}_1 d\vec{r}_2 \tag{6}$$

For the integration, the volume of each fragment is determined by its shape, itself parametrized by its deformation α_{20}. To calculate the Coulomb interaction, an integration mesh needs to be defined for each fragment. Since spherical coordinates (r,θ,φ) are used to define the shape of each fragment, the mesh is also defined in spherical coordinates to avoid numerical errors due to nonconservation of the fragment volume. However, with constant steps in r, θ, and φ, elementary volumes close to the fragment surface are bigger than the inner ones. In order to optimize the computation time, a special mesh is needed. This mesh is conceived to minimize the approximation error by considering elementary cells of similar volumes. The fragment volume is divided into $i_{\max}$ shells of equal thickness and each shell is divided according to θ coordinate. The θ step depends on the shell location and decreases with the shell number. The φ step depends on shell location and θ (see Fig. 2).

For a fixed distance between the surfaces of the two nuclei, the Coulomb energy decreases rapidly while the deformation increases from oblate to prolate shapes (Fig. 3) due to the increasing distance between the two centers of mass.

3. The available energy at scission

The energy balance at scission is calculated from Eq. (1) for all possible fragmentations (around 1000). To reduce

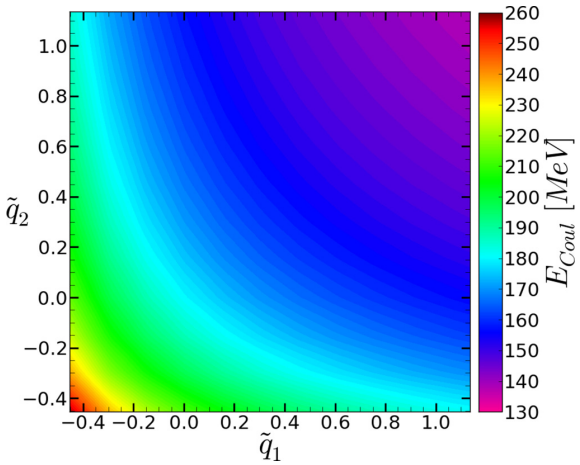

FIG. 3. (Color online) Coulomb energy between two fragments (fragment 1: ^{132}Sn; fragment 2: ^{104}Mo) as a function of their quadrupole deformation.

computational cost, the individual energies are tabulated, leading to a rather small computing time for exploring all possible fragmentations of a fissioning nucleus. As an example, we present the results of the energy balance performed for the thermal neutron-induced fission of ^{235}U. In this case, the excitation energy of the compound nucleus (^{236}U*) is 6.54 MeV. The calculation of the energy balance for all configurations on a single core computer takes around 10 minutes.

Before discussing the potential energy surface of a given fragmentation, we shall outline one preliminary feature. Two opposite effects occur in the available energy balance. On the one hand, the interaction energy decreases regularly from oblate to prolate shapes. On the other hand, the individual energy increases significantly with the fragment deformation far from the ground state. Therefore, two antagonistic effects act as the main drivers of the available energy: the individual energy, which favors ground state deformations, and the interaction energy, which favors prolate shapes.

On the basis of this general trend, the available energy for a given fragmentation reflects the composition of the nuclear structure for each of the two fragments. The available energy of the symmetric splitting (^{118}Pd + ^{118}Pd) is displayed in Fig. 4 and that of the asymmetric splitting (^{132}Sn + ^{104}Mo) is displayed in Fig. 5.

For both fragmentations, the available energy profile is very structured, reflecting the intrinsic energy variations of each nucleus. The available energy maximum for the asymmetric fragmentation (36.5 MeV) is steep, and is found for a spherical ($\tilde{q} = 0$) ^{132}Sn and a largely deformed ($\tilde{q} = 0.45$) ^{104}Mo. In contrast, the corresponding maximum of 28.6 MeV in the symmetric fragmentation is found for a smaller deformation ($\tilde{q} = 0.2$) of ^{118}Pd. The steepness of the energy maximum in the asymmetric fragmentation is due to the doubly magic ^{132}Sn. Therefore, the most energetically favorable fragmentation in thermal neutron-induced fission of ^{235}U is asymmetric due to the nuclear structure of nuclei around ^{132}Sn, compared to the moderated shell effects of soft nuclei around ^{118}Pd.

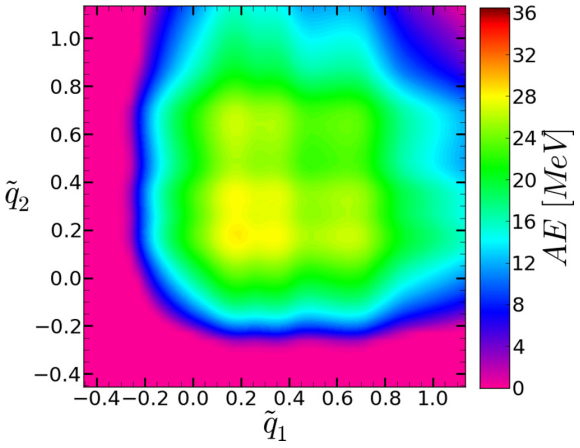

FIG. 4. (Color online) Available energy as a function of the fragments deformation calculated for symmetric (^{118}Pd + ^{118}Pd) fragmentation in the ^{235}U(n_{th}, f) reaction.

The role of shell effects as the main origin of the mass asymmetry is confirmed when looking at the maximum available energy for all possible fragmentations (Fig. 6). The configurations characterized by the largest available energy are favored since, within a statistical interpretation, they give access to the largest phase space. In the case of the thermal neutron-induced fission of ^{235}U, the well-known double-humped structure already appears clearly on the maximum available energy distribution over all fragmentations.

C. A statistical description of scission

In low-energy fission, we assume as Wilkins that a thermal equilibrium is reached at scission. Therefore, the system can be treated as a microcanonical ensemble where all available states of the system are equiprobable.

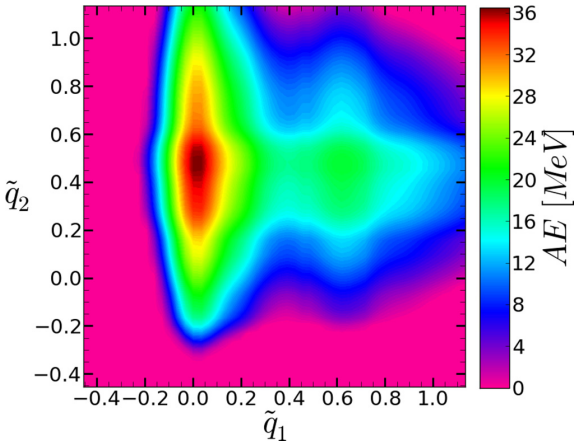

FIG. 5. (Color online) Available energy as a function of the fragments deformation calculated for asymmetric (^{132}Sn + ^{104}Mo) fragmentation in the ^{235}U(n_{th}, f) reaction.

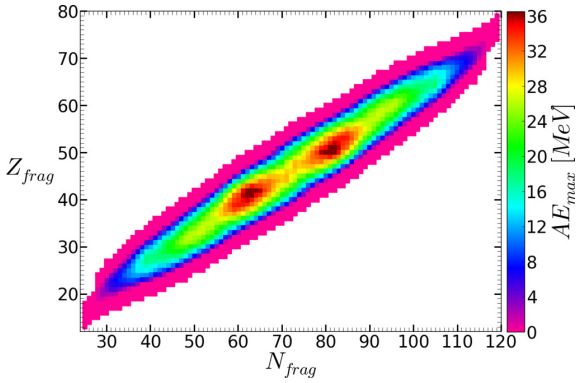

FIG. 6. (Color online) Maximum available energy as a function of the fragment proton and neutron numbers in the ^{235}U(n_{th},f) reaction.

1. The microcanonical description

In this framework, the fission fragment yields can be simply calculated by counting the number of available states at scission for all the different fragmentations. Since the probability for a given fragmentation is related to the available phase space, the knowledge of all exact states is not necessary and only their number for a given configuration is needed. Moreover, each configuration is fully defined by the intrinsic excitation of the two-fragment system as a function of the fragments' deformation. Therefore, only two inputs are required to perform a statistical description of the scission point: the available energy and the state density for each configuration.

The number of available states at scission for a given configuration (π) is assumed to be the product of the state densities of the two isolated fragments (ρ_1 and ρ_2) where a fraction x of the available energy is transferred to fragment 1 while the fraction $(1-x)$ goes to fragment 2:

$$\pi(Z_1,N_1,Z_2,N_2,\tilde{q}_1,\tilde{q}_2,x) = \rho_1(xE_{\text{avail}})\rho_2((1-x)E_{\text{avail}})\delta E^2. \quad (7)$$

Therefore, the probability of a given fragmentation at a given deformation is proportional to π. Finally, the total probability P to obtain a fragmentation is obtained by integrating the number of states π over the two deformation parameters and all energy partitions:

$$P(Z_1,N_1,Z_2,N_2) = \int_{-0.45}^{1.14}\int_{-0.45}^{1.14}\int_0^1 \pi\, dx\, d\tilde{q}_1 d\tilde{q}_2. \quad (8)$$

This probability, normalized to 200%, is the production yield of each fission fragment.

Presently, the calculation of the state density of fission fragments is performed in the framework of a Fermi gas description where the nucleons of a nucleus are considered as a gas of fermions confined in a box. Therefore the state density of a nucleus with intrinsic excitation energy ε is given by [24]

$$\rho(\varepsilon) = \frac{\sqrt{\pi}}{12}\frac{e^{2\sqrt{a\varepsilon}}}{a^{1/4}\varepsilon^{5/4}} \quad (9)$$

This state density is independent of the fragment deformation and only depends on the level density parameter a. In the framework of a Fermi gas model, where only single-particle states are considered, the value $a \approx A/13$, where A is the nuclear mass, is usually taken [25]. However, the comparison with experimental data shows that a level density parameter closer to $A/8$ is better adapted [25]. This difference comes from the presence of collective states that are not counted in a Fermi gas model. Therefore, this latter value has been chosen as a basis for the SPY model. However, It is worth mentioning that using $A/13$ instand of $A/8$ has minor impact on the results.

Since statistical treatment using a Fermi gas state density does not introduce any structure effect, the most probable fragmentation will be mainly defined by the highest energy available for the system. Given this statistical description, the mean value of all relevant observables can be calculated. For a given observable X, its mean value $\langle X\rangle$ is obtained as

$$\langle X\rangle = \int X\pi\, dx\, d\tilde{q}_1 d\tilde{q}_2 \quad (10)$$

The three main fission fragment observables that will be studied in this work are the production yields, the kinetic energy, and the excitation energy, this last observable leading to the number of evaporated neutrons. On this topic, the results will be presented and discussed for the thermal fission of ^{235}U. Then these results will be generalized in Sec. III to many other fissioning systems.

2. Yields

The fragment mass and charge yields in the thermal neutron-induced fission of ^{235}U calculated with SPY are presented in Fig. 7. The SPY model does not include any parameter or any adjustment. Since this model is focused on the scission-point description, the neutron evaporation of the fission fragments is not taken into account in the yield distributions.

The calculated yields present a double-humped distribution peaked around mass 132 and 104 and around corresponding charges 50 and 42. This result reflects the predominant effect of the double magic spherical ^{132}Sn whose high steep potential

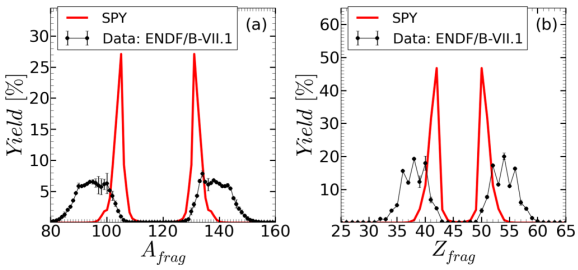

FIG. 7. (Color online) Fragment mass (a) and charge (b) yields in the ^{235}U(n_{th},f) reaction calculated with SPY (in red) compared to evaluated data (post neutron evaporation) from the ENDF/B-VII.1 data library (in black) [26].

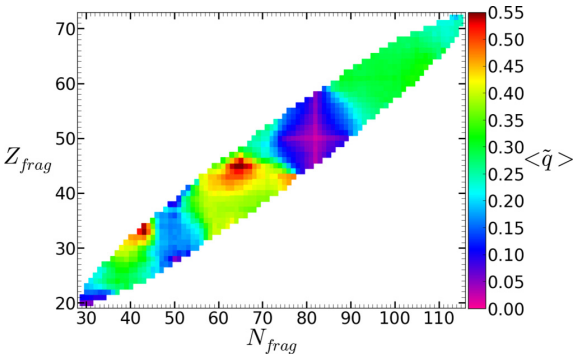

FIG. 8. (Color online) Mean fragment deformation in the ^{235}U(n_{th}, f) reaction.

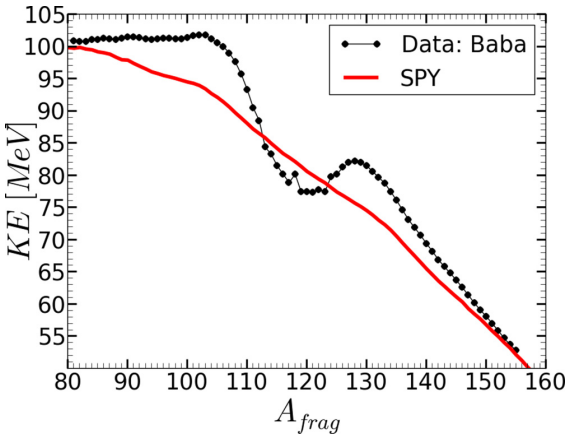

FIG. 9. (Color online) Fission fragment kinetic energy in the ^{235}U(n_{th}, f) reaction calculated with SPY (red line) compared to experimental data from Baba [27] (black line).

provides a very large available energy. Moreover, the soft nucleus ^{104}Mo is very deformed due to Coulomb repulsion, which favors prolate shape. This effect is observed in Fig. 8 where the mean deformation of each fragment is represented. The quadrupole moment varies from 0 (spherical nuclei) up to 0.55 (very prolate nuclei). As expected, oblate shapes are not favored in fission. The symmetric splitting, corresponding to $Z = 46$ and $N = 72$, is disfavored in comparison to configurations involving strong shell effects around ^{132}Sn and its strongly deformed ($\tilde{q} > 0.3$) partner.

Coming back to the fission fragment yields (Fig. 7), the mass and charge yields calculated with SPY are compared to the evaluated data from the ENDF/B-VII.1 library [26]. The experimental distributions are wider than the SPY predictions and span over larger mass and charge ranges. This difference, already observed and discussed by Wilkins *et al.*, is due to two main effects: first, the overestimated impact of shell effects makes double magic nuclei largely favored since they act as an "attractor" for most fragmentations. Second, the use of a Fermi gas state density amplifies this effect due to its exponential behavior with excitation energy.

3. Mean kinetic energy

The kinetic energy of fission fragments is essentially provided by the Coulomb repulsive interaction between the two charged nuclei. Therefore, the importance of a detailed prediction of the fragment deformation at scission is fundamental in order to provide reasonable predictions on the kinetic energy. The SPY results are presented in Fig. 9, together with the experimental data from [27]. The general trend is correctly reproduced since it is mainly driven by the product $Z_1 \times Z_2$. However, the structures seen in experimental data, which are related to strong structure effects, are strongly attenuated in the SPY results. While structure effects are dominant in the yield distributions, they are nearly absent in the kinetic energy distributions. Although the deformation of fragments is taken into account, its impact on kinetic energy distributions is weak.

4. Mean deformations and neutron evaporation

An experimental observable of great importance in thermal fission is the number of evaporated neutrons for each fragment. As already observed by Wilkins *et al.*, the average fragment deformations and evaporated neutrons [28] display similar behavior as can be seen in Fig. 10.

However, the average number of evaporated neutrons is not only due to fragment deformation. Compared to the conclusions reached by Wilkins *et al.*, the SPY model allows for further investigation into the excitation energy in each fragment and, consequently, into the number of evaporated neutrons. This excitation energy has two components. First, each fragment carries a fraction of the available energy at scission under an intrinsic excitation form. Second, since each fragment could undergo deformation at scission, they have a deformation energy defined as the difference between the potential energy at that given deformation and the energy of the ground state. Indeed, the expected saw-tooth form should emerge from the combination of the intrinsic excitation energy and the deformation energy.

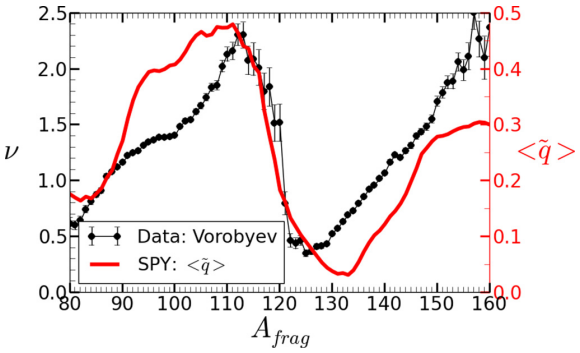

FIG. 10. (Color online) Mean fragment deformation calculated with SPY (red, right scale) in the ^{235}U(n_{th}, f) reaction, compared to the experimental mean number of evaporated neutrons ν (black, left scale) from Vorobyev [28].

A neutron evaporation model could then be used to calculate the number of evaporated neutrons. Since the SPY model only concentrates on the scission phase, the coupling to such a model has not been performed yet. However, as long as the process is energetically possible, we consider that the fission fragments are sequentially deexcited by neutron evaporation. The kinetic energy of evaporated neutrons is randomly taken from theoretical neutron energy spectra (Eq. (7) from [29]) where the temperature of energy spectra depends on excitation energy of fragment (Eq. (5) from [29]). Although the deexcitation cascade of each fragment is not modeled, a mean number of evaporated neutrons could be calculated within this simplified approach and compared to experimental data. The mean number of evaporated neutrons by one fragment in the thermal fission of ^{235}U is estimated at $\overline{\nu} = 2.07$ whereas the experimental total $\overline{\nu} = 2.4$ [30].

D. Impact of different parameters and theoretical choices

Although the SPY model has only one parameter associated with the definition of the scission point, multiple choices on the model ingredients have been made within its development. First, the impact of the scission-point definition will be discussed. Then, the effect of the major choices made within the development of SPY will be presented.

1. On the choice of the scission-point distance

The value of the scission-point distance used in the calculation has a direct and rather trivial first impact on the available energy. The Coulomb energy increases inversely with the distance; i.e. a shorter distance reduces the available energy and increases the kinetic energy of the fragments (Figs. 11 and 12).

However, the scission distance has a lower impact on the fission yields since it only modifies the peak-to-valley ratio without significantly changing the peak position or the maximum yield.

Moreover, second-order effects are more subtle and rather unpredictable because they depend on the sensitivity to the nuclear structure.

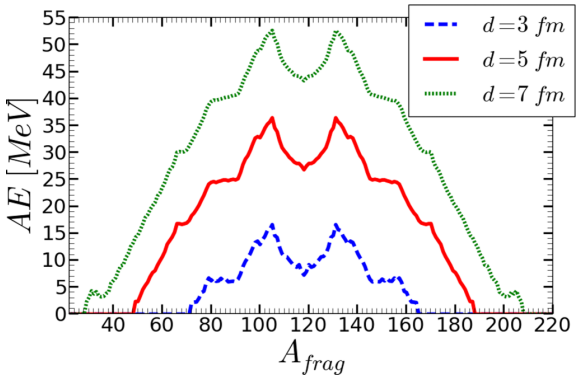

FIG. 11. (Color online) Mean available energy as a function of the fragment mass for different scission distances in the ^{235}U(n_{th}, f) reaction.

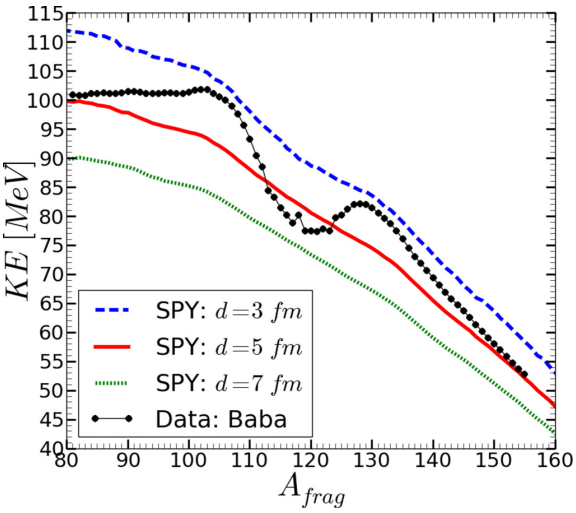

FIG. 12. (Color online) Fragment kinetic energy for different scission distances in the ^{235}U(n_{th}, f) reaction calculated with SPY, compared to experimental data from Baba [27] (black line).

Finally, an increase in sensitivity to the kinetic energy can be observed at short distances by the appearance of small structure effects (Fig. 12). In particular, at a distance of 3 fm, a bump appears in the region of 100–140 mass, similar to that observed experimentally. Moreover, the same tendency is obtained for the number of evaporated neutrons. A decrease in distance leads to lower excitation energy and, consequently, to increased sensitivity to the structure of the fragments.

2. On the statistical ensemble description

The SPY model is based on an absolute energy balance at scission, thus allowing a microcanonical description where the Wilkins model and its relative approach are limited to a canonical one. The results of the two approaches have been compared (Fig. 13).

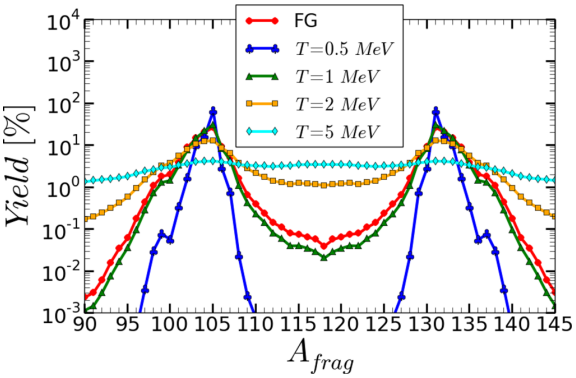

FIG. 13. (Color online) Fragment mass yields in the ^{235}U(n_{th}, f) reaction calculated within the canonical framework at different temperatures and compared to the microcanonical description.

In the canonical description, the probability of a given fragmentation is proportional to the Boltzmann factor e^{-E_A/k_BT}, where T is the temperature of the system. By changing this temperature in the canonical approach, the mass yield distribution could shift from asymmetric at low temperature to symmetric at $T = 5$ MeV (cyan with diamonds curve). SPY predictions based on a microcanonical description are in very good agreement with the canonical description at $T = 1$ MeV, the temperature chosen by Wilkins *et al.* A temperature slightly different of $T = 1.5$ MeV has been chosen in the canonical scission-point model of Ivanyuk *et al.* [31].

E. Evolutions in SPY compared to the Wilkins model

Just like the Wilkins model, SPY is based on the calculation of the energy balance at scission. The use of microscopical potentials is a major improvement in the description of the characteristics of fission fragments up to very exotic nuclei. With the use of a precise double-folding calculation for the Coulomb interaction between the two interacting nuclei, SPY gives access to an absolute value for the available energy at scission with well-defined deformation parameters.

Furthermore, the scission-point starts to have a better definition as we capitalize on advances in theoretical fission modeling and choose it to be within the range conforming to recent microscopic results [2,15].

The access to the absolute available energy allows changing the thermodynamical description and avoiding the inclusion of any temperature parameter. Indeed, Wilkins introduces two temperatures: an intrinsic one to partially wash out the nuclear structure effects and a collective one for the canonical description. We chose to avoid any parameter in order to draw clear answers based on perfect knowledge of the ingredients involved in the model. Furthermore, the microcanonical statistical description allows for the calculation of the distributions and the mean values for all observables.

These improvements were made without loss of computational speed. The calculation of a fissioning system takes a few minutes on a quad-core CPU and a systematic on 3000 fissioning systems takes around one day on a supercomputer using a few tens of CPUs.

III. DISCUSSION ON SEVERAL SPY PREDICTIONS

The model was presented, followed by discussion of the results on the thermal fission of ^{235}U. SPY can now be applied and tested on other fissioning systems. We begin with experimentally known systematics such as the thermal fission of actinides, and then extend the calculations to increasingly exotic systems, up to predictions concerning many nuclei from ytterbium ($Z = 70$) to meitnerium ($Z = 109$), from the proton to the neutron drip line.

A. Fission systematics

After the comparison of the SPY results with experimental data for the thermal fission of uranium, we can generalize to other actinides (Fig. 14). One important feature one can observe is the experimental mass stability of the heavy peak around 140 that is a strong argument for considering

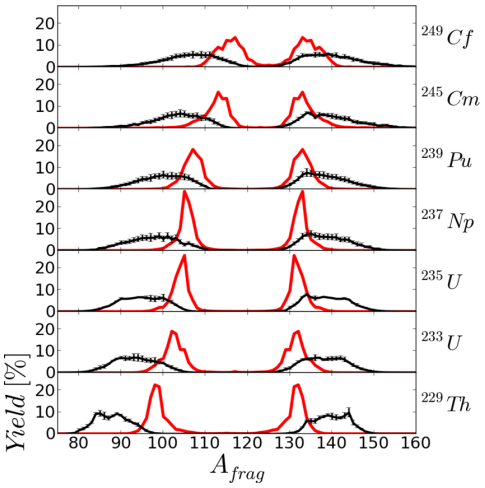

FIG. 14. (Color online) Mass yields in the thermal neutron-induced fission of different actinides calculated with SPY (in red) and compared to evaluated data from the ENDF/B-VII.1 data library [26].

the scission point as a key point for the mass and energy distributions due to the high sensitivity to the structure of the nascent fragments.

The SPY model results present a stability for the heavy peak of the mass distribution around $A = 132$ due to the spherical shell closure. Also, the drawbacks observed and discussed for uraniumare still present for the others actinides: the theoretical heavy peak remains different from the experimental one located at 140, and the width of the theoretical distribution is much narrower. The nuclear structure sensitivity of the SPY model and of the scission-point model in general is too high in the present formalism. To partially solve this problem, Wilkins *et al.* changed the shell correction for ^{132}Sn, introducing a temperature dependence to partially wash out too strong microscopic effects.

Another transition from asymmetric to symmetric charge distributions has been observed for light actinides in Coulomb-induced fission [9] (Fig. 15). SPY globally reproduces this transition, even though it is again shifted by one or two charge units. Beyond a satisfactory qualitative reproduction of existing data, SPY is likely to make predictions when the daughter nuclei exist and are available in the AMEDEE database.

As mentioned, throughout the mass-distribution systematic, the widths are much too narrow by a factor of around 2. Where is the hidden part of the widths? The introduction of a more sophisticated state density could improve the reproduction and, at the same time, reduce the sensitivity to the structure of the fragments included in the HFB individual potentials. Moreover, the absence of dynamic treatment of the fission process can have an impact on the distribution widths.

The width anomaly has a limited impact on energy distributions. The mean total kinetic energy is calculated for all known fissioning systems (red) and compared to the experimental

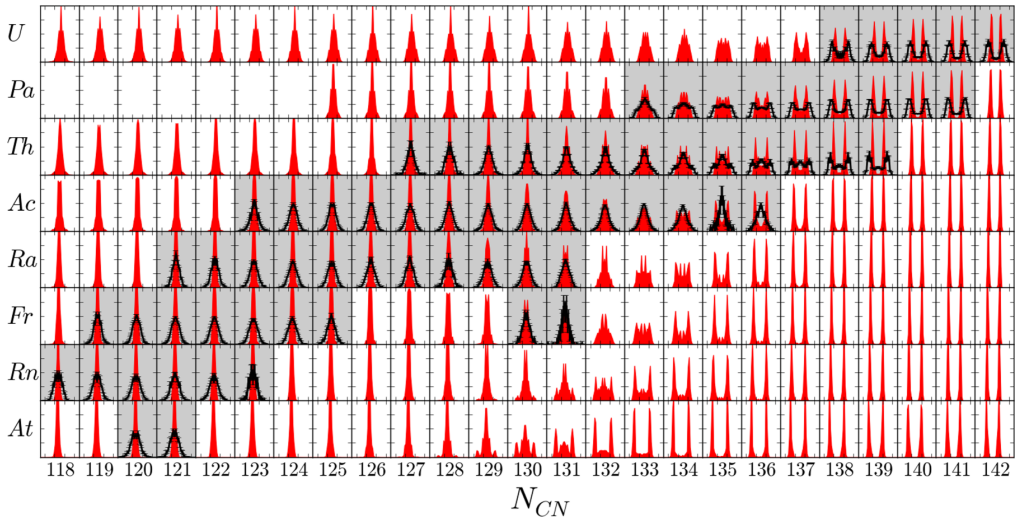

FIG. 15. (Color online) Charge yields for the fission of light actinides region calculated with SPY (in red) compared to data from Schmidt [9] (in black).

results (black) (Fig. 16). A reasonable agreement is achieved for nuclei that present an asymmetric mass-distribution. The results are also compared to the Viola formula [32]. The spread of the experimental points is of the same order of magnitude as the SPY ones. The anomaly on the total kinetic energy (TKE) around 235 MeV for two fermium isotopes and a mendelevium isotope, well above the systematic, is correlated to the preferred formation of two spherical fragments of the same mass. The effect is predicted by SPY but with much weaker amplitude.

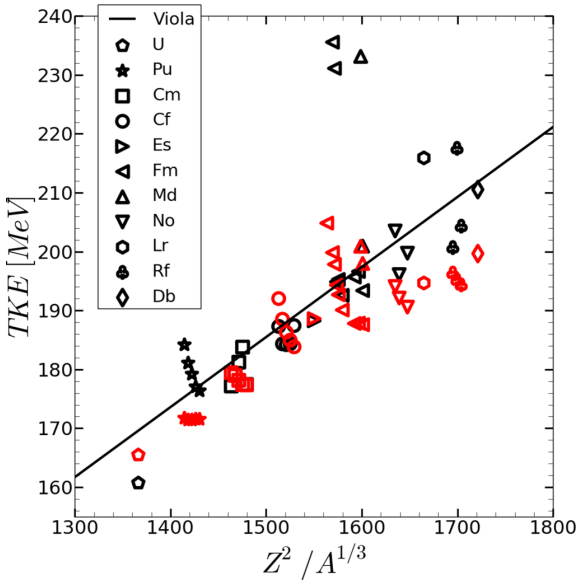

FIG. 16. (Color online) Mean kinetic energy as a function of the compound nucleus fissility calculated with SPY (in red) compared to experimental data [33] (in black) and to the Viola formula [32] (black line).

The SPY model presents satisfactory results to estimate the main variables linked to the last stage of the fission process, without any adjustable parameter. It allows us to find all the major trends of the low-energy fission observables. Therefore, with good confidence, it can be used in areas of the nuclear chart for which there is no experimental result, at least from a qualitative point of view, in particular with respect to the asymmetric or symmetric feature of the fission fragment distributions.

B. Up to exotic nuclei

This study has been generalized to all known and unknown nuclei from ytterbium to superheavy elements (Fig. 17). A peak analysis has been performed for each mass distribution in order to extract the peak multiplicity. This simple procedure allows identifying the zone of transition between symmetric distributions with one peak (yellow), asymmetric ones with two peaks (green) and some exotic distributions with three

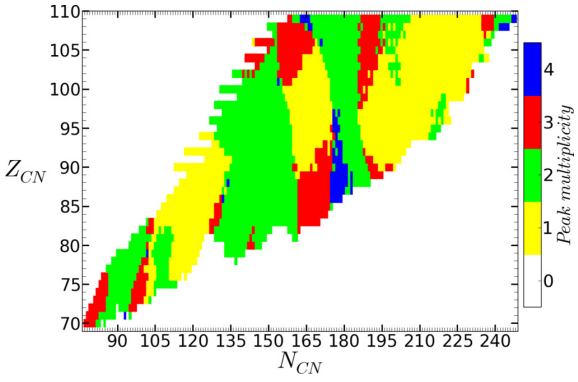

FIG. 17. (Color online) Peak multiplicity in the mass yields as a function of the compound nucleus for an excitation energy of 8 MeV.

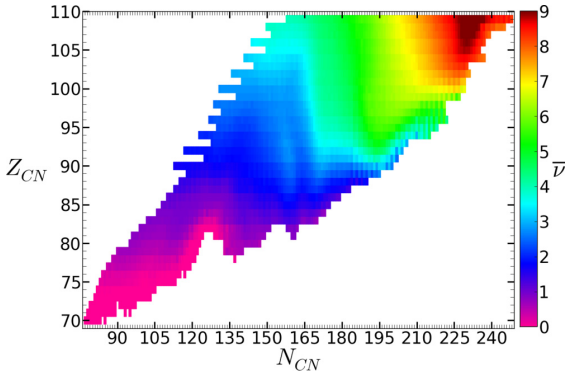

FIG. 18. (Color online) Estimated mean prompt neutron multiplicity per fragment as a function of the compound nucleus for an excitation energy of 8 MeV.

peaks (red), resulting from a symmetric-asymmetric competition, or even four peaks (blue), due to the competition between two asymmetric modes.

The large structures in the peak multiplicity mainly depend on the compound nucleus neutron number inducing mostly vertical structures in Fig. 17. This proves the predominance of the neutron shell closures in the structure of the fission fragment distributions. However, for light nuclei with less than 130 neutrons, the spherical closed neutron shell $N = 50$ does not drive the fission mode as in the fission of ^{180}Hg [16]. In this region, the fission modes are instead driven by deformed shell effects.

The blue area with multiplicity 4 is notable. This doubly asymmetric mode for very neutron-rich nuclei could be the source of the rare-earth production in collapsing neutron stars [12].

The systematic of the total kinetic energy presents a dominant evolution with the proton number of the compound nuclei due to the proton-number dependence of the Coulomb interaction.

The predictions on the excitation energy provided by SPY allows for the systematic calculation of the mean number of evaporated neutrons for each system in the gross approximation explained in Sec. II C 4 (Fig. 18). There are two general dependences. The first one lies in the increasing number of evaporated neutrons for the very neutron-rich nuclei. It has to be correlated with the decreasing separation energy for neutron-rich fragments produced by these nuclei. The second one lies in the general increase in this number with the mass of the compound nuclei. It is simply due to an increase in available energy with the nucleon number of the compound nucleus. This gross evaluation of the number of evaporated neutrons for all existing nuclei has already been used in [12].

IV. CONCLUSIONS AND PERSPECTIVES

Taking advantage of massive calculations to generate a nuclear database including the individual potential of more than 7000 nuclei determined by HFB calculations with the Gogny force, a new statistical scission-point model, called SPY, has been developed. SPY uses the richness and high predictive power of microscopy in a rather simple theoretical framework, leading to the prediction of the most important fission fragment properties, over a huge range of fissioning systems with a very limited computing cost. The model has been presented starting with the careful absolute calculation of the energy available at scission followed by the statistical description used to calculate the major observables associated with the fission fragments.

The SPY results have been compared to the observables measured in the thermal fission of ^{235}U. Since SPY is based on an absolute calculation of the energy available at the scission point, a rather satisfactory reproduction of the evolution of the total kinetic energy is obtained. The absolute available energies are used in a microcanonical description to determine the probability of all possible fragmentations. The general trend of the yield and the mean number of evaporated neutrons are qualitatively reproduced taking into account the absence of any adjustment in the modelization of such a complex process.

The model has been compared with various experimental systematics. In particular, SPY is able to reproduce the general trend of the mass and charge yields transition from asymmetry to symmetry and explains the stability of the heavy peak in the asymmetric regions. Moreover, the model allows for rather satisfactory reproduction of the experimental total kinetic energies. Finally, the model has also been used with success to interpret the fission of exotic mercury isotopes [16] and to predict fission yields for nuclei involved in the coalescence of neutron stars [12].

The model could be enriched in order to study its limits. The width of the mass distribution is too narrow and a shift of a few masses is present between the observed and predicted peak positions. The actual definition of the scission point is proven to be very efficient in performing the calculations but may be criticized due to its simplicity. However, we now have access to full microscopic calculations close to scission, which are actually generalized to all nuclei. They could lead to a better definition of the scission point. In particular, the actual statistical description is based on the basic assumption that the system state density at scission is the product of the state densities of the two nuclei. It has to be verified in the specific microscopical study of the scission point.

Furthermore, the Fermi gas state density is a poor approximation of the real nuclear one. It should be replaced by a microscopic state density calculated in the same framework as the individual potentials. The microscopical effects induced by realistic nuclear densities, will partially counterbalance the structural effects (shell closure and pairing effects) induced by the individual potential. This development of state density calculations for all nuclear deformations and over the whole nuclear chart is a major challenge that will specifically interest the nuclear reaction community, no matter how time-consuming this may seem [34].

ACKNOWLEDGMENT

The authors acknowledge the support and the framework of the COPHYNU (COllaboration between NUclear PHYsics divisions of CEA), within which this work was performed.

[1] B. D. Wilkins, E. P. Steinberg, and R. R. Chasman, Phys. Rev. C **14**, 1832 (1976).
[2] H. Goutte, J. F. Berger, P. Casoli, and D. Gogny, Phys. Rev. C **71**, 024316 (2005).
[3] P. Moller, D. G. Madland, A. J. Sierk, and A. Iwamoto, Nature (London) **409**, 785 (2001).
[4] M. Warda, A. Staszczak, and W. Nazarewicz, Phys. Rev. C **86**, 024601 (2012).
[5] K.-H. Schmidt, B. Jurado, and C. Amouroux, NEA JEFF Report 24, 2014 (unpublished).
[6] A. N. Andreyev, J. Elseviers, M. Huyse, P. Van Duppen, S. Antalic, A. Barzakh, N. Bree, T. E. Cocolios, V. F. Comas, J. Diriken *et al.*, Phys. Rev. Lett. **105**, 252502 (2010).
[7] Y. T. Oganessian, F. S. Abdullin, P. D. Bailey, D. E. Benker, M. E. Bennett, S. N. Dmitriev, J. G. Ezold, J. H. Hamilton, R. A. Henderson, M. G. Itkis *et al.*, Phys. Rev. Lett. **104**, 142502 (2010).
[8] Y. T. Oganessian, F. S. Abdullin, S. N. Dmitriev, J. M. Gostic, J. H. Hamilton, R. A. Henderson, M. G. Itkis, K. J. Moody, A. N. Polyakov, A. V. Ramayya *et al.*, Phys. Rev. Lett. **108**, 022502 (2012).
[9] K.-H. Schmidt, S. Steinhauser, C. Bockstiegel, A. Grewe, A. Heinz, A. Junghans, J. Benlliure, H.-G. Clerc, M. de Jong, J. Muller *et al.*, Nucl. Phys. A **665**, 221 (2000).
[10] S. Hilaire and M. Girod, Eur. Phys. J. A **33**, 237 (2007).
[11] J. Dechargé and D. Gogny, Phys. Rev. C **21**, 1568 (1980).
[12] S. Goriely, J.-L. Sida, J.-F. Lemaître, S. Panebianco, N. Dubray, S. Hilaire, A. Bauswein, and H.-T. Janka, Phys. Rev. Lett. **111**, 242502 (2013).
[13] W. Younes and D. Gogny, Phys. Rev. Lett. **107**, 132501 (2011).
[14] L. Bonneau, P. Quentin, and I. N. Mikhailov, Phys. Rev. C **75**, 064313 (2007).
[15] N. Dubray, H. Goutte, and J.-P. Delaroche, Phys. Rev. C **77**, 014310 (2008).
[16] S. Panebianco, J.-L. Sida, H. Goutte, J.-F. Lemaître, N. Dubray, and S. Hilaire, Phys. Rev. C **86**, 064601 (2012).
[17] P. Moller, J. Nix, W. Myers, and W. Swiatecki, At. Data .Nucl. Data Tables **59**, 185 (1995).
[18] http://www-phynu.cea.fr/HFB-Gogny.htm.
[19] T. R. Rodríguez, A. Arzhanov, and G. Martínez-Pinedo, Phys. Rev. C **91**, 044315 (2015).
[20] S. Goriely, S. Hilaire, M. Girod, and S. Péru, Phys. Rev. Lett. **102**, 242501 (2009).
[21] K. Krane, *Introductory Nuclear Physics* (Wiley, New York, 1988).
[22] R. Hasse and W. Myers, *Geometrical Relationships of Macroscopic Nuclear Physics*, Springer Series in Nuclear and Particle Physics (Springer-Verlag, Berlin, 1988).
[23] J. Blocki, J. Randrup, W. Swiatecki, and C. Tsang, Ann. Phys. (N.Y.) **105**, 427 (1977).
[24] H. A. Bethe, Phys. Rev. **50**, 332 (1936).
[25] J. Toke and W. Swiatecki, Nucl. Phys. A **372**, 141 (1981).
[26] M. Chadwick, M. Herman, P. Obloinsk, M. Dunn, Y. Danon, A. Kahler, D. Smith, B. Pritychenko, G. Arbanas, R. Arcilla *et al.*, Nucl. Data Sheets **112**, 2887 (2011), special issue on the ENDF/B-VII.1 library.
[27] H. Baba, T. Saito, N. Takahashi, A. Yokoyama, T. Miyauchi, S. Mori, D. Yano, T. Hakoda, K. Takamiya, K. Nakanishi *et al.*, J. Nucl. Sci. Technol. **34**, 871 (1997).
[28] A. S. Vorobyev, O. A. Shcherbakov, A. M. Gagarski, G. V. Val'ski, and G. A. Petrov, EPJ Web Conf. **8**, 03004 (2010).
[29] T. Kawano, P. Talou, I. Stetcu, and M. Chadwick, Nucl. Phys. A **913**, 51 (2013).
[30] L. I. Prokhorova, R. E. Bagdasarov, I. I. Kotukhov, V. G. Nesterov, B. Nurpeisov, G. N. Smirenkin, and Yu. M. Turchin, Atomnaya Energiya **30**, 250 (1971) [Sov. At. Energy **30**, 307 (1971)].
[31] F. A. Ivanyuk, S. Chiba, and Y. Aritomo, Phys. Rev. C **90**, 054607 (2014).
[32] V. E. Viola, K. Kwiatkowski, and M. Walker, Phys. Rev. C **31**, 1550 (1985).
[33] D. C. Hoffman, in *Proceedings of the International Conference on Actinides, Santa Fe, New Mexico*, September 1993 [J. Alloys Compd. **213–214**, 67 (1994)].
[34] J.-F. Lemaître, S. Hilaire, S. Panebianco, and J.-L. Sida, Acta Phys. Pol. B **46**, 585 (2015).

3.4 La fission des terres rares

L'article qui suit [47] montre comme l'approche théorique extrêmement simplifié que constitue le modèle de point de scission SPY peut devenir un outil prédictif puissant dans des contextes bien loins du champ d'application le plus courant. En effet, comme indiqué à la fin du chapitre 3.3, le pouvoir descriptif de SPY n'est pas comparable aux modèles basés sur des ingrédients plus phénoménologiques. Cependant, il permet d'effectuer des études systématiques dans un domaine très étendu (aussi étendu que le domaine couvert par les calculs microscopiques qu'il utilise en données d'entrée), d'explorer des régions inaccessibles à d'autres types de modèles, ce qui est le cas dans la région du Hg-180, ou même inaccessibles à l'investigation expérimentale. C'est le cas de la region des terres rares mais dans un domaine extrêmement exotique, à la limite de la *drip line* neutron.

Ce travail est le fruit plutôt fortuit d'une rencontre avec Stéphane Goriely de l'Université Libre de Bruxelles et d'un séminaire qu'il a tenu en 2012 dans mon laboratoire. Le sujet d'étude présenté lors de ce séminaire portait sur la modélisation des nombreux (et très complexes) phénomènes et mécanismes astrophysiques nécessaires pour expliquer la production des noyaux stables et riches en neutrons plus lourds que le fer (ce qu'on appelle le *r-process*). Les abondances de ces noyaux peuvent être mesurées dans des nombreux systèmes stellaires, dont le système solaire (à ce propos, dans un domaine bien loin de mes propres compétences, j'ai pu apprécier un article de synthèse de grande qualité [48]). La discussion qui a suivi le séminaire a permis de saisir l'importance des modèles nucléaires utilisés dans le cadre de calculs de *r-process* dans la coalescence d'étoiles à neutrons, et tout particulièrement le modèle de fission nucléaire. En effet, ce milieu astrophysique présente un grand nombre de neutrons libres qui sont très rapidement capturés de manière massive pour synthétiser tous les noyaux jusqu'à la drip line neutron. Ceux noyaux décroissent ensuite par émission de β et alimentent la région avec $Z \geqslant 103$ et proche de la drip line neutron où la fission spontanée ou induite joue un rôle clé dans la production des éléments de masses comprises entre 110 et 170.

Le modèle de fission utilisé jusqu'à là par Stéphane Goriely était basé sur une approche purement phénoménologique où les distributions des fragments de fission étaient calculées de manière paramétrique en extrapolant (bien loin à vrai dire...) à partir des données expérimentales des actinides. Ces modèles, dont en particulier GEF [15], appliqués à ce cas particulier très exotique, étaient plutôt déficients dans la reproduction des abondances solaire dans la zone de masse entre 110 et 170. Nous avons donc voulu profiter du pouvoir prédictif de SPY dans une région où aucune donnée expérimentale n'existe et où les extrapolations de modèles phénoménologiques ne semblent pas totalement justifiées. Le résultat de ce travail a montré que l'accord avec les abondances solaires dans la zone caractéristique du *r-process* entre la masse 140 et la masse 185 est bien plus satisfaisant lorsque l'on repose sur les prédictions de SPY, et ce indépendamment des taux de réaction nucléaires ou des modèles de décroissance beta utilisés.

Ce résultat très marquant est dû au caractère totalement singulier, jamais observé jusqu'alors, des distributions calculées avec SPY dans la région des pro-géniteurs des fragments de masse comprise entre 110 et 170, que l'on appelle les terres rares. Ce comportement consiste en une distribution doublement asymétrique des fragments de fission, comportement étonnant car tous les noyaux connus expérimentalement fissionnent de manière symétrique ou simplement asymétrique. Par ailleurs, ce comportement a été confirmé par des calculs plus microscopiques qui laissent entrevoir deux « modes » de fission asymétriques, un mode avec un fragment lourd en un fragment léger et un mode avec un fragment très lourd avec un très léger, le mode symétrique étant inhibé par une barrière de potentiel.

PRL 111, 242502 (2013) PHYSICAL REVIEW LETTERS week ending 13 DECEMBER 2013

New Fission Fragment Distributions and *r*-Process Origin of the Rare-Earth Elements

S. Goriely,[1] J.-L. Sida,[2] J.-F. Lemaître,[2] S. Panebianco,[2] N. Dubray,[3] S. Hilaire,[3] A. Bauswein,[4,5] and H.-T. Janka[5]

[1]*Institut d'Astronomie et d'Astrophysique, CP-226, Université Libre de Bruxelles, 1050 Brussels, Belgium*
[2]*C.E.A. Saclay, Irfu/Service de Physique Nucléaire, 91191 Gif-sur-Yvette, France*
[3]*CEA, DAM, DIF, F-91297 Arpajon, France*
[4]*Department of Physics, Aristotle University of Thessaloniki, 54124 Thessaloniki, Greece*
[5]*Max-Planck-Institut für Astrophysik, Postfach 1317, 85741 Garching, Germany*

(Received 10 September 2013; revised manuscript received 26 October 2013; published 9 December 2013)

3

Neutron star (NS) merger ejecta offer a viable site for the production of heavy *r*-process elements with nuclear mass numbers $A \gtrsim 140$. The crucial role of fission recycling is responsible for the robustness of this site against many astrophysical uncertainties, but calculations sensitively depend on nuclear physics. In particular, the fission fragment yields determine the creation of $110 \lesssim A \lesssim 170$ nuclei. Here, we apply a new scission-point model, called SPY, to derive the fission fragment distribution (FFD) of all relevant neutron-rich, fissioning nuclei. The model predicts a doubly asymmetric FFD in the abundant $A \simeq 278$ mass region that is responsible for the final recycling of the fissioning material. Using ejecta conditions based on relativistic NS merger calculations, we show that this specific FFD leads to a production of the $A \simeq 165$ rare-earth peak that is nicely compatible with the abundance patterns in the Sun and metal-poor stars. This new finding further strengthens the case of NS mergers as possible dominant origin of *r* nuclei with $A \gtrsim 140$.

DOI: 10.1103/PhysRevLett.111.242502 PACS numbers: 24.75.+i, 25.85.−w, 26.30.Hj, 26.60.Gj

Introduction.—The rapid neutron-capture process (*r* process) of stellar nucleosynthesis explains the production of the stable (and some long-lived radioactive) neutron-rich nuclides heavier than iron that are observed in stars of various metallicities and in the Solar System (see review of [1]). While *r*-process theory has made progress in understanding possible mechanisms that could be at the origin of the Solar System composition, the cosmic site(s) of the *r* process has (have) not been identified yet, and the astrophysical sources and specific conditions in which the *r* process takes place are still among the most longstanding mysteries of nuclear astrophysics.

Progress in modeling core-collapse supernovae (SNe) and γ-ray bursts has raised a lot of excitement about the so-called neutrino-driven wind environment [1–3]. While the light *r* elements up to the second abundance peak ($A \sim 130$) might be produced in such outflows of nascent neutron stars (NSs) [2,4], the extreme conditions required for stronger *r* processing have so far not been obtained in the most sophisticated SN models [3]. An alternative to the *r* process in high-temperature SN environments is the decompression of cold neutronized matter from violent collisions of binary NSs or NSs with companion black holes. While such a connection was suggested decades ago [5–7] and decompressed NS matter was found to be favorable for strong *r* processing [8], only more recent and increasingly sophisticated hydrodynamic simulations could determine the ejecta mass to be $\sim 10^{-3}$–$10^{-2} M_\odot$ [9–18]. This mass, combined with the predicted astrophysical event rate ($\sim 10^{-5}$ yr^{-1} in the Milky Way [19,20]) can account for the majority of *r* material in our Galaxy [10,12,17,18,21,22]. Nearly all of the ejecta are converted to *r*-process nuclei, whose radioactive decay heating leads to potentially observable electromagnetic radiation in the optical and infrared bands [22,23] with 100–1000 times fainter peak brightnesses than those of typical SNe and durations of only days [13,17,18,24–26]. These "macronovae" [27] or "kilonovae" [22] are intensely searched for (with a recent, possible first success [28,29]) and their unambiguous discovery would constitute the first detection of *r* material *in situ*.

In this specific *r*-process scenario, the number of free neutrons per seed nucleus reach a few hundreds. With such a neutron richness, fission plays a fundamental role by recycling the matter during the neutron irradiation and by shaping the final *r*-abundance distribution in the $110 \lesssim A \lesssim 170$ mass region at the end of the neutron irradiation. The final composition of the ejecta is then rather insensitive to details of the initial abundances and the astrophysical conditions, in particular, the mass ratio of the two NSs, the quantity of matter ejected, and the equation of state (EOS) [17,18,30]. This robustness, which is compatible with the uniform, solarlike abundance pattern of the rare-earth elements observed in metal-poor stars [31], might point to the creation of these elements by fission recycling in NS merger (NSM) ejecta.

However, the estimated abundance distribution remains sensitive to the adopted nuclear models. The ejecta are composed almost exclusively of $A > 140$ nuclei, and in particular, the $A \simeq 195$ third *r*-process peak appears in proportions similar to those observed in the Solar System, deviations resulting essentially from the still

difficult task to predict neutron capture and β-decay rates for exotic neutron-rich nuclei. The situation for the lighter $110 \lesssim A \lesssim 170$ species has been rather unclear up to now and extremely dependent on fission properties, including, in particular, the fission fragment distribution (FFD). In the present Letter, we apply a new state-of-the-art scission-point model, called SPY, to the determination of the FFD of all neutron-rich fissioning nuclei of relevance during the r-process nucleosynthesis and analyze its impact on the r-process abundance distribution.

NS merger simulations and the r-process.—Our NSM simulations were performed with a general relativistic smoothed particle hydrodynamics scheme [18,32,33] representing the fluid by a set of particles with constant rest mass, whose properties were evolved according to Lagrangian hydrodynamics, conserving the electron fraction of fluid elements. The Einstein field equations were solved assuming a conformally flat spatial metric. The r-abundance distributions resulting from binary simulations with different mass ratios or different EOSs are virtually identical [18]. For this reason, in the present analysis only symmetric $1.35M_\odot$–$1.35M_\odot$ systems with the DD2 EOS [34,35], including thermal effects and a resolution of $\sim$550 000 particles, are considered. The mass ejected by the NSM is $\sim 3 \times 10^{-3} M_\odot$. In [18,33], more details are given on gross properties of the ejecta, the influence of the EOS, and the postprocessing for the nucleosynthesis calculations. Note that the $1.35M_\odot$–$1.35M_\odot$ case is of particular interest since, according to population synthesis studies and pulsar observations, it represents the most abundant systems [36].

Our nuclear network calculations were performed as in [17,37], where the reaction network, temperature postprocessing, inclusion of pressure feedback by nuclear heating, and the density extrapolation beyond the end of the hydrodynamical simulations are described. The reaction network includes all 5000 species from protons up to $Z = 110$ that lie between the valley of β stability and the neutron-drip line. All fusion reactions on light elements as well as radiative neutron captures, photodisintegrations, α and β decays, and fission processes, are included. The corresponding rates are based on experimental data whenever available or on theoretical predictions otherwise, as obtained from the BRUSLIB nuclear astrophysics library [38]. In particular, the reaction rates are estimated with the TALYS code [39,40] on the basis of the Skyrme Hartree-Fock-Bogolyubov (HFB) nuclear mass model, HFB-21 [41], and the β decays with the gross theory 2 (GT2) [42], employing the same HFB-21 Q values.

The neutron-induced, photo-induced, β-delayed, and spontaneous fission rates are estimated on the basis of the HFB-14 fission paths [43]. The neutron- and photo-induced fission rates were calculated with the TALYS code for all nuclei with $90 \leq Z \leq 110$ [44]. Similarly, the β-delayed and spontaneous fission rates are estimated with the same TALYS fission barrier penetration calculation. The β-delayed fission rate takes into account the full competition between the fission, neutron, and photon channels, weighted by the population probability given by the β-decay strength function [45]. The main fission regions by one of the four fission processes are illustrated in Fig. 1(a).

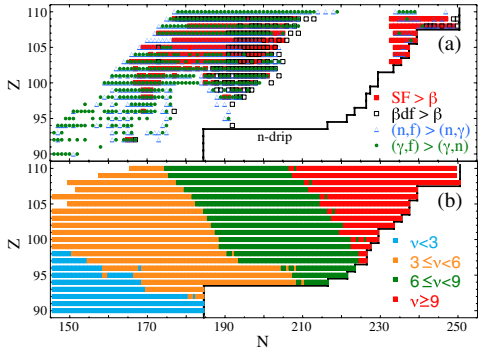

FIG. 1 (color online). (a) Dominant fission regions in the (N, Z) plane. Nuclei with spontaneous fission being faster than β decays are shown by full squares, those with β-delayed fission faster than β decays by open squares, those with neutron-induced fission faster than radiative neutron capture at $T = 10^9$ K by open triangles, and those for which photo-fission at $T = 10^9$ K is faster than photo-neutron emission by closed circles. For $Z = 110$, β-decay processes are not calculated. (b) SPY predictions of the average number of emitted neutrons for each fissioning nucleus in the (N, Z) plane.

SPY fission fragment distribution.—To study precisely the impact of the nascent fragment nuclear structure on the mass distribution, a renewed statistical scission-point model, called SPY, was developed [46]. It consists of a parameter-free approach based on up-to-date microscopic ingredients extracted with a mean-field description using the effective nucleon-nucleon Gogny interaction [47]. This renewed version of the Wilkins fission model [48] estimates first the absolute energy available for all possible fragmentations at the scission point for a given fissioning nucleus [46]. The main ingredient in these calculations is the individual potential energy of each fission fragment as a function of its axial deformation, as compiled in the AMEDEE database [47] for more than 8000 nuclei. Once the available energies are calculated for each fragmentation, a microcanonical description including nuclear Fermi gas state densities is used to determine the main fission fragment observables, more particularly, mass and charge yields, kinetic energy, and excitation energy of the fragments [49]. The number of evaporated neutrons is deduced from the mean excitation energy of each fragment. The scission-point models [48] have shown their ability to reproduce the general trends of the fission yields for actinides, and the SPY model has proven its capability to

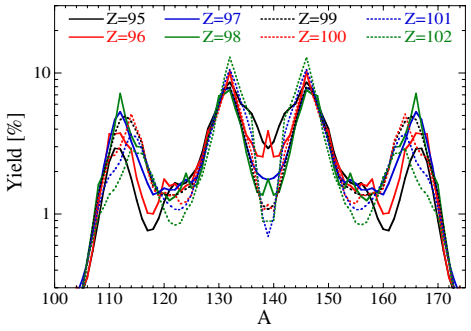

FIG. 2 (color online). FFDs from the SPY model for eight $A = 278$ isobars.

describe them up to exotic nuclei in the study of the mercury isotopes [46].

SPY has now been applied to all the neutron-rich nuclei of relevance for *r*-process nucleosynthesis. It is found that the $A \simeq 278$ fissioning nuclei, which are main progenitors of the $110 \lesssim A \lesssim 170$ nuclei in the decompression of NS matter, present an unexpected doubly asymmetric fission mode with a characteristic four-hump pattern, as illustrated in Fig. 2. Such fragment distributions have never been observed experimentally and can be traced back to the predicted potential energies at large deformations of the neutron-rich fragments favored by the $A \simeq 278$ fission. The two asymmetric fission modes can also be seen on the potential energy surface (Fig. 3) obtained from a detailed microscopic calculation [50] for ^{278}Cf in the deformation subspace (elongation $\langle \hat{Q}_{20} \rangle$, asymmetry $\langle \hat{Q}_{30} \rangle$). This calculation uses a state-of-the-art mean-field model with the Gogny interaction. The two fission valleys indicated by arrows in Fig. 3 lead to asymmetries similar to the distributions presented in Fig. 2 obtained with SPY. The

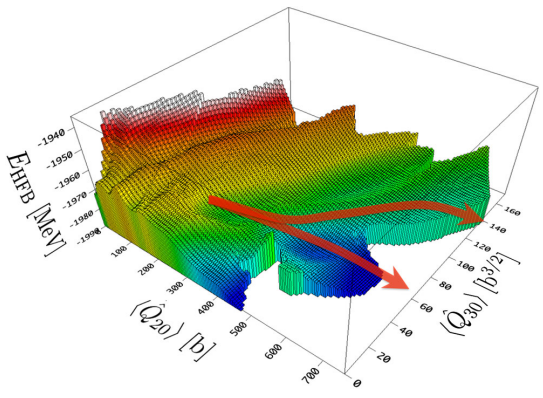

FIG. 3 (color online). ^{278}Cf potential energy surface as a function of the quadrupole $\langle \hat{Q}_{20} \rangle$ and octupole $\langle \hat{Q}_{30} \rangle$ deformations. Both asymmetric fission valleys are depicted by the red arrows.

symmetric valley, corresponding to a nil octupole moment, is disfavored by a smaller barrier transmission probability linked to the presence of a barrier, hidden in this subspace by a discontinuity [51].

Finally, we show in Fig. 1(b), the SPY prediction of the average number of evaporated neutrons for each spontaneously fissioning nucleus. This average number is seen to reach values of about four for the $A \simeq 278$ isobars and maximum values of $\sim$14 for the heaviest $Z \simeq 110$ nuclei lying at the neutron drip line.

Nucleosynthesis calculations.—Due to the specific initial conditions of high neutron densities (typically $N_n \simeq 10^{33-35}$ cm^{-3} at the drip density), the nuclear flow during most of the neutron irradiation will follow the neutron-drip line and produce in milliseconds, the heaviest drip-line nuclei. However, for drip-line nuclei with $Z \geq 103$, neutron-induced and spontaneous fission become efficient [Fig. 1(a)] prohibiting the formation of super-heavy nuclei and recycling the heavy material into lighter fragments, which restart capturing the free neutrons. Fission recycling can take place up to three times before the neutrons are exhausted, depending on the expansion time scales. When the neutron density drops below some 10^{20} cm^{-3}, the time scale of neutron capture becomes longer than a few seconds, and the nuclear flow is dominated by β decays back to the stability line (as well as fission and α decay for the heaviest species). The final abundance distribution of the $3 \times 10^{-3} M_\odot$ of ejecta during the NSM is compared with the Solar System composition in Fig. 4. The similarity between the solar abundance pattern and the prediction in the $140 \lesssim A \lesssim 180$ region is remarkable and strongly suggests that this pattern constitutes the standard signature of *r* processing under fission conditions.

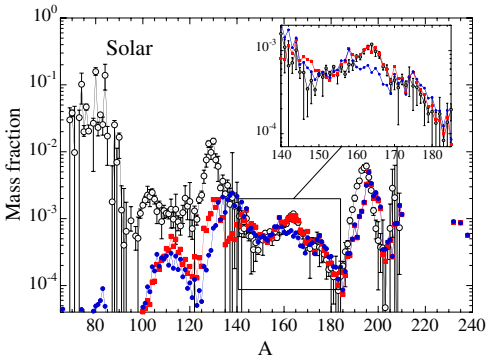

FIG. 4 (color online). Final abundance distribution vs atomic mass for ejecta from 1.35–1.35 $M_\odot$ NS mergers. The red squares are for the newly derived SPY predictions of the FFDs and the blue circles for essentially symmetric distributions based on the 2013 GEF model [52]. The abundances are compared with the solar ones [56] (dotted circles). The insert zooms on the rare-earth elements.

The $110 \lesssim A \lesssim 170$ nuclei originate exclusively from the spontaneous and β-delayed fission recycling that takes place in the $A \simeq 278$ region at the time all neutrons have been captured and the β decays dominate the nuclear flow. The $A \simeq 278$ isobars correspond to the dominant abundance peak in the actinide region during the irradiation phase due to the turn-off point at the $N = 184$ drip-line shell closure and the bottleneck created by β decays along the nuclear flow. The nuclei that β decay along the $A = 278$ isobar fission asymmetrically according to the SPY FFD model, as illustrated in Fig. 2, leading to a similar quadruple hump pattern visible in Fig. 4 (red squares). The asymmetric $A \simeq 165$ peak in the FFD (Fig. 2) can consequently explain the origin of the rare-earth peak by the r process, in contrast to more phenomenological FFD models [45], which predict symmetric mass yields for the $A \simeq 278$ fissioning nuclei and hence, an underproduction of the $A \simeq 165$ rare-earth nuclei (cf. Fig. 4 in [17]). An essentially symmetric FFD is also predicted by the 2013 version of the semiempirical GEF model [52], also leading to an underproduction of rare-earth elements, as shown in Fig. 4 and also discussed in Ref. [53]. Our NSM scenario thus offers a consistent explanation of the creation of the rare-earth elements connected to r processing, different from alternative suggestions for production sites of these elements, e.g., at freeze-out conditions in high-entropy r-process environments [54] with all the associated astrophysical problems [1–3].

In addition, with the SPY FFDs the r-abundance distribution is rather robust for different sets of fission barriers. As explained above, the $110 \lesssim A \lesssim 170$ abundances originate essentially from the fission of the nuclei that β decay along the $A \simeq 278$ isobars at the end of the neutron irradiation. The corresponding fissioning nuclei are all predicted by the SPY model to fission basically with the same doubly asymmetric distribution (Fig. 2), leading to similar r distributions, independent of the fissioning element along the isobar.

The emission of prompt neutrons also affects the r-abundance distribution. According to the SPY model, the fission of the most abundant nuclei around $A = 278$ is accompanied with the emission of typically four neutrons [Fig. 1(b)]. These neutrons are mainly recaptured by the abundant nuclei forming the $N = 126$ peak. For this reason, not only the abundance distribution for $A \lesssim 160$ is slightly shifted to lower masses, but the abundant $A = 196$ peak is shifted to higher masses by a few units. The impact, however, remains small due to the small average number of emitted neutrons. This even improves the agreement with the solar distribution for $A \simeq 145$ and $A \simeq 172$ nuclei but distorts slightly the $A = 195$ peak. However, the global abundance pattern for $A > 140$, in particular the $A = 195$ peak, can also be affected by the still uncertain neutron-capture and β-decay rates. Nevertheless, the production of the rare-earth peak remains qualitatively rather robust (Fig. 5), at least for the three additional sets of nuclear models tested here.

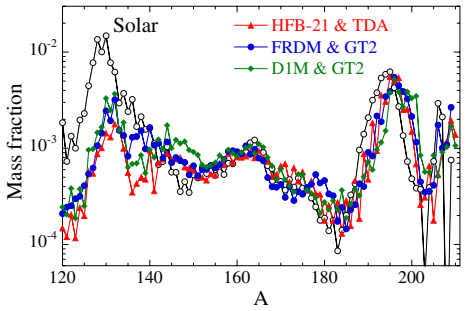

FIG. 5 (color online). Same as Fig. 4 but with abundance distributions obtained with three additional sets of nuclear rates, namely reaction rates obtained with the D1M [57] or FRDM [58] masses and β-decay rates from the GT2 or Tamm-Dancoff approximation (TDA) [59].

Conclusions.—The decompression of NS matter remains a promising site for the r process. This site is extremely robust with respect to many astrophysical uncertainties. We demonstrated here that the newly derived FFD based on the SPY model can consistently explain the abundance pattern in the rare-earth peak within this r-process scenario, in contrast to results with more phenomenological models predicting symmetric mass yields for the fissioning $A \simeq 278$ nuclei. Our new finding provides an even stronger hint to NSMs as possibly dominant site for the origin of $A > 140$ r nuclei in the Universe. In particular, the robustness of the ejecta conditions and associated fission recycling as well as the good quantitative agreement of the theoretical and solar abundances are fully compatible with the amazing uniformity of the rare-earth abundance patterns observed in many metal-poor stars [31].

The unexpected doubly asymmetric FFD predicted by SPY also opens new perspectives in theoretical and experimental nuclear physics concerning specific fission modes related to the nuclear structure properties of exotic nuclei. Dynamical mean field calculations [55] should quantitatively confirm the fission yields predicted by SPY, and future experiments producing fission fragments similar to those predicted by the doubly asymmetric fission mode could reveal the nuclear properties of the corresponding fission fragments.

S. G. acknowledges financial support of F. N. R. S. and "Actions de recherche concertées (ARC)" from the "Communauté française de Belgique". A. B. and H.-T. J. acknowledge support by Deutsche Forschungsgemeinschaft through the Transregional Collaborative Research Center SFB/TR 7 "Gravitational Wave Astronomy" and the

Cluster of Excellence EXC 153 "Origin and Structure of the Universe". A. B. received support from the Marie Curie Intra-European Fellowship within the 7th European Community Framework Programme (IEF 331873).

[1] M. Arnould, S. Goriely, and K. Takahashi, Phys. Rep. **450**, 97 (2007).
[2] S. Wanajo, H.-T. Janka, and B. Müller, Astrophys. J. Lett. **726**, L15 (2011).
[3] H.-T. Janka, Annu. Rev. Nucl. Part. Sci. **62**, 407 (2012).
[4] A. Arcones and F. Montes, Astrophys. J. **731**, 5 (2011).
[5] J. M. Lattimer and D. N. Schramm, Astrophys. J. **192**, L145 (1974).
[6] J. M. Lattimer and D. N. Schramm, Astrophys. J. **210**, 549 (1976).
[7] D. Eichler, M. Livio, T. Piran, and D. N. Schramm, Nature (London) **340**, 126 (1989).
[8] B. S. Meyer, Astrophys. J. **343**, 254 (1989).
[9] M. Ruffert, H.-T. Janka, G. Schäfer, Astron. Astrophys. **311**, 532 (1996).
[10] M. Ruffert, H.-T. Janka, K. Takahashi, and G. Schäfer, Astron. Astrophys. **319**, 122 (1997).
[11] S. Rosswog, M. Liebendörfer, F.-K. Thielemann, M. B. Davies, and T. Piran, Astron. Astrophys. **341**, 499 (1999).
[12] C. Freiburghaus, S. Rosswog, and F.-K. Thielemann, Astrophys. J. **525**, L121 (1999).
[13] L. F. Roberts, D. Kasen, W. H. Lee, and E. Ramirez-Ruiz, Astrophys. J. Lett. **736**, L21 (2011).
[14] S. Rosswog, Phil. Trans. R. Soc. A **371**, 20120272 (2013).
[15] S. Rosswog, O. Korobkin, A. Arcones, and F.-K. Thielemann, arXiv:1307.2939.
[16] K. Hotokezaka, K. Kiuchi, K. Kyutoku, H. Okawa, Y. I. Sekiguchi, M. Shibata, and K. Taniguchi, Phys. Rev. D **87**, 024001 (2013).
[17] S. Goriely, A. Bauswein, and H.-T. Janka, Astrophys. J. Lett. **738**, L32 (2011).
[18] A. Bauswein, S. Goriely, and H.-T. Janka, Astrophys. J. **773**, 78 (2013).
[19] M. Dominik, K. Belczynski, C. Fryer, D. E. Holz, E. Berti, T. Bulik, I. Mandel, and R. O'Shaughnessy, Astrophys. J. **759**, 52 (2012).
[20] V. Kalogera *et al.*, Astrophys. J. **601**, L179 (2004); V. Kalogera *et al.*, Astrophys. J. **614**, L137(E) (2004).
[21] Y.-Z. Qian, Astrophys. J. **534**, L67 (2000).
[22] B. D. Metzger, G. Martínez-Pinedo, S. Darbha, E. Quataert, A. Arcones, D. Kasen, R. Thomas, P. Nugent, I. V. Panov, and N. T. Zinner, Mon. Not. R. Astron. Soc. **406**, 2650 (2010).
[23] L.-X. Li and B. Paczyński, Astrophys. J. **507**, L59 (1998).
[24] J. Barnes and D. Kasen, Astrophys. J. **775**, 18 (2013).
[25] M. Tanaka and M. K. Hotokezaka, Astrophys. J. **775**, 113 (2013).
[26] D. Grossman, O. Korobkin, S. Rosswog, and T. Piran, arXiv:1307.2943.
[27] S. R. Kulkarni, arXiv:astro-ph/0510256.
[28] E. Berger, W. Fong, and R. Chornock, Astrophys. J. **774**, 23 (2013).
[29] N. R. Tanvir, A. J. Levan, A. S. Fruchter, J. Hjorth, K. Wiersema, R. Tunnicliffe, and A. de Ugarte Postigo, Nature (London) **500**, 547 (2013).
[30] O. Korobkin, S. Rosswog, A. Arcones, and C. Winteler, Mon. Not. R. Astron. Soc. **426**, 1940 (2012).
[31] C. Sneden, J. J. Cowan, and R. Gallino, Annu. Rev. Astron. Astrophys. **46**, 241 (2008).
[32] R. Oechslin, H.-T. Janka, and A. Marek, Astron. Astrophys. **467**, 395 (2007).
[33] A. Bauswein, H.-T. Janka, and R. Oechslin, Phys. Rev. D **82**, 084043 (2010).
[34] S. Typel, G. Röpke, T. Klähn, D. Blaschke, and H. H. Wolter, Phys. Rev. C **81**, 015803 (2010).
[35] M. Hempel and J. Schaffner-Bielich, Nucl. Phys. **A837**, 210 (2010).
[36] K. Belczynski, R. O'Shaughnessy, V. Kalogera, F. Rasio, R. E. Taam, and T. Bulik, Astrophys. J. Lett. **680**, L129 (2008).
[37] S. Goriely, N. Chamel, H.-T. Janka, and J. M. Pearson, Astron. Astrophys. **531**, A78 (2011).
[38] Y. Xu, S. Goriely, A. Jorissen, G. L. Chen, and M. Arnould, Astron. Astrophys. **549**, A106 (2013).
[39] A. J. Koning, S. Hilaire, and M. C. Duijvestijn, AIP Conf. Proc. **769**, 1154 (2005).
[40] S. Goriely, S. Hilaire, and A. J. Koning, Astron. Astrophys. **487**, 767 (2008).
[41] S. Goriely, N. Chamel, and J. M. Pearson, Phys. Rev. C **82**, 035804 (2010).
[42] T. Tachibana, M. Yamada, and Y. Yoshida, Prog. Theor. Phys. **84**, 641 (1990).
[43] S. Goriely, M. Samyn, and J. M. Pearson, Phys. Rev. C **75**, 064312 (2007).
[44] S. Goriely, S. Hilaire, A. J. Koning, M. Sin, and R. Capote, Phys. Rev. C **79**, 024612 (2009).
[45] T. Kodoma and K. Takahashi, Nucl. Phys. **A239**, 489 (1975).
[46] S. Panebianco, J.-L. Sida, H. Goutte, J.-F. Lemaître, N. Dubray, and S. Hilaire, Phys. Rev. C **86**, 064601 (2012).
[47] S. Hilaire and M. Girod, Eur. Phys. J. A **33**, 237 (2007).
[48] B. D. Wilkins, E. P. Steinberg, and R. R. Chasman, Phys. Rev. C **14**, 1832 (1976).
[49] J. F. Lemaître *et al.*, Fifth International Workshop on Nuclear fission and Fission-Product Spectroscopy (to be published).
[50] N. Dubray, H. Goutte, and J.-P. Delaroche, Phys. Rev. C **77**, 014310 (2008).
[51] N. Dubray and D. Regnier, Comput. Phys. Commun. **183**, 2035 (2012).
[52] K.-H. Schmidt and B. Jurado, Phys. Rev. Lett. **104**, 212501 (2010).
[53] S. Goriely, S. Hilaire, A. J. Koning, A. Bauswein, and H.-T. Janka, Phys. Procedia **47**, 115 (2013).
[54] M. R. Mumpower, G. C. McLaughlin, and R. Surman, Astrophys. J. **752**, 117 (2012).
[55] H. Goutte, J.-F. Berger, P. Casoli, and D. Gogny, Phys. Rev. C **71**, 024316 (2005).
[56] S. Goriely, Astron. Astrophys. **342**, 881 (1999).
[57] S. Goriely, S. Hilaire, M. Girod, and S. Péru, Phys. Rev. Lett. **102**, 242501 (2009).
[58] P. Möller, J. R. Nix, W. D. Myers, and W. J. Swiatecki, At. Data Nucl. Data Tables **59**, 185 (1995).
[59] H. V. Klapdor, J. Metzinger, and T. Oda, At. Data Nucl. Data Tables **31**, 81 (1984).

Résumé

Les études sur la fission nucléaire et ses propriétés constituent encore aujourd'hui un défis aussi bien théorique qu'expérimental. En effet, la compréhension de ce processus met en jeu un grand nombre de propriétés complexes de la matière nucléaire (dynamique des systèmes à n-corps, effets collectifs, déformations des noyaux, effets de structure,...), ce qui rend la fission un laboratoire idéal pour étudier la physique nucléaire. Parmi les observables physiques les plus étudiées, aussi bien du point de vue expérimental que théorique, les distributions de masse et charge des noyaux issus de la fission, les fragments de fission, jouent un rôle clé. Tout d'abord, ces distributions nous permettent de comprendre comment le grand nombre de nucléons (protons et neutrons) du noyau fissionnant se partage entre les deux fragments qui sont formés lors de la fission. Ce partage de nucléons est très grandement piloté par la structure microscopique des noyaux fils et son étude nécessite donc une connaissance fine des propriétés quantiques de ces noyaux. Aux effets statiques dus à la structure microscopique des noyaux s'ajoutent des effets dynamiques, telle la viscosité de la matière nucléaire, et des effets collectifs tel la rotation et la vibration des noyaux.

La compréhension de tous ces effets requiert une connaissance expérimentale très large des propriétés des fragments de fission, et ceci pour un grand nombre de systèmes fissionnants et dans des domaines d'énergie très divers. C'est dans ce cadre qu'un programme expérimental de mesure des distributions des fragments de fission de nombreux actinides à été mené auprès d'installations aussi diverses que les spectromètres Lohengrin à l'ILL (Grenoble) dans le domaine thermique et VAMOS au GANIL (Caen) en cinématique inverse à plus haute énergie. Ces mesures ont permis d'explorer des régions de masse encore peu connues, ce qui a nécessité le développement de techniques expérimentales innovantes, en particulier grâce à l'utilisation de la spectrométrie gamma. L'expérience acquise dans ces développements expérimentaux a également permis de développer des nouveaux instruments tels le spectromètre FALSTAFF qui sera utilisé, entre autres, auprès de l'installation NSF de SPIRAL2 au GANIL ou encore, dans une application plus exotique, la TPC FIDIAS.

L'interprétation des nombreuses données expérimentales disponibles sur les distributions de fragments de fission fait appel, en fonction du degré de précision et de prédictibilité demandés, à des approches théoriques très hétérogènes allant des calculs purement microscopiques de champ moyen aux méthodes plus phénoménologiques liées, par exemple, à la description des modes de fission. Un voie théorique intermédiaire qui a fait l'objet de nombreux développements est le modèle statistique de point de scission dont une version nouvelle et originale, appelé SPY et qui utilise une description très avancée des propriétés microscopiques des noyaux, a permis de dériver les distributions des fragments de fission dans des régions inexplorées jusqu'alors. Cette approche a permis entre autres

d'apporter un éclairage intéressant sur le rôle de la structure microscopique des fragments dans la fission asymétrique d'éléments relativement légers tels le Mercure, ainsi que de proposer une interprétation originale sur le rôle de la fission des terres rares dans la nucléosynthèse explosive.

III

Annexes

Dossier candidature HDR

Le document suivant présente mon *Curriculum Vitæ*, un court résumé de mes activités de recherche, la liste des publications auxquelles j'ai contribué de manière significative, ainsi que la liste des conférences dans lesquelles j'ai pu présenter mes travaux. Ce document a été soumis à l'Université Paris Saclay dans le cadre de mon dossier de candidature à l'obtention de l'HDR et constitue un complement au contenu de ce manuscrit.

Stefano Matthias PANEBIANCO
Né (e) le 13/01/1978 (40 ans)
CEA Saclay – Irfu – Service de Physique Nucléaire
91191 Gif-sur-Yvette CEDEX
Tél. : 01 69 08 73 57
@ : stefano.panebianco@cea.fr
Nationalité : française / italienne

Ingénieur chercheur en physique nucléaire et subnucléaire

CEA Saclay – Irfu – Service de Physique Nucléaire

FORMATIONS ET DIPLÔMES

2002-2005 Doctorat en physique – Université de Paris Sud

1996-2001 Diplôme de Laurea en physique (mention *110/110 avec félicitations du jury*) – Université de Cagliari (Italie)

1991-1996 Baccalauréat scientifique (mention *60/60*) – Lycée Scientifique « A. Pacinotti », Cagliari (Italie)

A

EXPERIENCES PROFESSIONNELLES

2005- Ingénieur chercheur – CEA Saclay – Service de Physique Nucléaire

- Technical Coordinator et Deputy Project Leader du Muon Forward Spectrometer – ALICE (CERN)
- Responsable du développement du modèle de point de scission SPY
- Porte-parole d'expériences de mesure des rendements en masse en isotopique des fragments issus de la fission d'actinides (ILL, Grenoble)
- Responsable du développement d'une TPC (FIDIAS) pour la détection d'ions lourds de basse énergie
- Développement du spectromètre FALSTAFF (NFS, Ganil) pour la mesure en coïncidence des fragments de fission
- Mesure des fragments de fission en cinématique inverse auprès de l'expérience VAMOS (Ganil)
- Développement d'un détecteur de neutrons auprès de l'expérience fELISE (FAIR, GSI)
- Responsable des mesures neutroniques in-core auprès de la cible de spallation MEGAPIE (PSI). Co-convener du working group « Neutron measurements »
- Mesure de sections efficaces de capture et fission d'actinides mineurs, expérience MiniInca (ILL)

2002-2005 Doctorat – CEA Saclay – Service de Physique Nucléaire

- Mesure de la polarisation des gluons dans le nucléon (expérience COMPASS – CERN)
- Caractérisation des chambres à dérive
- Développement et fabrication d'une électronique de lecture rapide pour le détecteur RICH
  Resp. : Dr. Alain Magnon, Dr. Jean-Marc Le Goff

2002-2002 Stage pré-thèse – CERN et CEA Saclay

- Installation et caractérisation d'une chambre à dérive dans l'expérience COMPASS
  Resp. : Dr. Alain Magnon

2001-2002 Chargé de TD – Università degli studi di Cagliari (Italie)
- TD et TP d'électromagnétisme et optique géométrique (niveau L2)
  Resp. : Prof. Giorgio Spano

2000-2001 Stage de Master (*Laurea*) – INFN Cagliari (Italie)
- Développement, construction et caractérisation des chambres à muon du spectromètre de l'expérience ALICE (CERN)
  Resp. : Prof. Sergio Serci, Dr. Corrado Cicalo

PRINCIPALES EXPERIENCES D'ENCADREMENT

2012-2015 Jean-François Lemaître – Thèse de Doctorat – Université Paris Sud
Etude des fragments de fission au point de scission avec le modèle SPY
Directeur de thèse : Dr. Jean-Luc Sida

2011-2014 Charlotte Amouroux – Thèse de Doctorat – Université Paris Sud
Mesure des rendements de fission de l'Am-242 auprès du spectromètre Lohengrin à l'ILL.
Directeur de thèse : Dr. Olivier Serot

2012-2012 Jean-François Lemaître – Stage M2 NPAC – Université Paris Sud
Etude de l'interaction coulombienne au point de scission.

2011-2011 Charlotte Amouroux – Stage fin d'études – Phelma Grenoble
Etude de sensibilité des rendements isobariques et isotopiques des produits de fission des actinides sur la chaleur résiduelle des combustibles usés.

2011-2011 Jean-François Lemaître – Stage M1 – Université Paris Sud
Etude des densités d'états microscopiques issues de calculs HFB à température finie.

2010-2010 Laetitia Vernoud – Stage fin d'études – ENSI Caen
Développement d'une TPC pour la détection des fragments de fission.

2007-2009 Franco Michel Sendis – Post-doctorat
Simulation et analyse des mesures neutroniques auprès de l'expérience MEGAPIE.

2007-2007 Arthur Babouty – Stage M1 – Université Paris Sud
Etude du vieillissement de chambres à fission.

AUTRES EXPERIENCES PROFESSIONNELLES

2013- Président du Comité National des écoles « E2Phy »

2013- Président du Comité de Rédaction de « Reflets de la physique »

2011- Responsable du module « Travaux de Laboratoire » – M2 NPAC – Université Paris Sud

2011- Co-responsable de l'école d'été « Rencontres des deux infinis » – P2IO

2008-2011 Encadrant dans le module « Travaux de Laboratoire » – M2 NPAC – Université Paris Sud

2006-2012 Président de la division « Physique Nucléaire » de la Société Française de Physique

2005- Activité de formation et communication autour de la science (scolaires, grand public)

Activité de recherche

Diplômé de l'Université de Cagliari (Italie) en 2001, j'ai effectué ma thèse de doctorat entre 2002 et 2005 au sein du Service de Physique Nucléaire du CEA Saclay sur l'expérience COMPASS au CERN. Mon travail portait sur la détermination de la polarisation des gluons dans le nucléon par la mesure d'asymétries de spin dans des réactions de muon-production de mésons charmés (D^0 et D*). Je me suis impliqué aussi bien dans les aspects expérimentaux que dans l'analyse et l'interprétation des données. Du côté expérimental, j'ai pu mettre à profit les compétences acquises pendant ma thèse de diplôme sur les détecteurs gazeux pour la trajectographie en physique des hautes énergies. En particulier, j'ai eu la responsabilité de l'installation, la caractérisation et l'exploitation des données d'un système de trois chambres à dérive de grande taille, assurant la couverture cinématique aux grands angles. Lors du travail d'analyse des données, je me suis fortement impliqué dans l'étude des performances d'identification des particules dans le spectromètre COMPASS, liées en particulier au détecteur RICH. En effet, la séparation entre pions et kaons est fondamentale pour la reconstruction des mésons charmés par leurs produits de décroissance. Pour améliorer les performances de ce détecteur, j'ai travaillé à un projet de remplacement de l'électronique frontale des chambres de trajectographie du RICH. Enfin, ma contribution principale à l'analyse des données a consisté à mettre en place une méthode originale pour la pondération des événements, ce qui a permis d'améliorer significativement la puissance statistique des mesures d'asymétrie. La détermination de la polarisation des gluons qui en a suivi, mesurée pour la première fois en fusion photon-gluon, a fait l'objet d'une publication importante. En effet, la valeur très petite de la polarisation qui a été mesurée était tout à fait inattendue et n'était pas en mesure, comme espéré, d'expliquer la « crise du spin ». Mon travail de thèse a été évidemment complété et précisé par des travaux successifs qui ont intégralement confirmé la mesure que j'avais obtenue et qui ton déclenché un fort débat au sein de la communauté. Dans le cadre de ma thèse, j'ai eu la charge de co-encadrer deux stagiaires de niveau M1, l'un, Bernardo Resende, sur la calibration des chambres à dérive, l'autre, Marianne Stare, sur la simulation Monte-Carlo du spectromètre COMPASS.

A

Immédiatement après la soutenance de ma thèse de doctorat en septembre 2005, j'ai été recruté en tant qu'ingénieur chercheur au Service de Physique Nucléaire du CEA Saclay pour travailler au sein du groupe « Mesures nucléaires et modélisation ». Dès le début, j'ai été impliqué dans deux projets de recherche : MEGAPIE et MiniInca.

Le projet MEGAPIE avait pour but de développer, construire et exploiter la première cible de spallation en plomb-bismuth liquide sous en faisceau de protons de haute puissance (1 MW). Ce type de cible est l'élément essentiel des réacteurs dits hybrides, ou ADS (Accelerator Driven System), systèmes innovants qui couplent un cœur de réacteur nucléaire sous-critique à un faisceau de proton apportant le contrôle de la réaction en chaine. Le projet, fruit d'une collaboration entre le Paul Scherrer Institut (Suisse) et un grand nombre de laboratoires en France et dans le monde, était dans sa phase de finalisation et la première irradiation a eu lieu en 2006. Dans ce cadre, j'ai pris la responsabilité de toutes les mesures neutroniques dites in-core. Ces mesures, réalisées à l'aide de chambres à fission micrométrique, développées au CEA dans le cadre d'une R&D très innovante avec l'entreprise PHOTONIS, ont permis de caractériser le flux de neutrons produits par la cible de spallation et d'en suivre l'évolution au cours du temps avec une précision et une rapidité de réaction tout à fait remarquables. En particulier, l'analyse de ces données a nécessité la mise en place d'une simulation très détaillée de la cible, des détecteurs, et de tout l'environnement de l'installation SINQ dans laquelle la

cible était installée. La comparaison entre les mesures et la simulation a mis en évidence l'importance de décrire très finement un nombre important de paramètres (température et impuretés dans l'eutectique Pb-Bi, blindages de l'installation, évolution du gaz des chambres à fission, etc.) dont le faisceau de protons, en particulier sa divergence angulaire, ce qui a fixé des limites contraignantes dans l'exploitation d'un tel système. De plus, les chambres à fission ont permis une reconstruction axiale du flux de neutrons et la mesure du taux d'incinération de plusieurs actinides (U-235, Am-241 et Np-237). Enfin, j'ai mené une campagne de mesure sur la production de neutrons retardés au sein de la cible MEGAPIE, ce qui a permis de déterminer avec bonne précision le taux de production de certains noyaux (essentiellement des isotopes du Br) produit lors des réactions de spallation. Ma participation dans ce projet a été importante également dans des tâches d'encadrement et management. En particulier, j'ai assuré le rôle de co-conveener du working group « Neutron measurements » avec le Dr. Luca Zanini et coordonné la rédaction de plusieurs articles de référence sur les cibles de spallation et la production de neutrons associée. J'ai également été invité à donner des cours sur la physique de la spallation dans plusieurs écoles organisées dans le cadre du projet européen Eurotrans. Enfin, j'ai encadré intégralement le travail postdoctoral du Dr. Franco Michel Sandis sur l'analyse des mesures neutroniques in-core et la simulation de la cible, travail qui a donné lieu à une publication de référence (**Nucl. Instrum. And Meth. B 268, 13, 2257-2271 (2010)**). J'ai ensuite œuvré pour que le Dr. Sandis soit recruté auprès de la NEA pour un poste d'officier de liaison pour la base de données nucléaire JEFF.

Parallèlement aux activités dans le projet MEGAPIE, j'ai été impliqué au sein du projet Mini-Inca, fruit d'une collaboration entre l'Institut Laue-Langevin de Grenoble, le CEA Saclay et le CEA Cadarache. Le projet visait à mesurer précisément des sections efficaces de capture radiative et de fission pour des actinides mineurs. Les mesures auxquelles j'ai participé, réalisées à l'ILL grâce au flux de neutrons thermiques le plus important au monde, visaient à déterminer les sections efficaces de fission et capture du Cm-243 et les sections efficaces de capture du Pu-238, Cm-248, Bk-249, Cf-249. En particulier, j'ai pris en charge une partie de l'analyse de ces données et animé une collaboration avec le Service de Spectrométrie de Masse du CEA Saclay avec lequel nous avons développé une technique expérimentale innovante de séparation isotopique en colonne, qui a donné lieu à une publication de référence. Les mesures des sections efficaces effectuées au sein du projet MiniInca ont toutes été publiés et présentées lors des conférences, et ont servi à la réévaluation des bases de données nucléaires (ENDF et JEFF). Dans le cadre de ce projet, j'ai pu contribuer à l'encadrement du travail de thèse Sébastien Chabod et Olivier Bringer, qui ont été par la suite recruté dans des laboratoires de recherche, et j'ai eu la responsabilité d'encadrer le stage M1 d'Arthur Babouty sur l'étude du vieillissement des chambres à fission.

Les travaux sur les projets Mini-Inca et MEGAPIE se sont terminés entre 2008 et 2009. Ces recherches présentaient un intérêt pour les applications nucléaires (systèmes innovants, transmutation des déchets) et il a semblé opportun de basculer sur un sujet d'étude plus centré sur la physique nucléaire fondamentale. La réflexion au sein de mon groupe de recherche, à laquelle j'ai largement contribué, a conduit à choisir l'étude de la fission nucléaire. En effet, bien qu'il s'agisse d'une réaction nucléaire largement étudiée, notamment dans le passé, des questions fondamentales existent encore aujourd'hui, en particulier concernant les caractéristiques des noyaux issus du processus de fission. En particulier, les rendements de production des produits de fission, aussi bien en fonction de leur masse que de leur isotopie, sont très compliqués à mesurer avec précision. D'autre part, les modèles de fission qui ont été développés depuis plus de 50 ans, sont pour la plupart basés sur des ingrédients phénoménologiques et nécessitent donc de données expérimentales précises pour assoir leur

fiabilité. J'ai donc initié une collaboration avec le Dr. Olivier Serot (CEA Cadarache), le Dr. Herbert Faust et le Dr. Ulli Koester (ILL) pour mener des campagnes de mesure des rendements des produits de fission auprès du spectromètre Lohengin à l'ILL. Nous avons pu mettre au point une technique expérimentale innovante, basée sur l'identification des noyaux par spectrométrie gamma, afin de mesurer avec une précision inégalée les rendements isotopiques des fragments lourds issus de la fission du Pu-239. Ce travail, grâce auquel j'ai pu contribuer à l'encadrement de la thèse d'Adeline Bail, a fait l'objet de nombreuses présentations en conférence et d'une publication dans PRC. Grâce aux développements expérimentaux réalisés dans ce travail, la collaboration a pu s'élargir au LPSC de Grenoble et a poursuivi par des nombreuses campagnes de mesure dans lesquelles j'ai eu le rôle de coordinateur pour le CEA Saclay. En particulier, j'ai mené en tant que porte-parole une campagne de plusieurs expériences consacrées à l'étude de la fission de l'Am-241. Ces mesures ont été l'objet principal de la thèse de Charlotte Amouroux, dont j'ai été l'encadrant, sous la responsabilité du Dr. Olivier Serot, son directeur de thèse. Après un stage de fin d'études effectué sur la chaleur produite par les produits de fission, la thèse de Charlotte Amouroux a été consacré à la mise en place, la réalisation et l'analyse de la mesure des rendements en masse et isotopiques issus de la fission den l'Am-241 dans le domaine thermique auprès du spectromètre Lohengrin. Ces mesures, effectuées pour la première fois en double capture sur un noyau à courte durée de vie et présentant un état isomère, ont montré des discordances entre les différentes bibliothèques de données nucléaires et ont permis également l'amélioration du code de calcul GEF, développé au GSI (Allemagne) par le Prof. Karl Heinz Schmidt. Parallèlement aux travaux effectués dans le cadre de cette thèse, j'ai participé aux mesures sur d'autres noyaux, en particulier l'U-233 et le Pu-241, et contribué à l'encadrement des thésards qui ont analysé ces expériences (Florence Martin et Abdelaziz Chebboubi). Tous ces travaux ont fait l'objet de nombreuses présentations en conférence et d'articles publiés ou en cours de finalisation. Bien que les activités de cette collaboration soient terminées, elles ont permis de lancer un nouveau programme de recherche, orienté sur l'étude de la spectroscopie gamma des fragments de fission (projet FIPPS).

A

Afin de complémenter les mesures obtenues dans le domaine thermique, j'ai fortement contribué au développement d'expériences auprès d'autres installations afin de déterminer les rendements de fission des actinides dans le domaine rapide. Dans ce cadre, j'ai participé à des mesures effectuées en cinématique inverse auprès du détecteur VAMOS au Ganil, en collaboration avec le Dr. Fanny Farget et au développement d'un projet innovant, appelé fELISE, pour effectuer des mesures, toujours en cinématique inverse, auprès de la future installation FAIR au GSI, avec le Dr. Julien Taieb du CEA DAM Ile de France. Ces deux projets ont fait l'objet de publications auxquelles j'ai largement contribué. L'expérience acquises sur ces deux projets m'a permis de développer, en collaboration avec le Dr. Diane Doré au sein de mon équipe, un dispositif expérimental, appelé FALSTAFF, pour la mesure en coïncidence de la masse, la charge nucléaire et l'énergie cinétique des fragments de fission auprès de la future installation NFS au Ganil. Le développement de ce dispositif, basé sur une mesure combinée de temps de vol et d'énergie résiduelle, a nécessité l'utilisation de détecteurs d'électrons secondaires et de chambres à ionisation en configuration axiale. Dans ce cadre, j'ai contribué à l'encadrement du travail post-doctoral du Dr. Cedric Golabek et je contribue actuellement à l'encadrement de la thèse de Loic Thuillez. Le projet est actuellement dans sa phase de finalisation de la R&D et la réalisation et l'installation du dispositif sont prévues pour la fin de l'année 2016.

Dans le cadre de l'étude de la fission en cinématique directe, les difficultés expérimentales liées à la détermination des pertes d'énergies d'ions lourds de basse énergie dans la matière, m'ont donné l'idée en 2009 de développer un dispositif à partir des techniques utilisées en physique

des hautes énergies et auxquelles j'avais été formé pendant mes années d'études universitaires et doctoraux. J'ai donc crée une collaboration entre le CEA Saclay et le laboratoire Demokritos (Athènes), pour réaliser une chambre à projection temporelle (TPC) basé sur le système de lecture Micromegas pour la détection des fragments de fission. Ce travail novateur a amené à la conception, à la réalisation et la caractérisation d'un détecteur appelé FIDIAS et qui, pour la première fois, a montré la faisabilité d'une mesure trajectographique et calorimétrique d'ions lourds de basse énergie dans une TPC à pression atmosphérique. Les résultats obtenus ont fait l'objet d'une publication (**Nucl. Instrum. And Meth. A 735, 339-407 (2014)**) et ont été en partie menés grâce au travail postdoctoral du Dr. Francisco Iguaz dont j'ai assuré l'encadrement. De même, le projet a vu un apport important de Laetitia Vernoud, dont le stage de fin d'étude que j'ai encadré a porté sur la simulation de la TPC FIDIAS et l'inclusion dans le code GEANT4 d'une description plus réaliste des échanges de charge entre les ions lourds de basse énergie et le milieu gazeux qu'ils traversent. La TPC FIDIAS est actuellement utilisée à l'ILL pour des mesures à basse pression et à pression atmosphérique, en utilisant une électronique frontale innovante, appelée GET et développée au CEA Saclay, et dont j'ai contribué à déterminer le cahier des charges et les premières performances sur prototype.

Les nombreuses mesures effectuées depuis 2009 sur les rendements en masse et isotopiques des actinides, aussi bien dans le domaine thermique que rapide, m'ont convaincu qu'une modélisation purement phénoménologique du mécanisme de fission nucléaire n'était pas suffisante pour comprendre et expliquer un grand nombre d'effets physique de nature quantique (effets pair-impair, répartition de l'énergie d'excitation, effets collectifs, …). D'autre part, la modélisation de la fission par des techniques microscopiques de champs moyen (HFB) comporte des difficultés majeures, même avec les moyens de calcul dont on dispose aujourd'hui, et ne permet que le calcul d'un nombre assez réduit de cas. J'ai donc lancé en 2010 avec le Dr. Jean-Luc Sida (CEA Saclay) et le Dr. Stéphane Hilaire (CEA DAM Ile de France) un projet pour développer un modèle statistique de point de scission intégralement basé sur des ingrédients microscopiques issus de calculs HFB. Nous avons donc développé un code de calcul, appelé SPY, unique en son genre. SPY permet de calculer précisément l'énergie du système fissionnant au point de scission et de la répartir de manière statistique entre les deux fragments. Le calcul de l'énergie disponible à la scission, ainsi que la densité d'états permettant un traitement statistique de type micro-canonique, sont intégralement issus de calculs HFB avec l'interaction nucléaire de Gogny. L'utilisation de données microscopiques confère au modèle un pouvoir prédictif totalement inaccessible aux modèles phénoménologiques, tout en permettant d'effectuer des milliers de calculs nécessitant une puissance compatible avec les moyens de calcul dont on dispose aujourd'hui. Grâce à cette approche, nous avons pu expliquer, par exemple, l'origine d'une distribution asymétrique dans les rendements en masse des fragments issus de la fission du Hg-180. Ce travail (**Phys. Rev. C 92, 3, 034617 (2015)**) prouve que le rôle des fermetures des couches nucléaires déformées (en présence d'états isomériques en particulier), totalement négligé jusqu'à lors, est tout à fait prépondérant dans la dynamique de la fission de noyaux de faible masse, comme le mercure. De plus, dans le cadre d'une collaboration très fructueuse avec le Dr. Stéphane Goriely (ULB), nous avons pu fournir pour la première fois une explication aux abondances des terres rares (**Phys. Rev. Lett. 111, 24 (2013)**). En effet, l'utilisation du modèle SPY a permis d'effectuer des calculs de processus r dans la coalescence d'étoiles à neutrons en prenant en compte une description réaliste et détaillée de la fission. Il est apparu en particulier que les terres rares présentes dans l'univers pourraient avoir été en partie produites par la fission d'actinides extrêmement exotiques, à la limite de la drip-line neutron, qui présente dans ce cas une fission doublement asymétrique. Tous les développements autour du modèle SPY ont vu la contribution majeure de Jean-François Lemaître dont j'ai encadré les stages de M1 et M2, ainsi que la thèse de doctorat. Le

travail de thèse de Jean-François Lemaître a permis d'inclure et améliorer un grand nombre d'ingrédients et outils qui n'existaient pas dans la version du modèle que j'avais développée initialement, ce qui a permis un nombre impressionnant d'études systématiques qui a abouti à la rédaction d'un long article de référence, publié dans PRC.

En parallèle à mon travail de recherche, j'ai contribué, depuis mon recrutement au CEA, à un nombre très important d'activités liées à l'enseignement et à la transmission des savoirs scientifiques. En 2008, j'ai intégré l'équipe d'encadrement des travaux de laboratoire du M2 NPAC (Paris Sud), dont j'ai en partie modifié les pratiques et techniques pédagogiques en prenant la responsabilité du module en 2011. J'ai été également sollicité pour donner des cours de physique nucléaire dans plusieurs écoles d'été et j'ai moi-même contribué à en créer une, adressée aux étudiants de niveau L3, appelée « Rencontres des deux infinis ». Depuis 2013, je préside le comité national de l'école « E2Phy » qui s'adresse aux enseignants du secondaire. Je suis également engagé au sein de la Société Française de Physique : en particulier, j'ai été président de la Division Physique Nucléaire de 2006 à 2012 et depuis 2013 je préside le comité de rédaction de la revue « Reflets de Physique ». Cette ouverture, m'a motivé à organiser, au sein de mon laboratoire, des ateliers de philosophie de sciences en collaboration avec le laboratoire Larsim (CEA). Enfin, j'interviens très régulièrement auprès des scolaires et du grand public et je suis impliqué dans diverses activités de communication scientifique du CEA.

A

Depuis septembre 2015, j'ai entamé une phase de transition thématique. En effet, j'ai été nommé Deputy Project Leader et Technical Coordinator du projet MFT (Muon Forward Tracker) au sein de l'expérience ALICE au CERN. Le travail au sein de l'expérience ALICE constitue un retour aux sources puisque j'y ai effectué ma thèse de diplôme entre 2000 et 2001. Dans ce cadre, j'ai la responsabilité de mener à bien le développement et la fabrication d'un spectromètre équipé de capteurs CMOS pour instrumenter la région avant d'ALICE et permettre des mesures totalement inédites en améliorant la reconstruction des muons, notamment à bas P_T. Mes activités sur les réactions nucléaires, et notamment la fission, sont donc en train de se réduire progressivement pour être totalement arrêtées d'ici la fin 2016.

Liste des publications

(La présente liste n'inclue que les articles publiés dans des journaux à comité de lecture et dans lesquels sont présentés des résultats scientifiques auquel j'ai contribué de manière significative.)

1. C. Bernet et al., *The 40 x 40 cm(2) gaseous microstrip detector micromegas for the high-luminosity COMPASS experiment at CERN*. Nucl. Instrum. And Meth. A 536, 1-2, 61-69 (2005)

2. E. S. Ageev et al. (COMPASS Collaboration), *Gluon polarization in the nucleon from quasi-real photoproduction of high-p(T) hadron pairs.* Phys. Lett. B 633, 25-32 (2006)

3. E.S. Ageev et al. (COMPASS Collaboration), *Spin asymmetry A1(d) and the spin-dependent structure function g1(d) of the deuteron at low values of x and Q**2*. Phys. Lett. B 647, 330-340 (2007)

4. V.Yu. Alexakhin et al. (COMPASS Collaboration), *The Deuteron Spin-dependent Structure Function g1(d) and its First Moment*. Phys. Lett. B 647, 8-17 (2007)

5. P. Abbon et al. (COMPASS Collaboration), *The COMPASS experiment at CERN*. Nucl. Instrum. Meth. A 577, 455-518 (2007)

6. P. Abbon et al., *Fast photon detection for particle identification with COMPASS RICH-1 detector*. Nucl. Instrum. Meth. A 580, 906-909 (2007)

7. P. Abbon et al., *A new analog sampling readout system for the COMPASS-RICH1 detector*. Nucl. Instrum. Meth. A 589, 362-369 (2008)

8. C. Fazio et al., *The MEGAPIE-TEST project: Supporting research and lessons learned in first-of a kind spallation target*. Nucl. Engin. And Des. 238, 1471-1795 (2008)

9. S. Panebianco et al,. *Neutronic characterization of the MEGAPIE target.* Annals of Nuclear Energy 36, 350-354 (2009)

10. P.M. Dighe et al., *Delayed gamma studies from photo-fission of ^{237}Np for nuclear waste characterization.* Annals of Nuclear Energy 36, 399-403 (2009)

11. L. Zanini et al., *Neutronic and nuclear Post-Test analysis of MEGAPIE*. PSI Bericht Nr. 08-04 (2008) ISSN 1019-0643

12. M. Alekseev et al. (COMPASS collaboration), *Gluon Polarisation in the Nucleon and Longitudinal Double Spin Asymmetries from Open Charm Muoproduction*. Phys. Lett. B 676, 31-38 (2009)

13. **F. Michel-Sendis et al., *Neutronic performance of the MEGAPIE spallation target under high power proton beam*. Nucl. Instrum. And Meth. B 268, 13, 2257-2271 (2010)**

14. A. Gourgiotis et al., *Accurate determination of Curium and Californium isotopic ratios by inductively coupled plasma quadrupole mass spectrometry (ICP-QMS) in Cm-248 samples for transmutation studies*. Intern. Journ. Of Mass Spectr. 291, 3, 101-107 (2010)

15. N. Thiollière et al., *Gas Production in the MEGAPIE Spallation Target*. Nucl. Science and engineering 169, 2, 178-187 (2011)

16. A. Bail et al., *Isotopic yield measurement in the heavy mass region for (239)Pu thermal neutron induced fission*. Phys. Rev. C 84, 3, 034605 (2011)

17. L. Zanini et al., *Experience from the post-test analysis of MEGAPIE*. Journ. Of Nucl. Materials 415, 3, 367-377 (2011)

18. A. N. Antonov et al., *The electron-ion scattering experiment ELISe at the International Facility for Antiproton and Ion Research (FAIR)-A conceptual design study*. Nucl. Instrum. And Meth. A 637, 1 60-76 (2011)

19. L. Mathieu et al., *New neutron long-counter for delayed neutron investigations with the LOHENGRIN fission fragment separator*. Journ. Of Instrum. 7, P08029 (2012)

20. P. Pawlowski et al., *Neutron recognition in the LAND detector for large neutron multiplicity*. Nucl. Instrum. And Meth. A 694, 47-54 (2012)

21. S. Panebianco et al., *Role of deformed shell effects on the mass asymmetry in nuclear fission of mercury isotopes*. Phys. Rev. C 86, 6 (2012).

22. A. Gourgiotis et al., *Bk and Cf chromatographic separation and $^{249}Bk/^{248}Cm$ and $^{249}Cf/^{248}Cm$ elemental ratios determination by inductively coupled plasma quadrupole mass spectrometry*. Talanta 106, 39-44 (2013)

23. **S. Goriely et al., *New Fission Fragment Distributions and r-Process Origin of the Rare-Earth Elements.* Phys. Rev. Lett. 111, 24 (2013)**

24. M. Vostinar et al., *Beam tracking with micromegas & wire chambers in secondary electron detection configuration*. Journ. Of Instrum. 8, C12023 (2013)

25. **F. J. Iguaz et al., *The FIDIAS project: Development of a Micromegas TPC for the detection of low-energy heavy ions.* Nucl. Instrum. And Meth. A 735, 339-407 (2014)**

26. A. Blanc et al., *Fission Product Prompt γ-ray spectrometer: Development of an instrumented gas-filled magnetic spectrometer at the ILL*. Nucl. Instrum. And Meth. B 317, 333-337 (2014)

27. O.Serot et al., *Recent Results from Lohengrin on Fission Yields and Related Decay Properties*. Nuclear Data Sheets 119, 320-323 (2014)

28. F. Martin et al. *Measurements of the Mass and Isotopic Yields of the U-233(n(th),f) Reaction by the Lohengrin Spectrometer*. Nuclear Data Sheets 119, 328-330 (2014)

29. D. Doré et al., *FALSTAFF: A New Tool for Fission Fragment Characterization*. Nuclear Data Sheets 119, 346-348 (2014)

30. X. Ledoux et al., *The Neutrons for Science Facility at SPIRAL-2*. Nuclear Data Sheets 119, 353-356 (2014)

31. J. F. Lemaître et al., *Nuclear fission modelling with SPY*. Acta Physica Polonica B 46, 3, 585-589 (2015)

32. **J. F. Lemaître et al., *New statistical scission-point model to predict fission fragment observables.* Phys. Rev. C 92, 3, 034617 (2015)**

A

Liste des conférences

1. ISINN-14 - International Seminar on Interaction of Neutrons with Nuclei, Dubna (Russie), 24-27/05/2006. *Neutron-induced cross section measurements at ILL and MEGAPIE for minor actinide transmutation purposes* (**oral contribution**)

2. ND-2007 - International Conference on Nuclear Data for Science and Technology, Nice (France), 22-27/04/2007. *Neutronic performances of the MEGAPIE target* (**oral contribution**). *Delayed neutron measurement at the MEGAPIE target* (**poster**)

3. The Eight International Topical Meeting on Nuclear Applications and Utilisation of Accelerators, Pocatello, Idaho (USA), 29/07-02/08/2007. *Neutronic characterization of the MEGAPIE target* (**oral contribution**)

4. PHYSOR 2008 – Nuclear Power: a sustainable resource, Interlaken (Suisse), 14-19/09/2008. *Neutronic characterization of the MEGAPIE target* (**oral contribution awarded the publication in a ANE Special Issue**)

5. **FINUSTAR 3 - Frontiers In NUclear STructure, Astrophysics and Reactions**, Rhodos (Grèce), 23-27/08/2010, *Development of a Micromegas TPC for Low Energy Heavy Ions Measurement for Nuclear Fission and Astrophysics Applications* (**oral contribution**)

6. 3rd Workshop on Level Density and Gamma Strength, Oslo (Norvège), 23-27/05/2011, *SPY: a microscopical statistical scission-point model to predict fission fragment distributions. A discussion about the level densities to be used* (**oral contribution**)

7. 3rd International Workshop on Nuclear Data Evaluation for Reactor applications, Aix-en-Provence (France), 25-28/09/2012, *SPY: a microscopic statistical scission-point model to predict fission fragment distributions* (**oral contribution**)

8. 4th International Workshop on Compound-Nuclear Reactions and Related Topics, São Paulo, Brazil, 7-11/10/2013, *SPY: A new scission-point model based on microscopic inputs to predict fission fragments properties* (**oral contribution**). *FALSTAFF: a novel apparatus for fission fragment characterization* (**oral contribution**)

9. Workshop on gas filled magnets for nuclear fission and fission product spectroscopy, Grenoble (France), 20-22/05/2014, *From Lohengrin to FIPPS: what can we do about fission* (**invited oral contribution**)

10. Challenges in the microscopic description of nuclear large amplitude collective dynamics, Caen (France), 13-14/10/2014, *The SPY model: how a microscopic description of the nucleus can shed some light on fission* (**invited oral contribution**)

11. Second Internation Workshop on Perspectives on Nuclear Data for the Next Decade, Bruyères-le-Châtel (France), 14-17/10/2014, *The SPY model: how a microscopic description of the nucleus can shed some light on fission* (**invited oral contribution**)

12. JEFF-NEEDS joint Workshop on Nuclear Data Measurements, Issy-les-Moulineaux (France), 24-28/11/2014, *Development of the FALSTAFF spectrometer for the determination of fission fragment characteristics and neutron multiplicity* (**invited oral contribution**)

Bibliographie

[1] F. Marie, A. Letourneau, G. Fioni, O. Déruelle, C. Veyssière, H. Faust, P. Mutti, I. AlMahamid, and B. Muhammad, "Thermal neutron capture cross-section measurements of 243am and 242pu using the new mini-inca α- and γ-spectroscopy station," *Nuclear Instruments and Methods in Physics Research Section A: Accelerators, Spectrometers, Detectors and Associated Equipment* **556** no. 2, (2006) 547 – 555. http://www.sciencedirect.com/science/article/pii/S016890020502084X.

Cité page 11

[2] O. Bringer, *Mesures des sections efficaces de capture et potentielsd'incinération des actinides mineurs dans les hauts flux de neutrons : impact sur la transmutation des déchets*. PhD thesis, Grenoble INPG, 2007. *2 citations pages 11 and 34*

[3] A. Gourgiotis, H. Isnard, M. Aubert, E. Dupont, I. AlMahamid, G. Tiang, L. Rao, W. Lukens, P. Cassette, S. Panebianco, A. Letourneau, and F. Chartier, "Accurate determination of curium and californium isotopic ratios by inductively coupled plasma quadrupole mass spectrometry (icp-qms) in 248cm samples for transmutation studies," *International Journal of Mass Spectrometry* **291** no. 3, (2010) 101 – 107. http://www.sciencedirect.com/science/article/pii/S1387380610000503.

Cité page 11

[4] F. Michel-Sendis, S. Chabod, A. Letourneau, S. Panebianco, and L. Zanini, "Neutronic performance of the megapie spallation target under high power proton beam," *Nuclear Instruments and Methods in Physics Research Section B: Beam Interactions with Materials and Atoms* **268** no. 13, (2010) 2257 – 2271. http://www.sciencedirect.com/science/article/pii/S0168583X10003009.

Cité page 11

[5] J.-F. Berger, *La Fission : de la phénoménologie à la théorie*. Ecole Joliot-Curie, 2006.

Cité page 12

[6] C. Wagemans, *The Nuclear Fission Process*. CRC Press, 1991. *Cité page 12*

[7] V. Macary, E. Berthoumieux, D. Doré, S. Panebianco, D. Ridikas, J.-M. Laborie, and X. Ledoux, "Photofission of 235u and 237np with bremsstrahlung photons below 20 mev: Measurements of delayed neutron yields and time spectra," *Nuclear Technology* **168** no. 2, (Nov, 2009) 287–292. http://dx.doi.org/10.13182/NT09-A9196. *Cité page 14*

[8] C. Rodríguez-Tajes, M. Caamaño, O. Delaune, F. Farget, L. Audouin, C.-O. Bacri, J. Benlliure, E. Casarejos, E. Clement, D. Cortina, X. Derkx, A. Dijon, D. Doré,

B. Fernández-Domínguez, L. Gaudefroy, C. Golabek, A. Heinz, B. Jurado, A. Lemasson, A. Navin, C. Paradela, D. Ramos, T. Roger, M. Salsac, C. Schmitt, K.-H. Schmidt, A. Shrivastava, and J. Taieb, "Isotopic distributions of fission fragments from transfer-induced fission," *Physics Procedia* **47** (2013) 125 – 130. http://www.sciencedirect.com/science/article/pii/S1875389213004471. Scientific Workshop on Nuclear Fission Dynamics and the Emission of Prompt Neutrons and Gamma Rays, Biarritz, France, 28-30 November 2012. *Cité page 14*

[9] J. L. Rodríguez-Sánchez, J. Benlliure, J. Taïeb, H. Álvarez-Pol, L. Audouin, Y. Ayyad, G. Bélier, G. Boutoux, E. Casarejos, A. Chatillon, D. Cortina-Gil, T. Gorbinet, A. Heinz, A. Keli ć Heil, B. Laurent, J.-F. Martin, C. Paradela, E. Pellereau, B. Pietras, D. Ramos, C. Rodríguez-Tajes, D. M. Rossi, H. Simon, J. Vargas, and B. Voss, "Complete characterization of the fission fragments produced in reactions induced by ^{208}Pb projectiles on proton at 500a MeV," *Phys. Rev. C* **91** (Jun, 2015) 064616. https://link.aps.org/doi/10.1103/PhysRevC.91.064616. *Cité page 14*

[10] U. Köster, H. Faust, T. Materna, and L. Mathieu, "Experience with in-pile fission targets at lohengrin," *Nuclear Instruments and Methods in Physics Research Section A: Accelerators, Spectrometers, Detectors and Associated Equipment* **613** no. 3, (2010) 363 – 370. http://www.sciencedirect.com/science/article/pii/S0168900209018361. Target and Stripper Foil Technologies for High Intensity Beams. *Cité page 18*

[11] A. Bail, O. Serot, L. Mathieu, O. Litaize, T. Materna, U. Koster, H. Faust, A. Letourneau, and S. Panebianco, "Isotopic yield measurement in the heavy mass region for Pu-239 thermal neutron induced fission," *Phys. Rev.* **C84** (2011) 034605. *Cité page 19*

[12] F. Martin, *Étude des distributions en masse, charge nucléaire et énergie cinétique des produits de fission de l'233U(nth,f) et du 241Pu(nth,f) mesurées auprès du spectromètre de masse Lohengrin (ILL)*. PhD thesis, Université de Grenoble, 2013. *Cité page 34*

[13] F. Martin, C. Sage, G. Kessedjian, O. Sérot, C. Amouroux, C. Bacri, A. Bidaud, A. Billebaud, N. Capellan, S. Chabod, X. Doligez, H. Faust, U. Köster, A. Letourneau, T. Materna, L. Mathieu, O. Méplan, and S. Panebianco, "Measurements of the mass and isotopic yields of the 233u(nth,f) reaction by the lohengrin spectrometer," *Nuclear Data Sheets* **119** (2014) 328 – 330. http://www.sciencedirect.com/science/article/pii/S0090375214006243. *Cité page 34*

[14] C. Amouroux, *Mesure des rendements de fission de l'Am-242 auprès du spectromètre Lohengrin (réacteur ILL) et amélioration et validation du code semi empirique GEF*. PhD thesis, Université Paris Sud, 2014. *Cité page 34*

[15] K.-H. Schmidt, B. Jurado, C. Amouroux, and C. Schmitt, "General description of fission observables: Gef model code," *Nuclear Data Sheets* **131** (2016) 107 – 221. http://www.sciencedirect.com/science/article/pii/S0090375215000745. Special Issue on Nuclear Reaction Data. *3 citations pages 35, 82, and 95*

[16] https://www.oecd-nea.org/dbdata/jeff/. *Cité page 35*

[17] G. de France, A. Blanc, F. Drouet, M. Jentschel, U. Köster, P. Mutti, J. Régis, G. Simpson, T. Soldner, O. Stezowski, and et al., "Exogam at the ill: the exill campaign," *Journal of Physics: Conference Series* **966** (Feb, 2018) 012012. http://dx.doi.org/10.1088/1742-6596/966/1/012012. *Cité page 43*

[18] A. Blanc, A. Chebboubi, H. Faust, M. Jentschel, G. Kessedjian, U. KöSter, T. Materna, S. Panebianco, C. Sage, and W. Urban, "FIssion Product Prompt γ-ray spectrometer: Development of an instrumented gas-filled magnetic spectrometer at the ILL," *Nucl. Instrum. Meth.* **B317** (2013) 333–337. *Cité page 43*

[19] A. Blanc *et al.*, "From EXILL (EXogam at the ILL) to FIPPS (FIssion Product Prompt γ-ray Spectrometer)," *EPJ Web Conf.* **93** (2015) 01015. *Cité page 43*

[20] S. Panebianco, D. Doré, F. Farget, F. R. Lecolley, G. Lehaut, T. Materna, J. Pancin, and T. Papaevangelou, "FALSTAFF: a novel apparatus for fission fragment characterization," *EPJ Web Conf.* **69** (2014) 00021. *Cité page 46*

[21] L. Thulliez, *Caractérisation des fragments de fission et développement du dispositif expérimental FALSTAFF*. PhD thesis, Université Paris Saclay, 2017. *Cité page 46*

[22] L. T. et al., "Impact of material thicknesses on fission observables obtained with the falstaff experimental setup," in *ND 2016: International Conference on Nuclear Data for Science and Technology*, E. W. Conf., ed., vol. 146. 2017. *Cité page 46*

[23] A. Oed, P. Geltenbort, R. Brissot, F. Gönnenwein, P. Perrin, E. Aker, and D. Engelhardt, "A mass spectrometer for fission fragments based on time-of-flight and energy measurements," *Nuclear Instruments and Methods in Physics Research* **219** no. 3, (1984) 569 – 574. http://www.sciencedirect.com/science/article/pii/0167508784902321. *Cité page 47*

[24] A. Oed, P. Geltenbort, F. Gönnenwein, T. Manning, and D. Souque, "High resolution axial ionization chamber for fission products," *Nuclear Instruments and Methods in Physics Research* **205** no. 3, (1983) 455 – 459. http://www.sciencedirect.com/science/article/pii/0167508783900091. *Cité page 47*

[25] A. Oed, P. Geltenbort, and F. Gönnenwein, "A new method to identify nuclear charges of fission fragments," *Nuclear Instruments and Methods in Physics Research* **205** no. 3, (1983) 451 – 453. http://www.sciencedirect.com/science/article/pii/016750878390008X. *Cité page 47*

[26] M. Frégeau and S. Oberstedt, "The fission-fragment spectrometer verdi," *Physics Procedia* **64** (2015) 197 – 203. http://www.sciencedirect.com/science/article/pii/S1875389215001431. Scientific Workshop on Nuclear Fission Dynamics and the Emission of Prompt Neutrons and Gamma Rays, THEORY-3. *Cité page 47*

[27] K. Meierbachtol, F. Tovesson, D. Shields, C. Arnold, R. Blakeley, T. Bredeweg, M. Devlin, A. Hecht, L. Heffern, J. Jorgenson, A. Laptev, D. Mader, J. O. Donnell, A. Sierk, and M. White, "The spider fission fragment spectrometer for fission product yield measurements," *Nuclear Instruments and Methods in Physics Research Section A: Accelerators, Spectrometers, Detectors and Associated Equipment* **788** (2015) 59 – 66. http://www.sciencedirect.com/science/article/pii/S0168900215002314. *Cité page 47*

[28] A. Smith, I. Tsekhanovich, J. Dare, D. Cullen, B. Varley, N. Lumley, T. Materna, U. Köster, M. Helmecke, and G. Simpson, "Fission-fragment spectroscopy with steff," in *Fourth International Conference Fission and properties of neutron-rich nuclei*, H. C. J.H. Hamilton, A.V. Ramayya, ed., pp. 193–199. World Scientific, Sanibel Island, United States, 2007. http://hal.in2p3.fr/in2p3-00376718. *Cité page 47*

[29] C. Guerrero, A. Tsinganis, E. Berthoumieux, M. Barbagallo, F. Belloni, F. Gunsing, C. Weiß, E. Chiaveri, M. Calviani, V. Vlachoudis, S. Altstadt, S. Andriamonje, J. Andrzejewski, L. Audouin, V. Bécares, F. Bečvář, J. Billowes, V. Boccone, D. Bosnar, M. Brugger, F. Calviño, D. Cano-Ott, C. Carrapiço, F. Cerutti, M. Chin, N. Colonna, G. Cortés, M. A. Cortés-Giraldo, M. Diakaki, C. Domingo-Pardo, I. Duran, R. Dressler, N. Dzysiuk, C. Eleftheriadis, A. Ferrari, K. Fraval, S. Ganesan, A. R. García, G. Giubrone, K. Göbel, M. B. Gómez-Hornillos, I. F. Gonçalves, E. González-Romero, E. Griesmayer, P. Gurusamy, A. Hernández-Prieto, P. Gurusamy, D. G. Jenkins, E. Jericha, Y. Kadi, F. Käppeler, D. Karadimos, N. Kivel, P. Koehler, M. Kokkoris, M. Krtička, J. Kroll, C. Lampoudis, C. Langer, E. Leal-Cidoncha, C. Lederer, H. Leeb, L. S. Leong, R. Losito, A. Manousos, J. Marganiec, T. Martínez, C. Massimi, P. F. Mastinu, M. Mastromarco, M. Meaze, E. Mendoza, A. Mengoni, P. M. Milazzo, F. Mingrone, M. Mirea, W. Mondalaers,

T. Papaevangelou, C. Paradela, A. Pavlik, J. Perkowski, A. Plompen, J. Praena, J. M. Quesada, T. Rauscher, R. Reifarth, A. Riego, F. Roman, C. Rubbia, M. Sabate-Gilarte, R. Sarmento, A. Saxena, P. Schillebeeckx, S. Schmidt, D. Schumann, P. Steinegger, G. Tagliente, J. L. Tain, D. Tarrío, L. Tassan-Got, S. Valenta, G. Vannini, V. Variale, P. Vaz, A. Ventura, R. Versaci, M. J. Vermeulen, R. Vlastou, A. Wallner, T. Ware, M. Weigand, T. Wright, and P. Žugec, "Performance of the neutron time-of-flight facility n_tof at cern," *The European Physical Journal A* **49** no. 2, (Feb, 2013) 27. https://doi.org/10.1140/epja/i2013-13027-6. *Cité page 47*

[30] W. Mondalaers and P. Schillebeeckx, "Gelina, a neutron time-of-flight facility for high-resolution neutron data measurements," in *Reasearch Infrastructures vol. II no. 2 p. 19-25.* Notiziario Neutroni e Luce di Sincrotrone, 2006. *Cité page 47*

[31] https://www.hzdr.de/db/Cms?pOid=10868&pNid=317. *Cité page 47*

[32] Wilson, J.N., Lebois, M., Qi, L., Amador-Celdran, P, Bleuel, D., Briz, J.A., Carroll, R., Catford, W., Witte, H. De, Doherty, D.T., Eloirdi, R., Georgiev, G., Gottardo, A., Goasduff, A., HadyÃ±ska-Klek, K., Hauschild, K., Hess, H., Ingeberg, V., Konstantinopoulos, T., Ljungvall, J., Lopez-Martens, A., Lorusso, G., Lozeva, R., Lutter, R., Marini, P., Matea, I., Materna, T., Mathieu, L., Oberstedt, A., Oberstedt, S., Panebianco, S., Podolyak, Zs., Porta, A., Regan, P.H., Reiter, P., Rezynkina, K., Rose, S.J., Sahin, E., Seidlitz, M., Serot, O., Shearman, R., Siebeck, B., Siem, S., Smith, A.G., Tveten, G.M., Verney, D., Warr, N., Zeiser, F., and Zielinska, M., "Studies of fission fragment yields via high-resolution î³-ray spectroscopy," *EPJ Web Conf.* **169** (2018) 00030. https://doi.org/10.1051/epjconf/201816900030. *Cité page 47*

[33] X. Ledoux *et al.*, "The Neutrons for Science Facility at SPIRAL-2," *Nucl. Data Sheets* **119** (2014) 353–356. *Cité page 47*

[34] Ledoux, X., Aïche, M., Avrigeanu, M., Avrigeanu, V., Balanzat, E., Ban-d'Etat, B., Ban, G., Bauge, E., Bélier, G., Bém, P., Borcea, C., Caillaud, T., Chatillon, A., Czajkowski, S., Dessagne, P., Doré, D., Fischer, U., Frégeau, M.O., Grinyer, J., Guillous, S., Gunsing, F., Gustavsson, C., Henning, G., Jacquot, B., Jansson, K., Jurado, B., Kerveno, M., Klix, A., Landoas, O., Lecolley, F.R., Lecouey, J.L., Majerle, M., Marie, N., Materna, T., Mràzek, J., Negoita, F., Novàk, J., Oberstedt, S., Oberstedt, A., Panebianco, S., Perrot, L., Plompen, A.J.M., Pomp, S., Prokofiev, A.V., Ramillon, J.M., Farget, F., Ridikas, D., Rossé, B., Sérot, O., Simakov, S.P., Šimečková, E., Štefánik, M., Sublet, J.C., Taïeb, J., Tarrio, D., Tassan-Got, L., Thfoin, I., and Varignon, C., "The neutrons for science facility at spiral-2," *EPJ Web Conf.* **146** (2017) 03003. https://doi.org/10.1051/epjconf/201714603003. *Cité page 47*

[35] G. Charpak, J. Derré, Y. Giomataris, and P. Rebourgeard, "Micromegas, a multipurpose gaseous detector," *Nuclear Instruments and Methods in Physics Research Section A: Accelerators, Spectrometers, Detectors and Associated Equipment* **478** no. 1, (2002) 26 – 36. http://www.sciencedirect.com/science/article/pii/S0168900201017132. Proceedings of the ninth Int.Conf. on Instrumentation. *2 citations pages 60 and 61*

[36] F. J. Iguaz, S. Panebianco, M. Axiotis, F. Druillole, G. Fanourakis, T. Geralis, I. Giomataris, S. Harissopulos, A. Lagoyannis, and T. Papaevangelou, "The FIDIAS project: Development of a Micromegas TPC for the detection of low-energy heavy ions," *Nucl. Instrum. Meth.* **A735** (2014) 399–407. *Cité page 61*

[37] B. D. Wilkins, E. P. Steinberg, and R. R. Chasman, "Scission-point model of nuclear fission based on deformed-shell effects," *Phys. Rev. C* **14** (Nov, 1976) 1832–1863. https://link.aps.org/doi/10.1103/PhysRevC.14.1832. *Cité page 74*

[38] S. Heinrich, *Développement d'un nouveau modèle de point de scission basé sur des ingrédients microscopiques.* PhD thesis, Université Paris Sud, 2006. *Cité page 74*

[39] J. Berger, M. Girod, and D. Gogny, "Time-dependent quantum collective dynamics applied to nuclear fission," *Computer Physics Communications* **63** no. 1, (1991) 365 – 374. http://www.sciencedirect.com/science/article/pii/001046559190263K. *Cité page 74*

[40] S. Hilaire and M. Girod, "Large-scale mean-field calculations from proton to neutron drip lines using the d1s gogny force," *The European Physical Journal A* **33** no. 2, (Aug, 2007) 237–241. https://doi.org/10.1140/epja/i2007-10450-2. *Cité page 74*

[41] A. N. A. et al., "New type of asymmetric fission in proton-rich nuclei," *Physical Review Letters* **105** no. 25, (2010) . *Cité page 75*

[42] S. Panebianco, J.-L. Sida, H. Goutte, J.-F. Lemaitre, N. Dubray, and S. Hilaire, "Role of deformed shell effects on the mass asymmetry in nuclear fission of mercury isotopes," *Phys. Rev.* **C86** (2012) 064601. *Cité page 75*

[43] J.-F. Lemaître, *Etude des fragments de fission au point de scission avec le modèle SPY*. PhD thesis, Université Paris Sud, 2015. *Cité page 81*

[44] J.-F. Lemaître, S. Panebianco, J.-L. Sida, S. Hilaire, and S. Heinrich, "New statistical scission-point model to predict fission fragment observables," *Phys. Rev.* **C92** no. 3, (2015) 034617. *Cité page 81*

[45] http://www-phynu.cea.fr/science_en_ligne/carte_potentiels_microscopiques/carte_potentiel_nucleaire_eng.htm. *Cité page 81*

[46] O. Litaize, O. Serot, and L. Berge, "Fission modelling with fifrelin," *The European Physical Journal A* **51** no. 12, (Dec, 2015) 177. https://doi.org/10.1140/epja/i2015-15177-9. *Cité page 82*

[47] S. Goriely, J. L. Sida, J. F. Lemaître, S. Panebianco, N. Dubray, S. Hilaire, A. Bauswein, and H. T. Janka, "New fission fragment distributions and r-process origin of the rare-earth elements," *Phys. Rev. Lett.* **111** no. 24, (2013) 242502, arXiv:1311.5897 [astro-ph.SR]. *Cité page 95*

[48] M. Arnould, S. Goriely, and K. Takahashi, "The r-process of stellar nucleosynthesis: Astrophysics and nuclear physics achievements and mysteries," *Physics Reports* **450** no. 4, (2007) 97 – 213. http://www.sciencedirect.com/science/article/pii/S0370157307002438. *Cité page 95*

Habilitation à Diriger des Recherches

Stefano Matthias PANEBIANCO

Few studies about nuclear fission

Quelques études autour de la fission nucléaire

Résumé

Les études sur la fission nucléaire et ses propriétés constituent encore aujourd'hui un défis aussi bien théorique qu'expérimental. Parmi les observables physiques les plus étudiées, les distributions de masse et charge des noyaux issus de la fission, les fragments de fission, jouent un rôle clé car elles permettent de comprendre comment le grand nombre de nucléons (protons et neutrons) du noyau fissionnant se partage entre les deux fragments qui sont formés lors de la fission.

Cette compréhension requiert une connaissance expérimentale très large des propriétés des fragments de fission, et ceci pour un grand nombre de système fissionnants et dans un large domaine en énergie. C'est dans ce cadre qu'un programme expérimental de mesure des distributions des fragments de fission de nombreux actinides à été mené auprès d'installations aussi diverses que les spectromètres Lohengrin à l'ILL (Grenoble) dans le domaine thermique et VAMOS au GANIL (Caen) en cinématique inverse à plus haute énergie. Ces mesures ont permis d'explorer des régions de masse encore peu connues et de développer des techniques expérimentales innovantes, en particulier grâce à la spectrométrie gamma. L'expérience acquise dans ces développements expérimentaux a également permis de développer des nouveaux instruments tels le spectromètre FALSTAFF qui sera utilisé, entre autres, auprès de l'installation NSF de SPIRAL2 au GANIL ou encore, dans une application plus exotique, la TPC FIDIAS.

L'interprétation des nombreuses données expérimentales sur les distributions des fragments de fission fait appel à des approches théoriques diverses. Un voie théorique qui a fait l'objet de nombreux développements est le modèle statistique de point de scission dont une version nouvelle et originale, appelée SPY et qui utilise une description très avancée des propriétés microscopiques des noyaux, a permis de dériver les distributions des fragments de fission dans des régions inexplorées . Cette approche a apporté un éclairage intéressant sur le rôle de la structure microscopique des fragments dans la fission asymétrique du Mercure, ainsi que de proposer une interprétation originale sur le rôle de la fission des terres rares dans la nucléosynthèse explosive.

Mots clés

Fission nucléaire, Lohengrin, ILL, Falstaff, NFS, point de scission, SPY, produits de fission, TPC, FIDIAS

Abstract

Studies on nuclear fission and its properties are still a challenge both theoretically and experimentally. Among the most studied physical observables, the mass and charge distributions of nuclei produced in fission, the so-called fission fragments, play a key role. First, these distributions allow us to understand how the large number of nucleons (protons and neutrons) of the fissioning nucleus are shared between the two fragments that are formed during fission.

The understanding of the process requires a very broad experimental knowledge of the properties of the fission fragments, and this for a large number of fissioning systems and in very wide energy range. It is within this framework that an experimental program for measuring the fission fragment distributions of several actinides has been conducted at facilities as diverse as the Lohengrin spectrometer at ILL (Grenoble) in the thermal domain and using the VAMOS spectrometer at GANIL (Caen) in inverse kinematics at higher energy. These measures have made it possible to explore regions of mass still poorly known, which has necessitated the development of innovative experimental techniques, in particular through the use of gamma spectrometry. The experience acquired in these experimental developments has also made it possible to develop new instruments such as the FALSTAFF spectrometer which will be used, among others, with the NSF installation of SPIRAL2 at GANIL or, in a more exotic application, the FIDIAS TPC.

The interpretation of the many experimental data available on fission fragment distributions makes use to different theoretical approaches. A theoretical approach that has been the subject of many developments is the statistical model of scission point. A new and original version of this model, called SPY and which uses a very advanced description of the microscopic properties of the nuclei, made it possible to derive the distributions of fission fragments in unexplored regions. This approach allowed, among other things, to shed interesting light on the role of the microscopic structure of fragments in the asymmetric fission of relatively light elements such as Mercury, as well as to propose an original interpretation on the role of fission of rare earth elements in explosive nucleosynthesis.

Key Words

Nuclear fission, Lohengrin, ILL, Falstaff, NFS, scission point, SPY, fission products, TPC, FIDIAS